Search for *CP* violation through an amplitude analysis of $D^0 \to K^+K^-\pi^+\pi^-$ decays at LHCb

THÈSE N^O 9166 (2018)

PAR

Maxime SCHUBIGER

EPFL

ÉCOLE POLYTECHNIQUE
FÉDÉRALE DE LAUSANNE

Suisse
2018

Science is not only a disciple of reason,
but also one of romance and passion.
— Stephen Hawking

Acknowledgements

These last four years have been an amazing journey through science and research. They have been made of a great deal of working, learning, coding, talking, meeting but especially a great deal of fun. It was a great privilege to work in an environment surrounded by passionate people always motivated and keen on helping one another.

I would like to start by thanking my thesis advisor, Olivier Schneider. Thank you for giving me the opportunity to do my PhD with you at the LPHE. It was a great pleasure to work with you and learn from you. I will always remember the alien named OTTO from your bachelor course. I am really thankful for all the time you always happily invested for me despite the many responsibilities you already have.

Thank you Maurizio Martinelli for being my direct supervisor throughout my thesis. I always felt safe to ask you stupid questions and I believe that this is one of the most important quality that a supervisor can have. I have learned a lot and this is greatly thanks to you.

Thank you Fred for supervising my service task on the magnetic field map. It was a delight working with you, you're always in a good mood and your motivation is contagious. Thank you Tatsuya for your challenging questions and for always suggesting a new angle to approach a problem. Thank you Aurelio for hiring me for a summer to work on a hardware project before my PhD, this allowed me to touch another branch of particle physics.

Thank you to all my colleagues from the lab for the great fun we had during these four years. Being in summer schools, in conferences or simply during lunch breaks at the "Banane", we always had very interesting discussions about the universe, alternate realities, Swiss votes, parsley, bidet, and many more. A special thanks to my fellow Swiss colleagues Axel, Brice and Olivier, with whom I spent most of my undergrad studies and formed the famous "quatuor du LPHE" during our PhD. What would we have said if in our first bachelor year, someone had told us we would all become doctors? Last but not least, thank you Erika, Esther and Corinne for all your help with the various administrative tasks and for the organisation of all the outings. I will keep fond memories of my time at the LPHE.

J'aimerais également remercier mes parents qui m'ont permis de faire des études, qui m'ont soutenu financièrement et moralement. Merci infiniment, sans vous je ne serais pas là aujourd'hui. Et finalement, un immense merci va à Marie-Céline. Merci pour ton soutien à toute épreuve, merci pour ta compréhension lors des périodes plus intenses, merci tout simplement d'être là. Je suis incroyablement heureux et fier de pouvoir désormais t'appeler ma femme. Je me réjouis de cette nouvelle aventure qui nous attend.

Lausanne, October 2018   Maxime

Abstract

This thesis presents a search for *CP* violation in the $D^0 \to K^+ K^- \pi^+ \pi^-$ Cabibbo-suppressed decay mode using an amplitude analysis. New sources of *CP* violation have to be discovered in order to explain the matter-antimatter imbalance observed in the universe today. *CP* violation has not been observed in charm decays up to now, where it is predicted by the Standard Model to be very small. This provides a clean environment to look for physics beyond the Standard Model, which could enhance *CP* violation in charm decays with, for example, the contribution of new particles entering through loop diagrams.

This analysis is performed with a sample of proton-proton collisions recorded by LHCb during 2011 and 2012 at centre-of-mass energies of 7 and 8 TeV, corresponding to an integrated luminosity of $3.0\,\text{fb}^{-1}$. LHCb is one of the four main experiments at CERN's Large Hadron Collider in Geneva in Switzerland. It is specialised in the study of *CP* violation in *b*- and *c*-hadron decays.

The D^0 candidates are selected from semileptonic *b*-hadron decays into $D^0 \mu^- X$ final states. More than 160 000 signal decays are studied, resulting in the most precise amplitude model of this decay to date. This amplitude model, built assuming *CP* conservation, is used to perform a search for *CP* violation. The result is compatible with no *CP* violation, with a sensitivity ranging from 1% to 15% on each amplitude. This result is compatible with the Standard Model predictions and is ruling out any large contribution from New Physics processes in the $D^0 \to K^+ K^- \pi^+ \pi^-$ decay mode.

The *CP* violation measurements presented here are statistically limited and will benefit from the addition of the Run 2 sample collected between 2015 and 2018 at a centre-of-mass energy of 13 TeV, which is expected to correspond to an integrated luminosity of $\sim 6\,\text{fb}^{-1}$. Beyond the additional luminosity, the increase in energy as well as various tracking and trigger improvements make this dataset much more powerful than the Run 1 sample. This thesis also presents one of the improvements made for Run 2, which is a more accurate description of the magnetic field of the dipole magnet through the development of a new field map.

Keywords: particle physics, LHCb, amplitude analysis, *CP* violation, charm decays, magnetic field.

Résumé

Cette thèse présente une recherche de violation de *CP* par une analyse en amplitudes du mode de désintégration $D^0 \to K^+ K^- \pi^+ \pi^-$. De nouvelles sources de violation de *CP* doivent être découvertes afin d'expliquer l'asymétrie entre matière et antimatière observée aujourd'hui dans l'univers. La violation de *CP* n'a pas encore été observée dans les désintégrations de hadrons charmés, où le Modèle Standard prédit de très petits effets. Cet environnement est propice à la recherche de physique au-delà du Modèle Standard, qui pourrait potentiellement amplifier la violation de *CP* dans les désintégrations charmées à l'aide, par exemple, de nouvelles particules contribuant à des diagrammes en boucle.

Cette analyse est réalisée avec un ensemble de collisions proton-proton enregistrées par LHCb en 2011 et 2012 à une énergie dans le centre de masse de 7 et 8 TeV, correspondant à une luminosité intégrée de $3.0\,\text{fb}^{-1}$. LHCb est l'une des quatre expériences principales au grand collisionneur de hadrons du CERN à Genève en Suisse. Elle est spécialisée dans l'étude de la violation de *CP* dans les désintégrations des hadrons *b* et *c*.

Les candidats D^0 sont sélectionnés à partir de désintégrations semi-leptoniques de hadrons *b* en états finaux $D^0 \mu^- X$. Plus de 160 000 désintégrations de signal sont étudiées, ce qui permet l'élaboration du modèle d'amplitudes le plus précis à ce jour pour ce mode de désintégration. Ce modèle d'amplitudes, construit en faisant l'hypothèse de conservation de *CP*, est utilisé pour rechercher la violation de *CP*. Le résultat est compatible avec la conservation de *CP*, avec une sensibilité allant de 1% à 15% selon les amplitudes. Ce résultat est en accord avec les prédictions du Modèle Standard et exclut toute grande contribution de Nouvelle Physique dans le mode de désintégration $D^0 \to K^+ K^- \pi^+ \pi^-$.

Les mesures de violation de *CP* présentées ici sont limitées statistiquement et bénéficieront de l'ajout de l'échantillon du Run 2 enregistré entre 2015 et 2018 à une énergie dans le centre de masse de 13 TeV, qui devrait correspondre à une luminosité intégrée de $\sim 6\,\text{fb}^{-1}$. Au-delà de la luminosité supplémentaire, l'augmentation en énergie ainsi que différentes améliorations dans la reconstruction et le système de déclenchement rendent cet échantillon beaucoup plus puissant que l'échantillon du Run 1. Cette thèse présente également l'une des améliorations apportées pour le Run 2, qui est une description plus précise du champ magnétique de l'aimant dipolaire à l'aide de l'élaboration d'une nouvelle carte de champ.

Mots-clés : physique des particules, LHCb, analyse en amplitudes, violation de *CP*, désintégrations de charme, champ magnétique.

Contents

Contents

Contents

1 | Introduction

Since the dawn of mankind, people have tried to explain and describe the world in which they were living. They first tried to explain natural phenomena happening around them, such as lightning or floods, as divine interventions. Over the centuries science moved from mystical beliefs to philosophical thinking and only recently to modern scientific methods. Well-known figures have helped to shape science as we know it today, such as Aristotle, Galileo, Newton, Darwin, Einstein, Schrödinger, etc.

One quest among many has always been to find the smallest constituents of matter. The first theory appeared in ancient Greece with the belief that everything was made of four elements: earth, water, fire and air. With the advance in science smaller and smaller scales were achieved, from small organisms to microbes, to molecules, to atoms until what we call today elementary particles such as leptons and quarks.

Elementary particle physics is the study of matter and fundamental interactions at the sub-atomic level. A very successful model developed in the last few decades, called the Standard Model (SM), has been accurately describing all results of particle physics experiments. It made many predictions that turned out to be true: the existence of the W and Z bosons, the gluon, the charm and top quarks and the now famous Higgs boson. The Higgs boson has been theorised in the 1960s and observed for the first time in 2012 at the LHC in ATLAS and CMS [1, 2].

The SM has been extensively tested and some hints for physics beyond the SM (BSM), also called New Physics (NP), have recently emerged [3–6], although still with low significance. One way to search for BSM phenomena is to increase the energy of the particle colliders to produce and observe directly new particles. Another approach, followed in this thesis and more generally in flavour physics, is to look for NP indirectly affecting decays of known particles.

Flavour physics is the study of interactions that act differently according to the flavour of particles, which is the property that distinguishes the elementary particles. Flavour physics

is very interesting because it relates to several fundamental questions that are still open and observations that are yet to be understood. For example the "SM flavour puzzle" refers to the fact that a hierarchy has been observed between the quarks masses and mixing angles, but not for the leptons. These observations have not been explained by any theory up to now.

Currently the leading experiment in flavour physics is LHCb. It is one of the four main experiments of the Large Hadron Collider (LHC) at CERN in Geneva. The LHCb collaboration, of which I am a member, involves around 800 physicists from 70 universities in 17 countries. Such a worldwide effort is needed in order to push further the boundaries of our knowledge of the universe.

1.1   The Standard Model

The Standard Model (SM) is currently the best verified theory of particle physics. The SM is a quantum field theory, which describes three of the four forces of nature: the strong nuclear force, the weak nuclear force and the electromagnetic force. The local gauge group of the SM can be written as

$$SU(3)_C \times SU(2)_L \times U(1)_Y, \tag{1.1}$$

which describes the various gauge symmetries of the SM. $SU(3)_C$, where C stands for colour, represents the symmetry of the strong nuclear force. It is described by quantum chromodynamics (QCD) and it contains eight generators that correspond to its eight mediators, the gluons. $SU(2)_L \times U(1)_Y$ represents the electroweak symmetry, where L stands for the coupling to left-handed particles and Y stands for the hypercharge. Due to the spontaneous symmetry breaking, the electroweak symmetry transforms into the electromagnetic symmetry $U(1)_{em}$, described by quantum electrodynamics (QED). The three generators of $SU(2)_L$ are the mediators of the weak force, the $W^{\pm}$ and the Z^0, and the generator of the $U(1)_Y$ is the photon, the mediator of the electromagnetic force.

There are therefore twelve gauge bosons, out of which nine are massless, the gluons and the photon and three are massive, the $W^{\pm}$ and the Z^0. These bosons are spin-1 particles. The SM also contains twelve spin-1/2 particles, which are the elementary constituents of matter. There are six leptons and six quarks, which are accompanied by their antimatter counterparts, the antileptons and the antiquarks. The last elementary particle of the SM is the Higgs boson, whose field gives mass to the other particles. All these particles, with their mass, charge and spin are shown in Fig. 1.1.

Figure 1.1 – Elementary particles of the SM listed with their mass, charge and spin [7].

The SM lagrangian $\mathscr{L}_{\text{SM}}$ can be written as

$$
\begin{aligned}
\mathscr{L}_{\text{SM}} = &- \frac{1}{4} F_{\mu\nu} F^{\mu\nu} && \text{the three fundamental forces and their gauge bosons,} \\
&+ i\overline{\psi} \slashed{D} \psi && \text{the interactions of the gauge bosons with the fermions,} \\
&+ \psi_i y_{ij} \psi_j \phi + h.c. && \text{how the fermions get their mass from the Higgs field,} \\
&+ \left| D_\mu \phi \right|^2 && \text{how the weak gauge bosons get their mass from the Higgs field,} \\
&- V(\phi) && \text{the Higgs field itself.}
\end{aligned}
\tag{1.2}
$$

As powerful and successful the SM is, it does not describe everything. A lot more work needs to be done in the field of particle physics. Some of the SM limitations are described below.

The SM does not describe gravity. Gravity is really well described by general relativity [8]. This theory, however, works well only on large scales. It breaks down at the particle level, where a quantum description of gravity is needed. Such a theory has not yet been established.

The big bang theory predicts that an equal amount of matter and antimatter has been created at the beginning. However, the cosmological observations show that the whole observable universe is made of matter today. One of the three necessary conditions to explain the disappearance of antimatter is *CP* violation, as described by the famous conditions of Sakharov [9]. However the amount of *CP* violation allowed in the SM is nowhere near enough to explain such a big difference today [10].

The SM contains 19 free parameters that need to be set from experiments: three masses for the electron, the muon and the tau, six quark masses, three mixing angles and one *CP* violation

phase for the CKM matrix, three gauge couplings for the three symmetry groups, the QCD vacuum angle, the Higgs vacuum expectation value and the Higgs mass. Some of these values seem to be fine-tuned as they span over many orders of magnitude without apparent reasons. Also there is no apparent symmetry in the hierarchy between the quark and lepton masses. All these observations lead to believe that the SM is only part of the story and that a more fundamental theory would make these parameters more natural.

Matter described by the SM, quarks and leptons, represent only 5% of the universe. Cosmological observations show that 27% of the universe is made of dark matter, that we have only observed through indirect gravitational effects, and 68% is dark energy, that we know nothing of [6, 11]. A lot of work is therefore invested in the search for dark matter. Some theorists think however that these observations could be explained by a revised theory of gravity (*e.g.* the MOND theory [12]).

The now well established phenomenon of neutrino flavour oscillations [5, 13, 14] implies that neutrinos have non-zero masses. This is however not predicted by the SM and therefore shows that the theory is not complete.

Finally, the SM assumes that lepton flavour universality is a fundamental symmetry of nature. It means that the couplings of leptons to the gauge bosons should be independent of their flavour. However recent measurements suggest that lepton flavour universality is perhaps broken. For example, while the decay rates of $B^0 \to K^{(*)} e^+ e^-$ and $B^0 \to K^{(*)} \mu^+ \mu^-$ are predicted to be almost equal by the SM, they may be different, as measured by LHCb [3, 15]. Similarly, hints of a non-SM ratio between the decay rates of $B^0 \to D^{(*)} \tau^+ \nu_\tau$ and $B^0 \to D^{(*)} \mu^+ \nu_\mu$ have been seen [4, 16]. In addition, small differences have been observed between the angular distributions of $B^0 \to K^* e^+ e^-$ and $B^0 \to K^* \mu^+ \mu^-$ in Refs. [17, 18] where they are predicted to be the same in the SM.

1.1.1 The Cabibbo-Kobayashi-Maskawa matrix

The Cabibbo-Kobayashi-Maskawa (CKM) matrix [19, 20] describes how the quarks of the SM mix between each other. Since there are three generations of quarks, it is a 3×3 matrix,

$$V_{\text{CKM}} = \begin{pmatrix} V_{ud} & V_{us} & V_{ub} \\ V_{cd} & V_{cs} & V_{cb} \\ V_{td} & V_{ts} & V_{tb} \end{pmatrix}, \tag{1.3}$$

where V_{ij} are complex values. Since the CKM matrix is unitary, only four parameters are needed to describe this matrix: three mixing angles $\theta_{12}, \theta_{13}, \theta_{23}$ and one phase δ. This phase is the only source of CP violation in the quark sector of the SM. The matrix can be written as

$$V_{\text{CKM}} = \begin{pmatrix} c_{12}c_{13} & s_{12}c_{13} & s_{13}e^{-i\delta} \\ -s_{12}c_{23} - c_{12}s_{23}s_{13}e^{i\delta} & c_{12}c_{23} - s_{12}s_{23}s_{13}e^{i\delta} & s_{23}c_{13} \\ s_{12}s_{23} - c_{12}c_{23}s_{13}e^{i\delta} & -c_{12}s_{23} - s_{12}c_{23}s_{13}e^{i\delta} & c_{23}c_{13} \end{pmatrix}, \tag{1.4}$$

Figure 1.2 – Sketch of the CKM matrix illustrating the size of its various elements.

where c_{ij} (s_{ij}) stands for $\cos\theta_{ij}$ ($\sin\theta_{ij}$). Another useful parametrisation of the CKM matrix is the Wolfenstein parametrisation [21]. It highlights the size of the various elements by providing the matrix as an expansion in powers of the parameter $\lambda = s_{12}$,

$$
V_{\mathrm{CKM}} = \begin{pmatrix} 1 - \lambda^2/2 & \lambda & A\lambda^3(\rho - i\eta) \\ -\lambda & 1 - \lambda^2/2 & A\lambda^2 \\ A\lambda^3(1 - \rho - i\eta) & -A\lambda^2 & 1 \end{pmatrix} + \mathcal{O}(\lambda^4), \tag{1.5}
$$

where

$$
A = \frac{s_{23}}{\lambda^2}, \qquad \rho = \cos\delta\,\frac{s_{13}}{\lambda s_{23}}, \qquad \eta = \sin\delta\,\frac{s_{13}}{\lambda s_{23}}. \tag{1.6}
$$

One can see from this parametrisation that the CKM matrix is rather close to the identity with small off-diagonal elements, as illustrated in Fig. 1.2. The original Wolfenstein parametrisation can be extended to higher orders of λ [22], which is needed in precision measurements,

$$
V_{\mathrm{CKM}} = \begin{pmatrix} 1 - \dfrac{\lambda^2}{2} - \dfrac{\lambda^4}{8} & \lambda & A\lambda^3(\rho - i\eta) \\ -\lambda + \dfrac{A^2\lambda^5}{2}\left[1 - 2\left(\rho + i\eta\right)\right] & 1 - \dfrac{\lambda^2}{2} - \dfrac{\lambda^4}{8}\left(1 + 4A^2\right) & A\lambda^2 \\ A\lambda^3(1 - \overline{\rho} - i\overline{\eta}) & -A\lambda^2 + \dfrac{A\lambda^4}{2}\left[1 - 2\left(\rho + i\eta\right)\right] & 1 - \dfrac{A^2\lambda^4}{2} \end{pmatrix} + \mathcal{O}(\lambda^6), \tag{1.7}
$$

where

$$
\overline{\rho} = \rho\left(1 - \frac{\lambda^2}{2}\right), \qquad \overline{\eta} = \eta\left(1 - \frac{\lambda^2}{2}\right). \tag{1.8}
$$

It is interesting to see that $\overline{\rho} + i\overline{\eta} = -\dfrac{V_{ud}V_{ub}^*}{V_{cd}V_{cb}^*}$ does not depend on a phase convention. Therefore, $\overline{\rho}$ and $\overline{\eta}$ are often used to parametrise the complex plane in which the unitarity of the CKM matrix is represented as triangles.

5
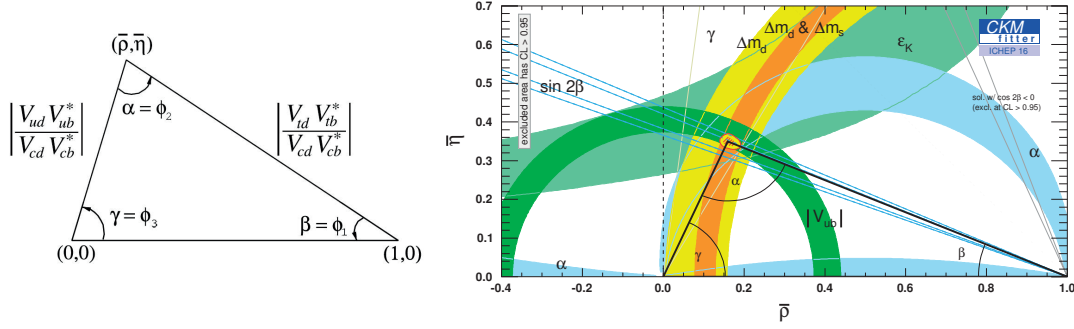
Figure 1.3 – Left: sketch of the unitarity triangle in the complex plane [24]. Right: current best constraints on the unitary triangle [25].

Indeed, the unitarity of the CKM matrix means that

$$V_{\mathrm{CKM}}^{\dagger} V_{\mathrm{CKM}} = V_{\mathrm{CKM}} V_{\mathrm{CKM}}^{\dagger} = 1\,, \tag{1.9}$$

which can be written as

$$\sum_{k=u,c,t} V_{ki}^{*} V_{kj} = \delta_{ij}\,, \quad i,j = d,s,b, \quad i \leq j\,, \tag{1.10}$$

$$\sum_{k=d,s,b} V_{ik}^{*} V_{jk} = \delta_{ij}\,, \quad i,j = u,c,t, \quad i \leq j\,. \tag{1.11}$$

Six of these conditions state that the sum of three complex numbers are equal to zero. This can be visualised as a triangle in the complex plane. The six resulting triangles have the same area, representing the amount of *CP* violation [23]. One of the triangles is often referred to as "the unitarity triangle" and is linked to the condition

$$V_{ud}^{*} V_{ub} + V_{cd}^{*} V_{cb} + V_{td}^{*} V_{tb} = 0\,. \tag{1.12}$$

This triangle is represented in Fig. 1.3, whose angles, α, β and γ, are well known *CP* violation observables.

1.2 *CP* violation

The *CP* symmetry, which is the combination of the charge (*C*) and the parity (*P*) symmetries, relates matter and antimatter. Together with the time reversal (*T*) symmetry, they form the *CPT* symmetry that is supposed to be an exact symmetry of nature holding for all physical phenomena. *CP* on the other hand is not an exact symmetry and has been observed to be violated in some processes. In the SM, there are three possible sources of *CP* violation. The first source is the weak phase in the CKM matrix, which has been extensively studied in the past few years. The second source is coming from the lepton counterpart of the CKM matrix, the Pontecorvo-Maki-Nakagawa-Sakata (PMNS) matrix, since it is established that neutrinos

have mass and that they can mix. Finally, *CP* violation should also be allowed in strong decays. Indeed, there is a term in the QCD Lagrangian that is able to violate *CP*. Experiments, however, have put stringent limits on this source as no *CP* violation has been observed in strong decays up to now. This is known as the strong *CP* problem.

Generally speaking, *CP* violation occurs when the probability of a certain process differs from that of the *CP*-conjugated process, *i.e.*

$$\Gamma(|i\rangle \rightarrow |f\rangle) \neq \Gamma(|\bar{i}\rangle \rightarrow |\bar{f}\rangle), \tag{1.13}$$

where $|i\rangle$ is some initial state, $|f\rangle$ some final state, and $|\bar{i}\rangle$ and $|\bar{f}\rangle$ their *CP* conjugates. *CP* violation manifests itself in three different ways.

Direct *CP* violation

Let $A_f = \langle f | \mathcal{H} | i \rangle$ and $\overline{A}_{\bar{f}} = \langle \bar{f} | \mathcal{H} | \bar{i} \rangle$ be the total amplitudes of a decay and its *CP* conjugate proceeding through an interaction described with an hamiltonian $\mathcal{H}$. Direct *CP* violation, or *CP* violation in the decay amplitudes, is defined by

$$\left| \frac{A_f}{\overline{A}_{\bar{f}}} \right| \neq 1. \tag{1.14}$$

It can be shown that at least two interfering amplitudes are needed in order to obtain direct *CP* violation. The total decay amplitude can be written as

$$A_f = \sum_k |a_k| e^{i\theta_k} e^{i\phi_k}, \tag{1.15}$$

where several complex amplitudes may contribute, each with a different modulus $|a_k|$, weak phase ϕ_k, and strong phase θ_k. The weak phase changes sign under *CP* whereas the strong phase stays invariant. Therefore, the amplitude of the *CP*-conjugated decay is written as

$$\overline{A}_{\bar{f}} = \sum_k |a_k| e^{i\theta_k} e^{-i\phi_k}. \tag{1.16}$$

Equation 1.14 implies that $|A_f|^2 - |\overline{A}_{\bar{f}}|^2$ must be different from zero. If there is only one amplitude contributing to the decay, this difference is trivially zero. Let's consider a process where two amplitudes contribute:

$$A_f = |a_1| e^{i(\theta_1 + \phi_1)} + |a_2| e^{i(\theta_2 + \phi_2)}, \quad \overline{A}_{\bar{f}} = |a_1| e^{i(\theta_1 - \phi_1)} + |a_2| e^{i(\theta_2 - \phi_2)}. \tag{1.17}$$

We obtain that

$$|A_f|^2 - |\overline{A}_{\bar{f}}|^2 = -4|a_1||a_2| \sin(\theta_1 - \theta_2) \sin(\phi_1 - \phi_2) \tag{1.18}$$

is nonzero when both the strong phase and the weak phase are different between the two contributing amplitudes.

CP violation in mixing

CP violation in mixing is defined as

$$\left|\frac{q}{p}\right| \neq 1. \tag{1.19}$$

Here p and q are two complex parameters defining the light (M_L) and heavy (M_H) mass eigenstates of a flavoured neutral meson,

$$|M_L\rangle = p|M^0\rangle + q|\overline{M}^0\rangle, \tag{1.20}$$

$$|M_H\rangle = p|M^0\rangle - q|\overline{M}^0\rangle, \tag{1.21}$$

with the normalisation $|p|^2 + |q|^2 = 1$ and where M^0 and $\overline{M}^0$ are the flavour eigenstates of the neutral meson. *CP* violation in mixing is a difference of transition rate between the two flavour eigenstates

$$\Gamma(|M^0\rangle \to |\overline{M}^0\rangle) \neq \Gamma(|\overline{M}^0\rangle \to |M^0\rangle). \tag{1.22}$$

CP violation in interference between mixing and decay

The third manifestation of *CP* violation is caused by the interference between the mixing and the decay amplitudes of a flavoured neutral meson. This happens when the meson can decay to a certain final state f either directly, $|M^0\rangle \to |f\rangle$, or first by mixing into its antiparticle, $|M^0\rangle \to |\overline{M}^0\rangle \to |f\rangle$. The interference between the two paths can introduce *CP* violation. The *CP*-violating observable is

$$\text{Im}\left(\frac{q}{p}\frac{\overline{A}_f}{A_f}\right) \neq 0, \tag{1.23}$$

which is non-zero in case of *CP* violation.

Experimental observations

CP violation was first observed in 1964 in the kaon system through the mixing between the K^0 and the $\overline{K}^0$ [26]. Then direct *CP* violation has been discovered in the decay $K \to \pi\pi$ [27–29]. More recently, *CP* violation has been observed in the decay of B mesons. It was first observed in 2001 in the interference of mixing and decay of the B^0 [30, 31]. Then direct *CP* violation was observed in the decay $B^0 \to K^+\pi^-$ [32, 33] and in B^+ decays [34–36]. And finally direct *CP* violation has been observed in the decay $B_s^0 \to K^+\pi^-$ [37].

$$V_{ud}^* V_{cd} \sim \lambda$$

$$\gamma_c \qquad V_{ub}^* V_{cb} \sim \lambda^5$$

$$\beta_c \qquad \alpha_c$$

$$V_{us}^* V_{cs} \sim \lambda$$
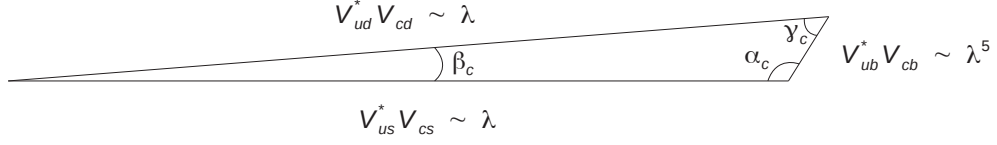
Figure 1.4 – Sketch of the charm unitarity triangle in the complex plane. For clarity purposes, the dimensions are not drawn to scale, the side $V_{ub}^* V_{cb}$ should be even smaller.

1.2.1 *CP* violation in charm

CP violation in charm decays has not been observed yet. Its prediction from the SM is very small, $\mathcal{O}(10^{-4} - 10^{-3})$ [38–40]. This can be explained by the fact that all the initial and final states particles of charmed hadron decays are made of quarks from the first two generations. This implies that, at tree level, these interactions are governed by a 2×2 real matrix, where no weak *CP*-violating phase exists. Access to the third generation can occur through loop corrections with virtual b quarks. However, these contributions are very small due to the CKM matrix elements $V_{ub}^* V_{cb}$. Indeed one can visualise this with the charm unitarity relation

$$V_{ud}^* V_{cd} + V_{us}^* V_{cs} + V_{ub}^* V_{cb} = 0, \qquad (1.24)$$

linked to the almost flat charm unitarity triangle shown in Fig. 1.4.

Precise predictions of the SM are however very difficult to compute due to the dominance of long-distance effects. Indeed short-distance effects (*i.e.* high-energy effects) can be computed using perturbative theories, while long-distance effects (*i.e.* low-energy effects) are non-perturbative QCD effects and therefore hard to compute.

NP processes could enhance *CP* violation in charm up to the percent level. Indeed, many theories have been proposed to extend the SM in order to fix some of its issues. Some of them have direct consequences on the amount of *CP* violation allowed in the charm sector. For example, a fourth generation of quarks could enhance the SM predictions by a factor 40 [41]. Another example is the addition of a scalar doublet, which could enhance *CP* violation to the percent level [42].

It is very important to study *CP* violation in charm decays. It is the only way to test this effect in the up-type quark sector, which is complementary to studies in the B and in the kaon systems. Furthermore, the fact that the SM contribution is small, means that there is a low SM background for NP searches. This makes the charm sector one of the cleanest place to look for NP [39, 43]. Finally, we have the opportunity to study such small effects thanks to the very large samples of charm decays collected at LHCb. The most precise measurement to date is the difference of integrated *CP* asymmetries computed between $D^0 \to K^+ K^-$ and

$D^0 \rightarrow \pi^+ \pi^-$ [44]

$$\Delta A_{CP} = A_{CP}(D^0 \rightarrow K^+ K^-) - A_{CP}(D^0 \rightarrow \pi^+ \pi^-) = (-1.0 \pm 0.8 \pm 0.3) \times 10^{-3}. \quad (1.25)$$

1.3 The $D^0 \rightarrow K^+ K^- \pi^+ \pi^-$ decay

1.3.1 Motivation

The determination of the resonant states contributing to multi-body D^0 decays is very important to make precise predictions of quantities like mixing and *CP* violation, or to interpret measurements of *CP* violation. The characterisation of such decays is also useful to perform other measurements, such as the contributions of strong phases in the various regions of the phase space. The $D^0 \rightarrow K^+ K^- \pi^+ \pi^-$ decay[1] studied in this thesis has some peculiarities that make it interesting for *CP* violation searches.

The decay $D^0 \rightarrow K^+ K^- \pi^+ \pi^-$ is singly Cabibbo-suppressed (SCS). It can be generated through various diagrams (see Fig. 1.5), whose interference gives rise to a weak phase allowing *CP* violation. New physics can enter through the loop diagrams and enhance *CP* violation [39]. Since *CP* violation is predicted by the SM to be very small in charm decays (see Sec. 1.2.1), any significant *CP* violation observation would be a sign for new physics [45].

As shown by previous analyses [46, 47], the $D^0 \rightarrow K^+ K^- \pi^+ \pi^-$ decay is dominated by amplitudes of the type $D^0 \rightarrow VV'$ and $D^0 \rightarrow AP$, V and V' indicating vector mesons ($J^P = 1^-$ where J is the spin of the particle and P its parity), A an axial meson ($J^P = 1^+$) and P a pseudoscalar meson ($J^P = 0^-$), like $D^0 \rightarrow \phi(1020)\rho(770)$, $D^0 \rightarrow K^*(892)^0 \bar{K}^*(892)^0$ or $D^0 \rightarrow K_1(1270)^+ K^-$. This decay mode contains also *P*-odd amplitudes, for example $D^0 \rightarrow VV'$ with angular momentum $L = 1$ between the two vector resonances, which could be particularly sensitive to *CP* violation.

Another point of interest is that both D^0 and $\bar{D}^0$ can decay to $K^+ K^- \pi^+ \pi^-$, therefore allowing for interference in the decay of mixed mesons, in which *CP* violation can potentially occur. This could happen for example in the $D^0 \rightarrow K_1(1270)^+ K^-$ amplitude, which is very suppressed in the *CP*-conjugate decay of the $\bar{D}^0$ meson. Therefore the study of the time evolution of $D^0 \rightarrow K_1(1270)^+ K^-$ and $D^0 \rightarrow \bar{D}^0 \rightarrow K_1(1270)^- K^+$ decays could highlight effects of *CP* violation in mixing.

Regarding *B*-meson decays, such final state is once more useful to study the effects of the interference between D^0 decaying directly and through mixing to the same final state. This feature is used in the so-called GGSZ technique [48] to measure the angle γ of the unitarity triangle with $B^\pm \rightarrow DK^\pm$ decays. In order to perform the analysis, however, a good amplitude model is required [49]. The current combination of the γ measurement at LHCb already uses the input from Cabibbo-favoured four-body D decays [50]. This thesis provides a model to perform the analysis with the $D^0 \rightarrow K^+ K^- \pi^+ \pi^-$ decay.

---

[1]Charge-conjugated states are implied throughout the document unless stated otherwise.
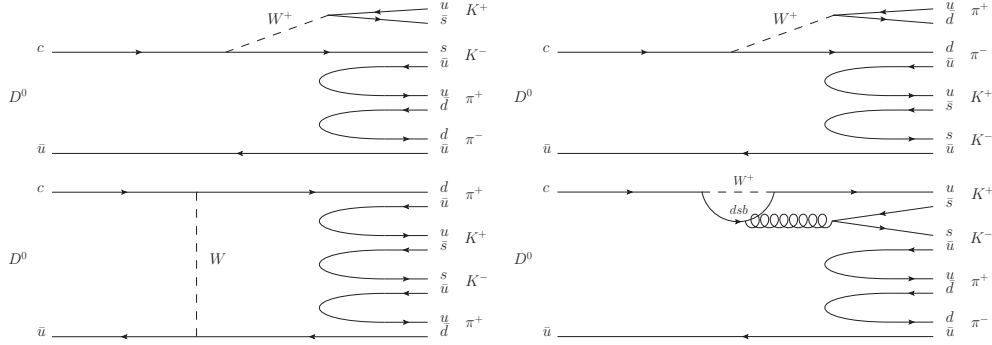
Figure 1.5 – $c \to s$ and $c \to d$ tree diagrams (top), exchange diagram (bottom left) and loop diagram (bottom right) of the $D^0 \to K^+ K^- \pi^+ \pi^-$ decay.

Aside all of the above, studying the amplitude distributions of $D^0 \to K^+ K^- \pi^+ \pi^-$ is an interesting topic by itself, since the current LHCb data sample allows the determination of the composition of such a complex decay with unprecedented precision.

1.3.2 State of the art

Several experiments have already studied $D^0 \to K^+ K^- \pi^+ \pi^-$ decays with the aim of determining the corresponding amplitude model.

The first attempt was made by the FOCUS collaboration in 2004 with a dataset of ∼ 1300 decays [51]. This analysis showed that the dominant components are $D^0 \to K_1(1270)^+ K^-$, $D^0 \to K_1(1400)^+ K^-$ and $D^0 \to \phi(1020)\rho^0(770)$.

A more precise determination of the model underlying the decay has been made by the CLEO collaboration in 2012 with a dataset of ∼ 3000 decays [46]. A first attempt at measuring *CP* violation has also been performed. In 2017 an analysis of CLEO legacy data [47] with an improved software for the model construction and fitting has superseded the previous results. No *CP* violation has been observed, where a sensitivity of 10% to 50% has been achieved on the various amplitudes. Their resulting model[2] is shown in Table 1.1.

At LHCb, where a significantly larger dataset is available, more than 160 000 signal decays in the Run 1 data have been used already to search for *CP* violation using T-odd correlations [52]. This analysis looked for global *CP* violation effects integrated over the phase space. The result is compatible with no *CP* violation.

---

[2]The notation used in this document for the decay chains omits to indicate the strong decay of the two-body resonances. The following decays are therefore implied throughout the document: $\phi(1020)^0 \to K^+ K^-$, $\rho(770)^0 \to \pi^+ \pi^-$, $\omega(782)^0 \to \pi^+ \pi^-$, $K^*(892)^0 \to K^+ \pi^-$ and $K^*(1430)^0 \to K^+ \pi^-$.

Table 1.1 – CLEO-legacy-data model for $D^0 \to K^+ K^- \pi^+ \pi^-$ [47]. The first quoted uncertainty is statistical, the second arises from systematic sources and the third arises from alternative models considered.

Contributing amplitude	Fit fraction [%]
$D^0 \to K_1(1270)^+ K^-, K_1(1270)^+ \to K^*(892)^0 \pi^+$	$5.5 \pm 1.4 \pm 2.7 \pm 2.0$
$D^0 \to K_1(1270)^+ K^-, K_1(1270)^+ \to K^*(1430)^0 \pi^+$	$6.1 \pm 1.2 \pm 1.3 \pm 1.3$
$D^0 \to K_1(1270)^+ K^-, K_1(1270)^+ \to \rho(770)^0 K^+$	$9.1 \pm 1.5 \pm 1.9 \pm 0.1$
$D^0 \to K_1(1270)^- K^+, K_1(1270)^- \to \rho(770)^0 K^-$	$5.4 \pm 0.7 \pm 1.1 \pm 0.7$
$D^0 \to K_1(1270)^+ K^-, K_1(1270)^+ \to \omega(782)^0 K^+$	$0.6 \pm 0.3 \pm 0.4 \pm 0.2$
$D^0 \to K_1(1400)^+ K^-, K_1(1400)^+ \to K^*(892)^0 K^-$	$12.4 \pm 2.6 \pm 3.9 \pm 5.0$
$D^0 \to K^*(1680)^+ K^-, K^*(1680)^+ \to K^*(892)^0 \pi^+$	$3.6 \pm 0.8 \pm 1.0 \pm 0.3$
$D^0 \to [K^*(892)^0 \overline{K}^*(892)^0]_{L=0}$	$4.5 \pm 0.8 \pm 1.1 \pm 1.7$
$D^0 \to [K^*(892)^0 \overline{K}^*(892)^0]_{L=1}$	$3.6 \pm 0.7 \pm 1.4 \pm 0.5$
$D^0 \to [K^*(892)^0 \overline{K}^*(892)^0]_{L=2}$	$4.0 \pm 0.6 \pm 0.7 \pm 0.2$
$D^0 \to [\phi(1020)^0 \rho(770)^0]_{L=0}$	$28.1 \pm 1.3 \pm 1.7 \pm 0.3$
$D^0 \to [\phi(1020)^0 \rho(770)^0]_{L=1}$	$1.6 \pm 0.3 \pm 0.6 \pm 0.3$
$D^0 \to [\phi(1020)^0 \rho(770)^0]_{L=2}$	$1.7 \pm 0.4 \pm 0.4 \pm 0.2$
$D^0 \to K^*(892)^0 [K^- \pi^+]_{L=0}$	$5.8 \pm 1.2 \pm 2.1 \pm 0.0$
$D^0 \to \phi(1020)^0 [\pi^+ \pi^-]_{L=0}$	$4.0 \pm 0.6 \pm 1.3 \pm 1.7$
$D^0 \to [K^+ K^-]_{L=0} [\pi^+ \pi^-]_{L=0}$	$11.1 \pm 1.2 \pm 2.1 \pm 0.7$
Sum	$106.9 \pm 4.5 \pm 6.9 \pm 6.1$

1.3.3 Analysis strategy

This analysis aims at a precise determination of the already known amplitudes contributing to the $D^0 \to K^+ K^- \pi^+ \pi^-$ decay, potential observations of previously unaccessible rare structures, and a search for *CP* violation in the individual amplitudes. It is based on events collected with the LHCb detector during Run 1 of the LHC (2011–2012), corresponding to an integrated luminosity of approximately $3\,\text{fb}^{-1}$.

Flavour-tagged D^0 mesons can be obtained from two main sources: semileptonic $B \to D^0 \ell^- X$ decays using the electric charge of the lepton ℓ^- as tag, and strong $D^{*+} \to D^0 \pi^+$ decays of promptly produced D^{*+} mesons using the electric charge of the soft π^+ as tag. The sample of D^0 mesons from prompt D^{*+} decays is slightly larger than the semileptonic sample; however, in Run 1, the HLT2 trigger line uses an asymmetric reconstruction between the four tracks of the D^0 resulting in some inefficiencies in certain regions of the phase space. Indeed, the signal candidates are built in sequence. First two tracks with a good vertex are identified. Then two additional tracks are added to this vertex, one at a time. The issue is that the additional tracks have looser selection cuts, therefore introducing an uneven momentum distribution in the phase space of the decay [53].

Therefore, like in Ref. [52], this analysis aims at exploiting only the sample of $D^0 \to K^+ K^- \pi^+ \pi^-$ decays from $B \to D^0 \mu^- X$ decays, for which the trigger selection efficiency is fairly constant over the full phase space. However, this analysis uses a re-optimized event selection with

better performance than the one of Ref. [52].

In addition to an improved selection, this analysis aims at looking for CP violation in each of the amplitudes contributing to the $D^0 \rightarrow K^+ K^- \pi^+ \pi^-$ decay. This method gives additional information compared to the integrated measurement performed in Ref. [52]. CP violation could be diluted in some parts of phase space and enhanced in others. This would not be detected with the model independent search, but could be observed in some amplitudes in this analysis.

As a first step, in order to develop a "CP-averaged" model, the $\overline{D}^0$ candidates are transformed through the CP symmetry to resemble the D^0 candidates (*i.e.* to have the same distribution as the D^0 candidates, if there was no CP violation). The CP symmetry is applied as follows on the three-momenta:

$$
\begin{array}{cccccccc}
\overline{D}^0 \rightarrow & K^+ & K^- & \pi^+ & \pi^- & \xrightarrow{CP} & D^0 \rightarrow & K^+ & K^- & \pi^+ & \pi^- \\
& \vec{p}_1 & \vec{p}_2 & \vec{p}_3 & \vec{p}_4 & & & -\vec{p}_2 & -\vec{p}_1 & -\vec{p}_4 & -\vec{p}_3
\end{array}
\tag{1.26}
$$

After this transformation, the flavour tag is no longer used and a single model is fitted on the data sample. This method allows to develop the signal model in a way that is blind to possible CP-violation effects. This analysis uses a dataset more than 50 times larger than CLEO, resulting in a more precise and complete model.

Once the model is finalised and that all the systematic uncertainties are computed, the data sample is split according to the flavour tag. The $\overline{D}^0$ subsample (on which the CP transformation is applied) and the D^0 subsample are fitted separately and each amplitude of the model is compared to search for CP violation.

1.4 Outline of the document

In the following the LHCb experiment is presented in Chapter 2, where one section is dedicated to the study of the magnetic field map that I performed during the first year of my PhD. Then the selection of the $D^0 \rightarrow K^+ K^- \pi^+ \pi^-$ decays is described in Chapter 3, followed by the description of the amplitude analysis itself in Chapter 4. All the systematic uncertainties and the cross-checks are described in Chapter 5 and finally, the developed signal model and the results of the CP violation search are reported in Chapter 6. This amplitude analysis is the main part of my thesis, on which I have worked for three years.

This thesis is based on two internal LHCb documents that I wrote to describe the study of the magnetic field map [54] and the $D^0 \rightarrow K^+ K^- \pi^+ \pi^-$ amplitude analysis [55].

2 The LHCb experiment

The LHC, based at CERN near Geneva in Switzerland, is the biggest and most powerful particle accelerator ever built. Several acceleration stages are required in order to reach the nominal energy for the two colliding proton beams. The protons are initially coming from hydrogen atoms, which are ionised with an electrical field. The protons are first accelerated in a linear accelerator up to 50 MeV. They are then injected in a series of circular accelerators: the proton synchrotron booster accelerates them up to 1.4 GeV, the proton synchrotron up to 25 GeV, and the super proton synchrotron up to 450 GeV. Finally, they are injected in the LHC, which will accelerate them up to the design energy of 14 TeV. The accelerator complex is shown in Fig. 2.1.
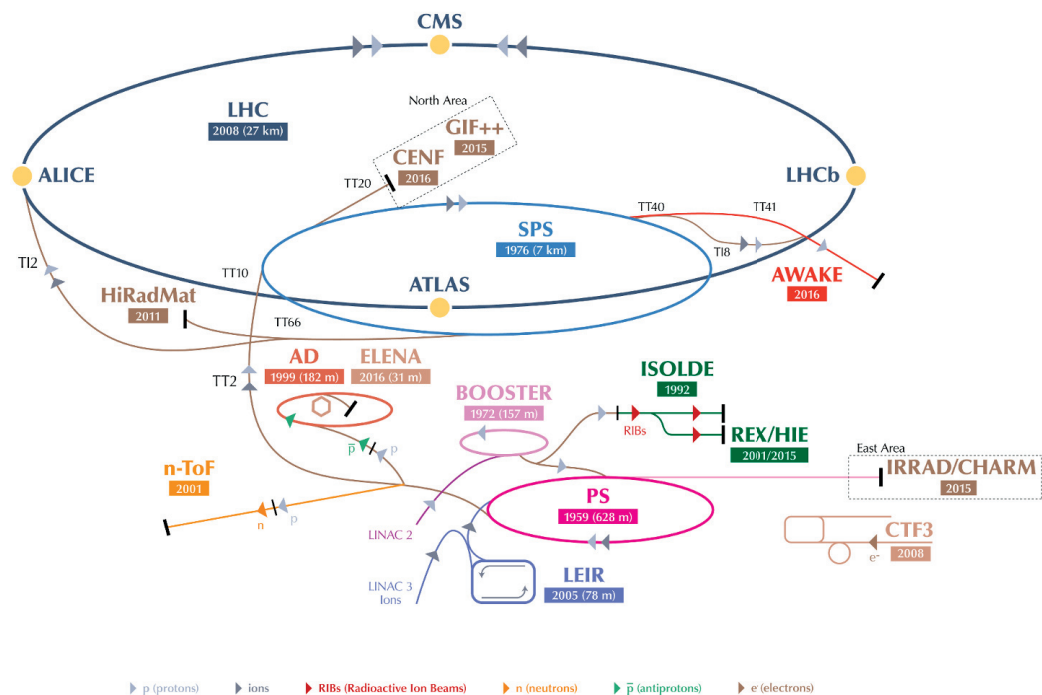
Figure 2.1 – CERN accelerator complex [56].
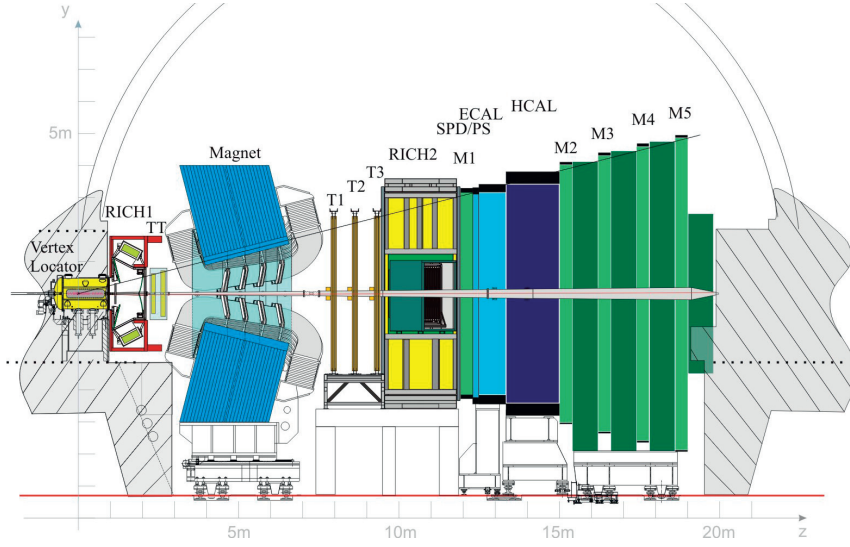
Figure 2.2 – Illustration of the LHCb detector along with the LHCb coordinate system.

The proton-proton (pp) collisions are happening at four points around the LHC, where CERN's four main experiments are located. ATLAS and CMS are two general-purpose detectors and ALICE is studying quark-gluon plasma.

The LHCb detector [57, 58], shown in Fig. 2.2, is a single-arm forward spectrometer covering the pseudorapidity range $2 < \eta < 5$, designed for the study of particles containing b or c quarks. The pseudorapidity is defined as

$$\eta \equiv -\ln\left[\tan\left(\frac{\theta}{2}\right)\right], \tag{2.1}$$

where θ is the angle between the momentum of the particle and the beam axis. This pseudorapidity range corresponds to $0.8° < \theta < 15.4°$. This narrow forward range is motivated by the fact that $b\bar{b}$ and $c\bar{c}$ pairs are mainly produced in the forward or backward regions as shown on Fig. 2.3. Due to space limitations in the cavern inherited from DELPHI (one of the four main experiments of LEP, the collider that preceded the LHC at CERN), the LHCb detector is covering only one of these two regions.

The LHCb coordinate system is a right-handed system where the y axis is vertical, pointing upwards, and the z axis is aligned with the beam pipe pointing from the interaction region towards the spectrometer. The origin is placed at the nominal pp interaction point.
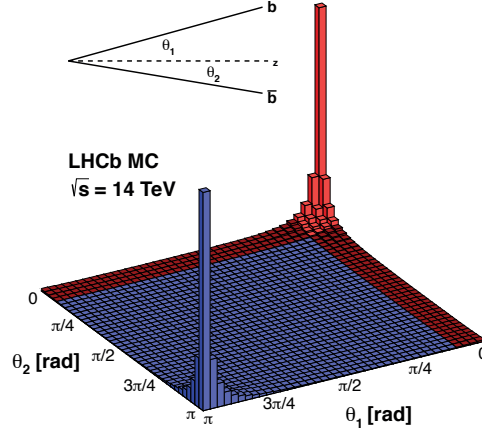
Figure 2.3 – Production angle of b and $\overline{b}$ quarks at the LHC with a pp centre-of-mass energy of 14 TeV. The red region represents the LHCb coverage [59].

2.1 Data taking

2.1.1 Luminosity

The luminosity L is a very important parameter of an accelerator, it measures the ability to produce interesting collision events. It is defined as the proportionality factor between the rate of events $\frac{dN}{dt}$ and the cross-section σ of a particular process:

$$\frac{dN}{dt} = L\sigma. \tag{2.2}$$

The unit of the luminosity is $b^{-1} s^{-1}$. A related quantity is the integrated luminosity

$$L_{\mathrm{int}} = \int L(t)dt, \tag{2.3}$$

where the integral is taken over the data taking period. It directly relates to the number of interesting events produced

$$N = L_{\mathrm{int}}\sigma. \tag{2.4}$$

The amount of data collected at a particle physics facility is therefore measured with the integrated luminosity in b^{-1}

17

2.1.2   Data samples

The LHCb detector has recorded a data sample corresponding to an integrated luminosity of $3.0\,\text{fb}^{-1}$ in 2011 and 2012, *i.e.* during Run 1 of LHC's operation. This data sample has been recorded with a *pp* centre-of-mass energy of 7 and 8 TeV in 2011 and 2012 respectively. Using the total *pp* cross-section of $\sim 100\,\text{mb}$ [60, 61], this corresponds to approximately 3×10^{14} collisions. The amplitude analysis presented in this document is based on this data sample.

The Run 2 of LHC's operation has started in 2015 and is currently ongoing. Between 2015 and 2017, a data sample corresponding to an integrated luminosity of $3.7\,\text{fb}^{-1}$ has been collected. By the end of 2018, the total dataset (Run 1 and Run 2) is expected to reach 9 to $10\,\text{fb}^{-1}$. In addition to this increase of integrated luminosity, the LHC has been running for the entire Run 2 at a centre-of-mass energy of 13 TeV. Since the $b\bar{b}$ and $c\bar{c}$ cross-sections roughly scale with the centre-of-mass energy, Run 2 provides an additional increase in the statistics of interesting events.

LHCb will undergo an important upgrade during the second long-shutdown (LS2) in 2019–2020, where the vertex locator and the tracker will be replaced by new detectors. The current plans for the future are to have Run 3 in 2021–2024 and Run 4 in 2026–2029, which are expected to provide a dataset corresponding to an integrated luminosity of $50\,\text{fb}^{-1}$. Speculative plans for Run 5 and beyond is to reach an integrated luminosity of $300\,\text{fb}^{-1}$ by the end of LHC operation in ~ 2037. This would require a second major upgrade of LHCb [62, 63].

The rest of this chapter describes the status of the experiment before any upgrade, as it was used in Run 1.

2.1.3   Trigger

The online event selection is implemented in three levels, one hardware and two software trigger levels [64]. The goal is to reduce the nominal bunch crossing rate of 40 MHz down to a storable rate of 5 kHz by selecting interesting events containing *b* or *c* quarks (see Fig. 2.4). The subdetectors involved in the trigger are described in Sec. 2.2.

2.1.3.1   Hardware trigger

The hardware trigger, called the level-0 trigger (L0), is based on electronic logical components that need to compute a decision on whether to keep the event or not in less than $4\,\mu\text{s}$. It uses the VELO veto stations to reject events with a large number of *pp* collisions (large pile-up), the SPD to reject events with a too large multiplicity and the calorimeters and the muon chambers in order to select events with a particle of high transverse energy and momentum. The L0 trigger reduces the rate from 40 MHz down to 1 MHz.

LHCb 2012 Trigger Diagram

40 MHz bunch crossing rate

L0 Hardware Trigger : 1 MHz readout, high E_T/P_T signatures

| 450 kHz $h^{\pm}$ | 400 kHz $\mu/\mu\mu$ | 150 kHz e/γ |

Software High Level Trigger

Introduce tracking/PID information, find displaced tracks/vertices

Offline reconstruction tuned to trigger time constraints

Mixture of exclusive and inclusive selection algorithms

5 kHz (0.3 GB/s) to storage

| 2 kHz Inclusive Topological | 2 kHz Inclusive/ Exclusive Charm | 1 kHz Muon and DiMuon |

Figure 2.4 – Trigger scheme used in 2012 [65].

2.1.3.2 Software triggers

The events that pass the hardware trigger are fully read out and forwarded to the software stage. This stage is split in two, the high level trigger 1 (HLT1) and the high level trigger 2 (HLT2). HLT1 is run first: it reconstructs partially the tracks and keeps events that contain at least one track with high transverse momentum, a good separation from any primary vertex (PV) and a good track quality in the overall tracking system. HLT2 performs a full event reconstruction, including all charged tracks with $p_T > 300\,(500)\,\mathrm{MeV}/c$ for 2012 (2011) data. HLT2 is composed of exclusive and inclusive trigger lines, such as topological lines selecting events containing vertices with two, three or four tracks. It also triggers the RICH reconstruction in specific cases. The output of the software trigger stage, which has a rate of 5 kHz (3 kHz) in 2012 (2011), is stored to disk.

2.2 Detectors

2.2.1 Vertex locator

The vertex locator (VELO) [66] is a high-precision silicon-strip detector surrounding the *pp* interaction region. It has been designed to precisely disentangle the primary vertices, where the *pp* collisions occur, from the secondary vertices, where the *b* and *c* hadrons decay. The ability to locate the positions of the displaced vertices is a key feature of LHCb. The VELO consists of a series of 21 modules arranged along the beam line (see Fig. 2.5), which provide
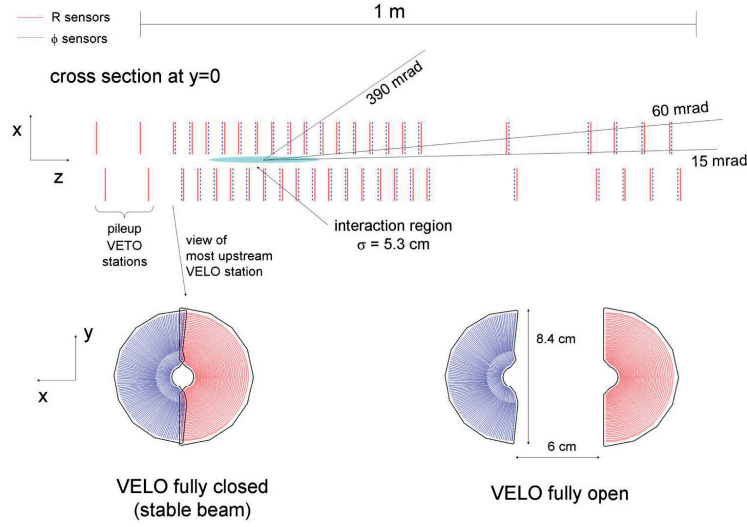
Figure 2.5 – Top: view of the VELO in the xz plane at $y = 0$, with the position of all modules shown in closed position. Bottom: front view of a VELO module in closed and open positions. [57].

the polar coordinates r and ϕ of the hits. The VELO provides a three-dimensional hit spatial resolution of 5–25 μm. Each module is made of two halves surrounding the beam axis. They are placed so close to the beam that they need to be retracted when the beams are not stable, *e.g.* during injection. In the closed position, the first active silicon strips are 8.2 mm away from the beam, which is the shortest distance between the LHC beam and any detector.

2.2.2 Tracker turicensis

The tracker turicensis (TT) [67] is a large-area silicon microstrip detector located between the VELO and the magnet. It is 150 cm wide and 130 cm high and covers the whole acceptance of the experiment. It consists of four layers arranged in two stations (TTa and TTb) in the "$x - u - v - x$" pattern as shown in Fig. 2.6. The "x" layers have vertical strips, whereas the "u" and "v" layers are tilted by $\pm 5°$. This pattern reduces the number of ambiguous hits and, together with the knowledge of the z position of the tracking layers, yields a three-dimensional information on the hit position. The silicon sensors are 500 μm thick, 9.64 cm wide and 9.44 cm long. They carry 512 strips with a pitch (distance between strips) of 183 μm. The achieved spatial resolution is around 50 μm.

2.2.3 Tracking stations

Three tracking stations [67] are the final elements of the tracking system of LHCb and are located downstream of the magnet. They are called T1, T2 and T3 and they all consist of two subdetectors, the inner tracker and the outer tracker. A front view is shown in Fig. 2.7.
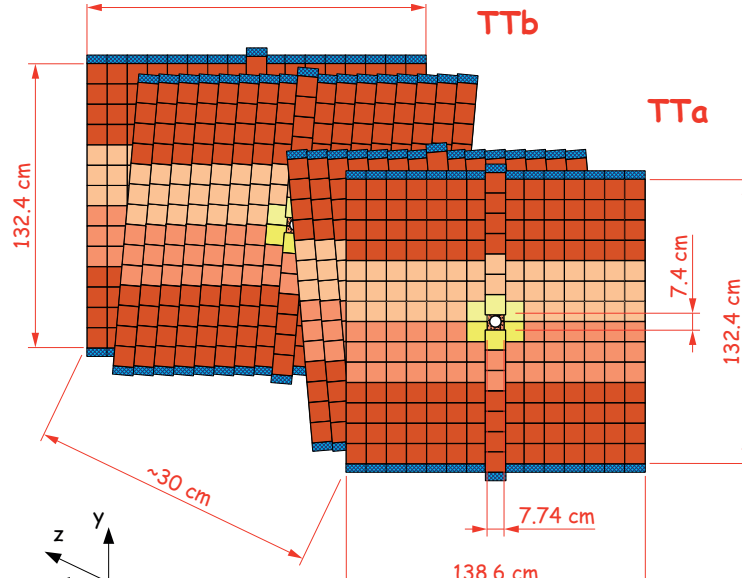
Figure 2.6 – Layout of the four layers of the TT [57]. Each small square represents a silicon sensor.

2.2.3.1 Inner tracker

The inner tracker (IT) [68] is made of four boxes arranged around the beam pipe as shown on Fig. 2.8. Each of the four boxes is made of four layers arranged in the "$x - u - v - x$" pattern. The IT is also a silicon microstrip detector and is designed to cope with a high density of tracks. The silicon sensors are 7.6 cm wide and 11 cm long. The top and bottom boxes contain one-sensor modules that are 320 μm thick, whereas the C-side and A-side boxes contain two-sensor modules that are 410 μm thick. These different thicknesses were chosen to obtain a high enough signal-to-noise ratio while limiting the materiel budget of the detector. The pitch of the read-out strips is 198 μm, providing a spatial resolution of about 50 μm. Overall, the IT contains 129 024 strips and has a hit efficiency above 99%.

2.2.3.2 Outer tracker

The outer tracker (OT) [67] is a detector based on straw drift tubes, covering most of the area of the stations. The drift tubes are 2.4 m long and are filled with argon (70%), carbon dioxide (28.5%) and oxygen (1.5%). The drift time achieved is below 50 ns and the resolution is about 200 μm. This technology was chosen because it is cheaper than silicon detectors and its resolution is good enough for the low occupancy in this region of the acceptance. Each of the stations is arranged in the "$x - u - v - x$" pattern as shown in Fig. 2.9.
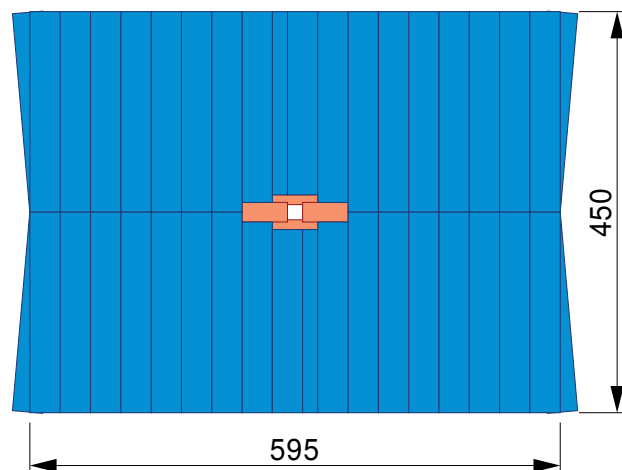
Figure 2.7 – Front view of one of the tracking stations, where the OT is shown in blue and the IT is shown in orange [68]. The dimensions are in cm.
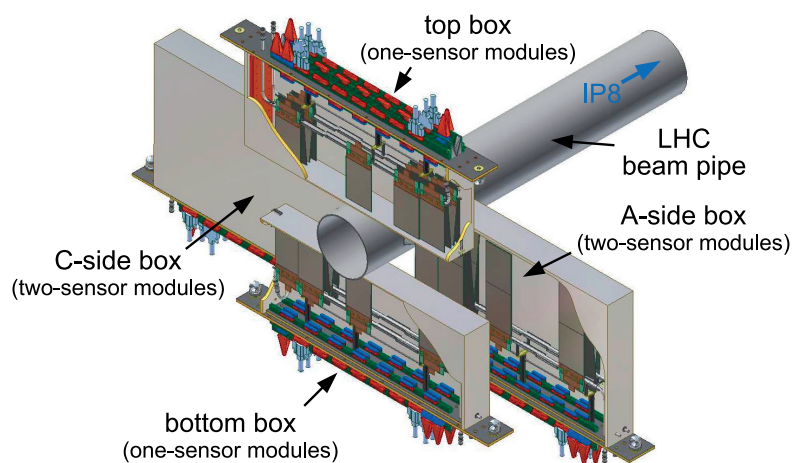
Figure 2.8 – Layout of the four boxes of an IT station around the beam pipe [57].
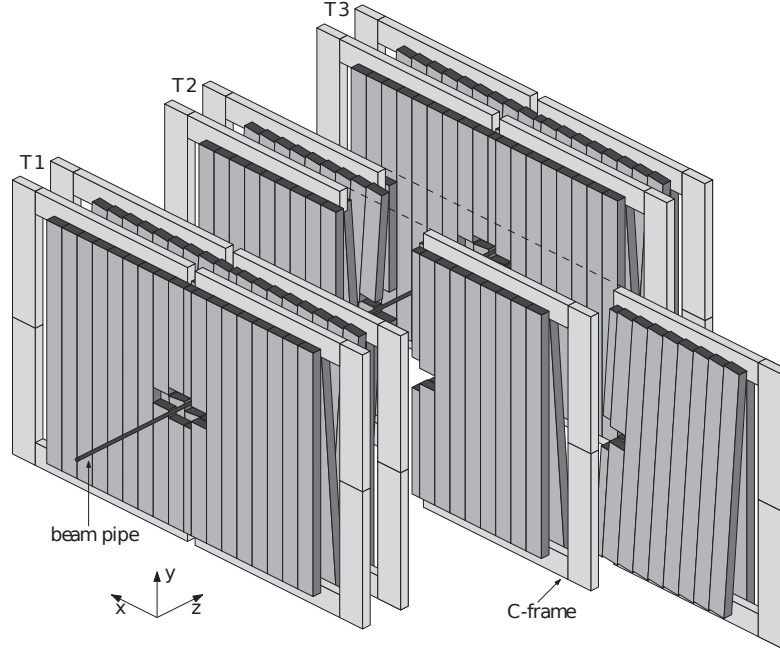
Figure 2.9 – Layout of the three OT stations [67].

2.2.4 Ring imaging Cherenkov detectors

Different types of charged particles are distinguished using information from two ring-imaging Cherenkov detectors (RICH) [69]. Cherenkov light is emitted by particles that travel faster than light in the medium of the detector. The RICH 1 is located between the VELO and the TT. It identifies low momentum particles (1–60 GeV/c) and uses C_4F_{10} as radiator. During Run 1, it also used some aerogel to work below the Cherenkov threshold of the C_4F_{10}; it was however found to be ineffective and removed for Run 2. The RICH 2 is located right after the tracking stations. It identifies high momentum particles (15–100 GeV/c) and uses CF_4 as radiator.

The emission angle of the Cherenkov light θ_C depends on the velocity v of the traversing particle and the refraction index of the medium n:

$$\cos(\theta_C) = \frac{c}{nv}.$$ (2.5)

As seen on Fig. 2.10, one can determine the particle type when θ_C and its momentum are measured.

The design of the two RICH detectors are shown in Fig. 2.11. A set of spherical and plane mirros are used to reflect and direct the Cherenkov light to the photodetectors, which are placed outside the acceptance in order to reduce the material that the particles have to traverse.
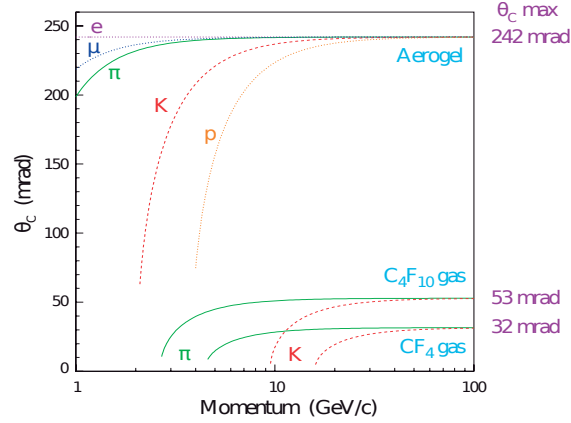
Figure 2.10 – Cherenkov light emission angle versus momentum for various media and particles [57].
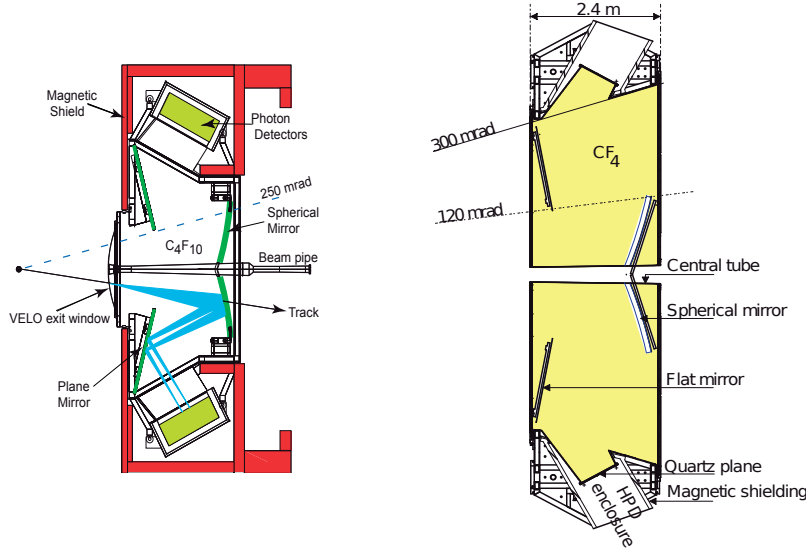
Figure 2.11 – Left: side view of RICH 1. Right: top view of RICH 2 [57].

2.2.5 Calorimeters

The calorimeters [70] are used to measure the energy and the position of the final state particles, as well as to identify electrons, photons and hadrons. They contribute also to the first level of trigger. The calorimeters are made of alternating layers of dense material (iron or lead) and scintillating material. They rely on the fact that a particle traversing dense matter will create showers, which will in turn excite the scintillator's atoms. While deexciting, these atoms will emit scintillation light that are transmitted to photomultipliers through wavelength-shifting fibres. There are four subdetectors forming the calorimeter system: the scintillator pad detector (SPD), the preshower (PS), the electromagnetic calorimeter (ECAL) and the hadronic calorimeter (HCAL). The different energy depositions in these four detectors help to identify the particles as shown in Fig. 2.12. The SPD identifies charged particles, the PS identifies
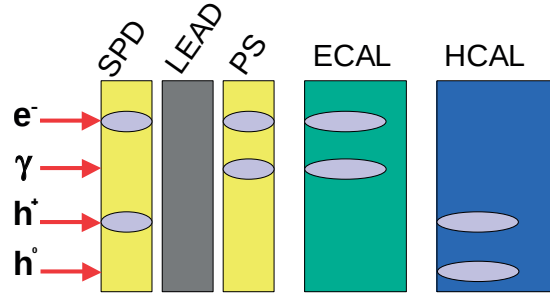
Figure 2.12 – Simplified sketch of the energy deposits of an electron, a photon, a charged hadron, and a neutral hadron in the LHCb calorimeter system [71].
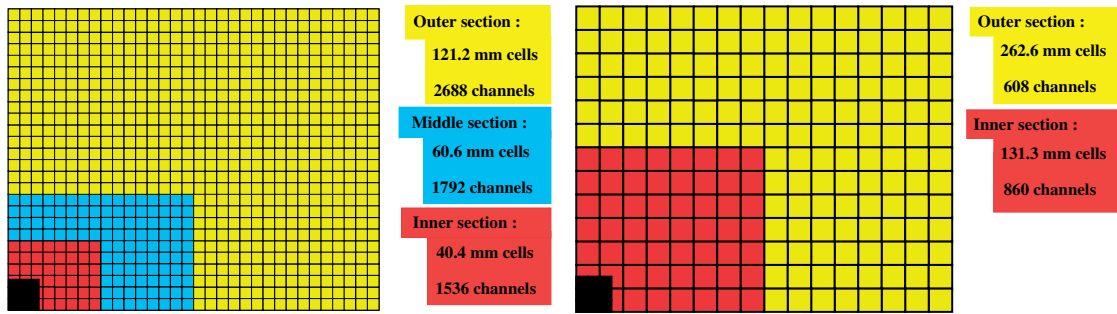
Figure 2.13 – Left: Segmentation of the SPD, PS and ECAL. Right: Segmentation of the HCAL [57]. One quarter of the detector front face is shown, with the beam passing in the bottom left corner.

electromagnetic particles, the ECAL measures the energy of electromagnetic particles and the HCAL measures the energy of hadrons. The SPD and the PS are separated by a 15 mm lead layer that helps initiate the showers of the incoming electrons and photons.

In order to obtain spatial information, the calorimeters are segmented. The SPD, the PS and the ECAL are divided in three regions and the HCAL in two regions (see Fig. 2.13). The ECAL is dedicated to detect photons and electrons, which produce electromagnetic showers in the detector. In order to fully contain the showers, its thickness corresponds to 25 electromagnetic interaction lengths. Its energy resolution is $\sigma(E)/E = 10\%\sqrt{E/\,\mathrm{GeV}} \oplus 0.9\%$. The HCAL is dedicated to measure the energy of hadrons, which have strong interaction in the detector. Due to limited available space, the HCAL only has a thickness equivalent to 5.6 nuclear interaction lengths. Its energy resolution is $\sigma(E)/E = 69\%\sqrt{E/\,\mathrm{GeV}} \oplus 9\%$.

2.2.6 Muon chambers

Muons are very important at LHCb. In particular, they play a major role for the trigger and the flavour tagging [72]. The muon chambers are arranged in five stations, one (M1) upstream and the remaining four (M2–M5) downstream of the calorimeters. M2 to M5 are separated by 80 cm thick iron plates acting as absorbers. The minimum momentum needed for a muon to cross the whole detector is 6 GeV/c. The chambers are gaseous multi-wire proportional
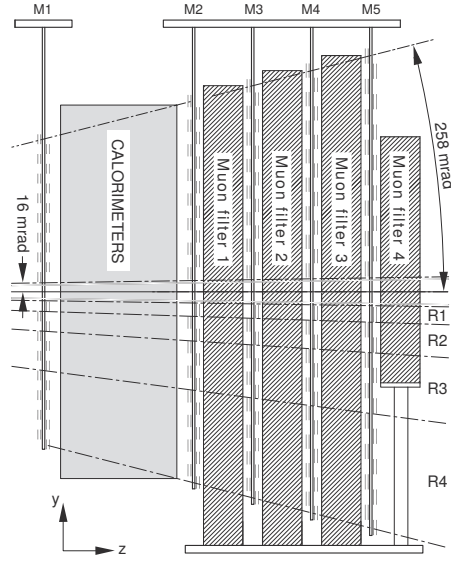
Figure 2.14 – Side view of the five muon chamber stations [57].

detectors containing 40% of argon, 55% of carbon dioxide and 5% of CF_4. The inner region of M1 uses a different technology due to the high occupancy of the detector; it uses gas electron multiplier chambers. The muon chambers have a hit efficiency above 95%.

2.3 Dipole magnet and its magnetic field map

The LHCb magnet [58] is a warm dipole magnet with a bending power of about 4 Tm. Its maximum field intensity is 1.1 T along the vertical axis, making the horizontal plane the main bending plane. The magnetic field can be oriented upwards (MagUp) or downwards (MagDown) at will. Data is collected with both polarities in equal proportions in order to minimise the effect of the left-right detection asymmetries. The magnet is made of two coils of conical saddle shape of 27 tons each mounted on a frame of 1500 tons (see Fig. 2.15). By bending the charged particle trajectories, it allows a momentum measurement with a resolution of about 0.5% for particles below 20 GeV/c, rising to 1.0% for particles at 200 GeV/c. The resolution of the reconstructed mass of particles decaying to two charged tracks is about 0.5% up to the Υ masses.

In order to ensure a precise track reconstruction, a good momentum resolution, as well as a good alignment of the detector, the magnetic field produced by the LHCb magnet needs to be precisely known. This knowledge, expressed through a magnetic field map, is also needed in the LHCb simulation software.

The magnetic field map was initially based on measurement campaigns held in 2005 and 2009 [73] along with numerical simulations [74]. It has then been corrected in 2011 with a new
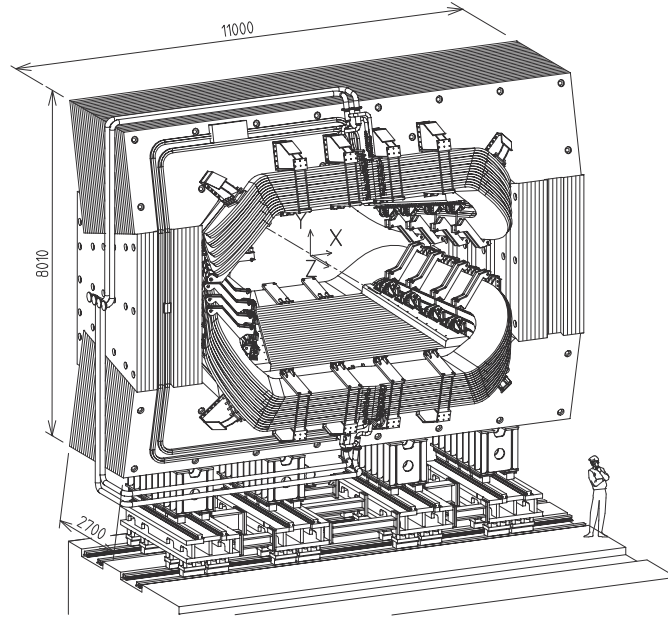
Figure 2.15 – Perspective view of the dipole magnet [57]. The dimensions are in mm.

set of measurements. The 2011 survey was made with the detector closed and with the beam pipe installed, such that the measurements were limited to a scan in the yz plane at $x = 22$ cm [75].

This section is dedicated to the analysis of a new measurement campaign conducted in August 2014, during the first Long Shutdown of the LHC (LS1) while the TT, IT and OT were open and the beam pipe section inside the magnet dismantled. Therefore, a larger coverage in the xy plane compared to the 2011 measurements was possible (Fig. 2.16), allowing the determination of possible field map asymmetries.

The measurement campaign was performed to improve the quality of the magnetic field map, but also to verify the field configuration after the consolidation work on the magnet (exchange of the protection layers between support clamps and coils) carried out in 2013.

A new map has been created by fitting the 2011 map to the new measurements. Various validation tests have been performed in order to verify that the new map describes more accurately the real magnetic field. This work has been documented in an internal note [54], which forms the basis for this section.

2.3.1 Measurement setup

The setup used for the magnetic field measurements was designed and constructed by the detector technologies group of the CERN physics departement. Figure 2.17 shows a photograph of the bench as installed in the dipole magnet. A ~ 2.1 m long horizontal bar carries 39 magnetic field sensor printed circuit boards (PCB) and three support rods for survey tar-
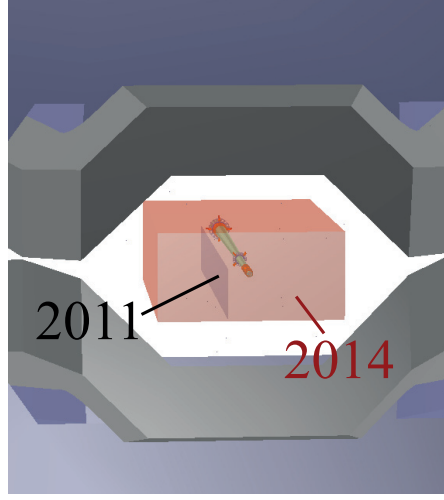
Figure 2.16 – Illustration of the regions covered by the surveys in 2011 (vertical plane at $x = 22$ cm) and 2014 (volume covering 2m × 1m × 3.5m) inside the LHCb magnet.
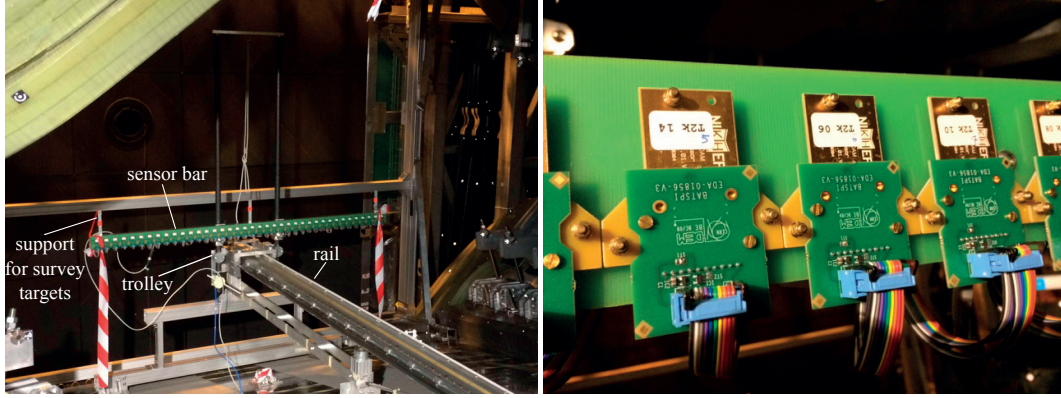
Figure 2.17 – Left: Measurement setup inside the magnet. Right: closeup of the sensor bar.

gets. Each PCB contains three Siemens KSY44 Hall probes which are glued to a glass cube of $4 \times 4 \times 2.4 \, \text{mm}^3$ (Fig. 2.18, left). The sensors are estimated to have an orientation error of 1 mrad, and the relative orientation error of B_x, B_y, B_z is estimated to be approximately 0.2 mrad. The accuracy of the Hall probes after calibration is estimated to be approximately 2 G.

The sensor bar is attached to two vertical poles which are fixed to a "trolley" sitting on a rail. The rail has holes in intervals of 50 mm which are used for locking the trolley during a measurement by means of a pin. To move the trolley along the rail the pin is released by a pneumatic system.

Measurements were made at 24 positions along the rail, with position 0 being the point closest to RICH1 ($z = 2.5$ m) and position 23 the one closest to the T stations ($z = 6$ m). The spacing Δz between neighbouring positions increases with z,
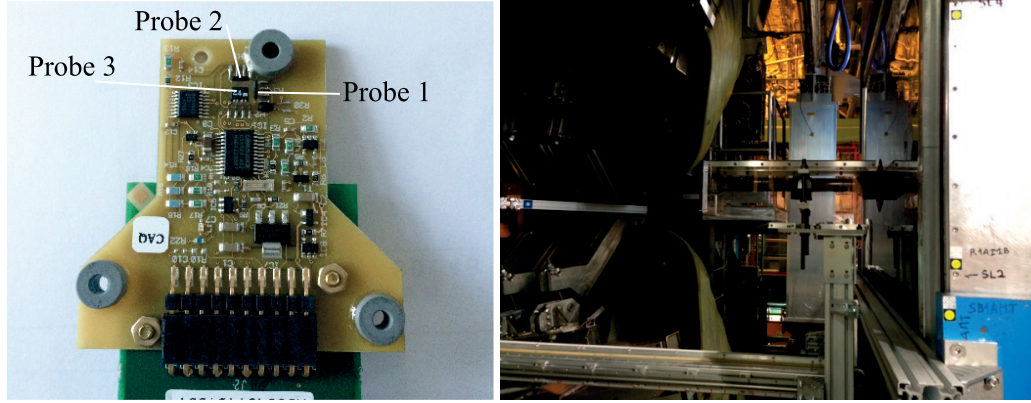
Figure 2.18 – Left: Hall probes on the sensor PCB. Probe 1 is used for measuring B_x, probe 2 for measuring B_y, and probe 3 for measuring B_z. Right: beam pipe support structure.

- positions $0 - 9$: $\Delta z \sim 50$ mm,

- positions $9 - 14$: $\Delta z \sim 100$ mm,

- positions $14 - 22$: $\Delta z \sim 300$ mm,

- positions $22 - 23$: $\Delta z \sim 150$ mm.

Scans were made at five vertical levels, with level 0 being the lowest one ($y \sim -480$ mm) and level 4 the highest one ($y \sim +480$ mm). Positions $0 - 6$ at vertical level 1 and vertical level 2 were not accessible due to the beam pipe and its support structure (Fig. 2.18, right).

Survey measurements are necessary to determine the coordinates of the magnetic field probes in the global LHCb coordinate system. Supports for survey targets are mounted at the two ends and the centre of the sensor bar. The coordinates of these targets were measured without magnetic field at all 24 positions along the rail and for all five vertical levels, with the theodolite placed in the IT/OT region. With the magnetic field turned on, the measurements were made from the side of the LHCb detector. From this position, only a subset of the survey target positions is visible, as shown in Fig. 2.19.

2.3.2 Fit strategy

It is assumed that the 2011 magnetic field map is correct up to global transformations. Seven transformations of the magnetic field map are allowed in the fit: translations along the three axes (T_x, T_y and T_z), clockwise rotations around the three axes (R_x, R_y and R_z) and a global scale factor α_{SF}, applied on each component of the magnetic field. The translations and rotations put the map in the correct position and orientation whereas the global scale factor takes into account small differences of the current in the coils. The three rotation matrices are
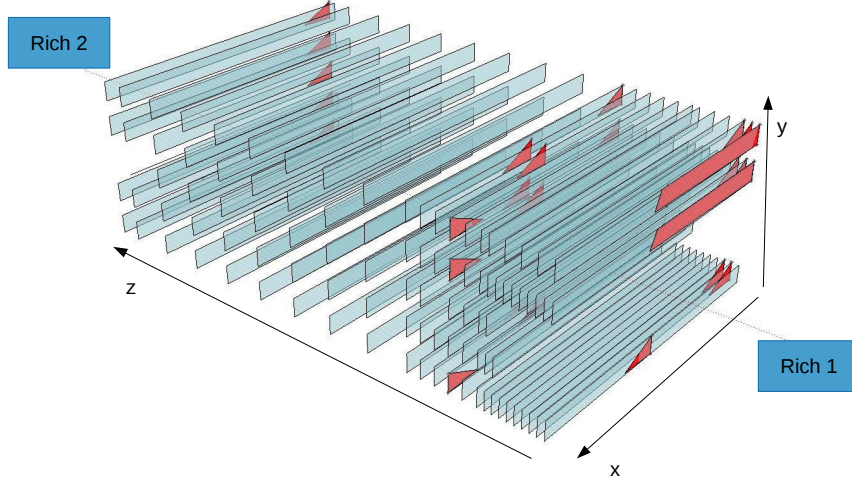
Figure 2.19 – All positions of the bar during the measurements. In red are the positions that were measured from the side with the magnetic field turned on and in blue are the ones measured without magnetic field.

applied after the translations in the following order:

$$R_x R_y R_z = \begin{pmatrix} 1 & 0 & 0 \\ 0 & \cos\psi & \sin\psi \\ 0 & -\sin\psi & \cos\psi \end{pmatrix} \begin{pmatrix} \cos\theta & 0 & -\sin\theta \\ 0 & 1 & 0 \\ \sin\theta & 0 & \cos\theta \end{pmatrix} \begin{pmatrix} \cos\phi & \sin\phi & 0 \\ -\sin\phi & \cos\phi & 0 \\ 0 & 0 & 1 \end{pmatrix} \tag{2.6}$$

The function to be minimised in the fit is defined as

$$\chi^2_{x,y,z} = \chi^2_x + \chi^2_y + \chi^2_z, \quad \text{with } \chi^2_i = \sum_{\vec{r}_k \in V} \frac{B_{i,\text{meas}}(\vec{r}_k) - B_{i,\text{map}}(\vec{r}_k)}{\sigma^2_i}, \quad i = x, y, z,$$

where $B_{i,\text{meas}}$ are the measured values of the components of the magnetic field at position $\vec{r}_k$, $B_{i,\text{map}}$ are the values from the map at the same position after the transformations are applied, and V represents the volume containing all positions with measurements. The minimisation is performed using the Minuit package [76] with respect to the three translations (T_x, T_y, T_z), the three rotation angles (ψ, θ, ϕ) and the scale factor (α_{SF}).

2.3.3   Fit results

The fit is performed on the total dataset. Its result, given in Table 2.1, is compared to the previous measurement campaign, which was performed in 2011, where the 2010 map was

Table 2.1 – Left: Fit results of the 2011 map to the data of the 2014 measurement campaign along with the statistical uncertainties returned by the fit and those found from the standard variation between subsamples of the data (σ_{tot}). Right: Fit results of the 2010 map to the data of the 2011 measurement campaign [75].

Variable	2014 fit result	σ_{tot}	2011 fit result
T_x [mm]	-6.3 ± 0.2	10.1	–
T_y [mm]	-0.03 ± 0.06	0.55	-7.98 ± 0.57
T_z [mm]	-0.18 ± 0.06	0.13	-11.26 ± 0.07
ψ [mrad]	-3.32 ± 0.04	0.56	0.72 ± 0.02
θ [mrad]	2.59 ± 0.10	1.18	-3.6 ± 1.2
ϕ [mrad]	1.47 ± 0.04	0.48	-0.40 ± 0.16
α_{SF}	0.99917 ± 0.00004	0.00026	1.00056 ± 0.00195

fitted to the 2011 magnetic field measurements. The 2010 map was built from simulations using TOSCA simulations and early magnetic-field measurements [74]. One can see that the large translations applied in 2011 along the y and z axes do not need significant adjustments. This confirms that the map had been placed in the correct position in y and z. The translation in x was not a part of the fit in 2011 since the measurements were confined in a plane. This new parameter can now be fitted. The rotations found in 2011 are rather small compared to the new ones. Finally the scale factor increased the intensity by 0.056% in 2011 while it is lowering it by 0.083% in the new measurement.

The measurements are dominated by systematic uncertainties. One could consider the following sources :

- The positions of the probes are not perfectly known. As mentioned in Sec. 2.3.1, the survey could be done only at a few positions inside the magnet.

- The horizontal bar on which the probes are fixed moves when the magnetic field is turned on. It is however difficult to correct for theses shifts because of the limited number of survey measurements inside the magnet.

- The simulation, on which the first magnetic field map is based, is not perfect and also introduces some uncertainties.

However, these effects are difficult to disentangle. In order to estimate the total uncertainties on the fitted parameters, the full data set is divided in 8 independent subsets each composed of the measurements of three different probes at two heights and five positions along z. This small number of data points evenly distributed is enough to have a global description of the field. The standard deviation of the results of the fit applied on those independent subsamples is used as an estimate of the total (statistical and systematic) uncertainty, as shown in Table 2.2.

Table 2.2 – Results of the fit of the eight subsamples and computation of the standard deviation as an estimation of the total uncertainty σ_{tot}.

Probes	T_x [mm]	T_y [mm]	T_z [mm]	ψ [mrad]	θ [mrad]	ϕ [mrad]	α_{SF}
1,17,31	12.5 ± 11.0	-1.36 ± 0.66	-0.69 ± 0.75	-4.16 ± 0.49	5.19 ± 1.77	1.37 ± 0.40	0.99924 ± 0.00048
2,18,32	8.2 ± 11.5	-0.88 ± 0.60	-0.65 ± 0.67	-3.76 ± 0.45	4.06 ± 1.73	1.54 ± 0.36	0.99964 ± 0.00044
3,19,33	6.8 ± 14.0	-1.01 ± 0.66	-0.82 ± 0.74	-3.66 ± 0.50	4.02 ± 2.03	0.81 ± 0.40	0.99908 ± 0.00049
4,20,34	9.8 ± 12.3	-0.90 ± 0.56	-0.74 ± 0.63	-3.62 ± 0.42	4.35 ± 1.77	1.54 ± 0.34	0.99956 ± 0.00041
6,21,35	-0.7 ± 12.5	-0.33 ± 0.56	-0.75 ± 0.63	-3.06 ± 0.42	3.44 ± 1.79	0.87 ± 0.34	0.99923 ± 0.00041
7,22,36	5.5 ± 10.3	-0.24 ± 0.54	-1.03 ± 0.60	-2.84 ± 0.40	3.45 ± 1.55	0.66 ± 0.32	0.99895 ± 0.00039
8,23,37	-4.8 ± 9.4	-0.68 ± 0.56	-0.94 ± 0.64	-2.98 ± 0.42	2.47 ± 1.52	1.61 ± 0.34	0.99962 ± 0.00041
9,24,38	-18.5 ± 7.8	0.40 ± 0.57	-0.75 ± 0.66	-2.52 ± 0.42	1.37 ± 1.39	0.35 ± 0.34	0.99924 ± 0.00041
σ_{tot}	10.1	0.55	0.13	0.56	1.18	0.48	0.00026

Table 2.3 – Fit results of the fit with the up polarity measurements compared to those with the down polarity.

Variable	Up result	Down result
T_x [mm]	-6.3 ± 10.1	-6.4 ± 10.8
T_y [mm]	-0.03 ± 0.55	-0.14 ± 0.56
T_z [mm]	-0.18 ± 0.13	-0.24 ± 0.11
ψ [mrad]	-3.32 ± 0.56	-3.36 ± 0.55
θ [mrad]	2.59 ± 1.18	2.51 ± 1.29
ϕ [mrad]	1.47 ± 0.48	1.50 ± 0.46
α_{SF}	0.99917 ± 0.00026	0.99929 ± 0.00024

2.3.4 Cross checks

Magnet polarity

The 2014 results shown in Table 2.1 were obtained only with the up polarity of the magnet. The fit has also been applied on the data that were taken with the down polarity and the total uncertainties have been recomputed with the subsample method explained in Sec. 2.3.3. The results are compared in Table 2.3 with those of Table 2.1. This test shows no evidence for differences between the two polarities since the results are absolutely compatible within the total uncertainties. The maximum difference between the two polarities is 46% of the total uncertainty (for T_z and the scale factor). The fact that the difference between the two polarities is so small also indicates that the uncertainties contain identical systematic effects for both polarities. Following this check, only the up polarity is used.

Up-down asymmetry

Another cross-check is to fit the map to the data taken only in the upper part of the detector (*i.e.* at $y > 0$) and compare the results with the fit applied on the lower part of the detector (*i.e.* at $y < 0$). This test shows some differences, which may give rise to an up-down asymmetry

Table 2.4 – Results of the fit for $y > 0$, $y < 0$, $x > 0$ and $x < 0$ along with the uncertainties computed with the method explained in Sec. 2.3.3 applied on each subsample separately.

Variable	$y > 0$ result	$y < 0$ result	$x > 0$ result	$x < 0$ result
T_x [mm]	1.1 ± 10.9	-12.0 ± 8.5	12.9 ± 7.0	-19.9 ± 8.0
T_y [mm]	-0.03 ± 0.58	-1.33 ± 0.77	0.93 ± 0.90	-0.53 ± 0.76
T_z [mm]	-3.51 ± 0.43	2.00 ± 0.54	-0.55 ± 0.85	-0.36 ± 0.57
ψ [mrad]	-5.09 ± 0.62	-3.67 ± 0.70	-3.22 ± 0.79	-3.51 ± 0.83
θ [mrad]	3.95 ± 0.92	1.51 ± 0.55	5.32 ± 1.30	0.88 ± 1.15
ϕ [mrad]	1.41 ± 0.41	1.52 ± 0.57	2.12 ± 0.60	1.16 ± 0.54
α_{SF}	0.99884 ± 0.00027	0.99960 ± 0.00030	0.99919 ± 0.00042	0.99894 ± 0.00035

(Table 2.4). It is particularly significant for the translation in z where the two results are $\sim 40\sigma$ apart, where σ is the total uncertainty from the full sample fit (0.13 mm). It is however, difficult to correct this effect with the current method, which applies only global transformations. One would need to add some degrees of freedom to the fit, for example to allow different z translations at different heights. This however introduces other issues linked to distortions and discontinuities of the map. This is outside the scope of this analysis.

Left-right asymmetry

A similar test is performed by looking at the data for the left side of the detector (*i.e.* at $x > 0$) and the right side of the detector (*i.e.* at $x < 0$). Small differences are also observed (Table 2.4), which may give rise to a small left-right asymmetry. If the full sample fit uncertainties are taken here as well, the main differences arise on θ with $\sim 4\sigma$ and T_x with $\sim 3\sigma$. Again, correcting for such asymmetries would require local transformations and is outside the scope of this study.

2.3.5 Validation

The 2014 corrections from Table 2.1 are applied to the 2011 field map in order to create a new field map, which will be referred to as the 2014 map in the following. The next step is to assess if this new map actually describes better the magnetic field inside the magnet. In order to test this, the two maps are compared to the 2014 magnetic field measurements, low level tracking parameters are analysed, and finally particles are reconstructed using the two maps. With the latter study, the direct impact of the new field map on the mass distributions is quantified.

2.3.5.1 Difference between map and data

This test takes the difference between the two maps (2011 and 2014) and the measurements taken during August 2014. The difference is computed at every measurement point and, in order to obtain a smoother result, the differences are averaged over 4 neighbours at the same
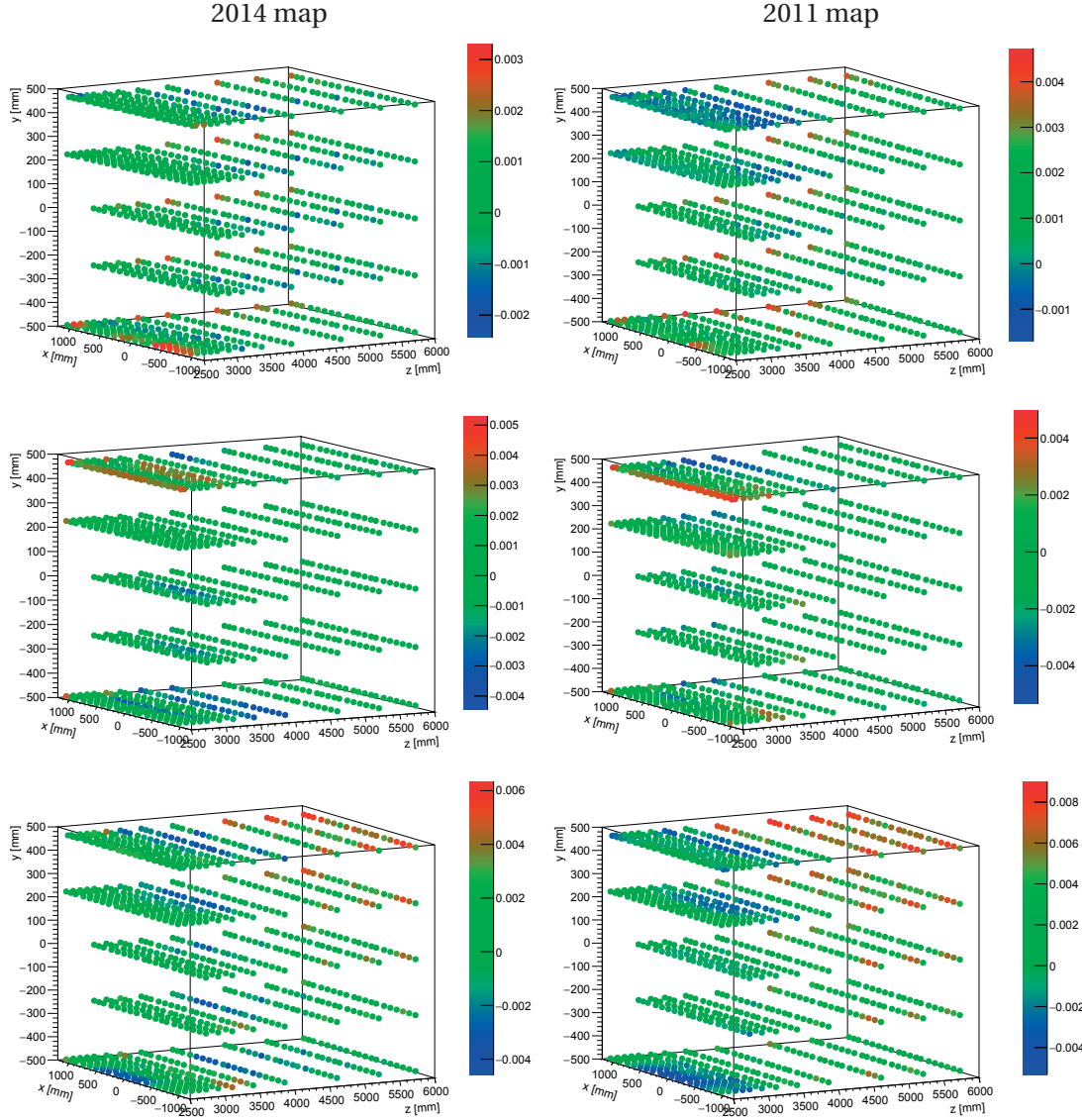
2014 map   2011 map

Figure 2.20 – Difference between the 2014 map and the 2014 data (left) and between the 2011 map and the 2014 data (right) for the B_x (top), B_y (middle) and B_z (bottom) components of the magnetic field. The values on the z axis are given in gauss.

height (*i.e.* same y coordinate). The result is shown in Fig. 2.20. One can see that the range of differences is smaller for the 2014 map. This is an indication that the 2014 map describes better the data than the 2011 map.

2.3.5.2 Particle reconstruction

Low level reconstruction parameters, such as number of reconstructed tracks and track effi-ciencies, have been compared between the two maps using 2012 data. No differences have

been found: the two maps have similar reconstruction performances.

Higher level parameters are also studied. The tracker is first aligned for the new magnetic field map and then a particular decay is reconstructed. This reconstruction is compared to the usual online reconstruction of Run 1 (*i.e.* with the 2011 map and its alignment). The decays of five different particles with a wide range of kinematic properties are reconstructed int the $D^0 \to K^- \pi^+$, $J/\psi \to \mu^+ \mu^-$, $\Upsilon(1S) \to \mu^+ \mu^-$, $K^0_S \to \pi^+ \pi^-$ and $B^+ \to J/\psi(\mu^+ \mu^-)K^+$ decay modes. Their selection, based on 2012 data, is described in Ref. [54].

Mass distributions

Figure 2.21 shows the mass distributions of all five reconstructed particles, each of them obtained with the two field maps. The first observation is that the mean value of the mass peaks is always closer to the PDG value with the new map. This is summarised in Fig. 2.22 where one can directly see the improvement achieved by the 2014 map. The improvement for the B^+ meson is slightly smaller than for the other particles but this is due to the mass constraint applied on the J/ψ meson.

The mass resolution is similar between the two maps for all five particles, which implies that the method used (applying only global transformation to the map) does not influence the width of the mass distributions. If one wants to make some improvement on the resolution, one might need to consider local transformations.

Mass dependencies

We also check the dependence of the central value of the mass distributions on the following variables:

- p : the momentum of the mother particle

- p_T: the transverse momentum of the mother particle

- $tx = \frac{p_x}{p_z}$: the horizontal slope of the mother particle

- $ty = \frac{p_y}{p_z}$: the vertical slope of the mother particle

- $\Delta p = p_A - p_B$: the difference of the momenta of the two daughter particles

- $A_p = \frac{p_A - p_B}{p_A + p_B}$: the momentum asymmetry between the two daughter particles

- $\phi = \tan^{-1}\left(\frac{(\vec{p}_A \wedge \vec{p}_B)_y}{(\vec{p}_A \wedge \vec{p}_B)_x}\right)$: the decay plane azimuthal angle

- $\phi' = \cos^{-1}\left(\left(\frac{\vec{p}_A \wedge \vec{p}_B}{\|\vec{p}_A \wedge \vec{p}_B\|}\right)_y\right)$: decay plane angle w.r.t the vertical axis

- η : the pseudorapidity of the mother particle
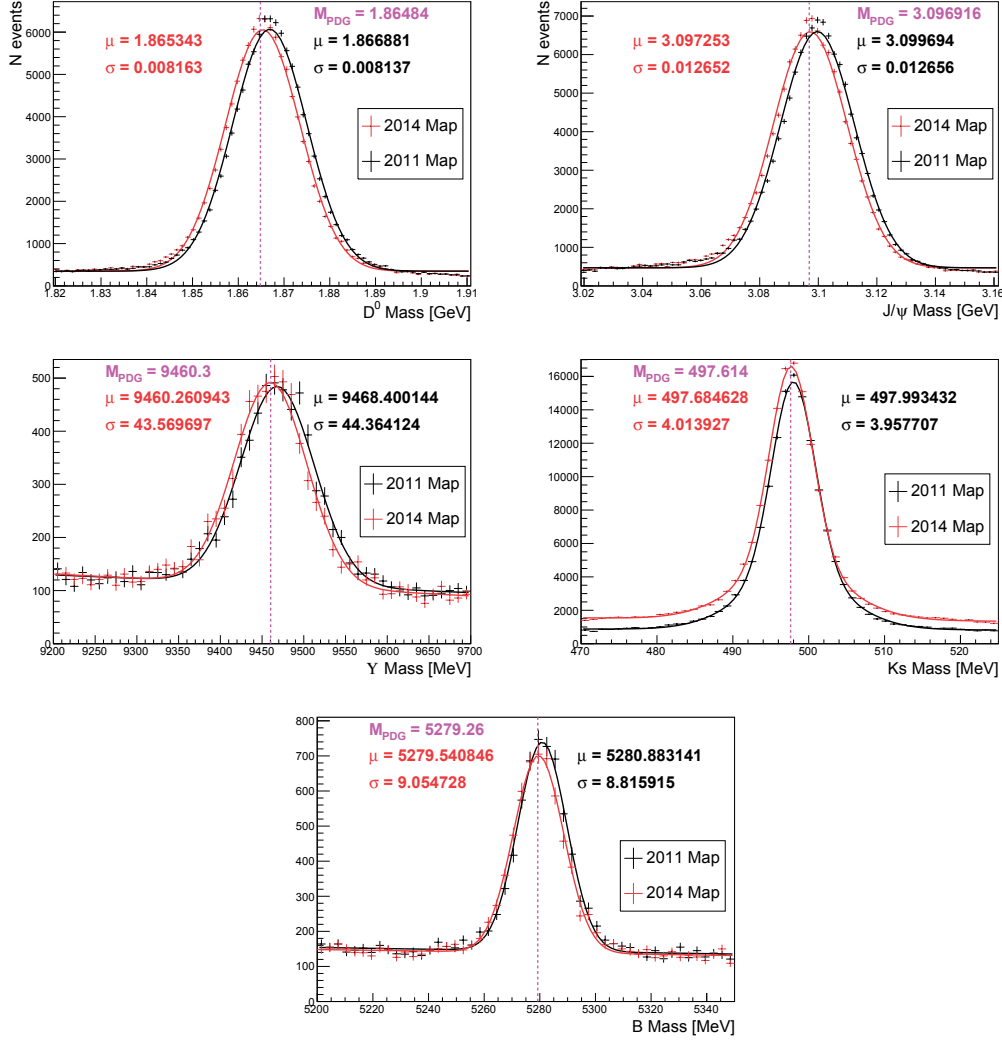
Figure 2.21 – Invariant mass distributions of five different mesons reconstructed with the two maps.

- θ_{12} : the opening angle between the momenta of the two daughter particles

The profile of the mass with respect to these variables should be flat. Therefore, the fit of a constant is performed and the χ^2 is taken as a measure of this dependence. All the related plots are shown in Appendix A and the results are summarised in Table 2.5, which shows how the mass dependence on these variables is affected by the new map. As examples of extreme cases, the χ^2 of the mass dependence on the momentum asymmetry is improved in average by 40% whereas for the dependence on the vertical slope, the χ^2 is degraded in average by 40%. In most cases, either an improvement or an absence of degradation is observed. It is therefore concluded that the reconstruction is globally better with the 2014 map.
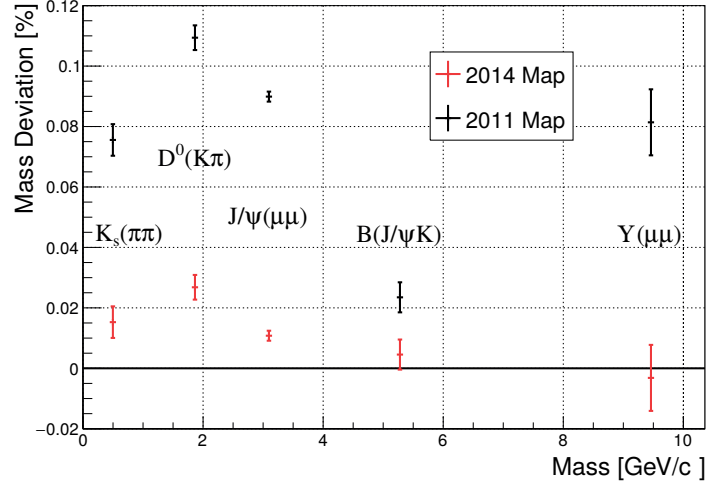
Figure 2.22 – Relative bias with respect to the PDG value [24] of the mean of the mass distribution for the reconstruction of five different particles with the 2014 and the 2011 maps.

2.3.6 Discussion

A new magnetic field map has been created and tested. It has been created by applying global transformations (three translations, three rotations and a field intensity scaling) on the 2011 map. Those corrections have been determined by fitting the map to new magnetic field measurements. The corrections are taken to be the same for the two polarities of the magnet and for the different parts of the detector (up/down, left/right) even if there are residual

Table 2.5 – Summary table that shows which dependency has been improved, which stayed constant and which has been degraded for the reconstruction with the 2014 map compared to the 2011 map. The categorisation is based on the comparison of the χ^2 values of a fit to a constant for the two maps.

Variable	Improved	Similar	Degraded
Mass vs p	D^0, B^+	J/ψ, $\Upsilon(1S)$	K_s^0
Mass vs p_T	D^0, J/ψ, B^+	$\Upsilon(1S)$, K_s^0	
Mass vs t_x	J/ψ, $\Upsilon(1S)$, B^+	K_s^0	D^0
Mass vs t_y	$\Upsilon(1S)$		D^0, J/ψ, K_s^0, B^+
Mass vs Δp	D^0, J/ψ, B^+	$\Upsilon(1S)$, K_s^0	
Mass vs A_p	D^0, J/ψ, K_s^0	$\Upsilon(1S)$, B^+	
Mass vs ϕ	J/ψ	$\Upsilon(1S)$, B^+	D^0, K_s^0
Mass vs ϕ'		J/ψ, $\Upsilon(1S)$, K_s^0, B^+	D^0
Mass vs η	D^0, J/ψ, B^+	$\Upsilon(1S)$, K_s^0	
Mass vs θ_{12}	D^0, K_s^0	$\Upsilon(1S)$, B^+	J/ψ
Total number	21	19	10

asymmetries. The 2014 map has been shown to bring the mean of the mass distributions closer to the known values and to improve on average the dependencies of the mass over several variables. It has been approved by the LHCb collaboration to be used for the entire Run 2 data taking period. It has therefore had a beneficial impact on all the analyses based on the Run 2 dataset.

The best possible map has been achieved within the scope of the current fitting method. As shown by the remaining asymmetries and dependencies, there is still room for improvement. This would however need a new approach. One possibility would be to go from global to local transformations. This might be done by adding some new degrees of freedom to the fit. For example, one could modify the translation in z to make it dependent on the height : $T_z' = T_z + \beta \cdot y$, where β would be a new parameter of the fit. This might improve the resulting map, but there are constraints that must be enforced. For example the map needs to be continuous at the boundaries and should respect Maxwell's equations as best as possible.

Finally, if further measurement campaigns are commissioned, one should aim at measuring the positions of all the probes when the magnetic field is on. This is expected to reduce significantly the systematic uncertainty on the measurements.

3 $D^0 \to K^+ K^- \pi^+ \pi^-$ candidate selection

This section describes the selection of $D^0 \to K^+ K^- \pi^+ \pi^-$ candidate decays. Candidates, pre-selected from a central stripping process, are required to have passed specific trigger requirements. A multivariate analysis (MVA) is then optimized to reject combinatorial background while maintaining high signal efficiency. Finally, specific backgrounds are identified and removed with targeted requirements.

3.1 Variables describing the decay

The four-body $D^0 \to K^+ K^- \pi^+ \pi^-$ decay mode has a five-dimensional phase space. Indeed, the four-momenta of the 4 daughter particles in the D^0 rest frame form a set of 16 kinematic variables subject to 8 constraints: 4 constraints from the known masses of the daughter particles and 4 constraints from energy-momentum conservation in the D^0 decay. Furthermore, the orientation of the decay in space, which is described by three parameters (for example the Euler angles), is arbitrary because the D^0 meson has no spin. Hence the decay is completely characterized by $16 - 8 - 3 = 5$ independent kinematic variables. In principle, any choice of five independent variables should be equivalent to describe the decay.

Ideally, there should be no need to make a choice of five variables and indeed, this analysis is largely independent of any choice. However, for visualisation purposes (as well as other practical applications where the 5D phase space needs to be binned, such as the computation of a χ^2 between the data and fit model), one set of variables needs to be chosen. The Cabibbo-Maksymowicz (CM) variables [77] form an appealing set:

- $m(K^+ K^-)$, the invariant mass of the two-kaon system;

- $m(\pi^+ \pi^-)$, the invariant mass of the two-pion system;

- $\cos\left(\theta_{K^+}^{K^+ K^-}\right)$, the cosine of the helicity angle for the two-kaon system, where $\theta_{K^+}^{K^+ K^-}$ is defined as the angle between the direction of the D^0 and that of one of the kaons in the rest frame of the two kaons (see Fig. 3.1);
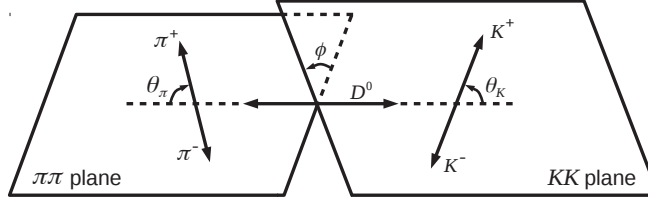
Figure 3.1 – Definition of the helicity angle $\theta_K = \theta_{K^+}^{K^+ K^-}$ ($\theta_\pi = \theta_{\pi^+}^{\pi^+ \pi^-}$) in the $K^+ K^-$ ($\pi^+ \pi^-$) rest frame, and the angle $\phi = \phi_{KK,\pi\pi}$ in the D^0 rest frame.

- $\cos\left(\theta_{\pi^+}^{\pi^+ \pi^-}\right)$, the cosine of the helicity angle for the two-pion system, where $\theta_{\pi^+}^{\pi^+ \pi^-}$ is defined similarly to $\theta_{K^+}^{K^+ K^-}$;

- $\phi_{K^+ K^-, \pi^+ \pi^-}$, the angle in the D^0 rest frame between the plane defined by the directions of the two kaons and the plane defined by the directions of the two pions.

Table 3.1 – List of the 31 variables used to visualise the five-dimensional phase space, grouped in 7 different sets. Set 1 corresponds to the CM variables shown in Fig. 3.1.

	two-body systems			three-body systems	
masses	helicity angles	decay plane angles		masses	helicity angles
Set 1:				**Set 4:**	
$m(K^+ K^-)$	$\cos\left(\theta_{K^+}^{K^+ K^-}\right)$	$\phi_{K^+ K^-, \pi^+ \pi^-}$		$m(K^+ K^- \pi^+)$	$\cos\left(\theta_{K^+}^{K^+ K^- \pi^+}\right)$
$m(\pi^+ \pi^-)$	$\cos\left(\theta_{\pi^+}^{\pi^+ \pi^-}\right)$				$\cos\left(\theta_{K^-}^{K^+ K^- \pi^+}\right)$
					$\cos\left(\theta_{\pi^+}^{K^+ K^- \pi^+}\right)$
Set 2:				**Set 5:**	
$m(K^+ \pi^-)$	$\cos\left(\theta_{K^+}^{K^+ \pi^-}\right)$	$\phi_{K^+ \pi^+, K^- \pi^-}$		$m(K^+ K^- \pi^-)$	$\cos\left(\theta_{K^+}^{K^+ K^- \pi^-}\right)$
$m(K^- \pi^+)$	$\cos\left(\theta_{K^-}^{K^- \pi^+}\right)$				$\cos\left(\theta_{K^-}^{K^+ K^- \pi^-}\right)$
					$\cos\left(\theta_{\pi^-}^{K^+ K^- \pi^-}\right)$
Set 3:				**Set 6:**	
$m(K^+ \pi^+)$	$\cos\left(\theta_{K^+}^{K^+ \pi^+}\right)$	$\phi_{K^+ \pi^-, K^- \pi^+}$		$m(K^+ \pi^+ \pi^-)$	$\cos\left(\theta_{K^+}^{K^+ \pi^+ \pi^-}\right)$
$m(K^- \pi^-)$	$\cos\left(\theta_{K^-}^{K^- \pi^-}\right)$				$\cos\left(\theta_{\pi^+}^{K^+ \pi^+ \pi^-}\right)$
					$\cos\left(\theta_{\pi^-}^{K^+ \pi^+ \pi^-}\right)$
				Set 7:	
				$m(K^- \pi^+ \pi^-)$	$\cos\left(\theta_{K^-}^{K^- \pi^+ \pi^-}\right)$
					$\cos\left(\theta_{\pi^+}^{K^- \pi^+ \pi^-}\right)$
					$\cos\left(\theta_{\pi^-}^{K^- \pi^+ \pi^-}\right)$

Table 3.2 – Trigger lines used in this analysis. At least one line per level is required to be fired. The definition of each trigger line is given in Ref. [53] at the table number specified in the right column.

Trigger level	Trigger line	Reference table in Ref. [53] for (2011) 2012
L0	Muon TOS on μ Hadron TOS on D^0	(4.1.1) 5.1.1
HLT1	TrackALLMuon TOS on μ TrackALLL0 TOS on B	(4.1.7) 5.1.7
HLT2	SingleMuon TOS on μ TopoMu(2,3,4) TOS on B	(4.1.80 & 4.1.81) 4.1.80, 4.1.81 & 5.2.2 (4.1.11 to 4.1.17) 5.1.10 to 5.1.16

The CM variables describe the K^+K^- and $\pi^+\pi^-$ systems. In analogy to this parametrisation, two other sets of variables are defined to describe the $K^+\pi^-$ and $K^-\pi^+$ systems, as well as the $K^+\pi^+$ and $K^-\pi^-$ systems. Furthermore, the three-body systems can also be described in analogy to this parametrisation. Four sets of variables are selected to describe the $K^+\pi^+\pi^-$, $K^-\pi^+\pi^-$, $K^+K^-\pi^+$ and $K^+K^-\pi^-$ systems. These seven sets of variables are listed in Table 3.1. In total 31 variables are defined and used to visualise the complicated five-dimensional phase space.

3.2 Pre-selection: stripping and choice of trigger lines

The candidates are initially required to have fired a set of trigger lines. The choice of trigger lines is listed in Table 3.2. All these lines are listed as triggered on signal (TOS), which means that our signal decay chain ($B \rightarrow D^0(\rightarrow K^+K^-\pi^+\pi^-)\mu^- X$) has to be the reason why the trigger line has fired.

The candidates are then filtered with a set of pre-selection criteria, called a stripping line. All requirements applied in this stripping line are listed in Table 3.3 and are in common between the two years of data taking.

As the Monte Carlo (MC) sample without the stripping and trigger selection applied was not available, an ad-hoc phase-space sample has been generated without any acceptance or selection cuts. The efficiency of the stripping and trigger selection together with the efficiency of the generator level cuts is studied in the five-dimensional phase space and found to be rather constant (within 10–25%) across the entire phase space. It is shown in Fig. 3.2 as a function of each of the five CM variables. The average efficiency is arbitrarily set to the average efficiency of the stripping and trigger selections, which is $\sim 3.5\%$. A different behaviour is observed for the two kaon invariant mass and the two pion invariant mass. This is in part due to the different particle identification cuts applied on kaons and pions.

Table 3.3 – List of the requirements applied at the stripping level. Some of the variables used are the momentum (p) and the transverse momentum (p_T). The vertex χ^2 (χ^2_{vtx}) is the χ^2 of the fit of the vertex. The impact parameter (IP) χ^2 (χ^2_{IP}) is the difference of χ^2_{vtx} between a vertex fit with and without the particle. The best primary vertex is defined as the vertex with the minimum χ^2_{IP}. The cosine of the angle between the momentum of the particle and the direction of flight from the best primary vertex to the decay vertex is referred to as DIRA. The χ^2 of the distance of closest approach (DOCA) between any combination of two of the daughter tracks (χ^2_{DOCA}) is defined as the square of the distance divided by the square of its uncertainty. The χ^2 of the distance between the best primary vertex and the end vertex (χ^2_{BPVVD}) is similarly defined as the χ^2_{DOCA}. The DLLX variables are particle identification variables further explained in Sec. 3.4.2. Prob(ghost) is the probability calculated by the tracking algorithms for the track being an artefact.

Candidate	Requirement
K	track fit $\chi^2/\mathrm{ndf} < 4$
	$p > 2$ GeV/c
	$p_T > 300$ MeV/c
	$\chi^2_{\mathrm{IP}} > 9$
	DLLK > 4
	Prob(ghost) < 0.5
π	track fit $\chi^2/\mathrm{ndf} < 4$
	$p > 2$ GeV/c
	$p_T > 300$ MeV/c
	$\chi^2_{\mathrm{IP}} > 9$
	DLLK < 10
	Prob(ghost) < 0.5
μ	track fit $\chi^2/\mathrm{ndf} < 4$
	$p > 3$ GeV/c
	$p_T > 1.2$ GeV/c
	$\chi^2_{\mathrm{IP}} > 9$
	DLL$\mu > 0$
	Prob(ghost) < 0.5
D^0	$m \in [1.805, 1.925]$ GeV/c^2
	$\sum\limits_{i=1}^{4} p_{T,i} > 1.8$ GeV/c
	$\chi^2_{\mathrm{vtx}}/\mathrm{ndf} < 6$
	DIRA > 0.99
	$\chi^2_{\mathrm{DOCA}} < 9$
	$\chi^2_{\mathrm{BPVVD}} > 100$
B	$m \in [2.5, 6.0]$ GeV/c^2
	$M(p_{D^0} + p_\mu) < 6.2$ GeV/c^2
	$\chi^2_{\mathrm{vtx}}/\mathrm{ndf} < 6$
	DIRA > 0.999
	$z_{D^0\mathrm{vtx}} - z_{B\mathrm{vtx}} > 0$
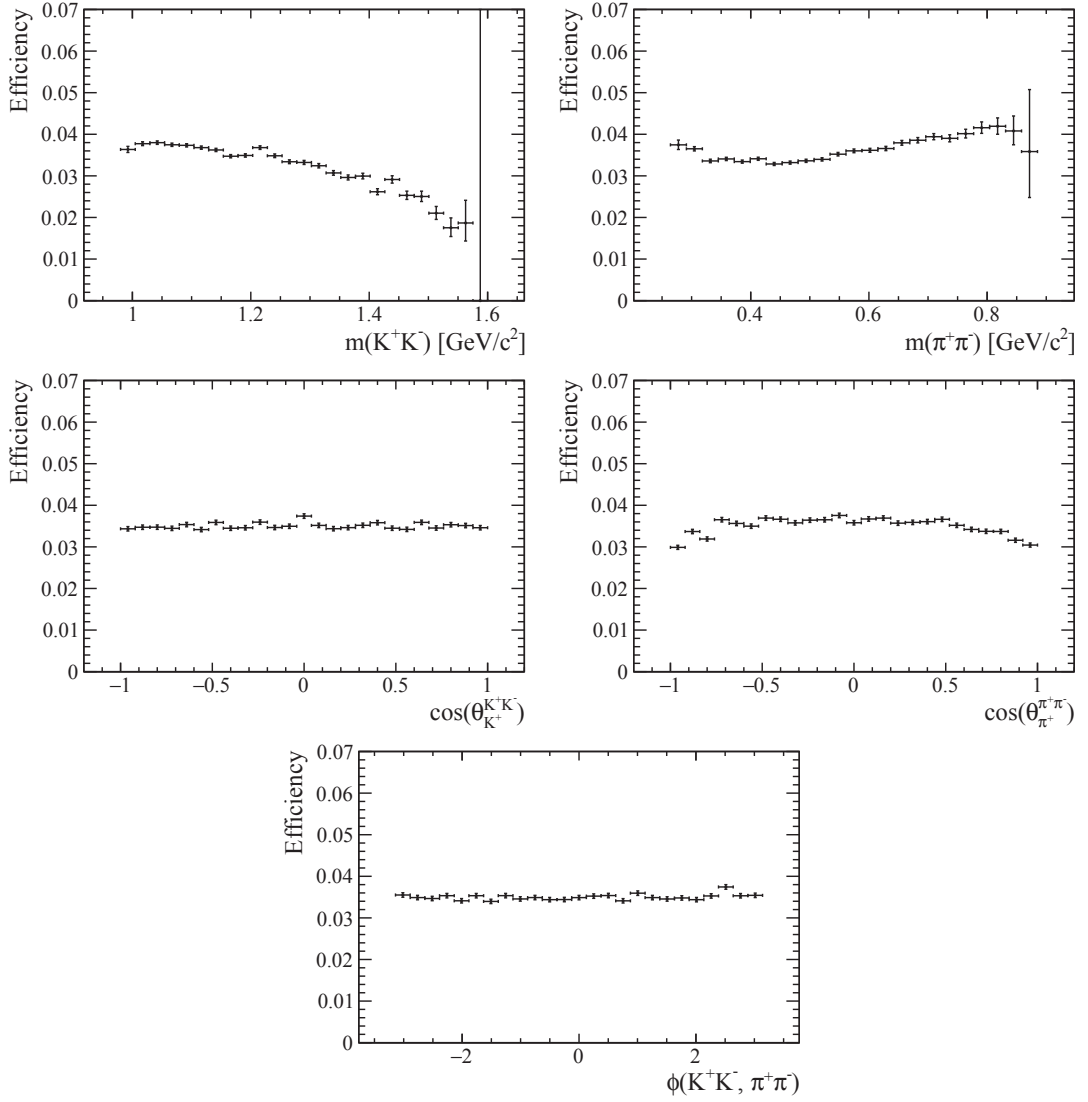
Figure 3.2 – Efficiency of the pre-selection (which contains the generator level cuts, the stripping and trigger selections) as a function of the CM variables.

3.3 Tuning and calibration

Previous analyses [78–80] have shown that the absolute momentum scale as well as improvements on the mass resolution can be achieved with a momentum calibration procedure. This procedure [81] is therefore also applied in this analysis after the pre-selection. In order to further improve the resolution of the reconstruction, we impose that the D^0 mass, reconstructed from its four daughter particles, matches exactly its known mass given in Ref. [24]. The "decay tree fitter" (DTF) algorithm [82] refits the whole decay chain under this constraint.
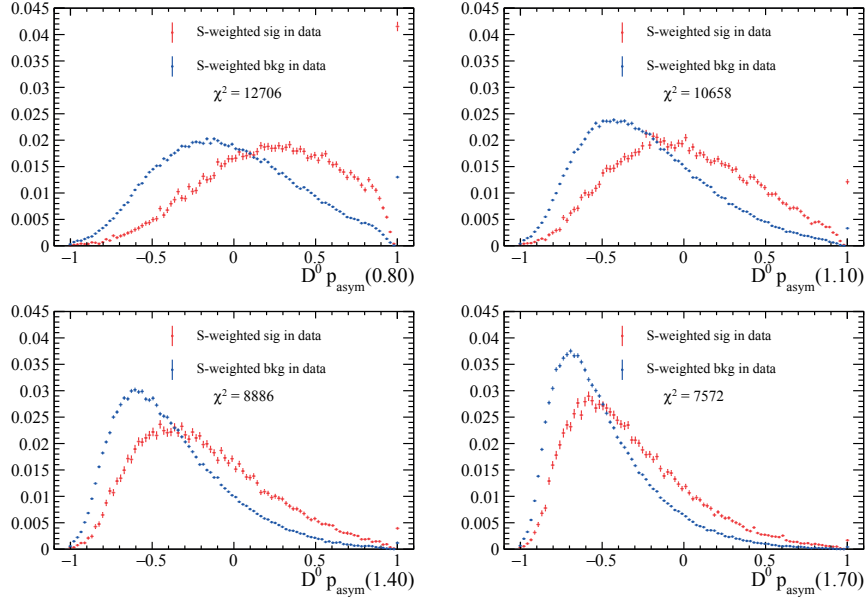
Figure 3.3 – Signal and background distributions of the momentum asymmetry inside a cone around the D^0 for four different values of the cone size (0.8, 1.1, 1.4 and 1.7 rad, from top left to bottom right).

3.4 Multivariate analysis

3.4.1 Isolation variables

Along with the usual kinematic variables describing the decay, some more sophisticated variables, called isolation variables, have a significant discriminating power between signal and background. The first set of variables is analysing the tracks that do not belong to the signal decay channel inside a cone around either the D^0, the B or the μ candidate [83]. The following variables are studied:

- cmult: number of tracks in the cone;

- p_{cone}, $p_{\text{T,cone}}$: vectorial sum of all the (transverse) momenta inside the cone;

- A_p, $A_{p_{\text{T}}}$: the (transverse) momentum asymmetry defined as

$$A_{p_{(\text{T})}} = \frac{p_{(T,)D^0} - p_{(\text{T,})\text{cone}}}{p_{(T,)D^0} + p_{(\text{T,})\text{cone}}} \, ; \tag{3.1}$$

- $\Delta\eta, \Delta\phi$: difference in pseudorapidity η and azimuthal angle ϕ between the total vector momentum of the tracks inside the cone and the D^0 momentum;

The discriminating power of these variables depends on the size of the cone. This cone size is defined as the distance between the D^0 candidate and the edge of the cone in the $\eta - \phi$ plane.

A distance in this plane is defined as

$$\Delta R = \sqrt{\left(\Delta\eta\right)^2 + \left(\Delta\phi\right)^2}. \tag{3.2}$$

The signal and background distributions in data (extracted with the sPlot technique) are compared for four different values of the cone size, between 0.8 and 1.7 rad. The difference between the two distributions is assessed by the χ^2 test. An example of the resulting behaviour is shown in Fig. 3.3 for the momentum asymmetry of the D^0 after the pre-selection. The most discriminating power is achieved with the smallest value of the cone size, 0.8 rad, which is used for the rest of this analysis. The peaking bin at 1 is expected from the definition of the asymmetry in Eq. 3.1. If there is no track in the cone, the asymmetry is 1. The number of events falling in this bin decreases when the cone size increases. The same behaviour is observed for the other cone isolation variables and for the other particles (the B and the μ).

The second set of isolation variables are analysing the vertex of the particle X (here the D^0 or the B) [84]:

- min $\Delta\chi^2(X + 1\ (2)$ trk): the smallest change in vertex χ^2 when one (two) track(s) are added to the vertex;

- $m(X + 1\ (2)$ trk)$_{\min\ \Delta\chi^2}$: the invariant mass of all the tracks assigned to the vertex when one (two) track(s), assumed to be pion(s), are added to the vertex to produce the smallest change in vertex χ^2.

An additional variable, the "corrected mass" of the B meson, is found to help isolating the signal. There is some uncertainty in the reconstruction of the B meson due to the missing momentum of the neutrino that is not reconstructed. By using the missing momentum perpendicular to the B-meson direction of flight ($p_\perp$), we can reduce part of that uncertainty. This missing momentum is equal to the momentum of the $D^0\mu$ system perpendicular to the B-meson direction of flight. The corrected mass is defined as

$$m_{\text{corr}} = \sqrt{m^2 + p_\perp^2} + |p_\perp|, \tag{3.3}$$

where m is the reconstructed mass of the $D^0\mu$ system. Its distribution is shown in Fig. 3.4. The χ^2 test on the signal and background distributions shows that, indeed, the corrected mass has a better discriminating power than the $D^0\mu$ mass and is therefore used in the MVA.

3.4.2 Multivariate selection

The MVA analyses a set of selected variables in control samples of signal and backgroud events to create a new variable that is used to discriminate between the two categories. In addition to all previously mentioned isolation variables, the following variables are studied in order to find the ones with the most discriminating power:
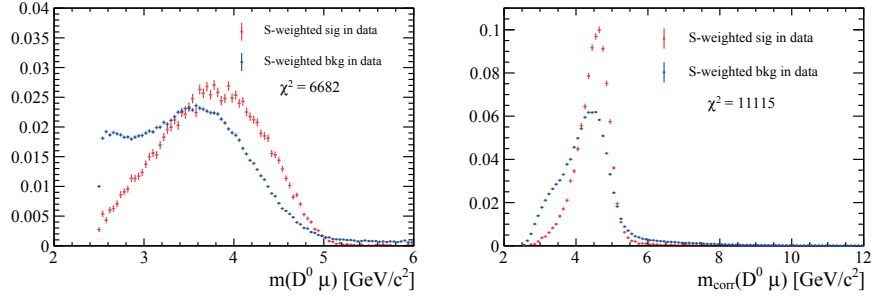
Figure 3.4 – Signal and background distributions of the $D^0 \mu$ invariant mass and of the $D^0 \mu$ corrected invariant mass.

- B: momentum (p), transverse momentum (p_T), χ^2_{IP}, DTF χ^2_{vtx}/ndf and mass (m);

- D^0: p, p_T, χ^2_{IP}, DTF χ^2_{vtx}/ndf, decay length significance (DLS, *i.e.* the decay length divided by its uncertainty) and proper time (τ);

- μ: longitudinal momentum (p_z), p_T, χ^2_{IP};

- D^0 daughter tracks: maximum ghost probability (max Prob(ghost)), χ^2_{IP}, particle identification (PID) variables.

The PID variables are divided in two classes:

- Delta log likelihood variables: these variables combine the informations coming from several subdetectors. They are called DLLX and represent the logarithm of the ratio between the likelihood of being a particle X and the likelihood of being a pion.

- The neural network variables: these variables are the output of a neural network discrimination and are called Prob_NNX, which represent the probability of being a particle X.

The MVA is performed with the TMVA [85] package included in ROOT [86]. All previously mentioned variables are used in the first test for the MVA. The set of variables is then reduced until the performance of the MVA decreases significantly. The following 11 most powerful variables are kept in the final MVA:

- m_{corr}

- $m(D^0 + 1 \text{ trk})_{\min \Delta \chi^2}$

- $\ln(\min \Delta \chi^2(D^0 + 2 \text{ trk}))$

- $D^0 A_{p_T}$

- $D^0 \ln(\text{DLS})$

- $D^0 \chi^2_{vtx}$/ndf

- K^+ Prob_NNK

- K^- Prob_NNK

- π^+ Prob_NNπ

- π^- Prob_NNπ

- max Prob(ghost)

The correlations between these 11 variables is quite low for both the signal and the background samples, as shown in Fig. 3.5.
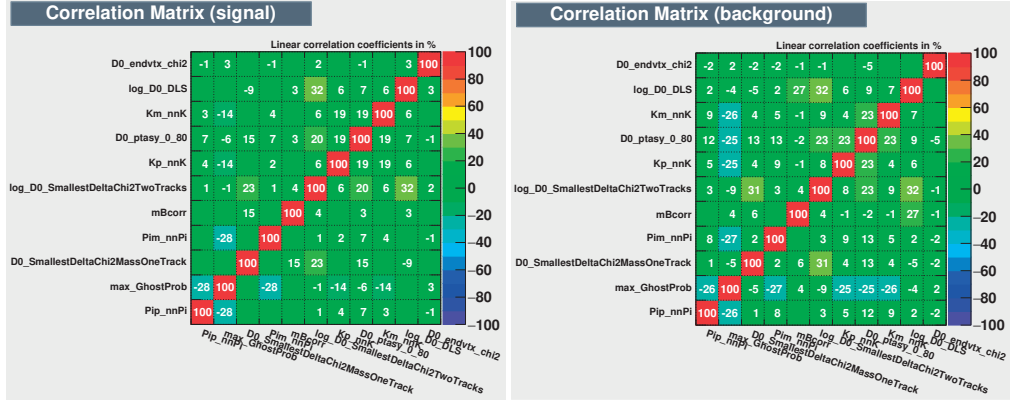
Figure 3.5 – Correlation matrices for the signal and background sample of the 11 variables used in the MVA.

The Run 1 dataset can be separated in four subsamples, according to the year of data taking (2011 or 2012) and the polarity of the magnet (up or down). These four subsamples are studied separately in order to spot any difference that might motivate the use of a different treatment for each subset. No significant differences are observed, the four subsamples are therefore used without any distinction for the BDT training and optimisation as well as for the rest of the analysis.

The background is taken from the D^0 sidebands in the full Run 1 data. They are defined as where the invariant mass of the $K^+K^-\pi^+\pi^-$ system belongs to $[1.81, 1.835]$ GeV/c^2 or $[1.895, 1.92]$ GeV/c^2. There are ~ 1 M events in the sidebands, which are split for the two stages of the MVA. 75% are used for the training and the remaining 25% for the testing of the classifier.

The description of the signal is taken from the MC samples. In order to save some CPU-time, the entire MC sample is not used. ~ 3 M MC events are sufficient to have a reliable description of the signal. This sample is also split, the same number of events as for the background is used for the training (750 k) and the rest is used for the testing.

Five different classifiers have been tested in order to find the most appropriate one for this analysis:

- Likelihood

- k^{th} nearest neighbour (KNN)

- Fisher

- Multilayer perceptron (MLP)

- Boosted decision tree (BDT)

The resulting Receiver Operating Characteristic (ROC) curves are shown in Fig. 3.6. The performance of the classifiers is measured by the integral under the ROC curve, where 0.5 corresponds to random guessing. Since the BDT shows the best result with an integral of 0.828, it is chosen as the default classifier for the selection. The BDT consists of a sequence
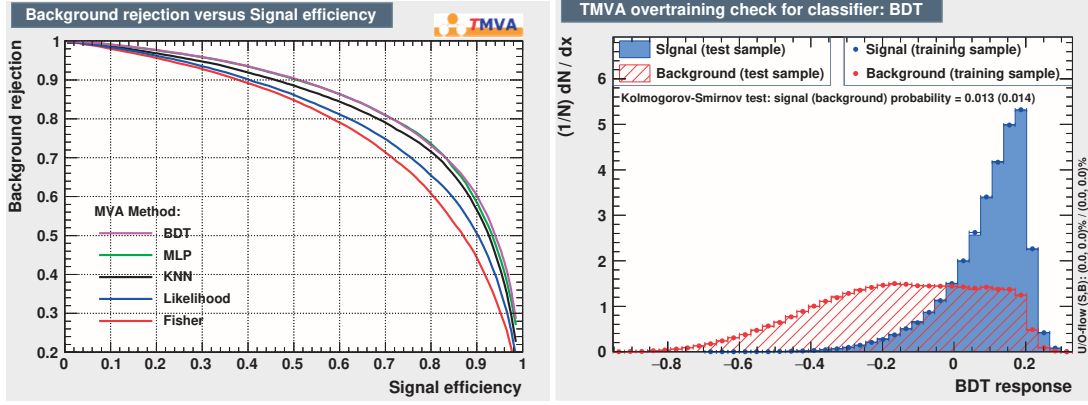
Figure 3.6 – Left: ROC curves of the five classifiers tested. Right: Signal and background distributions of the BDT output for the training and testing samples.

of different possible cuts on each variable which builds up a decision tree. This decision tree is boosted using AdaBoost [87], where a weight is added to each event in the training set in order to focus more on the poorly predicted events on the next iteration. This has the power to combine weak predictions into a strong model. The BDT output for the signal and background components are shown in Fig. 3.6 for the training and test samples. No evidence for over-training is observed.

3.4.3   BDT optimisation

The BDT output of the MVA is studied to find the best cut to separate the signal from the background. The optimisation is done on the data since $D^0 \to K^+ K^- \pi^+ \pi^-$ is a well established decay mode and its signal yield is very large. The figure of merit chosen for the optimisation is the significance

$$\mathcal{S} = \frac{N_{\mathrm{s}}}{\sqrt{N_{\mathrm{s}} + N_{\mathrm{b}}}} \tag{3.4}$$

where N_{s} is the number of signal and N_{b} the number of background events in the D^0 mass signal region defined as $\pm 2\sigma$ around the central value of the D^0 mass. These yields are extracted from a fit to the D^0 mass spectrum in data. Details about the fit are described in Sec. 3.6. Fits are performed for 23 different values of the BDT cut between -1 and 0.1. The significance is plotted against the cut value applied on the BDT output in Fig. 3.7. The condition that maximises the significance is to retain all the candidates with BDT > -0.1, resulting in a purity of $(80.7 \pm 0.3)\%$ at this stage.

The efficiency of this BDT cut with respect to pre-selection is studied over the phase space and found to be flat within 0.5–3%. It is shown in Fig. 3.8 as a function of the five CM variables.
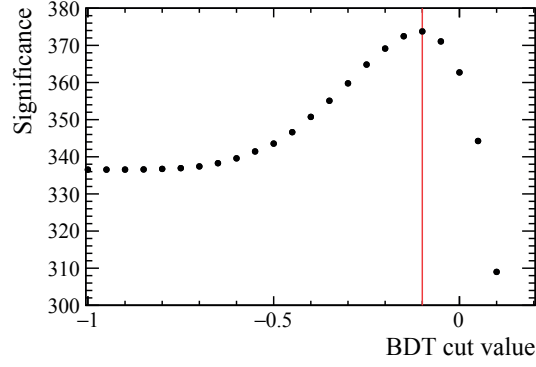
Figure 3.7 – Significance of the D^0 signal as a function of the requirement on the BDT output. The red line indicates the value of the optimal cut.
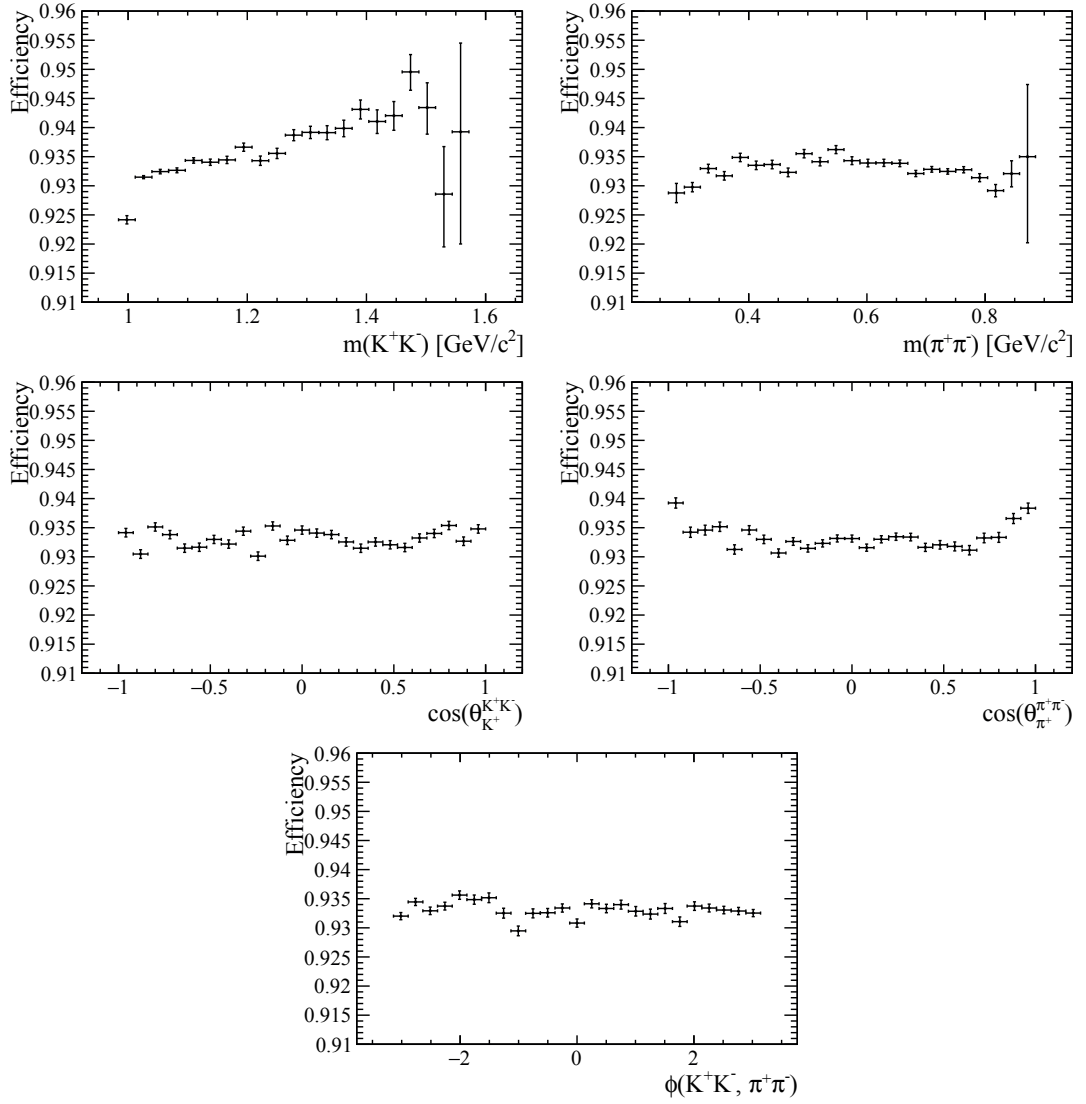
Figure 3.8 – Efficiency of the BDT cut with respect to the pre-selection as a function of the CM variables.
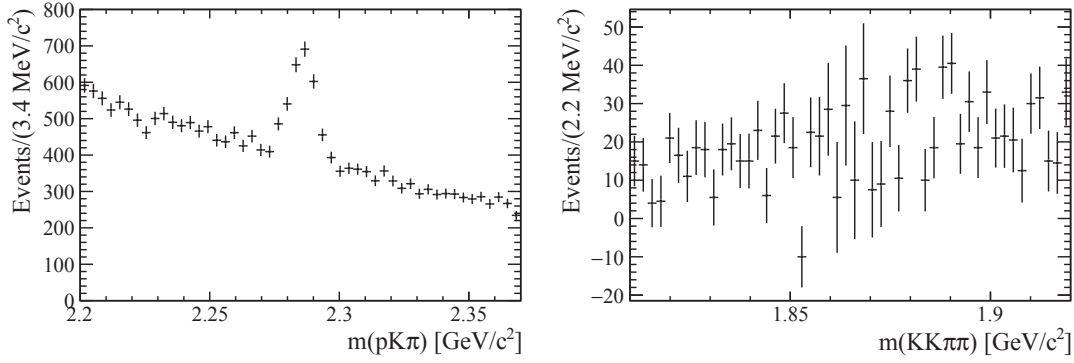
Figure 3.9 – Left: $pK^-\pi^+$ $\left(\overline{p}K^+\pi^-\right)$ invariant mass distribution of selected $K^+K^-\pi^+\pi^-$ combinations (two entries per $D^0 \rightarrow K^+K^-\pi^-\pi^+$ candidate with weight 0.5 each) where the kaon candidate with the same charge as the pion is given the proton mass. Right: $K^+K^-\pi^+\pi^-$ invariant mass distribution for the sideband-subtracted Λ_c signal.

3.5 Further requirements

3.5.1 Removal of specific backgrounds

This section describes three background components observed after the MVA selection: a small contribution from $\Lambda_c^+ \rightarrow pK^-\pi^+$ decays, a peak in the $KK\pi$ invariant mass, and three-body $D^0 \rightarrow K_S^0 K^+ K^-$ decays. Their impact on the analysis is evaluated carefully and a decision is made whether an action needs to be taken or not.

Λ_c^+ background

In the background distribution, some kaon candidates are misidentified protons, and a structure is observed in the $pK^-\pi^+$ invariant mass (Fig. 3.9 left). This structure is attributed to the Λ_c^+ baryon. In order to assess its impact, the signal and sideband regions are defined in the Λ_c^+ mass peak and then the $K^+K^-\pi^+\pi^-$ invariant mass is examined in the Λ_c^+ signal region after subtracting the Λ_c^+ sidebands (Fig. 3.9 right); no peak is seen in the D^0 signal region, meaning that Λ_c^+ background can be treated together with the combinatorial background.

Misreconstructed background

A strange peak is observed in the $K^+K^-\pi^\pm$ invariant mass, in the upper end of the spectrum (Fig. 3.10 left). It is not due to any resonance, but is explained by taking the difference between the $K^+K^-\pi^+\pi^-$ and $K^+K^-\pi^\pm$ invariant masses. We define

$$\Delta m = \begin{cases} m(K^+K^-\pi^+\pi^-) - m(K^+K^-\pi^-) & \text{for } D^0 \\ m(K^+K^-\pi^+\pi^-) - m(K^+K^-\pi^+) & \text{for } \overline{D}^0 \end{cases} \tag{3.5}$$

$$\Delta m' = \begin{cases} m(K^+K^-\pi^+\pi^-) - m(K^+K^-\pi^+) & \text{for } D^0 \\ m(K^+K^-\pi^+\pi^-) - m(K^+K^-\pi^-) & \text{for } \overline{D}^0 \end{cases} \tag{3.6}$$
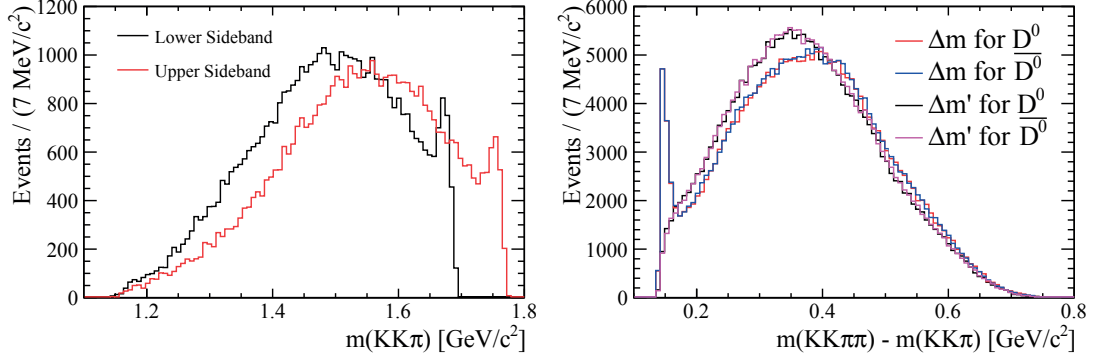
Figure 3.10 – Left: invariant mass distributions of the two $K^+K^-\pi^\pm$ systems (two entries per $D^0 \to K^+K^-\pi^-\pi^+$ candidate with weight 0.5 each) for each D^0 mass sideband. Right: distribution of the Δm and $\Delta m'$ variables shown for all the D^0 and $\overline{D}^0$ candidates.

The distributions of these two variables are shown in Fig. 3.10 (right). The peak appears only in the Δm variable, not in $\Delta m'$. This observation actually clarifies the source of the peak. We conclude that the peak appears only when the D^0 comes from a D^{*+} coming from the B. The D^0 is in fact decaying to $K^+K^-\pi^+\pi^-$ but is reconstructed using the slow π^+ coming from the D^{*+} decay instead of the correct π^+ from the D^0 decay (missed pion). In this way, the peaks appear only when the charge of the missed pion matches the charge of the slow pion from the D^*:

- $B^0(\to D^{*+}(\to D^0(\to K^+K^-\pi^+\pi^-)\pi^+)\mu^-)$,

- $\overline{B}^0(\to D^{*-}(\to \overline{D}^0(\to K^+K^-\pi^+\pi^-)\pi^-)\mu^+)$.

This background is easily removed with the requirement $\Delta m > 0.18$ GeV/c^2. The efficiency of this cut with respect to the BDT cut is studied in five dimensions, and shown as a function of the five CM variables in Fig. 3.11; it drops drastically at large K^+K^- masses approaching the kinematic boundary.

K_S^0 background

The $\pi^+\pi^-$ invariant mass distribution shows a structure around 500 MeV/c^2 in the signal region (see Fig. 3.12). This peak is due to the presence of real K_S^0 mesons in the sample, coming from $D^0 \to K_S^0 K^+K^-$ decays. These decays have a different topology than $D^0 \to K^+K^-\pi^+\pi^-$ decays. They are either Cabibbo-favoured or doubly Cabibbo-suppressed, whereas $D^0 \to K^+K^-\pi^+\pi^-$ is singly Cabibbo-suppressed. Furthermore, $K_S^0 \to \pi^+\pi^-$ is a weak decay whereas all the resonances taken into account in this analysis decay strongly. All these reasons lead to the decision of applying a K_S^0 veto: all candidates that have a $\pi^+\pi^-$ invariant mass in the region $[480.2, 507.2]$ MeV/c^2 are removed. This cut is applied on the data after the DTF has been applied with the D^0 mass constraint. This is necessary in order to align the cut for the sidebands of the D^0 which will be used in the background description in Sec. 4.5. The
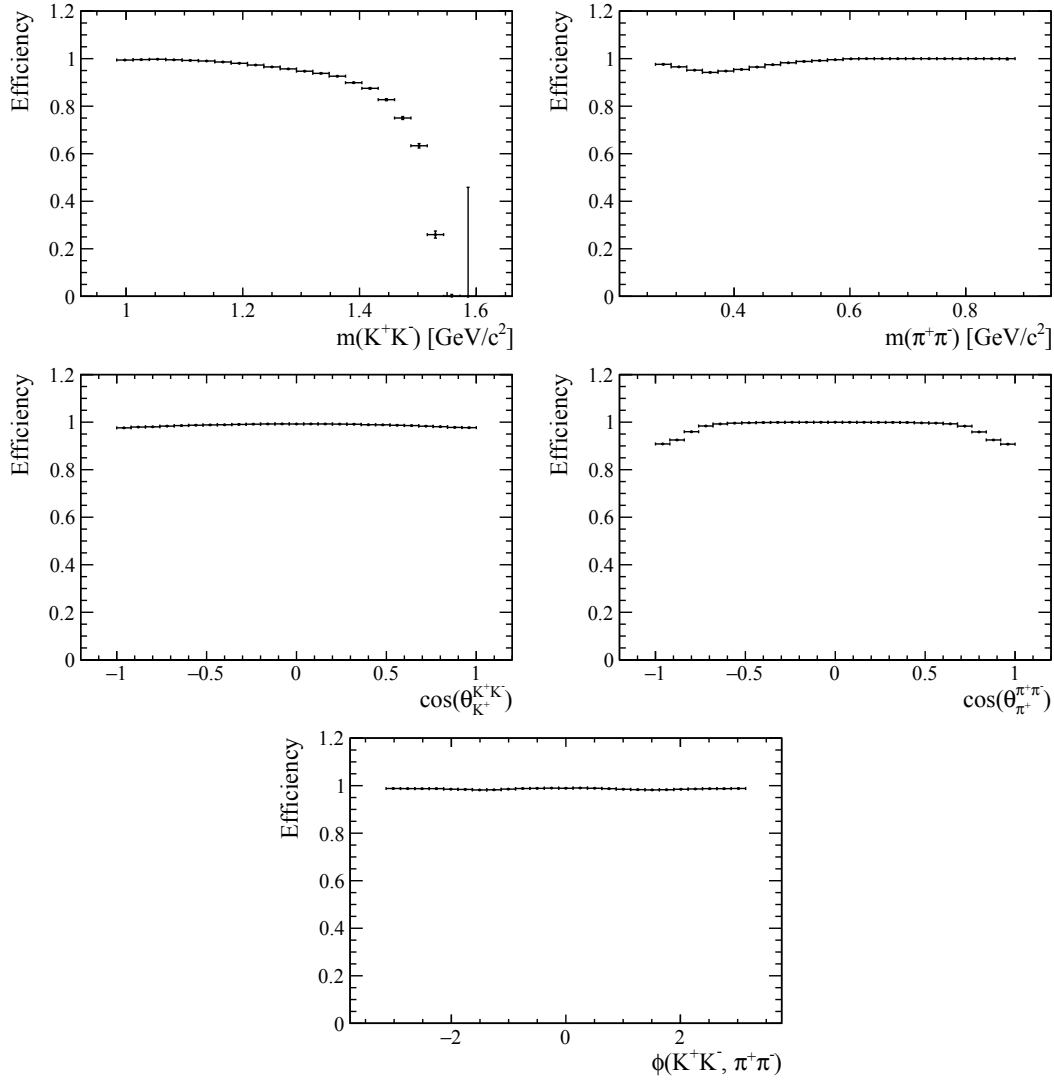
Figure 3.11 – Efficiency of the cut on Δm with respect of the BDT cut as a function of the CM variables.
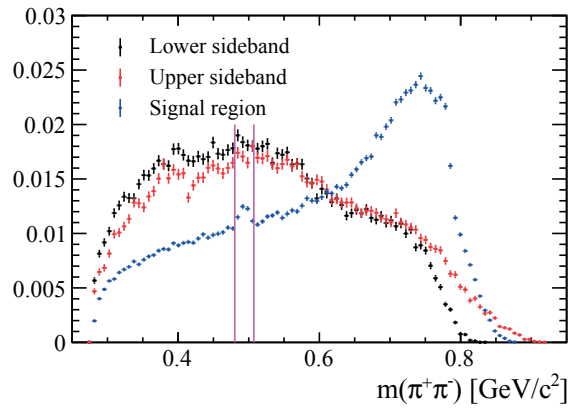
Figure 3.12 – $\pi^+\pi^-$ invariant mass distribution of the $D^0 \rightarrow K^+K^-\pi^+\pi^-$ candidates, showing a K_S^0 peak in the D^0 signal region.
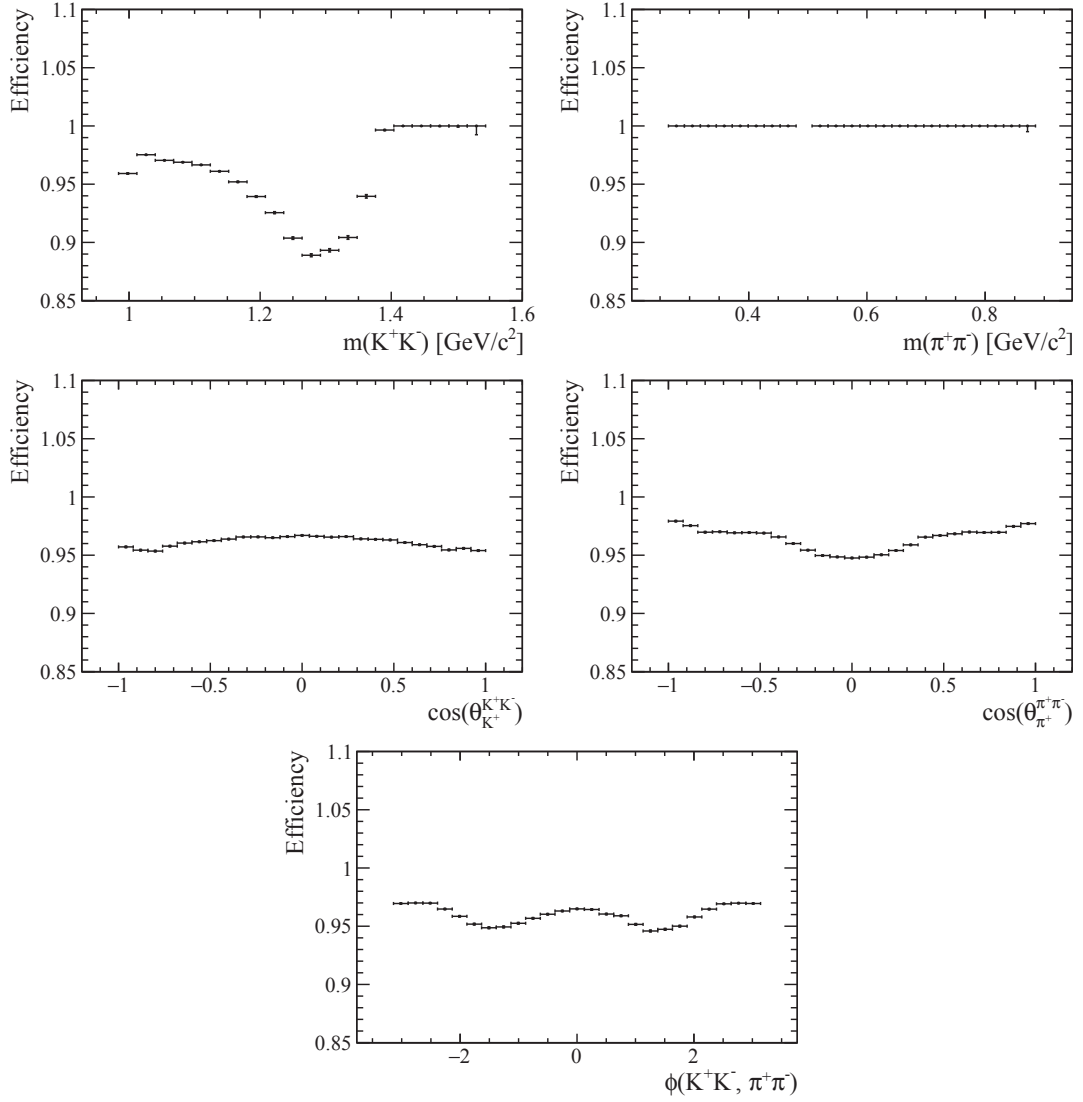
Figure 3.13 – Efficiency of the K_S^0 veto with respect to the Δm cut as a function of the CM variables.

efficiency of this selection is studied in five dimensions, and shown as a function of the five CM variables in Fig. 3.13.

3.5.2 Removal of multiple candidates

A fraction of 1.5% of the events contain more than one D^0 candidate. Only one candidate per event is kept while the others are discarded. The choice is made randomly. In order to keep the reproducibility of the selection, the seed of the random number generator is chosen to be the sum of the run number and the event number.

Table 3.4 – Offline selection applied to the candidates passing the stripping requirements of Table 3.3.

Variable	Requirement
BDT	> -0.1
Δm	$> 0.18 \, \text{GeV}/c^2$
$m(\pi^+\pi^-)$	$\notin [480.2, 507.2] \, \text{MeV}/c^2$
multiple candidates	randomly rejected
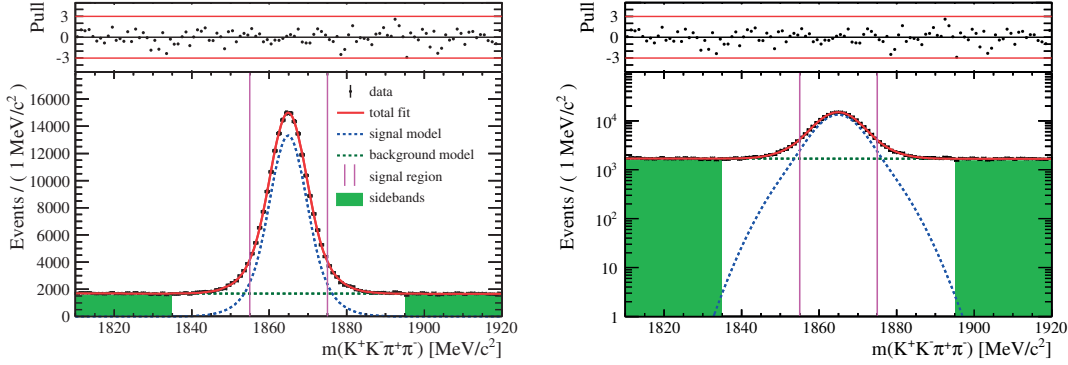
Figure 3.14 – Mass distribution of the $D^0 \rightarrow K^+ K^- \pi^+ \pi^-$ candidates after the final selection, with fit result superimposed. The top plot shows the normalised residuals (differences between the data points and the fit results, divided by the statistical uncertainty of the data).

3.6 Final selection and efficiency

The final selection requirements are summarized in Table 3.4. There are 365 634 data events selected in the full D^0 mass region (FR) (*i.e.* $1.81 \, \text{GeV}/c^2 < m(K^+K^-\pi^+\pi^-) < 1.92 \, \text{GeV}/c^2$), 42 245 in the lower sideband, 196 648 in the signal region (SR) and 41 669 in the upper sideband. The SR is defined as ± 2 standard deviations around the central value of the D^0 mass (*i.e.* $1.855 \, \text{GeV}/c^2 < m(K^+K^-\pi^+\pi^-) < 1.875 \, \text{GeV}/c^2$). The resulting D^0 mass distribution is shown in Fig. 3.14 for the full Run 1 dataset. A fit is performed using as signal model the sum of two Gaussian functions sharing the same mean value and as background model an exponential function. The resulting signal and background distributions are integrated over the SR in order to obtain the yields. The resulting fit parameters are listed in Table 3.5.

This selection provides a significant improvement compared to the cut-based selection of the previous LHCb analysis of $D^0 \rightarrow K^+ K^- \pi^+ \pi^-$ decays [52]: 5% more signal candidates and 30% less background candidates are retained. The total yields in the previous analysis were $N_{\text{sig}} = 171\,298 \pm 765$ and $N_{\text{bkg}} = 240\,412 \pm 808$ in the full D^0 mass window.

The total efficiency is shown in Fig. 3.15 as a function of each of the five CM variables. Since this efficiency compares the final MC sample to the generated sample before the stripping has been applied, the same procedure as for the pre-selection efficiency is applied. The distributions of the final MC sample are compared to the one of an ad-hoc phase-space sample generated without any generator level cuts.

Table 3.5 – Results of the fit to the D^0 mass distribution after the final selection.

	Parameter	Fitted value
Double Gaussian	μ	$1\,864.91 \pm 0.02$ MeV/c^2
	σ_1	4.48 ± 0.06 MeV/c^2
	σ_2	7.94 ± 0.18 MeV/c^2
	f_1	0.604 ± 0.003
Exponential	c	-0.14 ± 0.07
Yields	N_{sig} in FR	$180\,551 \pm 572$
	N_{bkg} in FR	$185\,084 \pm 576$
	N_{sig} in SR	$162\,909 \pm 516$
	Purity in SR	0.828 ± 0.003
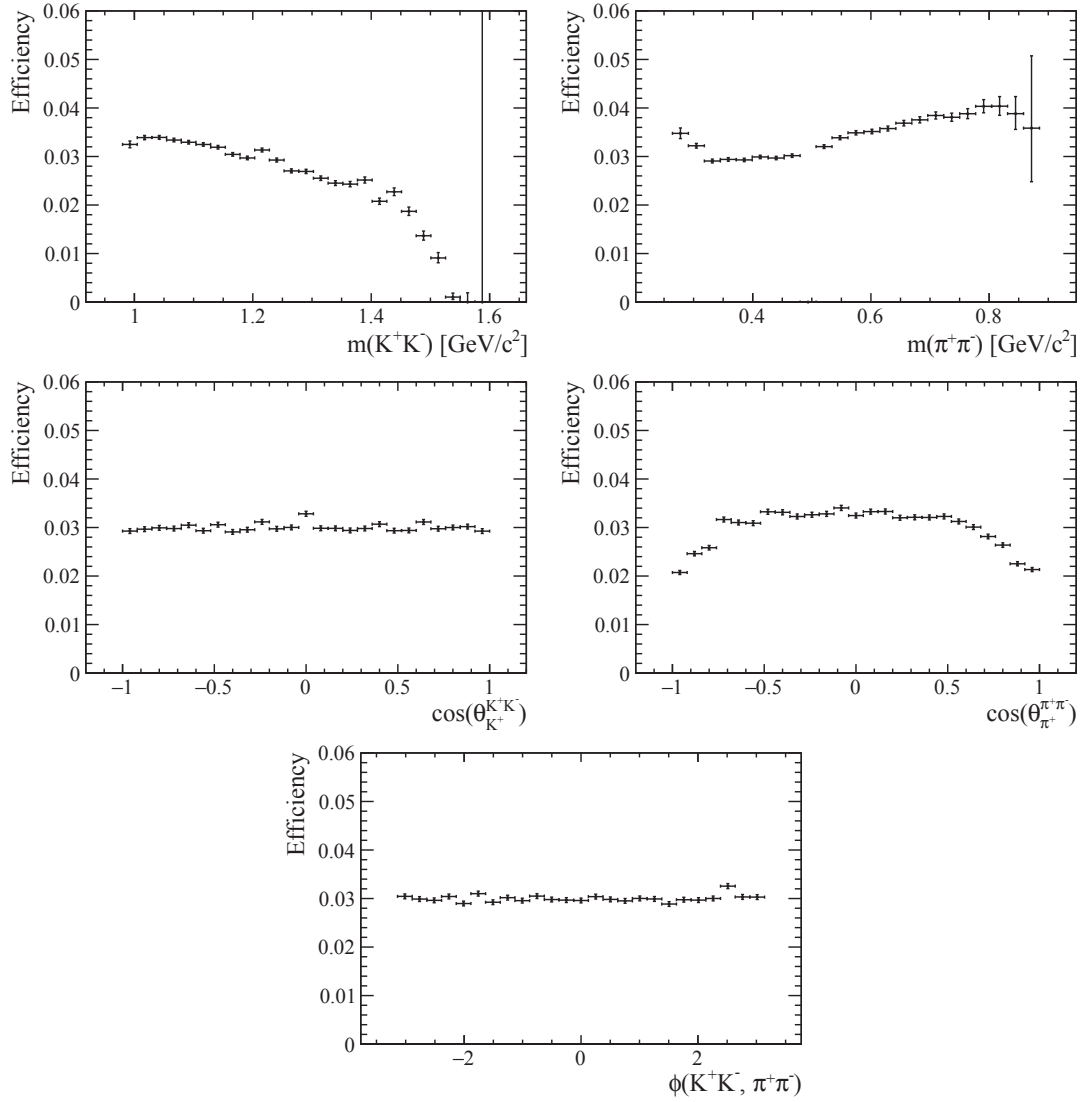
Figure 3.15 – Total efficiency as a function of the CM variables.

Table 3.6 – Cuts applied at the generator level for the two MC samples generated for this analysis.

Name	Particle	Cut
DaughtersInLHCb	all charged tracks	10 mrad $< \theta <$ 400 mrad
DinSLBdecays	D^0 daughters	$p_T >$ 300 MeV/c
	D^0 daughters	$p >$ 2 GeV/c
	μ	$p_T >$ 1.2 GeV/c
	μ	$p >$ 3 GeV/c
	D^0	$p_T >$ 1.8 GeV/c

3.7   Simulation

Fully simulated MC samples of events containing a $D^0 \rightarrow K^+ K^- \pi^+ \pi^-$ decay have been produced. These samples are used at different stages of the analysis; they are used to estimate the efficiencies of the selection, to train the MVA classifier, and to integrate the signal probability density in the amplitude fit. Two different $D^0 \rightarrow K^+ K^- \pi^+ \pi^-$ decay models have been used to produce these samples: a phase-space model in order to cover suitably the whole phase space, and a more realistic model in order to populate the phase space sufficiently in regions where narrow resonances exist. The latter model is taken from the first analysis of the CLEO data [46] and generated with AmpGen.

It is known that the PID variables show some discrepancies in the MC with respect to the data. Therefore, these variables have been corrected using a calibration channel as described in Refs. [88, 89].

The generator level cuts, applied on the generated MC events, are listed in Table 3.6. The MC events are further filtered with all the stripping and trigger cuts described in Sec. 3.2, except for the PID cuts that are known to be poorly simulated. These cuts are applied only once the PID variables have been corrected.

The MC has been shown to not fully reproduce the momentum resolution of the data. In order to minimise these discrepancies a momentum smearing is applied. The details of the procedure are described in Refs. [90, 91].

After the reconstruction of the MC samples, some particles might have been mis-identified. In order to ensure the MC samples to contain only signal candidates, a truth matching procedure is applied. This procedure verifies that the hypotheses made after the reconstruction match the true ID of the generated particles.

The MC can be used in the MVA provided it describes well the data. Since no 2011 MC sample is available, the data from 2011 and 2012 are compared to the 2012 MC sample. The MC sample matches relatively well the data for most variables. However some small differences exist. They are accounted for by reweighting the MC sample for all the variables that are used in the MVA

(*cf.* list in Sec. 3.4.2) except the PID variables, which have already been corrected separately, as well as the total number of tracks in the event and the momenta and transverse momenta of the D^0 and its daughters. This is done with a tool developed by Yandex, `hep_ml` [92], which reweights a multidimensional space using decision trees with gradient boosting. The signal distributions from the data are extracted with the sPlot technique [93]. The MC is reweighted to the full Run 1 s-weighted data.

The MC sample has been selected with the same set of cuts as for the data and the final samples contain 9.8 M which is ~ 50 times more than the ~ 200 k data events that have been selected in the signal region.

4 $D^0 \rightarrow K^+ K^- \pi^+ \pi^-$ amplitude analysis description

An amplitude analysis consists of describing a decay chain with a coherent sum of amplitudes, each corresponding to a specific decay path from the mother particle to the final state (called "component" from here on). These complex amplitudes may interfere. The main goal of the analysis is to find the correct components that contribute to the decay and compute their respective fraction. Each of these amplitudes is multiplied by a complex number c_k, whose magnitude $|c_k|$ and phase $\arg(c_k)$ will be extracted.

4.1 Likelihood

The likelihood to be used in the fit should have the form

$$\mathscr{L}_f(\boldsymbol{c}) = \prod_{j=1}^{N_{\text{data}}} f(\boldsymbol{x}_j; \boldsymbol{c}), \tag{4.1}$$

where N_{data} is the total number of selected candidates in the data sample, $f(\boldsymbol{x}; \boldsymbol{c})$ is the joint probability density function (PDF) in five dimensions of the $D^0 \rightarrow K^+ K^- \pi^+ \pi^-$ four-body phase space (for example $\boldsymbol{x}$ can be viewed as the five CM variables), and $\boldsymbol{c}$ represents the fit parameters. The PDF is written as

$$f(\boldsymbol{x}; \boldsymbol{c}) = f_s \, a(\boldsymbol{x}; \boldsymbol{c}) + (1 - f_s) \, b(\boldsymbol{x}), \tag{4.2}$$

where f_s is the signal fraction, $a(\boldsymbol{x}; \boldsymbol{c})$ is the signal PDF (which depends on the fit parameters $\boldsymbol{c}$) and $b(\boldsymbol{x})$ is the background PDF. All PDFs are normalized for all values of $\boldsymbol{c}$, *i.e.*

$$\int f(\boldsymbol{x}; \boldsymbol{c}) d^5 \boldsymbol{x} = \int a(\boldsymbol{x}; \boldsymbol{c}) d^5 \boldsymbol{x} = \int b(\boldsymbol{x}) d^5 \boldsymbol{x} = 1. \tag{4.3}$$

The signal PDF is expressed as

$$a(\boldsymbol{x}; \boldsymbol{c}) = \frac{\epsilon_s(\boldsymbol{x}) S(\boldsymbol{x}; \boldsymbol{c}) \mathscr{R}_4(\boldsymbol{x})}{I(\boldsymbol{c})} \quad \text{with} \quad I(\boldsymbol{c}) = \int \epsilon_s(\boldsymbol{x}) S(\boldsymbol{x}; \boldsymbol{c}) \mathscr{R}_4(\boldsymbol{x}) d^5 \boldsymbol{x}, \tag{4.4}$$

where $\mathcal{R}_4(\boldsymbol{x})$ is the function representing the four-body phase space density, $S(\boldsymbol{x}; \boldsymbol{c})$ is the signal model described in Sec. 4.2, and $\epsilon_s(\boldsymbol{x})$ is the signal efficiency. Note that the function $S(\boldsymbol{x}; \boldsymbol{c})$ is not normalised: it is defined up to an arbitrary constant multiplicative factor and only its shape conveys information. A signal model characterised by a constant function $S(\boldsymbol{x}; \boldsymbol{c})$ would correspond to a pure phase-space decay, without any resonant structures.

Since the functions $\mathcal{R}_4(\boldsymbol{x})$ and $\epsilon_s(\boldsymbol{x})$ are difficult to deal with analytically, we compute the normalisation integral $I(\boldsymbol{c})$ using a MC sample of fully-simulated signal events generated according to a known and arbitrary signal model $S^{\text{gen}}(\boldsymbol{x})$. After reconstruction and selection, this MC sample "encodes" both the four-body phase space and the signal efficiency. Assuming the simulation correctly reproduces the efficiency, the MC events are distributed according to the PDF

$$a^{\text{gen}}(\boldsymbol{x}) = \frac{\epsilon_s(\boldsymbol{x}) S^{\text{gen}}(\boldsymbol{x}) \mathcal{R}_4(\boldsymbol{x})}{I^{\text{gen}}} \ \text{ with } \ I^{\text{gen}} = \int \epsilon_s(\boldsymbol{x}) S^{\text{gen}}(\boldsymbol{x}) \mathcal{R}_4(\boldsymbol{x}) d^5\boldsymbol{x}. \tag{4.5}$$

The MC estimate of the normalisation integral $I(\boldsymbol{c})$ is then given by

$$I(\boldsymbol{c}) = \frac{1}{N_{\text{MC}}} \sum_{i=1}^{N_{\text{MC}}} \frac{\epsilon_s(\boldsymbol{x}_i) S(\boldsymbol{x}_i; \boldsymbol{c}) \mathcal{R}_4(\boldsymbol{x}_i)}{a^{\text{gen}}(\boldsymbol{x}_i)} = \frac{1}{N_{\text{MC}}} \sum_{i=1}^{N_{\text{MC}}} \frac{S(\boldsymbol{x}_i; \boldsymbol{c})}{S^{\text{gen}}(\boldsymbol{x}_i)} I^{\text{gen}}, \tag{4.6}$$

where N_{MC} is the number of events in the MC sample.

On the other hand, we describe the background component using the same signal MC sample. For each MC event at position $\boldsymbol{x}_i$ in phase space, a weight $w(\boldsymbol{x}_i)$ is assigned so that the weighted MC distribution matches the distribution of the background in five dimensions. By definition, this weight must be the ratio between the background PDF and the MC PDF, *i.e.*

$$w(\boldsymbol{x}) = \frac{b(\boldsymbol{x})}{a^{\text{gen}}(\boldsymbol{x})}. \tag{4.7}$$

Note that, because $\int b(\boldsymbol{x}) d^5\boldsymbol{x} = \int a^{\text{gen}}(\boldsymbol{x}) d^5\boldsymbol{x} = 1$, we must have $\frac{1}{N_{\text{MC}}} \sum_{i=1}^{N_{\text{MC}}} w(\boldsymbol{x}_i) = 1$. The assumptions on the background distribution $b(\boldsymbol{x})$ as well as the relevant technical details on the computation of $w(\boldsymbol{x})$ are given in Sec. 4.5.2.

Using Eqs. 4.4–4.7, the total PDF of Eq. 4.2 can now be rewritten as

$$f(\boldsymbol{x}; \boldsymbol{c}) = f_s \frac{\epsilon_s(\boldsymbol{x}) S(\boldsymbol{x}; \boldsymbol{c}) \mathcal{R}_4(\boldsymbol{x})}{I(\boldsymbol{c})} + (1 - f_s) w(\boldsymbol{x}) a^{\text{gen}}(\boldsymbol{x}) \tag{4.8}$$

$$= \frac{\epsilon_s(\boldsymbol{x}) \mathcal{R}_4(\boldsymbol{x})}{I^{\text{gen}}} \left(f_s \frac{S(\boldsymbol{x}; \boldsymbol{c})}{I(\boldsymbol{c})/I^{\text{gen}}} + (1 - f_s) w(\boldsymbol{x}) S^{\text{gen}}(\boldsymbol{x}) \right) \tag{4.9}$$

$$= \frac{\epsilon_s(\boldsymbol{x}) \mathcal{R}_4(\boldsymbol{x})}{I^{\text{gen}}} \left(f_s \frac{S(\boldsymbol{x}; \boldsymbol{c})}{\frac{1}{N_{\text{MC}}} \sum_{i=1}^{N_{\text{MC}}} \frac{S(\boldsymbol{x}_i; \boldsymbol{c})}{S^{\text{gen}}(\boldsymbol{x}_i)}} + (1 - f_s) w(\boldsymbol{x}) S^{\text{gen}}(\boldsymbol{x}) \right). \tag{4.10}$$

We then define

$$B(\boldsymbol{x}) = \frac{b(\boldsymbol{x})I^{\text{gen}}}{\epsilon_s(\boldsymbol{x})\mathcal{R}_4(\boldsymbol{x})} = w(\boldsymbol{x})S^{\text{gen}}(\boldsymbol{x}), \tag{4.11}$$

$$F(\boldsymbol{x};\boldsymbol{c}) = \frac{f(\boldsymbol{x};\boldsymbol{c})I^{\text{gen}}}{\epsilon_s(\boldsymbol{x})\mathcal{R}_4(\boldsymbol{x})} = f_s \frac{S(\boldsymbol{x};\boldsymbol{c})}{\frac{1}{N_{\text{MC}}}\sum_{i=1}^{N_{\text{MC}}}\frac{S(\boldsymbol{x}_i;\boldsymbol{c})}{S^{\text{gen}}(\boldsymbol{x}_i)}} + (1 - f_s)B(\boldsymbol{x}), \tag{4.12}$$

and, instead of maximising $\mathcal{L}_f(\boldsymbol{c})$, we maximise

$$\mathcal{L}_F(\boldsymbol{c}) = \prod_j^{N_{\text{data}}} F(\boldsymbol{x}_j;\boldsymbol{c}) = \prod_j^{N_{\text{data}}}\left(f_s \frac{S(\boldsymbol{x}_j;\boldsymbol{c})}{\frac{1}{N_{\text{MC}}}\sum_{i=1}^{N_{\text{MC}}}\frac{S(\boldsymbol{x}_i;\boldsymbol{c})}{S^{\text{gen}}(\boldsymbol{x}_i)}} + (1 - f_s)B(\boldsymbol{x}_j)\right). \tag{4.13}$$

This is equivalent because $\mathcal{L}_F(\boldsymbol{c}) = \mathcal{L}_f(\boldsymbol{c})/C$, where the constant

$$C = \prod_j^{N_{\text{data}}}\frac{\epsilon_s(\boldsymbol{x}_j)\mathcal{R}_4(\boldsymbol{x}_j)}{I^{\text{gen}}} \tag{4.14}$$

does not depend on the parameters $\boldsymbol{c}$ of the amplitude model of the signal.

For an efficient and accurate MC integration, it is important that the signal model used in the MC generation, $S^{\text{gen}}(\boldsymbol{x})$, be close to the final fitted model $S(\boldsymbol{x};\boldsymbol{c})$. Indeed if narrow features (such as the ϕ peak in the K^+K^- mass or the $K^*(892)^0$ peak in the $K^+\pi^-$ mass) are already present in the MC, the modelling of the data, which also has these features, will be eased. On the other hand it is important that the full phase space be covered with a reasonable density of MC events, especially for the description of the background. We have therefore decided to use a MC sample that is a mixture of events generated according to phase space, *i.e.* $S^{\text{gen}}(\boldsymbol{x})$ = constant, and events generated according to the CLEO model of Ref. [46], *i.e.* $S^{\text{gen}}(\boldsymbol{x}) = S^{\text{CLEO}}(\boldsymbol{x})$. The above formalism can easily be extended to this case where different parts of the MC sample have been generated with different signal models (basically replacing $S^{\text{gen}}(\boldsymbol{x}_i)$ with $S_i^{\text{gen}}(\boldsymbol{x}_i)$).

4.2 Signal description

The formalism chosen for this amplitude analysis is the so-called "isobar" model [94, 95], which assumes that each component can be built as a series of two-body decays. The two allowed patterns for $D^0 \to abcd$ are shown in Fig. 4.1, both involving two resonances, r_1 and r_2. The first is the quasi two-body decay $D^0 \to r_1r_2$ followed by $r_1 \to ab$ and $r_2 \to cd$, and the second is the cascade decay $D^0 \to r_1a$ followed by $r_1 \to r_2b$ and $r_2 \to cd$. In both cases the amplitude is computed as

$$A(\boldsymbol{x}) = B'_{L_{D^0}}(q_{D^0}(\boldsymbol{x}),0)\,\mathcal{T}_{r_1}(m_{r_1}(\boldsymbol{x}),L_{r_1})\,\mathcal{T}_{r_2}(m_{r_2}(\boldsymbol{x}),L_{r_2})\,W(\boldsymbol{x}), \tag{4.15}$$

where $B'_{L_{D^0}}$ is the normalised Blatt–Weisskopf barrier factor [96] of the D^0 candidate, given in Table 4.1. The function $\mathcal{T}_r$ is the lineshape of resonance r and W is the spin factor, described
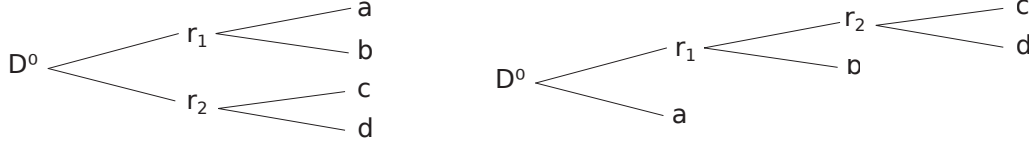
Figure 4.1 – Decay topologies allowed by the isobar model.

with the covariant formalism [97]. The variable $\boldsymbol{x}$ represents the five dimensions of the $D^0 \to K^+ K^- \pi^+ \pi^-$ four-body phase space, and q_r is the magnitude of the momentum of one of the two daughter particles of resonance r in its rest frame. The variable m_r is the invariant mass of the daughter particles of resonance r, and L_r is the angular momentum between them.

The total signal function is then described by a coherent sum of all the amplitudes included in the model,

$$S(\boldsymbol{x}; \boldsymbol{c}) = \left| \sum_k^N c_k A_k(\boldsymbol{x}) \right|^2 , \tag{4.16}$$

where A_k is computed as in Eq. 4.15, $c_1 = 1$ and the other complex coefficients c_k are defined relative to c_1. The moduli $|c_k|$ and phases $\arg(c_k)$ are left floating in the fit.

In order to express the relative importance of each component, the fit fraction can be computed. The fit fraction of an amplitude is defined as

$$\mathcal{F}_k = \frac{\int |c_k A_k(\boldsymbol{x})|^2 \mathcal{R}_4(\boldsymbol{x}) d^5 \boldsymbol{x}}{\int |\sum_j c_j A_j(\boldsymbol{x})|^2 \mathcal{R}_4(\boldsymbol{x}) d^5 \boldsymbol{x}} . \tag{4.17}$$

Note that the above expression takes into account the four-body phase space $\mathcal{R}_4(\boldsymbol{x})$, but not

Table 4.1 – Normalised Blatt-Weisskopf coefficients for the first three values of the angular momentum L between the decay products [24]. They prevent the amplitude to diverge at infinity. The parameter R is the radius of the resonance, q the norm of the momentum of one of the two daughter particles in the reference frame of the resonance and q_0 is the same momentum when the resonance has its nominal mass. The normalisation $q_0 = 0$, used in Eqs. 4.15, 4.18, 4.24 and 4.27, is arbitrarily chosen to normalise the Blatt-Weisskopf barrier factor to unity at $q = 0$.

L	$B_L'(q, q_0)$
0	1
1	$\sqrt{\frac{1+q_0^2 R^2}{1+q^2 R^2}}$
2	$\sqrt{\frac{(q_0^2 R^2 - 3)^2 + 9 q_0^2 R^2}{(q^2 R^2 - 3)^2 + 9 q^2 R^2}}$

Table 4.2 – List of all the resonances considered in the analysis, classified according to their spin-parity and decay products.

	KK	$\pi\pi$	$K\pi$	$KK\pi$	$K\pi\pi$
$J^P = 0^+$	$a_0(980)$ $f_0(980)$ $f_0(1370)$	$f_0(980)$ $f_0(1370)$	$K_0^*(1430)$		
$J^P = 1^+$				$a_1(1260)$	$K_1(1270)$ $K_1(1400)$
$J^P = 1^-$	$\phi(1020)$	$\rho(770)$ $\omega(782)$ $\rho(1450)$	$K^*(892)$ $K^*(1680)$		$K^*(1680)$
$J^P = 2^+$	$f_2(1270)$ $a_2(1320)$	$f_2(1270)$	$K_2^*(1430)$		$K_2^*(1430)$

the efficiency function $\epsilon_s(\boldsymbol{x})$, as we want the fit fractions to be free of detector effects. The integrals of Eq. 4.17 are computed with an independent MC sample generated according to phase space where no selection has been applied (*i.e.* the MC sample is different from the one used in the likelihood fit).

The tool chosen to perform the amplitude fit is a software developed at LHCb, called AmpGen [98]. It has been fully tested and verified against other well known fitters in the $D^0 \to K^\mp \pi^\pm \pi^\pm \pi^\mp$ analysis [99].

Many resonances are hypothesised to contribute to the decay, as listed in Table 4.2. All the combinations matching the $K^+ K^- \pi^+ \pi^-$ final state are considered; they are listed in Appendix B. In order to avoid strong *CP* violation, the two charges of the three-body resonances are constrained to have the same decay pattern.

It seems that a K^* meson with high mass contributes to the decay. Two resonances can take this role, the $K^*(1410)$ and the $K^*(1680)$. However, they both have similar contributions and the fit does not manage to distinguish them. One of the two needs therefore to be removed. The $K^*(1680)$ has been chosen as the fit shows a slightly better χ^2 but the $K^*(1410)$ is considered in an alternative model in the systematic uncertainties studies.

The $K(1460)$ meson (with $J^P = 0^-$) could be considered as a possible contributing resonance. However, each time this resonance is added to the model, a huge interference with the other components appears. Furthermore, this meson can have a cascade decay and the various decay chains have huge interferences among each other (up to $\mathcal{O}(1000\%)$). This suggests that this component just accounts for some fluctuations by adding some strong cancellations between some amplitudes. Finally, this resonance does not seem to be well established according to the PDG. All these observations lead to the choice of removing this resonance from the pool of potential amplitudes.

4.3 Lineshapes

4.3.1 Relativistic Breit-Wigner function

The default lineshape used for most resonances is the relativistic Breit–Wigner (RBW) function [100],

$$\mathcal{T}(m, L) = \frac{\sqrt{k} B'_L(q, 0)}{m_0^2 - m^2 - i m_0 \Gamma(m, L)}, \tag{4.18}$$

where

$$\Gamma(m, L) = \Gamma_0 \left(\frac{q}{q_0}\right)^{2L+1} \left(\frac{m_0}{m}\right) B'^2_L(q, q_0), \tag{4.19}$$

is the running width of the resonance, m_0 and Γ_0 are the nominal values of the mass and width of the resonance, respectively, and q_0 is the value of q when $m = m_0$. Indeed, q is a function of m

$$q = \sqrt{\frac{m^2}{4} - \frac{m_1^2 + m_2^2}{2} + \frac{(m_1^2 - m_2^2)^2}{4m^2}}, \tag{4.20}$$

where m_1 and m_2 are the masses of the daughter particles. If one of the daughter particles is itself also a resonance, its mass (m_1 or m_2) is not fixed but depends on $\boldsymbol{x}$; this adds an extra dependence on $\boldsymbol{x}$ in the expression of the lineshape (not indicated in Eqs. 4.15 and 4.18). The factor k normalises the lineshape if the Blatt–Weisskopf form-factor and the energy dependence of the width are neglected, and reduces the correlations between the coupling to the channel and the mass and width of the resonance. It is given by

$$k = \frac{2\sqrt{2} m_0 \gamma \Gamma_0}{\pi \sqrt{m_0^2 + \gamma}} \quad \text{with} \quad \gamma = m_0 \sqrt{m_0^2 + \Gamma_0^2}. \tag{4.21}$$

The expression of the width given in Eq. 4.19 is not valid for the $a_1(1260)^\pm$ and the $K_1(1270)^\pm$ resonances, which both couple to various channels and resonances. Indeed, the finite widths of the intermediate resonances have an impact on the width of the mother. In this case a correction has to be implemented. Following the formalism presented in Ref. [101], the width is computed as an integral over the phase space of the three-body decay $r \to abc$

$$\Gamma(m_r, L_r) \propto \frac{1}{m_r^2} \int |\mathcal{M}_{r \to abc}|^2 \, dm_{ab}^2 dm_{bc}^2, \tag{4.22}$$

where the integral is performed over the Dalitz plot, expressed in terms of the two-body invariant masses m_{ab} and m_{bc}, and the matrix element $\mathcal{M}_{r \to abc}$ contains all contributing subdecays. For the $K_1(1270)^\pm$ resonance, the integral is performed using the analysed dataset. However, since the $a_1(1260)^\pm$ resonance is mainly decaying to three pions, the $KK\pi$ channel
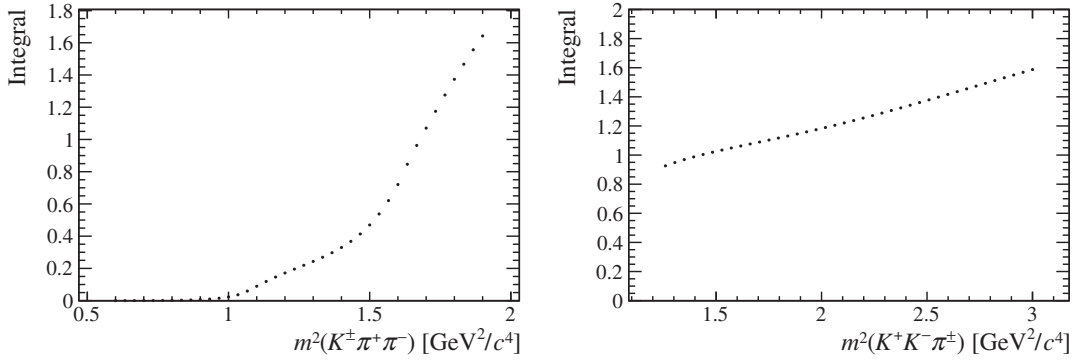
Figure 4.2 – Cubic splines parametrising the integral of Eq. 4.22 for the $K_1(1270)^\pm$ meson (left) and the $a_1(1260)^\pm$ meson (right).

is very small and not suitable to compute correctly this correction to the width. Its integral is therefore taken from a $D^0 \to K^\mp \pi^\pm \pi^\pm \pi^\mp$ analysis [99], where the same formalism is used. The integrals are parametrised by interpolating cubic splines, which can then be exported and reused. The resulting splines describing the integrals over the analysed dataset are shown in Fig. 4.2.

Furthermore, the Blatt–Weisskopf form factors do not suppress the $a_1(1260)^\pm$ and $K_1(1270)^\pm$ width sufficiently as the mass of the decaying resonance grows, with the width eventually diverging. An exponential form factor derived from Ref. [101, 102],

$$F(q) = e^{-R^2 q^2/2},\tag{4.23}$$

is therefore used instead of $B'_L(q, q_0)$ in Eq. 4.18.

The masses and widths of the resonances are taken from the PDG [24] for all the well known resonances. For the $a_1(1260)$ and the $K_1(1270)$ resonances, which are poorly known, a special treatment is applied. The $K_1(1270)$ has a relatively important contribution to $D^0 \to K^+ K^- \pi^+ \pi^-$, therefore its mass and width are left floating in the final fit. The resulting mass and width, $1297 \pm 1\,\text{MeV}/c^2$ and $148 \pm 4\,\text{MeV}/c^2$, can be compared to the PDG values [24], $1272 \pm 7\,\text{MeV}/c^2$ and $90 \pm 20\,\text{MeV}/c^2$, respectively. One has to keep in mind however that these values are model-dependent, the lineshape of three-body resonances is not as well agreed upon as for the two-body resonances. Concerning the $a_1(1260)$, its contribution is too small in this analysis to set sensible values. Its mass and the width are therefore taken from the $D^0 \to K^\mp \pi^\pm \pi^\pm \pi^\mp$ analysis [99]: $1195 \pm 1\,\text{MeV}/c^2$ for the mass and $422 \pm 2\,\text{MeV}/c^2$ for the width.

The radius[1] R of the various resonances is poorly known and needs to be set. In order to find the best value, a likelihood profile is performed for each resonance. The fit is sensitive to three radii, for the D^0, the $K^*(892)^0$ and the $K^*(1680)^0$, as shown in Fig. 4.3. For the D^0, this results in a minimum at $1.21 \pm 0.09\,\text{GeV}^{-1}$, for the $K^*(892)^0$ at $1.13 \pm 0.34\,\text{GeV}^{-1}$ and for the

---

[1]The radii are given in GeV^{-1} assuming $\hbar c = 1$.
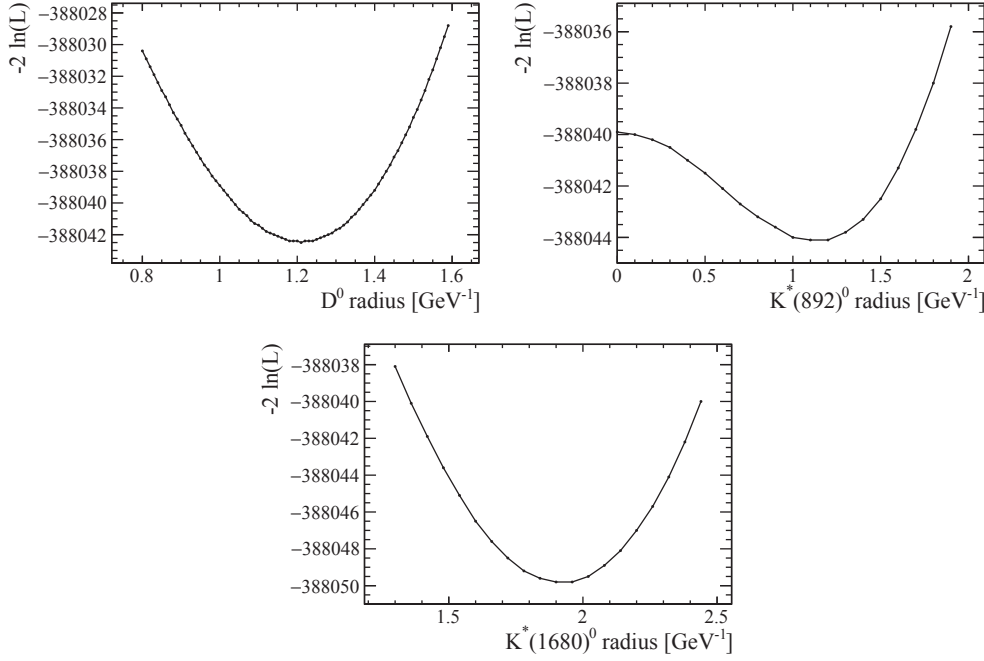
Figure 4.3 – Likelihood profile as a function of the radius of the D^0, $K^*(892)^0$ and $K^*(1680)^0$.

$K^*(1680)^0$ at $1.93 \pm 0.17\,\text{GeV}^{-1}$, where the uncertainty is taken as a raise of 1 unit of $-2\ln(\mathscr{L})$. For all the other resonance the default value of $1.5\,\text{GeV}^{-1}$ is used. As mentioned previously, the parametrisation of the $a_1(1260)^+$ lineshape is taken from the $D^0 \to K^\mp \pi^\pm \pi^\pm \pi^\mp$ analysis [99]. The radius used has to be consistent with this description and is therefore set to the same value of $1.7\,\text{GeV}^{-1}$. A systematic uncertainty will be assigned for these choices.

4.3.2 Flatté distribution

The Flatté distribution [103] is used for the $a_0(980)^0$ resonance near the KK threshold. In order to handle correctly the behaviour of the lineshape, it uses an analytical extension below the threshold. The $a_0(980)^0$ meson couples to KK and $\pi\eta$, its width is thus affected by these two channels. This distribution is defined as

$$\mathscr{T}(m, L) = \frac{\sqrt{k} B_L'(q, 0)}{m_0^2 - m^2 - i m_0 (\Gamma_{KK}(m) + \Gamma_{\pi\eta}(m))} \tag{4.24}$$

with

$$\Gamma_{KK}(m) = g_{KK}^2 \sqrt{1 - \left(\frac{2 m_K}{m}\right)^2}, \tag{4.25}$$

$$\Gamma_{\pi\eta}(m) = g_{\pi\eta}^2 \sqrt{\left[1 - \left(\frac{m_\pi + m_\eta}{m}\right)^2\right]\left[1 - \left(\frac{m_\pi - m_\eta}{m}\right)^2\right]}, \tag{4.26}$$

66

where the couplings $g^2_{KK} = 0.210 \pm 0.032\,\text{GeV}/c^2$ and $g^2_{\pi\eta} = 0.175 \pm 0.015\,\text{GeV}/c^2$ are taken from Ref. [104] and where m_π and m_η are taken from Ref. [24]. An analytical extension returns an imaginary width when the argument of the square root is negative. The normalisation factor k is the same as described in Eq. 4.21.

4.3.3   Gounaris-Sakurai distribution

The Gounaris–Sakurai parametrisation [105] is used for the $\rho_0(770)^0$ meson decaying to two pions. This resonance is quite broad and is therefore not perfectly described by the RBW parametrisation. The lineshape is defined as

$$\mathcal{T}(m,L) = \frac{\sqrt{k}B'_L(q,0)(1+D\Gamma_0/m_0)}{m_0^2 - m^2 + f(m) - im_0\Gamma(m,L)}, \tag{4.27}$$

where the width $\Gamma(m,L)$ is the same as in Eq. 4.19, the normalisation factor k is the same as in Eq. 4.21 and the constant D is given by

$$D = \frac{3m_\pi^2}{\pi q_0^2}\ln\left(\frac{m_0+2q_0}{2m_\pi}\right) + \frac{m_0}{2\pi q_0} - \frac{m_\pi^2 m_0}{\pi q_0^3}. \tag{4.28}$$

The function $f(m)$ is given by

$$f(m) = \Gamma_0\frac{m_0^2}{q_0^3}\left(q^2\left(h(m)-h(m_0)\right) + q_0^2\frac{m^2-m_0^2}{2m}\frac{dh}{dm}\bigg|_{m_0}\right), \tag{4.29}$$

$$h(m) = \frac{2}{\pi}\frac{q}{m}\ln\left(\frac{m+2q}{2m_\pi}\right), \tag{4.30}$$

and where $\frac{dh}{dm}$ is the total derivative of h with respect to m, taking into account that $q = \sqrt{\frac{m^2}{4} - m_\pi^2}$.

4.3.4 ρ-ω interference

The $\rho(770)^0$ and the $\omega(782)^0$ mesons are very close in mass and interfere therefore heavily. The two separate resonances can be considered as a single state described by the superposition of the two individual states. During the model building, whenever a $\rho(770)^0$ meson is added to the model, an $\omega(782)^0$ meson is added as well. The $\rho-\omega$ state is therefore described as

$$\left|\rho-\omega\right\rangle = \left|\rho\right\rangle + \tilde{c}\left|\omega\right\rangle, \tag{4.31}$$

where $\tilde{c}$ is a complex coefficient that is left floating in the fit. It is not clear whether the $\rho-\omega$ relative proportions should be the same in all the production modes (*i.e.* for example $D^0 \to \phi(\rho-\omega)^0$ vs $D^0 \to K_1(1270)^+ K^-$ followed by $K_1(1270)^+ \to (\rho-\omega)^0 K^+$). A test has been performed where the same proportions have been used for all the components and the fit did

not converge. No theoretical argument have been found in the literature to support any of the two hypotheses. Therefore a different complex coefficient is used in the fit for each of the decay chains.

4.3.5   K-matrix formalism

The RBW lineshape describes accurately well separated narrow resonances. In the case of broad overlapping resonances the K-matrix formalism [106] is used instead. Advantages of this formalism are a correct description of the interferences and compliance with unitarity. The K-matrix formalism describes the resonances by taking into consideration all the channels to which they couple. This is an important feature, since all the channels contribute to the width of the resonance. This formalism was traditionally used for scattering processes and is slightly modified in this analysis to be used for production processes. The lineshapes are defined as

$$\hat{\mathscr{T}} = \left(I - i\hat{K}\rho \right)^{-1} \hat{P},$$

(4.32)

where I is the identity matrix and ρ is a diagonal phase-space matrix, which describes the behaviour of the various channels. For the two-body channels, the diagonal elements of ρ have the form [106]

$$\rho(m) = \sqrt{\left(\frac{m^2 - (m_1 + m_2)^2}{m^2} \right) \left(\frac{m^2 - (m_1 - m_2)^2}{m^2} \right)},$$

(4.33)

where m_1 and m_2 are the daughter masses taken from Ref. [24]. The matrix $\hat{K}$ is a $n \times n$ matrix, with n being the number of channels to which the resonance couples. It describes both the resonant structure and the non-resonant scattering part of the amplitude. Finally, $\hat{P}$ is the production vector. It has the same pole structure as the K-matrix, such that the amplitude does not vanish at the K-matrix poles. This formalism is used for the two components described in the next subsections.

4.3.5.1 $\pi\pi/KK$ S-waves

The $\pi\pi$ and the KK S-waves are both described by the same K-matrix that couples to five different channels and five different poles. The parametrisation is taken from Ref. [107], where the K-matrix is defined as

$$\hat{K}_{ij}(m) = f(m) \left(\sum_\alpha \frac{g_{\alpha i} g_{\alpha j}}{m_\alpha^2 - m^2} + f_{ij}^{\text{scatt}} \frac{1 \text{ GeV}^2/c^4 - s_0^{\text{scatt}}}{m^2 - s_0^{\text{scatt}}} \right),$$

(4.34)

where $i, j = 1, 2, 3, 4, 5$ indicate the channels $\pi\pi$, KK, $\pi\pi\pi\pi$, $\eta\eta$ and $\eta\eta'$ and $\alpha = 1, 2, 3, 4, 5$ indicates the poles $f_0(980)$, $f_0(1300)$, $f_0(1500)$, $f_0(1200-1600)$ and $f_0(1750)$. The masses of the

poles m_α are [108]

$$m_\alpha = \begin{pmatrix} 0.651 \\ 1.2036 \\ 1.55817 \\ 1.21 \\ 1.82206 \end{pmatrix} \text{GeV}/c^2.$$
(4.35)

The factors $g_{\alpha i}$ are the coupling constants between the channel i and the pole α. They have been measured from scattering data and their values are [108]

$$g_{\alpha i} = \begin{pmatrix} 0.22889 & -0.55377 & 0.00000 & -0.39899 & -0.34639 \\ 0.94128 & 0.55095 & 0.00000 & 0.39065 & 0.31503 \\ 0.36856 & 0.23888 & 0.55639 & 0.18340 & 0.18681 \\ 0.33650 & 0.40907 & 0.85679 & 0.19906 & -0.00984 \\ 0.18171 & -0.17558 & -0.79658 & -0.00355 & 0.22358 \end{pmatrix} \text{GeV}/c^2.$$
(4.36)

The second term of Eq. 4.34 describes the non-resonant scattering contribution of the amplitude. The parameters needed are also taken from Ref. [108], where $s_0^{\text{scatt}} = -3.93 \text{ GeV}^2/c^4$ and

$$f_{ij}^{\text{scatt}} = \begin{pmatrix} 0.23399 & 0.15044 & -0.20545 & 0.32825 & 0.35412 \\ 0.15044 & 0.00000 & 0.00000 & 0.00000 & 0.00000 \\ -0.20545 & 0.00000 & 0.00000 & 0.00000 & 0.00000 \\ 0.32825 & 0.00000 & 0.00000 & 0.00000 & 0.00000 \\ 0.35412 & 0.00000 & 0.00000 & 0.00000 & 0.00000 \end{pmatrix}.$$
(4.37)

The elements f_{ij}^{scatt} terms have only been measured for the scattering between the $\pi\pi$ channel and the others, not among the other channels. There is a non-physical singularity below the $\pi\pi$ threshold, sometimes called the "Adler zero", that is suppressed by the term $f(m)$. It is defined in Ref. [109] as

$$f(m) = \frac{1 \text{ GeV}^2/c^4 - s_{A0}}{m^2 - s_{A0}} \left(m^2 - s_A \frac{m_\pi^2}{2} \right),$$
(4.38)

where $s_{A0} = -0.15 \text{ GeV}^2/c^4$ and $s_A = 1$. The phase-space term of the two-body channels ($i = 1, 2, 4, 5$) is described in Eq. 4.33. The phase-space term for the four-pion channel ($i = 3$) is

$$\rho_3(m) = \begin{cases} \sqrt{1 - \dfrac{(4m_\pi)^2}{m^2}} & \text{if } m \geq 1 \text{ GeV}/c^2, \\ \rho_3'(m) & \text{if } m < 1 \text{ GeV}/c^2, \end{cases}$$
(4.39)

Table 4.3 – Parameters of the $\pi\pi$ and KK K-matrices for all the relevant amplitudes. The moduli of the parameters β_α are expressed in GeV/c^2.

Amplitude	Parameter	Modulus	Phase [rad]
	f_{KK}^{prod}	1 (fixed)	0 (fixed)
$D^0 \to [K^+K^-]_{L=0}[\pi^+\pi^-]_{L=0}$	$K^+K^-\ \beta_1$	$0.30 \ \pm \ 0.03$	$0.43 \ \pm \ 0.09$
	$K^+K^-\ \beta_2$	$1.08 \ \pm \ 0.04$	$1.38 \ \pm \ 0.03$
	$f_{\pi\pi}^{\text{prod}}$	1 (fixed)	0 (fixed)
	$\pi^+\pi^-\ \beta_1$	$0.60 \ \pm \ 0.08$	$-2.53 \ \pm \ 0.12$
$D^0 \to (\rho-\omega)^0[K^+K^-]_{L=0}$	f_{KK}^{prod}	1 (fixed)	0 (fixed)
	β_1	$0.12 \ \pm \ 0.08$	$2.59 \ \pm \ 0.82$
$D^0 \to \phi(1020)[\pi^+\pi^-]_{L=0}$	$f_{\pi\pi}^{\text{prod}}$	1 (fixed)	0 (fixed)
	β_1	$2.54 \ \pm \ 0.51$	$1.12 \ \pm \ 0.18$

where

$$\rho_3'(m) = \rho_0 \int \frac{dm_1^2}{\pi} \int \frac{dm_2^2}{\pi} \frac{M_0^2 \Gamma(m_1)\Gamma(m_2)\sqrt{(m^2+m_1^2-m_2^2)^2-4m^2m_1^2}}{m^2[(M_0^2-m_1^2)^2+M_0^2\Gamma^2(m_1)][(M_0^2-m_2^2)^2+M_0^2\Gamma^2(m_2)]} \quad (4.40)$$

and ρ_0 ensures that $\rho_3(m)$ is continuous at $m = 1\,\text{GeV}/c^2$. The integration variables m_1^2 and m_2^2 are the squares of the invariant masses of the two di-pion states, M_0 is the pole mass of the $\rho(770)^0$ resonance [24] and $\Gamma(m) = \Gamma_0(1-(4m_\pi^2/m^2))^{3/2}$ is the energy-dependent width, where Γ_0 is set to $0.3\,\text{GeV}/c^2$. As shown in Ref. [110], the function $\rho_3'(m)$ can be approximated by a 6th order polynomial in m^2 (with m expressed in GeV/c^2)

$$\rho_3'(m) = 0.0005 - 0.0193m^2 + 0.1385m^4 - 0.2084m^6 - 0.2974m^8 + 0.1366m^{10} + 1.0789m^{12}. \quad (4.41)$$

The production vector is given by

$$\hat{P}_i(m) = \sum_\alpha \frac{\beta_\alpha g_{\alpha i}}{m_\alpha^2 - m^2} + f_i^{\text{prod}} \frac{1\,\text{GeV}^2/c^4 - s_0^{\text{prod}}}{m^2 - s_0^{\text{prod}}}, \quad (4.42)$$

where the complex parameter β_α describes the production strength of pole α, the complex parameter f_i^{prod} describes the direct coupling to channel i and s_0^{prod} is a single real parameter. The production vector therefore contains 21 free parameters that should be left floating in the fit. Despite the large data sample in the analysis, some of these parameters are not well constrained. In order to improve the fit stability during the model building, only the main component is kept, *i.e.* the direct coupling to the relevant channel (f_1^{prod} for the $\pi\pi$ channel and f_2^{prod} for the KK channel). The direct couplings to the other channels ($f_{3,4,5}^{\text{prod}}$) and to the poles ($\beta_{1,2,3,4,5}$) are set to 0. All the poles and channels still contribute in the K-matrix computation of Eq. 4.34; their direct couplings are only removed from the production vector.

Once the model is built, all the pole couplings β_α are tested. The fit does not converge if all the

fit parameters are left floating in addition to these couplings. Therefore all the fit parameters are fixed to their nominal values and only the parameters of the K-matrix are fitted. The fit is not sensitive to all of them because the available phase space is relatively small. The direct coupling to $f_0(980)$ is added to all the amplitudes containing a KK or $\pi\pi$ S-wave and the coupling to $f_0(1300)$ is only added to the KK K-matrix in the $D^0 \to [K^+K^-]_{L=0}[\pi^+\pi^-]_{L=0}$ amplitude, because it is the only one where there is enough phase space. The contribution of the poles with higher masses ($f_0(1500)$, $f_0(1750)$ and $f_0(1200-1600)$) is negligible. The decision of keeping the direct coupling to a pole or not is only based on the convergence or non-convergence of the fit. The values obtained, shown in Table 4.3, are then fixed in the main fit. The fit is only mildly sensitive to s_0^{prod}, with a preferred value in the range $[-0.20, -0.07]\,\mathrm{GeV}^2/c^4$. It is decided to fix s_0^{prod} to $-0.17\,\mathrm{GeV}^2/c^4$ for all the components.

4.3.5.2 $K\pi$ S-wave

The $K\pi$ S-wave couples to two channels, $K\pi$ and $K\eta'$, and contains only one pole, the $K_0^*(1430)$ resonance. Two isospin states contribute to the $K\pi$ S-wave, $I = \frac{1}{2}$, which couples to both channels, and $I = \frac{3}{2}$, which couples to $K\pi$ only. The parametrisation is taken from Ref. [111] and the K-matrix for $I = \frac{1}{2}$ is given by

$$\hat{K}_{ij}^{\frac{1}{2}}(m) = \frac{m^2 - s_{0\frac{1}{2}}}{m_K^2 + m_\pi^2} \left(\frac{g_{1i}g_{1j}}{m_1^2 - m^2} + C_{ij0} + C_{ij1}\tilde{s} + C_{ij2}\tilde{s}^2 \right), \tag{4.43}$$

where the mass of the $K_0^*(1430)$ pole is $m_1 = 1.3386\,\mathrm{GeV}/c^2$, the Adler zero is located at $s_{0\frac{1}{2}} = 0.23\,\mathrm{GeV}^2/c^4$, the couplings g_{1i} between the pole and the channels are

$$g_{1i} = \begin{pmatrix} 0.31072 \\ -0.02323 \end{pmatrix} \mathrm{GeV}/c^2, \tag{4.44}$$

and the coefficients of the second-order polynomial in $\tilde{s} = \frac{m^2}{m_K^2 + m_\pi^2} - 1$ describing the non-resonant scattering contribution are

$$C_{ij0} = \begin{pmatrix} 0.79299 & 0.15040 \\ 0.15040 & 0.17054 \end{pmatrix},$$
$$C_{ij1} = \begin{pmatrix} -0.15099 & -0.038266 \\ -0.038266 & -0.0219 \end{pmatrix}, \tag{4.45}$$
$$C_{ij2} = \begin{pmatrix} 0.00811 & 0.0022596 \\ 0.0022596 & 0.00085655 \end{pmatrix}.$$

The K-matrix for $I = \frac{3}{2}$ does not couple to any resonance, it contains therefore only the non-

Table 4.4 – Parameters of the $K\pi$ K-matrices for all the relevant amplitudes.

Amplitude	Parameter	Modulus	Phase [rad]
$D^0 \rightarrow [K^+\pi^-]_{L=0}[K^-\pi^+]_{L=0}$	$K^+\pi^-\ \alpha_{1/2}$	1 (fixed)	0 (fixed)
	$K^+\pi^-\ \alpha_{3/2}$	0.31 ± 0.02	2.51 ± 0.08
	$K^-\pi^+\ \alpha_{1/2}$	1 (fixed)	0 (fixed)
	$K^-\pi^+\ \alpha_{3/2}$	0.36 ± 0.02	-2.95 ± 0.05
$D^0 \rightarrow K^*(1680)^0[K^-\pi^+]_{L=0}$	$\alpha_{1/2}$	1 (fixed)	0 (fixed)
	$\alpha_{3/2}$	0.29 ± 0.02	-2.96 ± 0.08
$D^0 \rightarrow \bar{K}^*(1680)^0[K^+\pi^-]_{L=0}$	$\alpha_{1/2}$	1 (fixed)	0 (fixed)
	$\alpha_{3/2}$	0.27 ± 0.04	-2.09 ± 0.14
$K_1(1270)^+ \rightarrow [K^+\pi^-]_{L=0},\pi^+$	$\alpha_{1/2}$	1 (fixed)	0 (fixed)
	$\alpha_{3/2}$	0.44 ± 0.04	-2.79 ± 0.08

resonant part

$$\hat{K}^{\frac{3}{2}}(m) = \frac{m^2 - s_{0\frac{3}{2}}}{m_K^2 + m_\pi^2}\left(D_{110} + D_{111}\tilde{s} + D_{112}\tilde{s}^2\right), \tag{4.46}$$

where the Adler zero is located at $s_{0\frac{3}{2}} = 0.27\ \mathrm{GeV}^2/c^4$ and

$$D_{110} = -0.22147, \quad D_{111} = 0.026637, \quad D_{112} = -0.00092057. \tag{4.47}$$

An approximation is made in order to describe the production vector of the $K\pi$ S-wave. It has been shown in Ref. [112] that, in a limited phase space, one can consider

$$\hat{K}^{-1}\hat{P} \approx \hat{\alpha}, \tag{4.48}$$

where $\hat{\alpha}$ is a diagonal matrix containing a complex parameter for each channel, which is left floating in the fit. Therefore, the pole structure of the production vector cancels the pole structure of the K-matrix. This simplifies Eq. 4.32 to

$$\hat{\mathcal{T}} = \hat{T}\hat{K}^{-1}\hat{P} = \hat{T}\hat{\alpha}, \tag{4.49}$$

which describes the lineshape only in terms of the scattering process

$$\hat{T} = \left(I - i\hat{K}\rho\right)^{-1}\hat{K}. \tag{4.50}$$

The phase-space term of the $K\pi$ K-matrix is described by Eq. 4.33.

Again, some assumptions are made while the model is being built. Only the dominant term is kept, which is the direct coupling to the $K\pi$ channel in the isospin state $I = \frac{1}{2}$. Once the model is built, the direct coupling to the $K\pi$ channel in the isospin state $I = \frac{3}{2}$ as well as to the $K\eta'$ channel are tested in all the amplitudes containing a $K\pi$ S-wave. It turns out that the fit is not sensitive to the contribution of the $K\eta'$ channel, so only the two isospin states of the

$K\pi$ channel are considered. Again, the fit does not converge if all the fit parameters are left floating in addition to the K-matrix parameters. Therefore all the fit parameters are fixed to the nominal values of the final model and the values of the K-matrix parameters are fitted. These parameters, shown in Table 4.4, are then fixed in the main fit.

4.4 Spin factors

The covariant formalism, chosen to compute the spin factors, uses the contraction of orbital angular momentum tensors and spin tensors [97]. For completeness, a detailed description is given here, starting from the individual polarisation vector as well as the orbital angular momentum tensor followed by the general rules to construct all needed spin factors.

4.4.1 Polarisation factors

A spin-0 particle is not affected by spatial rotation, its polarisation factor is thus trivially set to 1. A spin-1 particle with momentum p, mass m and spin projection s_z, is represented in momentum space by the polarisation vector $\epsilon^\mu(p, s_z)$. The four components of this vector are not independent. They must satisfy the first Rarita-Schwinger condition [113],

$$\text{1}^{\text{st}} \text{ Rarita-Schwinger condition: } \epsilon^\mu(p, s_z) p_\mu = 0, \tag{4.51}$$

which implies that the polarisation vector is orthogonal to the momentum vector and thus, that the time component vanishes in the particle's rest frame. The three independent solution to this Rarita-Schwinger condition are interpreted as the three spin projections of a spin 1 along the z axis:

$$\text{longitudinal component: } \epsilon^\mu(p = 0, s_z = 0) = \begin{pmatrix} 0 \\ 0 \\ 0 \\ 1 \end{pmatrix}, \tag{4.52}$$

$$\text{transverse component: } \epsilon^\mu(p = 0, s_z = \pm 1) = \frac{1}{\sqrt{2}} \begin{pmatrix} 0 \\ \mp 1 \\ -i \\ 0 \end{pmatrix}. \tag{4.53}$$

This is only valid in the particle's rest frame, however for a general purpose, the polarisation vectors are needed in an arbitrary rest frame. A Lorentz transformation is thus applied on

Eqs. 4.52 and 4.53:

$$\epsilon^\mu(p, s_z = 0) = \frac{1}{m} \begin{pmatrix} p_z \\ p_z p_x/(E+m) \\ p_z p_y/(E+m) \\ m + p_z^2/(E+m) \end{pmatrix}, \tag{4.54}$$

$$\epsilon^\mu(p, s_z = \pm 1) = \frac{\mp 1}{\sqrt{2}m} \begin{pmatrix} p_x \pm i p_y \\ m + p_x(p_x \pm i p_y)/(E+m) \\ \pm i m + p_y(p_x \pm i p_y)/(E+m) \\ p_z(p_x \pm i p_y)/(E+m) \end{pmatrix}. \tag{4.55}$$

Spin-2 particles are described by the polarisation tensors $\epsilon^{\mu\nu}(p, s_z)$. These tensors are constructed by combining spin-1 vectors,

$$\epsilon^{\mu\nu}(p, s_z) = \sum_{s_{z1}, s_{z2}} \langle 1 s_{z1}, 1 s_{z2} | 2 s_z \rangle \epsilon^\mu(p, s_{z1}) \epsilon^\nu(p, s_{z2}), \tag{4.56}$$

where $\langle 1 s_{z1}, 1 s_{z2} | 2 s_z \rangle$ are the relevant Clebsch-Gordon coefficients. These tensors satisfy the condition of Eq. 4.51 as well as two further Rarita-Schwinger conditions. They are symmetric:

$$2^{\text{nd}} \text{ Rarita-Schwinger condition: } \epsilon^{\mu\nu}(p, s_z) = \epsilon^{\nu\mu}(p, s_z), \tag{4.57}$$

and they are traceless:

$$3^{\text{rd}} \text{ Rarita-Schwinger condition: } g_{\mu\nu} \epsilon^{\mu\nu}(p, s_z) = 0, \tag{4.58}$$

where $g_{\mu\nu}$ is the Minkowski metric:

$$g_{\mu\nu} = g^{\mu\nu} = \begin{pmatrix} +1 & 0 & 0 & 0 \\ 0 & -1 & 0 & 0 \\ 0 & 0 & -1 & 0 \\ 0 & 0 & 0 & -1 \end{pmatrix}. \tag{4.59}$$

These conditions reduce the 16 elements of the 4×4 tensor to only 5 independent elements.

4.4.2   Spin projection operators

Now that the spin-0,-1 and -2 polarisation factors have been determined, their related projection operators need to be described:

$$
\begin{aligned}
&\text{spin 0:} && P_0 = 1\,, \\
&\text{spin 1:} && P_1^{\mu\nu}(p) = \sum_{s_z} \epsilon^\mu(p,s_z)\epsilon^{*\nu}(p,s_z) = -g^{\mu\nu} + \frac{p^\mu p^\nu}{m^2}\,, \\
&\text{spin 2:} && P_2^{\mu\nu\alpha\beta}(p) = \sum_{s_z} \epsilon^{\mu\nu}(p,s_z)\epsilon^{*\alpha\beta}(p,s_z) \\
& && \qquad = \frac{1}{2}\left(P_1^{\mu\alpha}(p)P_1^{\nu\beta}(p) + P_1^{\mu\beta}(p)P_1^{\nu\alpha}(p)\right) - \frac{1}{3}\left(P_1^{\mu\nu}(p)P_1^{\alpha\beta}(p)\right).
\end{aligned}
\tag{4.60}
$$

The spin-1 projection operator, for example, projects any four-vector into the spin-1 subspace spanned by the three polarisation vectors $\epsilon^\mu(p,s_z)$.

4.4.3   Orbital angular momentum

The states of orbital angular momentum L of a system $r \to ab$ are constructed from the momenta of the daughters, p_a and p_b. One can define the total momentum $p_r = p_a + p_b$ and the relative momentum $q_r = p_a - p_b$. The orbital angular momentum tensors are obtained by projecting the relative momentum q_r onto the spin L subspace. This is done using the same projection operators as for the spins in the previous section,

$$
L_L^{\mu_1\dots\mu_L}(p_r,q_r) = (-1)^L P_L^{\mu_1\dots\mu_L\nu_1\dots\nu_L}(p_r)q_{r,\nu_1}\dots q_{r,\nu_L}\,,
\tag{4.61}
$$

which yields

$$
\begin{aligned}
&L = 0: && L_0 = 1\,, \\
&L = 1: && L_1^\mu(p_r,q_r) = -P_1^{\mu\nu}(p_r)q_{r,\nu}\,, \\
&L = 2: && L_2^{\mu\nu}(p_r,q_r) = P_2^{\mu\nu\alpha\beta}(p_r)q_{r,\alpha}q_{r,\beta}\,.
\end{aligned}
\tag{4.62}
$$

4.4.4   Spin factor construction rules

The final spin factor is constructed following a well defined recipe:

1. Assign a polarisation term to the decaying particle.

2. Construct the spin projection operator of the decaying particle.

3. Construct the orbital angular momentum tensor between the decay products.

4. Assign conjugated polarisation terms to the decay products.

5. Add the Levi-Civita tensor if amplitude is P-odd.

6. Contract all the terms together to obtain a Lorentz scalar.

This results in the following general expression for a system $r \to ab$:

$$
\langle ab, s_{z,a}, s_{z,b}, L_r | \mathcal{M} | r, s_{z,r} \rangle =
$$
$$
\epsilon(p_r, s_{z,r}) \, P_{s_r}(p_r, q_r) \, L_{L_r}(p_r, q_r) \epsilon^*(p_a, s_{z,a}) \epsilon^*(p_b, s_{z,b}) \zeta(s_r, L_r, s_a, s_b), \tag{4.63}
$$

where the two daughters of the resonance r have an orbital angular momentum L_r. The function ζ adds either the metric tensor $g_{\mu\nu}$ or the Levi-Civita tensor $\varepsilon_{\mu\nu\rho\sigma}$ contracted with the momentum of the resonance r, in order to contract all the components together and to ensure the correct behaviour under the parity transformation:

$$
\zeta(S, L, S_1, S_2) = \begin{cases} g_{\mu\nu} & \text{if } S + L + S_1 + S_2 \text{ is even,} \\ \varepsilon_{\mu\nu\rho\sigma} p_r^\sigma & \text{if } S + L + S_1 + S_2 \text{ is odd.} \end{cases} \tag{4.64}
$$

All needed spin factors can be constructed following this recipe and they are all listed in Ref. [99]. The final value of the spin factor for a decay $D^0 \to r_1 r_2$ with $r_1 \to ab$ and $r_2 \to cd$, where a, b, c and d are pseudoscalars, is given by

$$
W = \langle abcd | \mathcal{M} | D^0 \rangle \tag{4.65}
$$
$$
= \sum_{s_{z,r_1}, s_{z,r_2}} \langle r_1 r_2, s_{z,r_1}, s_{z,r_2}, L_{D^0} | \mathcal{M} | D^0 \rangle \langle ab, L_{r_1} | \mathcal{M} | r_1, s_{z,r_1} \rangle \langle cd, L_{r_2} | \mathcal{M} | r_2, s_{z,r_2} \rangle,
$$

where the sum is taken over all the allowed combinations of s_{z,r_1} and s_{z,r_2}.

As an example, the construction of the spin factor of $D^0 \to \phi\rho$ in S-wave is shown:

1. The D^0 is a spin 0 particle and has therefore a polarisation term equal to 1.

2. Trivially, the spin projection operator of the D^0 is 1 as well.

3. Being in S-wave, the orbital angular momentum tensor between the ϕ and the ρ is 1.

4. The ϕ and the ρ are spin-1 particles and thus have the polarisation vectors $\epsilon^{*\mu}(p_\phi, s_{z,\phi})$ and $\epsilon^{*\nu}(p_\rho, s_{z,\rho})$.

5. The sum $s_{D^0} + L_{D^0} + s_\phi + s_\rho = 0 + 0 + 1 + 1 = 2$ is even, so no Levi-Civita tensor is needed.

6. Finally $\langle \phi\rho, L = 0 | \mathcal{M} | D^0 \rangle = \epsilon^{*\mu}(p_\phi, s_{z,\phi}) \epsilon^{*\nu}(p_\rho, s_{z,\rho}) g_{\mu\nu}$.

4.5 Background description

The sidebands of the D^0 mass distribution are used to describe the background, assuming that the sum of the lower and upper sidebands (even if different) gives a good description of the background in the signal region. The distributions of the five CM variables for events in the D^0 mass sidebands are shown in Fig. 4.4.
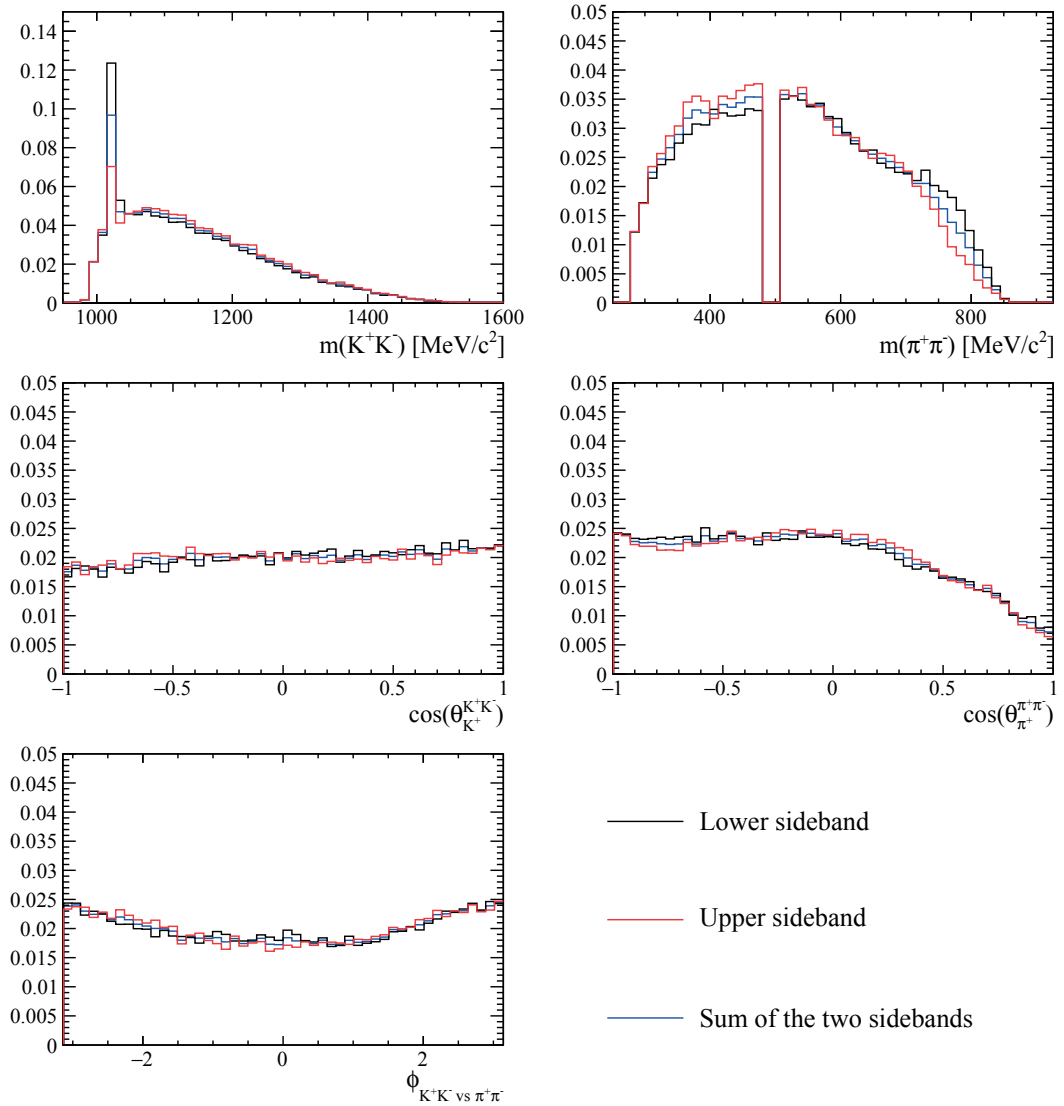
Figure 4.4 – Normalised distributions of the five CM variables for $D^0 \to K^+ K^- \pi^+ \pi^-$ candidates falling in the lower and upper sidebands of the Dz mass. The $K^+ K^-$ mass distribution shows a clear and narrow peak due to the $\phi(1020)^0$ resonance. The $\pi^+ \pi^-$ mass distribution shows an unpronounced and broad shoulder due to the $\rho(770)^0$ resonance, as well as an empty region due to the K_S^0 veto.
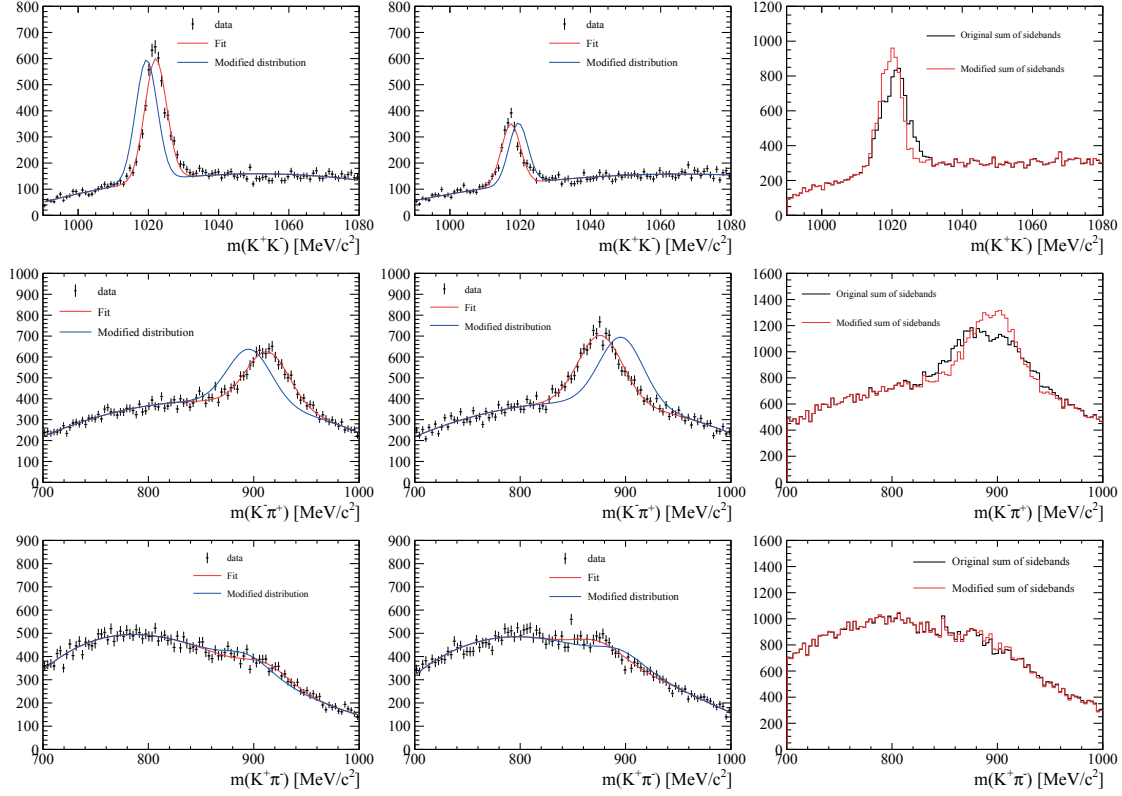
Figure 4.5 – Lower sideband (left), upper sideband (middle) and the sum of the two (right) projected on the K^+K^- (top), $K^-\pi^+$ (middle) and $K^+\pi^-$ (bottom) masses. The data is presented along with its fits and its corrections.

4.5.1 Correction

In order to have the same phase-space boundaries for the signal and the background samples, the $K^+K^-\pi^+\pi^-$ invariant mass has been constrained to the D^0 mass. As a side effect, the peaks of the resonances present in the background are slightly shifted. These shifts are of opposite direction for the upper and the lower sidebands. By summing the two sidebands, the peaks are roughly at the correct place, however, the width of the resonances is broadened. This effect is clearly visible for the $\phi(1020)^0 \to K^+K^-$ and $K^*(892)^0 \to K^-\pi^+$ resonances.

The data sidebands are therefore reweighted in $m(K^+K^-)$, $m(K^-\pi^+)$ and $m(K^+\pi^-)$ to let the resonances have the correct width, which is obtained by performing fits in each of the two sidebands separately. The fit is parametrised as a polynomial for the combinatorial background and a Gaussian for the resonance signal (red curves in Fig. 4.5 left and middle columns). The mean of the resulting distributions is then shifted to the PDG mass in both sidebands separately (blue curves in Fig. 4.5 left and middle columns). The weighting function is then obtained by dividing the corrected distribution by the original fitted distribution. The two sidebands are reweighted separately such that their sum shows resonance peaks at the correct position with the correct width (red histograms in Fig. 4.5 right column).

The correction is applied on the $\phi(1020)^0$ in the K^+K^- invariant mass for $990\,\mathrm{MeV}/c^2 < m_{K^+K^-} < 1080\,\mathrm{MeV}/c^2$ with a second order polynomial for the combinatorial background. It is also applied on the $\overline{K}^*(892)^0$ in the $K^-\pi^+$ invariant mass with a second order polynomial for the combinatorial background and on the $K^*(892)^0$ in the $K^+\pi^-$ invariant mass with a third order polynomial for the combinatorial background, for $700\,\mathrm{MeV}/c^2 < m_{K^\pm\pi^\mp} < 1000\,\mathrm{MeV}/c^2$ in both cases. The $K^*(892)^0$ peak is much less pronounced than its CP conjugate. Therefore a simultaneous fit is performed on the $K^+\pi^-$ and $K^-\pi^+$ invariant masses with the same width and the same mean. Outside of these bounds, no correction is applied. The continuity at the boundaries is ensured by normalising the weights by the number of events in those regions.

There might be some $\rho(770)^0$ present in the sidebands as well, but no suitable correction could be implemented. It is a small and wide component, close to the phase-space threshold, with a non trivial mass distribution. All this justifies the absence of correction. All the other two-body and three-body invariant masses have been inspected and do not show any peaking structure.

If the K^* and $\overline{K}^*$ were coming from combinatorial background, we would expect them to have similar rates. Therefore, we conclude that they have to come from partially reconstructed backgrounds. As mentioned earlier, all the $\overline{D}^0$ candidates have been transformed into D^0 candidates by applying CP to the momenta and charges of the tracks. The events in the sidebands do not come from a D^0, however, the same procedure is performed on the tracks, according to the charge of the muon. The fact that one of the flavour of the K^* almost disappears when CP is applied means that it is strongly correlated with the charge of the muon. A favoured transition, which explains this correlation, is $b \to c \to s$, which creates a $\overline{K}^*$ (decaying to $K^-\pi^+$) rather than a K^*. These two tracks could then be associated to a random kaon and a random pion present in the event to form the $K^+K^-\pi^+\pi^-$ candidate in the sidebands of the D^0 mass.

4.5.2 Background modelling

The method chosen to create a 5D background function is to reweight the MC integration sample to make it match the 5D distribution observed in the data sidebands. It has been observed that reweighting only five variables (for example the five CM variables) does not reproduce resonant structures in other projections (for example in the $K^-\pi^+$ invariant mass). This can be explained by the fact that the mechanisms used to reweight the distributions do not take all the correlations into account. Ideally one would use one 5D histogram, which would obviously contain all the correlations. However, the limited statistics in the D^0 sidebands ($\sim$ 90k events) makes this impossible: if we require at least ten events per cell in 5D space, this would allow only 6 or 7 bins in each of the five dimensions. This coarse binning is not suitable to describe fine structures such as the narrow ϕ peak.

The solution found to overcome this correlation problem, is to reweight significantly more than five different projections of the same five-dimensional phase space in order to describe correctly all the features. The 31 different variables, listed in Table 3.1, have been chosen
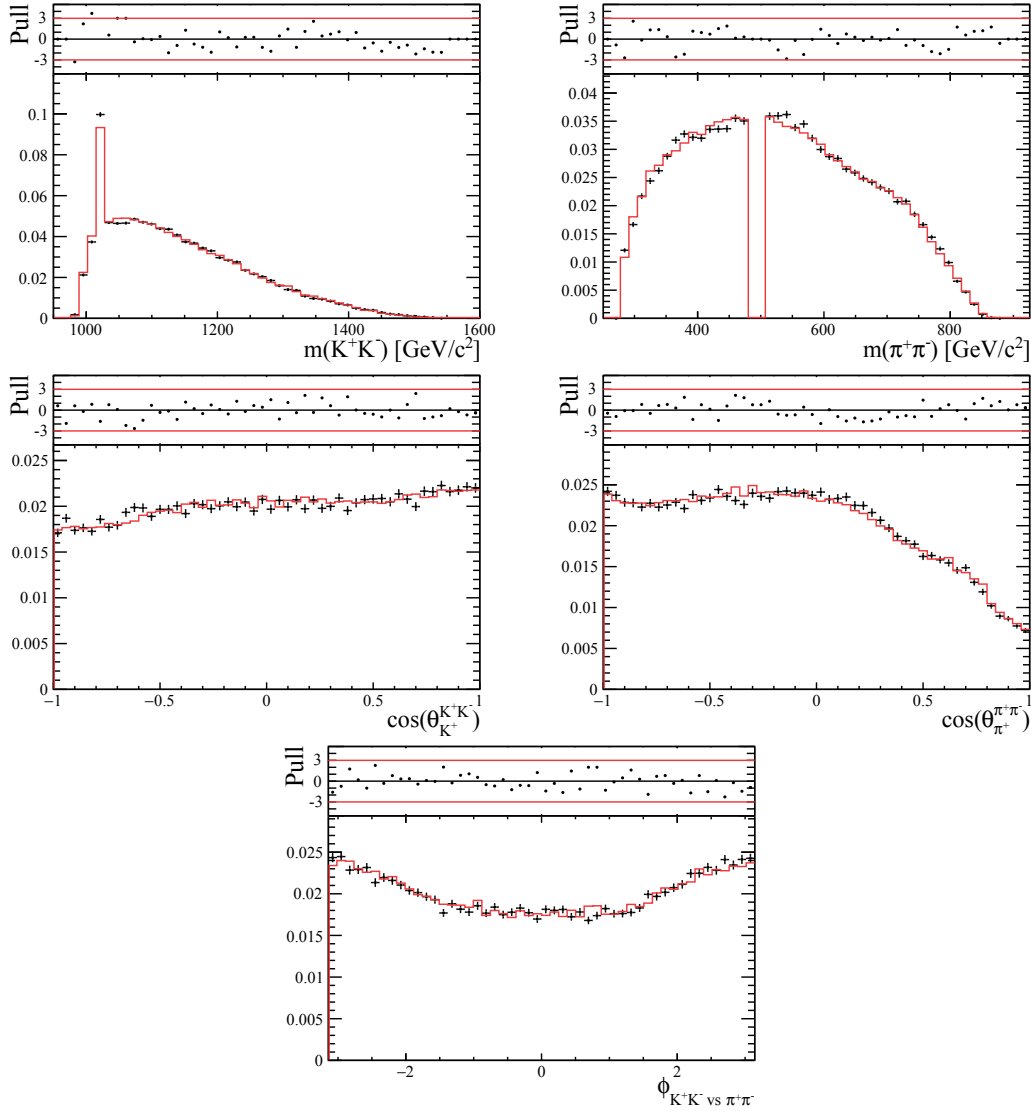
Figure 4.6 – Background distributions of the five variables of Set 1 (*i.e.* the CM variables). The black points represent the data sideband events, and the red points the MC events after the reweighting procedure.

for this purpose. The reweighting is performed simultaneously on these 31 variables using `hep_ml` [92].

After this procedure, the distributions of the weighted MC sample match well those of the data sidebands, for all 31 variables, as shown in Fig. 4.6 for the five CM variables and in Appendix C for the remaining 26 variables.

After the weights are normalised to satisfy $\sum_{i=1}^{N_{\text{MC}}} w(\boldsymbol{x}_i) = N_{\text{MC}}$, they can be used to evaluate the background component of the fitting function of Eq. 4.12. However, a slight technical difficulty arises because the computation of the likelihood function $\mathscr{L}_F(\boldsymbol{c})$ requires $B(\boldsymbol{x}) = w(\boldsymbol{x})S^{\text{gen}}(\boldsymbol{x})$

to be evaluated at the phase-space points x_j of the data events, not at the phase-space points x_i of the MC events. As there is no one-to-one correspondence between the data events and the MC events, a pseudo five-dimensional interpolation is used. The MC sample is binned in the five dimensions defined by the CM variables using the `HyperPlot` [114] tool. The binning process loops over the five dimensions and on each dimension, it splits each bin into two smaller bins with approximately the same number of events. This adaptive binning results in bins with similar number of events, but with smaller volumes in high density regions. One can choose the minimum number of events required and a limit of 5 has been set (*i.e.* between 5 and 9 MC events can be present in each bin). Since the MC sample contains ∼ 10M events, the binning process results in ∼ 1.5M bins. The evaluation of $B(x_j)$ for a data event at point x_j is taken as the average of the weights $B(x_i)$ of the MC events inside the bin containing x_j.

4.6 Fit validation

pseudoexperiments are run to demonstrate that the background description works and is usable in the amplitude fit. As a first step the pseudoexperiments use only a signal model. For each pseudoexperiment, 200k signal events are generated according to an arbitrary model. This model was inspired by the CLEO model of Ref. [46]. A fit is performed with a MC integration sample of 10M events and the result of the fit is then compared to the input values. 1000 pseudoexperiments have been run and their results are summarised in Table 4.5. The biases, although rather small, will be addressed with a systematic uncertainty.

The same pseudoexperiments have been run again but in addition to the signal contribution of 200k events, a background contribution is generated according to the empirical background PDF described in Sec. 4.5 with 50k events. The fit is also performed with an integration of 10M MC events. The results are summarised in Tables 4.6 and the pulls of the fit fractions are shown in Fig. 4.7.

The two sets of pseudoexperiments show similar accuracies. We conclude that the description of the background works as expected and does not introduce any significant bias. The small remaining discrepancies will be accounted for in a systematic uncertainty.

Table 4.5 – Fit validation with 1000 pseudoexperiments, each with 200k signal events and an integration sample of 10M events. The statistical uncertainties on the mean and width of the pulls are specified in the header line.

Real and imaginary parts of c_k coefficients		Input value	Mean result	Mean uncertainty	$\mu \pm 0.03$	Pulls $\sigma \pm 0.02$	χ^2/ndf
$D^0 \rightarrow K^*(892)^0 \bar{K}^*(892)^0$	Re	−0.061	−0.061	0.001	0.040	1.021	0.608
	Im	−0.153	−0.153	0.001	−0.176	1.052	0.630
$D^0 \rightarrow \phi(1020)^0 \rho(770)^0$	Re	0.202	0.202	0.005	0.077	1.050	0.834
	Im	−0.577	−0.578	0.004	−0.038	1.017	0.702
$D^0 \rightarrow [\phi(1020)^0 \rho(770)^0]_{L=2}$	Re	0.531	0.535	0.023	0.150	1.060	0.876
	Im	−1.663	−1.663	0.018	0.013	1.041	0.625
$D^0 \rightarrow \phi(1020)^0 [\pi^+\pi^-]_{L=0}$	Re	0.342	0.343	0.006	0.198	0.977	0.749
	Im	0.361	0.361	0.005	−0.052	0.990	1.134
$D^0 \rightarrow K_1(1270)^+ K^-, K_1(1270)^+ \rightarrow K^*(892)^0 \pi^+$	Re	−0.173	−0.173	0.002	0.090	1.034	1.076
	Im	0.282	0.283	0.002	0.235	1.014	0.838
$D^0 \rightarrow K_1(1270)^- K^+, K_1(1270)^- \rightarrow \bar{K}^*(892)^0 \pi^-$	Re	0.164	0.164	0.002	0.099	1.011	0.446
	Im	−0.121	−0.121	0.002	−0.110	0.958	0.709
$D^0 \rightarrow K_1(1270)^+ K^-, K_1(1270)^+ \rightarrow \rho(770)^0 K^+$	Re	0.239	0.241	0.003	0.424	0.980	0.905
	Im	0.114	0.114	0.003	−0.006	1.011	0.799
$D^0 \rightarrow K_1(1270)^- K^+, K_1(1270)^- \rightarrow \rho(770)^0 K^-$	Re	−0.296	−0.296	0.003	−0.113	1.023	1.004
	Im	−0.439	−0.438	0.003	0.073	1.056	0.622
$D^0 \rightarrow K^*(1410)^+ K^-, K^*(1410)^+ \rightarrow K^*(892)^0 \pi^+$	Re	−0.268	−0.268	0.006	−0.119	0.956	0.659
	Im	−0.736	−0.737	0.005	−0.281	0.988	1.066
$D^0 \rightarrow K^*(1410)^- K^+, K^*(1410)^- \rightarrow \bar{K}^*(892)^0 \pi^-$	Re	−0.112	−0.112	0.005	0.000	0.983	0.496
	Im	0.389	0.390	0.005	0.185	1.057	0.738
$D^0 \rightarrow [K^+K^-]_{L=0}[\pi^+\pi^-]_{L=0}$	Re	1 (fixed)	1 (fixed)				
	Im	0 (fixed)	0 (fixed)				
Fit fractions $\mathscr{F}_k$							
$D^0 \rightarrow K^*(892)^0 \bar{K}^*(892)^0$		0.082	0.082	0.001	0.094	1.048	0.828
$D^0 \rightarrow \phi(1020)^0 \rho(770)^0$		0.212	0.211	0.001	−0.464	0.998	0.635
$D^0 \rightarrow [\phi(1020)^0 \rho(770)^0]_{L=2}$		0.026	0.026	0.000	−0.090	1.032	0.663
$D^0 \rightarrow \phi(1020)^0 [\pi^+\pi^-]_{L=0}$		0.036	0.036	0.001	0.103	0.991	0.468
$D^0 \rightarrow K_1(1270)^+ K^-, K_1(1270)^+ \rightarrow K^*(892)^0 \pi^+$		0.130	0.130	0.001	0.056	1.010	0.544
$D^0 \rightarrow K_1(1270)^- K^+, K_1(1270)^- \rightarrow \bar{K}^*(892)^0 \pi^-$		0.049	0.050	0.001	0.252	0.968	0.934
$D^0 \rightarrow K_1(1270)^+ K^-, K_1(1270)^+ \rightarrow \rho(770)^0 K^+$		0.033	0.033	0.001	0.410	0.985	0.641
$D^0 \rightarrow K_1(1270)^- K^+, K_1(1270)^- \rightarrow \rho(770)^0 K^-$		0.131	0.131	0.001	−0.100	1.027	1.263
$D^0 \rightarrow K^*(1410)^+ K^-, K^*(1410)^+ \rightarrow K^*(892)^0 \pi^+$		0.077	0.078	0.001	0.514	0.943	0.368
$D^0 \rightarrow K^*(1410)^- K^+, K^*(1410)^- \rightarrow \bar{K}^*(892)^0 \pi^-$		0.021	0.021	0.000	0.054	1.043	0.424
$D^0 \rightarrow [K^+K^-]_{L=0}[\pi^+\pi^-]_{L=0}$		0.182	0.182	0.001	0.015	1.016	0.571

Table 4.6 – Fit validation with 1000 pseudoexperiments, each with 200k signal events, 50k background events and 10M MC events for the integration sample. The statistical uncertainties on the mean and width of the pulls are specified in the header line.

Real and imaginary parts of c_k coefficients		Input	Mean result	Mean uncertainty	$\mu \pm 0.03$	Pulls $\sigma \pm 0.02$	χ^2/ndf
$D^0 \to K^*(892)^0 \bar{K}^*(892)^0$	Re	−0.061	−0.061	0.002	0.193	1.048	0.687
	Im	−0.153	−0.153	0.001	0.140	0.980	0.905
$D^0 \to \phi(1020)^0 \rho(770)^0$	Re	0.202	0.203	0.005	0.171	0.996	0.754
	Im	−0.577	−0.576	0.004	0.371	0.952	0.842
$D^0 \to [\phi(1020)^0 \rho(770)^0]_{L=2}$	Re	0.531	0.542	0.027	0.379	0.998	0.702
	Im	−1.663	−1.654	0.021	0.450	0.995	0.377
$D^0 \to \phi(1020)^0 [\pi^+\pi^-]_{L=0}$	Re	0.342	0.342	0.006	−0.059	0.949	0.635
	Im	0.361	0.360	0.006	−0.176	0.970	0.735
$D^0 \to K_1(1270)^+ K^-, K_1(1270)^+ \to K^*(892)^0 \pi^+$	Re	−0.173	−0.173	0.003	−0.009	0.986	0.843
	Im	0.282	0.282	0.002	−0.006	1.004	0.510
$D^0 \to K_1(1270)^- K^+, K_1(1270)^- \to \bar{K}^*(892)^0 \pi^-$	Re	0.164	0.165	0.002	0.153	1.000	0.973
	Im	−0.121	−0.121	0.002	0.128	0.987	0.606
$D^0 \to K_1(1270)^+ K^-, K_1(1270)^+ \to \rho(770)^0 K^+$	Re	0.239	0.240	0.003	0.083	1.017	0.555
	Im	0.114	0.114	0.003	0.082	0.986	0.826
$D^0 \to K_1(1270)^- K^+, K_1(1270)^- \to \rho(770)^0 K^-$	Re	−0.296	−0.296	0.004	−0.029	0.981	0.525
	Im	−0.439	−0.437	0.004	0.490	0.990	0.668
$D^0 \to K^*(1410)^+ K^-, K^*(1410)^+ \to K^*(892)^0 \pi^+$	Re	−0.268	−0.266	0.008	0.256	0.978	0.582
	Im	−0.736	−0.737	0.006	−0.142	0.988	0.727
$D^0 \to K^*(1410)^- K^+, K^*(1410)^- \to \bar{K}^*(892)^0 \pi^-$	Re	−0.112	−0.112	0.006	−0.086	0.948	0.586
	Im	0.389	0.389	0.006	0.014	0.962	0.572
$D^0 \to [K^+K^-]_{L=0}[\pi^+\pi^-]_{L=0}$	Re	1 (fixed)	1 (fixed)				
	Im	0 (fixed)	0 (fixed)				

| Fit fractions $\mathscr{F}_k$	Input	Mean result	Mean uncertainty	$\mu \pm 0.03$	$\sigma \pm 0.02$	χ^2/ndf
$D^0 \to K^*(892)^0 \bar{K}^*(892)^0$	0.082	0.082	0.001	−0.097	1.013	0.630
$D^0 \to \phi(1020)^0 \rho(770)^0$	0.212	0.211	0.001	−0.624	0.970	0.671
$D^0 \to [\phi(1020)^0 \rho(770)^0]_{L=2}$	0.026	0.026	0.001	−0.290	1.009	0.936
$D^0 \to \phi(1020)^0 [\pi^+\pi^-]_{L=0}$	0.036	0.036	0.001	−0.072	0.947	0.469
$D^0 \to K_1(1270)^+ K^-, K_1(1270)^+ \to K^*(892)^0 \pi^+$	0.130	0.131	0.001	0.203	0.984	0.598
$D^0 \to K_1(1270)^- K^+, K_1(1270)^- \to \bar{K}^*(892)^0 \pi^-$	0.049	0.050	0.001	0.317	0.968	0.720
$D^0 \to K_1(1270)^+ K^-, K_1(1270)^+ \to \rho(770)^0 K^+$	0.033	0.033	0.001	0.245	0.993	0.534
$D^0 \to K_1(1270)^- K^+, K_1(1270)^- \to \rho(770)^0 K^-$	0.131	0.131	0.001	−0.338	0.965	0.694
$D^0 \to K^*(1410)^+ K^-, K^*(1410)^+ \to K^*(892)^0 \pi^+$	0.077	0.078	0.001	0.398	0.943	0.639
$D^0 \to K^*(1410)^- K^+, K^*(1410)^- \to \bar{K}^*(892)^0 \pi^-$	0.021	0.021	0.001	0.054	0.947	0.439
$D^0 \to [K^+K^-]_{L=0}[\pi^+\pi^-]_{L=0}$	0.182	0.183	0.001	0.436	0.966	1.046
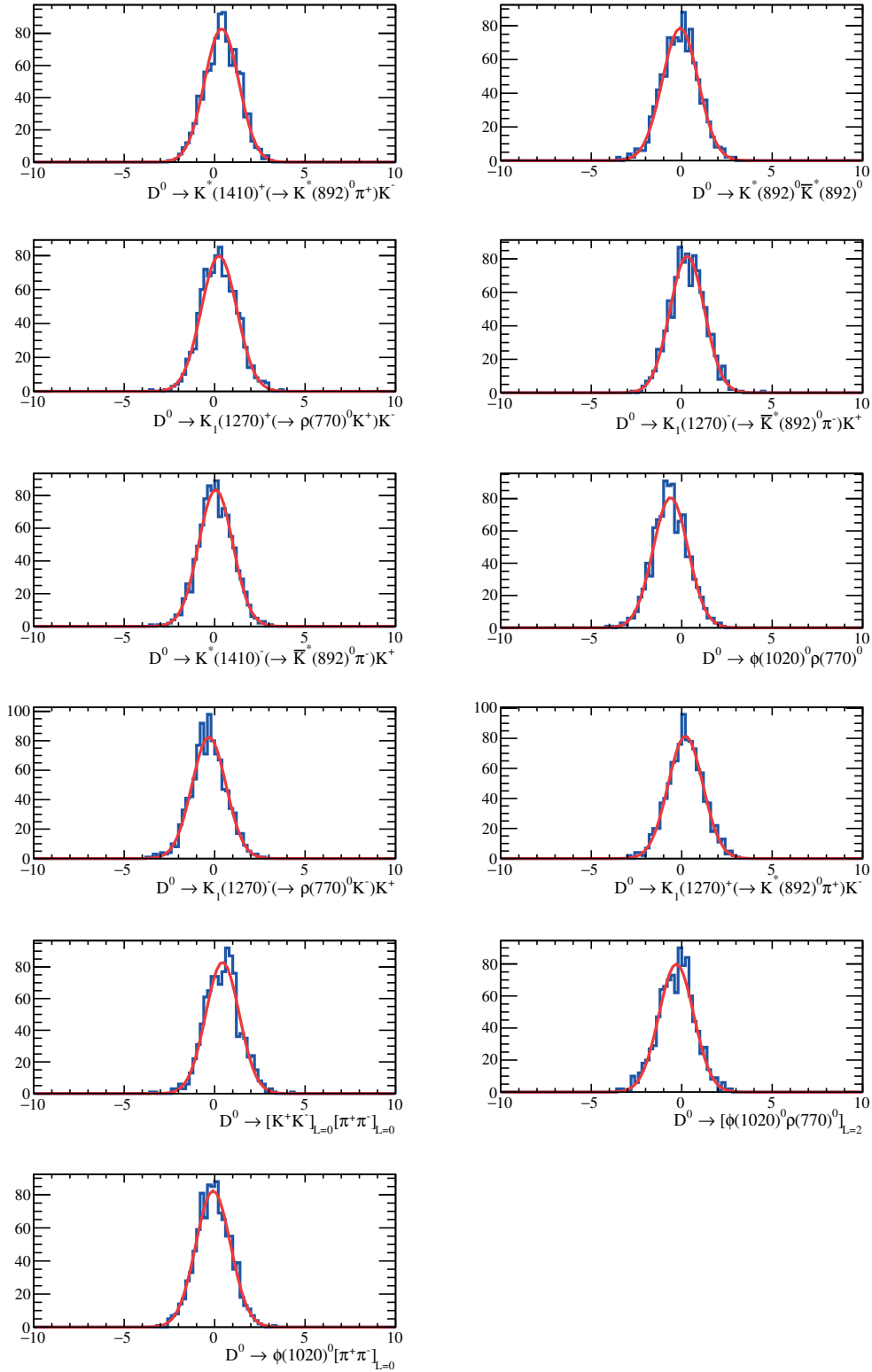
Figure 4.7 – Pulls of the fit fractions obtained with 1000 pseudoexperiments fitting each 200k signal and 50k background events with an integration sample of 10M events.

4.7 Model building

The signal model is built with an iterative method. A list of all possible amplitudes is defined (see Appendix B) along with a base model. The base model contains six amplitudes, that are expected to contribute to the decay $D^0 \to K^+ K^- \pi^+ \pi^-$:

- $D^0 \to \phi(1020)^0 (\rho - \omega)^0$ (S,P,D waves),

- $D^0 \to K^*(892)^0 \overline{K}^*(892)^0$ (S,P,D waves).

All the amplitudes of the list are added one by one to the base model and fitted to the data. As no *CP* violation is expected to arise in strong decays, the two charges of the same three-body resonance are constrained to have the same substructure. This means that the two charges of the same three-body component are always added together in the model building method.

The amplitude that produces the largest decrease in $-2\ln\mathcal{L}$ is kept and added permanently to the base model. The remaining amplitudes are tested again in the subsequent loop and so on. The sum of the fit fractions is not equal to 1 because of interference, which is expected. However, if the sum becomes too high, it is a sign that non physical amplitudes are cancelling each-other and are not really contributing to the decay $D^0 \to K^+ K^- \pi^+ \pi^-$. It is observed that the sum is quite stable while adding amplitudes but at some point it diverges. The procedure is therefore stopped and the amplitude that is responsible for this divergence is removed.

4.8 Resulting nominal model

In order to assess the quality of the fit, a χ^2 test is performed using an adaptive binning. The same method as described in Sec. 4.5.2 is used for the adaptive binning on the CM variables. In order to have a sufficient statistics in each bin to compute a sensible χ^2 value, the minimum number of events required per bin is 10. This results in 8192 bins covering the whole phase space, with smaller bins in higher density regions.

The χ^2 is computed as

$$\chi^2 = \sum_i^{N_{\text{bins}}} \frac{(N_i - N_i')^2}{\sigma_i^2 + \sigma_i'^2} \,, \tag{4.66}$$

where N_i is the number of data events in the bin i and N_i' is the expected number of events in the same bin i, determined from the fitted PDF,

$$N_i' = \sum_j^M \omega_j \,, \tag{4.67}$$

with M being the number of events in bin i and ω_j is the weight of the MC integration event j.
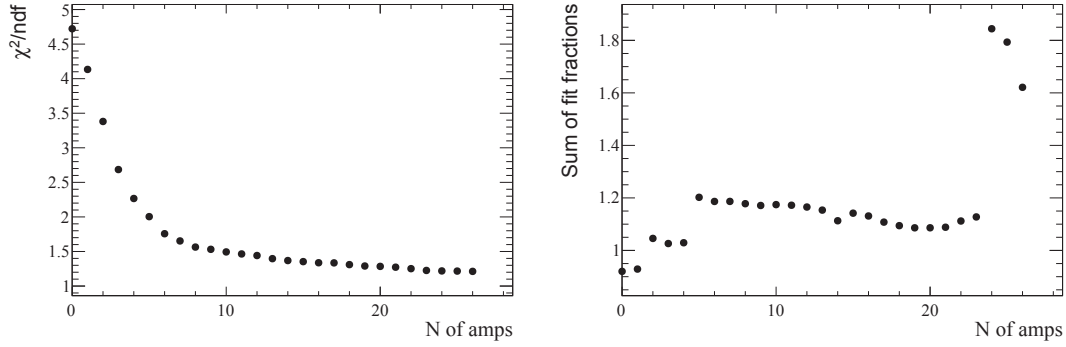
Figure 4.8 – Evolution of the χ^2/ndf and the sum of the fit fractions during the model building procedure. The horizontal axis shows the number of added amplitudes.

The uncertainty on the number of data events is the Poisson statistical uncertainty:

$$\sigma_i = \sqrt{N_i}. \tag{4.68}$$

The uncertainty on the expected number of events is given by

$$\sigma_i'^2 = \sum_j^M \omega_j^2. \tag{4.69}$$

Throughout the note, the χ^2/ndf will be quoted to assess the quality of the various fits. The number of degrees of freedom (ndf) is computed as the number of bins minus the number of parameters in the fit minus one, because the total number of events is known.

Figure 4.8 shows the evolution of the χ^2/ndf of the fit and the sum of the fit fractions during the model building procedure. The base model corresponds to 8176 degrees of freedom and at each iteration the number of degrees of freedom is decreased, since one or more complex fit parameter is added for each amplitude. The procedure is stopped at the iteration preceding the divergence in the sum of fit fractions.

The resulting model, referred to as the nominal model in the following, contains more than 25 components yielding a χ^2 value of 9242 for 8121 degrees of freedom. Such χ^2 value is good in comparison to other high-statistics amplitude analyses. The resulting fit parameters and fit fractions of all the components as well as projections on the five CM variables of the fit and the data are shown in in Tables 6.1–6.3 and Fig. 6.1 in Chapter 6.

The statistical significance of each selected amplitude is computed using Wilks' theorem [115]. The final fit is the null hypothesis H_0 and contains N_0 degrees of freedom. As many fits as there are amplitudes in the model are performed, each time by removing one amplitude from the model. These fits are the alternative hypotheses H_i with N_i degrees of freedom. The likelihood ratio of these fits with respect to the final fit is performed to assess the difference between the

various fits:

$$D = -2\ln\left(\frac{\mathscr{L}(H_0)}{\mathscr{L}(H_1)}\right) \tag{4.70}$$

$$= 2\left(\ln\left(\mathscr{L}(H_1)\right) - \ln\left(\mathscr{L}(H_0)\right)\right). \tag{4.71}$$

This difference D is distributed as a χ^2 of $(N_i - N_0)$ degrees of freedom. The related p-value can be extracted from the χ^2, which in turn can be converted to a significance. Every amplitude in the nominal model has a very high statistical significance, as shown in Tables 6.1 and 6.2.

4.9 *CP* violating observables

Once the *CP* averaged D^0 model has been determined, one can use it to perform a search for *CP* violation. The data is split according to the flavour of the muon such that there is a D^0 sample and a $\overline{D}^0$ sample, where *CP* has been applied on all $\overline{D}^0$ candidates. The $\overline{D}^0$ sample is kept like this in order to use the same model for both samples, and to be able to compare the observables that are *CP* sensitive. The integration MC sample does not contain any *CP* violation and is therefore not split (*i.e.* the entire sample of 10M events is used for fitting both the D^0 and $\overline{D}^0$ samples). No *CP* violation is expected in the background data events present in the D^0 sidebands. Therefore the sidebands are also not separated and the background PDF is the same for the D^0 and the $\overline{D}^0$ samples.

In the following this measurement will be referred to as the *CP* violation fit in contrast to the nominal fit, which is the *CP* averaged fit. We decide to parametrise the *CP* violation with the average modulus $\overline{|c_k|}$, modulus asymmetry $A_{|c_k|}$, average phase $\overline{\arg(c_k)}$ and phase difference $\Delta\arg(c_k)$, as already done in Ref. [116]:

$$\overline{|c_k|} = \frac{|c_k|_{D^0} + |c_k|_{\overline{D}^0}}{2} \qquad\qquad A_{|c_k|} = \frac{|c_k|_{D^0} - |c_k|_{\overline{D}^0}}{|c_k|_{D^0} + |c_k|_{\overline{D}^0}} \tag{4.72}$$

$$\overline{\arg(c_k)} = \frac{\arg(c_k)_{D^0} + \arg(c_k)_{\overline{D}^0}}{2} \qquad\qquad \Delta\arg(c_k) = \frac{\arg(c_k)_{D^0} - \arg(c_k)_{\overline{D}^0}}{2}, \tag{4.73}$$

where $|c_k|$ and $\arg(c_k)$ are the polar coordinates (modulus and phase) of the complex fit parameter multiplying amplitude k. These coordinates can be expressed in terms of the *CP* violation parameters:

$$|c_k|_{D^0} = \overline{|c_k|}(1 + A_{|c_k|}) \qquad\qquad \arg(c_k)_{D^0} = \overline{\arg(c_k)} + \Delta\arg(c_k) \tag{4.74}$$

$$|c_k|_{\overline{D}^0} = \overline{|c_k|}(1 - A_{|c_k|}) \qquad\qquad \arg(c_k)_{\overline{D}^0} = \overline{\arg(c_k)} - \Delta\arg(c_k). \tag{4.75}$$

The fit is performed directly on the *CP* violation parameters. Therefore it takes both samples, D^0 and $\overline{D}^0$, and minimises the sum of the two negative log-likelihoods. No *CP* violation is expected in the strong decays of the three-body resonances; their modulus and phases are therefore simultaneously fitted to common values for the two samples.

An additional information of the *CP* violation in each amplitude can be obtained from the fit fractions. The following asymmetry is considered:

$$A_{\mathscr{F}_k} = \frac{\mathscr{F}_k^{D^0} - \mathscr{F}_k^{\bar{D}^0}}{\mathscr{F}_k^{D^0} + \mathscr{F}_k^{\bar{D}^0}}, \tag{4.76}$$

where $\mathscr{F}_k^{D^0}$ and $\mathscr{F}_k^{\bar{D}^0}$ are the fit fractions for the D^0 and the $\bar{D}^0$ samples respectively.

5 Systematic uncertainties and cross-checks

Various sources are considered as systematic uncertainties in the nominal fit. They are all described in the following sections and all the values are summarised in Tables 5.4 and 5.5.

Several types of systematic uncertainties are considered. The first type is evaluated by comparing two different hypotheses (a and b) while fitting the same sample. This type of systematic uncertainties is computed as:

$$\sigma_k^{\mathrm{syst}} = \begin{cases} ||c_k^a| - |c_k^b|| \\ |\arg(c_k^a) - \arg(c_k^b)| \\ |\mathscr{F}_k^a - \mathscr{F}_k^b| \end{cases} \tag{5.1}$$

where $|c_k|$, $\arg(c_k)$ and $\mathscr{F}_k$ are the modulus, phase and fit fraction of the amplitude k.

The second type of systematic uncertainties are evaluated with pseudoexperiments, where a signal sample is generated according to a certain model and fitted back to verify that the input parameters can be retrieved. In this case, a pull is computed as:

$$\mathrm{pull}_k = \frac{|c_k^{\mathrm{fit}}| - |c_k^{\mathrm{input}}|}{\sigma_k^{\mathrm{fit}}}, \tag{5.2}$$

where σ_k^{fit} is the statistical uncertainty of the amplitude k in each pseudoexperiment. The pulls are similarly computed for the phase and fit fraction of each amplitude. The pseudoexperiment is repeated 1000 times and for each modulus, phase and fit fraction, a histogram is filled as shown in Fig. 5.1.

The systematic uncertainty is then assigned as:

$$\sigma_k^{\mathrm{syst}} = \sigma_k^{\mathrm{stat}} \sqrt{\mu_k^2 + \sigma_{\mu_k}^2}, \tag{5.3}$$

where μ_k and σ_{μ_k} are the mean of the pull and its uncertainty and σ_k^{stat} is the statistical uncertainty for the amplitude k of the final fit to the data. This assigns as systematic uncertainty the
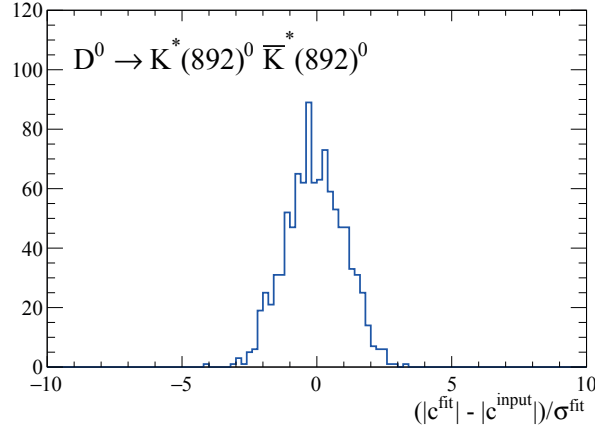
Figure 5.1 – Pull of one fit parameter as example. This particular pull has been obtained on a pseudoexperiment using signal only, for the modulus of the parameter of the amplitude $D^0 \to K^*(892)^0 \overline{K}^*(892)^0$ in S-wave.

mean of the distribution if there is a bias or the resolution of the test if the bias is negligible.

The third type of systematic uncertainties is also linked to pseudoexperiments, but where an additional effect is tested. For example, if a pseudoexperiment is performed with signal and background, it will contain both effects, while the effect of the signal is already taken into account in another systematic uncertainty. We assume that both effects are independent and therefore assign the systematic uncertainties in analogy to Eq. 5.3:

$$\sigma_k^{\text{syst}} = \sigma_k^{\text{stat}} \sqrt{\Delta\mu_k^2 + \sigma_{\Delta\mu_k}^2}, \tag{5.4}$$

where $\Delta\mu_k$ is the difference of the means of the pulls between the signal-only pseudoexperiment and the pseudoexperiment with the additional effect. And $\sigma_{\Delta\mu_k}$ is the uncertainty on this difference, taken as the quadratic sum of the uncertainties on the two means of the pulls.

Finally, the fourth type of systematic uncertainties is evaluated by comparing many slightly different models to test statistical fluctuations (*e.g.* comparing different background models elaborated by resampling the data sidebands). For this type of systematic uncertainties, 1000 fits are performed to the data and the resulting spread of each parameter σ_k is taken as the systematic uncertainty:

$$\sigma_k^{\text{syst}} = \sigma_k. \tag{5.5}$$

5.1 Selection efficiencies

Reconstruction and selection efficiencies are accounted for by using a MC sample that has gone through the same reconstruction steps as the data. This MC sample is directly used as the integration sample in the fit, as described in Sec. 4.1. However, the simulation is not a

perfect description of the data and this choice might introduce some bias and a systematic uncertainty needs to be assigned.

Since the integration MC sample used in the fit has been reweighted to match the data, the idea is to compare various reweightings. The default reweighting is performed before the offline selection. Another possibility is to perform the reweighting after the offline selection. This second reweighting is performed and the resulting MC sample is used in a fit. The fit results are compared and systematic uncertainties are assigned according to Eq. 5.1.

5.2 Background description

Two sources of systematic uncertainties are identified for the background description:

- First, the finite size of the D^0 sidebands has an implication on the description of the background PDF. In order to assign a systematic uncertainty to take this effect into account, the D^0 sidebands have been resampled 1000 times using the bootstrap method [117]. This generates various background descriptions with simulated statistical fluctuations. These various background PDFs are used to fit the data in order to check how much the statistical uncertainty of the background description affects the signal fit. The systematic uncertainty is computed according to Eq. 5.5.

- Second, the reweighting method used to generate the background PDF, as described in Sec. 4.5.2, might introduce a bias. We used `hep_ml` for the multi-dimensional reweighting procedure in the nominal fit and we compare it to another method that we developed to assign a systematic uncertainty. The description of this alternative method is given in Appendix D. The fit is performed again with this alternative background PDF. The χ^2/ndf is similar and the systematic uncertainties are computed according to Eq. 5.1.

5.3 Signal fraction

In the nominal fit to the data, the signal fraction f_s is fixed to the value obtained in the one-dimensional mass fit described in Sec. 3.6. However this fraction has a statistical uncertainty that needs to be propagated to the final result. In order to test the impact of the signal fraction on the final results, the fit is performed 1000 times on data with the value of the signal fraction taken from a Gaussian random number generation with a mean value of 0.828 and a width of 0.003. The background fraction is always taken as $f_{\mathrm{bkg}} = 1 - f_{\mathrm{sig}}$. The pulls of the fit parameters are found to be negligible and therefore no systematic uncertainty is assigned for this effect.

5.4 Resonance description

Some choices have been made for the description of the resonances. Some other parametrisations are used to assign a systematic uncertainty for these choices.

- The Gounaris-Sakurai description for the $\rho(770)^0$ is tested against the RBW. The systematic uncertainty is computed according to Eq. 5.1.

- The K-matrix description of the $\pi\pi$ and KK S-waves is varied among the various solutions published in Ref. [107]. Eq. 5.1 is used for both alternative solutions and the maximum value between the two is kept as the systematic uncertainty.

- A systematic uncertainty is also assigned for the choice of values used for the fixed masses and widths of the resonances. 1000 fits are performed on the data, where these values are fluctuated according to a Gaussian with a mean and width taken as the value and its uncertainty quoted by the PDG [24]. The systematic uncertainty is assigned according to Eq. 5.5. This systematic uncertainty is dominated by the less well-known resonances which have large uncertainties, such as the $K^*(1680)^0$.

- The radius of the various resonances is poorly known. A value has been determined for the D^0, the $K^*(892)^0$ and the $K^*(1680)^0$, as described in Sec. 4.3.1. The radii of these three resonances are therefore fluctuated as a Gaussian with mean and width taken as their determined mean value and uncertainty. For the other resonances, since no preferred value has been found, a uniform distribution is taken around the default value of $1.5\,\text{GeV}^{-1}$ with a similar range ($1.3\,\text{GeV}^{-1} < R < 1.7\,\text{GeV}^{-1}$). The radius of the $a_1(1260)^+$ is similarly fluctuated around its set value ($1.5\,\text{GeV}^{-1} < R < 1.9\,\text{GeV}^{-1}$). 1000 fits are performed to the data and the systematic uncertainty is assigned according to Eq. 5.5.

5.5 Fit bias

pseudoexperiments are performed, where a signal sample is generated according to the final model and is fitted back in order to retrieve the input values. This tests whether that the fit is unbiased. For each pseudoexperiment a different MC sample is generated such that they are completely independent. As the nominal MC integration sample, these MC samples are a combination of phase space and CLEO model. In order to use reasonable CPU and storage resources as well as performing the pseudoexperiments in a reasonable time, the statistics of the pseudoexperiments has been chosen to be smaller than the nominal statistics present in the data. In the nominal fit, the data contains $\sim$ 200k events with a purity of 82.8% and the MC integration sample contains $\sim$ 10M events. A similar ratio is used for the pseudoexperiments, where the generated sample has 50k events and the MC sample has 2.5M events. We use the assumption that these systematic effects do not scale with statistics.

Five different effects, described in the following subsections, are tested with pseudoexperiments. Summary plots showing the mean and the width of all the distributions are shown in Appendix E.

5.5.1 Signal

The signal sample is fitted alone in order to test the stability of the fitter. Here 50k events of signal are generated for each pseudoexperiment. The pulls are computed according to Eq. 5.2 and the systematic uncertainties according to Eq. 5.3.

5.5.2 Background

The signal sample is combined to a background sample. Here 41 440 signal events and 8 560 background events are generated for each pseudoexperiments. The signal sample is generated according to the final signal model and the background sample is generated according to the background model used in the nominal fit. The pulls are computed according to Eq. 5.2 and the systematic uncertainties according to Eq. 5.4.

5.5.3 Mistag

The signal sample is modified in order to add a mistag effect. The probability of mistag due to the wrong assignment of the charge of the muon has been determined in the previous analysis of this same data at LHCb [118]. It is relatively low at 0.5%. Therefore in the pseudoexperiments, we randomly apply CP to the four four-momenta of the daughters particles on 0.5% of the 50k signal events generated. The pulls are again computed according to Eq. 5.2 and the systematic uncertainties according to Eq. 5.4.

5.5.4 Detection asymmetry

This analysis is not sensitive to the production asymmetries between D^0 and $\overline{D}^0$ since only their substructure is studied. It might however be sensitive to detection asymmetries between the four tracks in non-symmetric final states such as $D^0 \to K_1(1270)^+ K^-$. In order to assign a systematic for this effect, we run the same pseudoexperiment with the signal component only, but we modify the signal sample to introduce the detection asymmetries. The size of the effect is taken from Ref. [119]. We neglect the detection asymmetries of the pions and focus on the kaons. According to the paper, the detection asymmetry is defined as shown in Eq. 5.6 and therefore depends on the momentum of the kaon as shown in Fig. 5.2,

$$A_K(p) = \frac{\epsilon_{K^-}(p) - \epsilon_{K^+}(p)}{\epsilon_{K^-}(p) + \epsilon_{K^+}(p)},$$

(5.6)
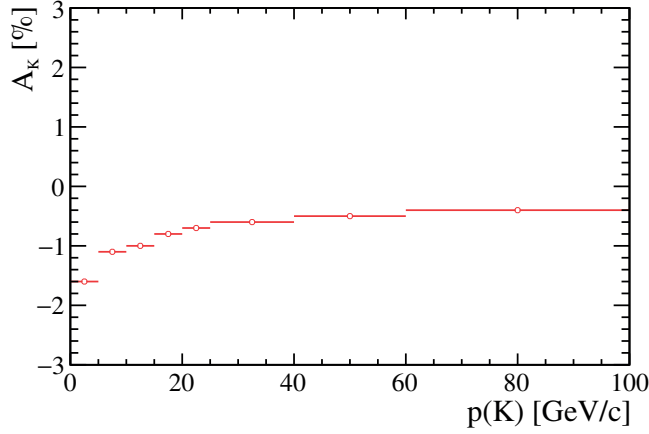
Figure 5.2 – Detection asymmetry as a function of the momentum of the kaon [119].

where ϵ_{K^-} is the detection efficiency of a K^- and ϵ_{K^+} is the detection efficiency of a K^+. Since there is no detection efficiencies in pseudoexperiments, we reweight the generated sample in order to simulate these efficiencies to match the detection asymmetry of Fig. 5.2. In order to do this, two variables have to be set (ϵ_{K^-} and ϵ_{K^+}), we therefore need a second input in addition to the asymmetry and this is the average efficiency:

$$\bar{\epsilon} = \frac{\epsilon_{K^-} + \epsilon_{K^+}}{2}. \tag{5.7}$$

The efficiencies become

$$\epsilon_{K^\mp} = \bar{\epsilon}(1 \pm A_K). \tag{5.8}$$

We decide to set the average efficiency $\bar{\epsilon}$ to 1. This is an arbitrary choice as valid as any, since we are only interested in the asymmetry.

Since there are two kaons in $D^0 \to K^+ K^- \pi^+ \pi^-$, we need to correct every event for both of them. Therefore the final weight applied on each event is:

$$w = (1 + A_K(p_{K^-})) \cdot (1 - A_K(p_{K^+})). \tag{5.9}$$

The opposite effects on the two kaons partially cancel each other in CP eigenstates (*e.g.* $D^0 \to \phi(1020)^0 \rho(770)^0$), but not necessarily in asymmetric components (*e.g.* $D^0 \to K_1(1270)^+ K^-$). 1000 pseudoexperiments are performed, the pulls are computed according to Eq. 5.2 and the systematic uncertainties according to Eq. 5.4.

5.6 Alternative models

The model building method described in Sec. 4.7 is completely deterministic and produces the best model possible with the given list of amplitudes and the given set of criteria used for the selection of amplitudes. Slightly different criteria could lead to slightly different models with similar fit qualities. We therefore assign a systematic uncertainty for this choice of the model. pseudoexperiments are performed by generating a signal model according to an alternative model and fitting it back with the nominal model. This tests the effect of fitting the data with the chosen nominal model when the real underlying model is slightly different. The systematic uncertainties are assigned according to Eq. 5.4 for each alternative model. Several alternative models are studied and all the models with a similar fit quality as the nominal fit ($\chi^2/\text{ndf} = 9226/8123 = 1.14$) are used to assign the systematic uncertainty. The maximum value between the retained alternative models is taken as the final systematic uncertainty due to the alternative models.

5.6.1 a_0 vs f_0

The stopping criterion appears when the amplitude $D^0 \to a_0(980)^0[\pi^+\pi^-]_{L=0}$ is added to the model which tries to describe the same contribution as $D^0 \to [K^+K^-]_{L=0}[\pi^+\pi^-]_{L=0}$, where the main component of the KK K-matrix is the $f_0(980)^0$. The fit does not manage to disentangle the contributions of the a_0 and the f_0; these two amplitudes interfere heavily in an unphysical way. In the nominal fit, the amplitude with the f_0 is kept. For the alternative model, the a_0 is kept instead. The χ^2/ndf is worse ($9755/8123 = 1.16$), which justifies the choice to keep the f_0 for the nominal fit and no systematic uncertainty is assigned for this model.

5.6.2 High-mass K^*

It has been mentioned that the high-mass K^* had two possible sources, the $K^*(1680)$ or the $K^*(1410)$. An alternative model is presented in Table 5.1 where the $K^*(1410)$ is used instead of the $K^*(1680)$. The resulting fit quality is very similar, the $K^*(1680)$ has nevertheless been chosen because it produces a slightly better χ^2/ndf. Since the quality of the two models is so close, this alternative model is used to assign the systematic uncertainty.

Table 5.1 – Modulus and phase of the fit parameters along with the fit fractions of the amplitudes included in the alternative model using $K^*(1410)$ instead of $K^*(1680)$.

Amplitude	$|c_k|$	arg(c_k) [rad]	Fit fraction [%]
$D^0 \to [\phi(1020)(\rho-\omega)^0]_{L=0}$	1 (fixed)	0 (fixed)	23.78 ± 0.38
$D^0 \to K_1(1400)^+ K^-$	0.63 ± 0.01	1.03 ± 0.02	18.93 ± 0.46
$D^0 \to [K^-\pi^+]_{L=0}[K^+\pi^-]_{L=0}$	0.28 ± 0.00	−0.60 ± 0.02	18.76 ± 0.36
$D^0 \to K_1(1270)^+ K^-$	0.46 ± 0.01	2.03 ± 0.02	18.40 ± 0.37
$D^0 \to [K^*(892)^0 \bar{K}^*(892)^0]_{L=0}$	0.28 ± 0.00	−0.28 ± 0.02	9.23 ± 0.21
$D^0 \to [K^*(1410)^0[K^-\pi^+]_{L=0}]_{L=1}$	1.82 ± 0.03	0.44 ± 0.02	6.59 ± 0.15
$D^0 \to [K^*(892)^0 \bar{K}^*(892)^0]_{L=1}$	0.27 ± 0.01	1.21 ± 0.02	5.00 ± 0.16
$D^0 \to K_1(1270)^- K^+$	0.22 ± 0.01	2.12 ± 0.03	4.20 ± 0.17
$D^0 \to [K^+K^-]_{L=0}[\pi^+\pi^-]_{L=0}$	0.12 ± 0.00	−2.53 ± 0.03	3.12 ± 0.17
$D^0 \to [K^*(1410)^0 \bar{K}^*(892)^0]_{L=0}$	0.69 ± 0.02	2.95 ± 0.03	2.97 ± 0.15
$D^0 \to K_1(1400)^- K^+$	0.24 ± 0.01	0.10 ± 0.04	2.73 ± 0.18
$D^0 \to [\bar{K}^*(1410)^0 K^*(892)^0]_{L=1}$	0.82 ± 0.02	−2.78 ± 0.02	2.62 ± 0.10
$D^0 \to [\bar{K}^*(1410)^0[K^+\pi^-]_{L=0}]_{L=1}$	1.03 ± 0.02	1.07 ± 0.02	2.32 ± 0.09
$D^0 \to [\phi(1020)(\rho-\omega)^0]_{L=2}$	1.31 ± 0.03	0.54 ± 0.02	2.28 ± 0.08
$D^0 \to [K^*(892)^0 \bar{K}^*(892)^0]_{L=2}$	0.69 ± 0.02	2.87 ± 0.03	1.80 ± 0.10
$D^0 \to \phi(1020)[\pi^+\pi^-]_{L=0}$	0.05 ± 0.00	−1.70 ± 0.04	1.47 ± 0.09
$D^0 \to [K^*(1410)^0 \bar{K}^*(892)^0]_{L=1}$	0.61 ± 0.02	0.09 ± 0.03	1.46 ± 0.08
$D^0 \to [\phi(1020)\rho(1450)^0]_{L=1}$	0.76 ± 0.04	1.18 ± 0.04	0.97 ± 0.09
$D^0 \to a_0(980)^0 f_2(1270)^0$	1.46 ± 0.06	0.33 ± 0.04	0.64 ± 0.05
$D^0 \to a_1(1260)^- \pi^+$	0.19 ± 0.01	0.18 ± 0.06	0.47 ± 0.06
$D^0 \to a_1(1260)^+ \pi^-$	0.19 ± 0.01	−2.80 ± 0.07	0.47 ± 0.06
$D^0 \to [\phi(1020)(\rho-\omega)^0]_{L=1}$	0.16 ± 0.01	0.27 ± 0.07	0.43 ± 0.05
$D^0 \to [K^*(1410)^0 \bar{K}^*(892)^0]_{L=2}$	1.03 ± 0.08	−2.52 ± 0.08	0.33 ± 0.05
$D^0 \to [K^+K^-]_{L=0}(\rho-\omega)^0$	0.21 ± 0.02	3.06 ± 0.08	0.29 ± 0.04
$D^0 \to [\phi(1020)f_2(1270)^0]_{L=1}$	1.40 ± 0.10	1.72 ± 0.06	0.19 ± 0.02
$D^0 \to [K^*(892)^0 \bar{K}_2^*(1430)^0]_{L=1}$	1.51 ± 0.09	1.98 ± 0.07	0.16 ± 0.02
		Sum of fit fractions	129.62 ± 0.95
		χ^2/ndf	9224/8123 = 1.14
$a_1(1260)^+ \to [\phi(1020)\pi^+]_{L=0}$	1 (fixed)	0 (fixed)	100
$K_1(1270)^+ \to [K^*(892)^0\pi^+]_{L=0}$	0.62 ± 0.02	0.59 ± 0.03	51.64 ± 0.89
$K_1(1270)^+ \to [(\rho-\omega)^0 K^+]_{L=0}$	1 (fixed)	0 (fixed)	48.33 ± 1.82
$K_1(1270)^+ \to [K^+\pi^-]_{L=0}\pi^+$	0.58 ± 0.03	−1.89 ± 0.04	5.35 ± 0.44
$K_1(1270)^+ \to [K^*(892)^0\pi^+]_{L=2}$	0.92 ± 0.05	−2.56 ± 0.04	2.06 ± 0.17
$K_1(1270)^+ \to [\rho(1450)^0 K^+]_{L=0}$	0.43 ± 0.07	−2.29 ± 0.11	1.12 ± 0.38
		Sum of fit fractions	108.49 ± 2.08
$K_1(1400)^+ \to [K^*(892)^0\pi^+]_{L=0}$	1 (fixed)	0 (fixed)	100

5.6.3 LASS lineshape

The K-matrix description of the $K\pi$ S-wave is tested against the alternative LASS parametrisation [120], which is often used to describe the lineshape of the $K^{*0}(1430)$ meson. It is defined as

$$\mathcal{T}(m, L=0) = \left(\sin(\delta_B(m))e^{i\delta_B(m)} + \sin(\delta_R(m))e^{i\delta_R(m)}e^{2i\delta_B(m)}\right)\frac{m}{q}, \tag{5.10}$$

where the resonant phase $\delta_R(m)$ is given by

$$\delta_R(m) = \tan^{-1}\left(\frac{m_0\Gamma(m,L)}{m_0^2 - m^2}\right) \tag{5.11}$$

and where the non-resonant phase $\delta_B(m)$ is given by

$$\delta_B(m) = \tan^{-1}\left(\frac{2aq}{2 + arq^2}\right). \tag{5.12}$$

The parameters

$$a = 2.07 \pm 0.1 \, \text{GeV}^{-1}c \tag{5.13}$$

$$r = 3.32 \pm 0.34 \, \text{GeV}^{-1}c \tag{5.14}$$

are taken from Ref. [120]. The χ^2 is significantly worse for this parametrisation ($9755/8123 = 1.20$), no systematic uncertainties are therefore assigned.

5.6.4 Fewer amplitudes

The D^0 model built in this analysis contains many amplitudes, it is therefore logical to test models with less amplitudes. One possibility could be to remove all amplitudes that have a fit fraction below 1%. One could think that these small amplitudes are useless and therefore a fit without them would be as valid as the nominal fit. A test has been performed by removing the nine D^0 amplitudes that are below 1% in Table 6.1. This fit is significantly worse, the $\chi^2/$ndf is $12769/8133 = 1.57$. This is not a viable solution.

Another possibility would be to stop the model building iterations sooner, by, for example, removing the five amplitudes that were added last. One could think that these amplitudes do not really contribute to the model. These five amplitudes are :

- $D^0 \rightarrow [a_0(980)^0 f_2(1270)^0]_{L=2}$

- $D^0 \rightarrow [K^*(1680)^0 \bar{K}^*(892)^0]_{L=2}$

- $D^0 \rightarrow [K^*(892)^0 K_2^*(1430)^0]_{L=1}$

- $D^0 \rightarrow [K^+K^-]_{L=0}[\pi^+\pi^-]_{L=0}$

- $K_1(1270)^+ \rightarrow [K^+\pi^-]_{L=0}\pi^+$

This fit resulted in a χ^2/ndf of $10166/8133 = 1.25$. It seems that these amplitudes are also important to the description of the data. No alternative models with less amplitudes seem to have a similar fit quality. No systematic are therefore assigned for such models.

5.6.5 More amplitudes

The other way to test the choice of the stopping criterion in the model building method is to stop adding amplitudes later. For example one could let the model building method add five more amplitudes to the model, with the exception that we need to make a choice between the a_0 and the f_0. Since the χ^2/ndf is better with the f_0, we will keep this amplitude. The five additional amplitudes are :

- $D^0 \rightarrow [K_2^*(1430)^0 \overline{K}_2^*(1430)^0]_{L=0}$

- $K_1(1400)^+ \rightarrow [\rho(1450)^0 K^+]_{L=2}$

- $D^0 \rightarrow [\overline{K}^*(892)^0 K_2^*(1430)^0]_{L=2}$

- $D^0 \rightarrow [\phi(1020)^0 f_2(1270)^0]_{L=2}$

- $D^0 \rightarrow [f_2(1270)^0 f_2(1270)^0]_{L=0}$

The model is shown in Table 5.2. The χ^2/ndf is slightly better, which is expected since we introduce more degrees of freedom to fit the data. However the improvement is not very big for an addition of five amplitudes. Therefore the stopping criterion is not modified and this model is used to assign the systematic uncertainty.

5.6.6 $\rho(1450)^0$

The resonance $\rho(1450)^0$ was added in the list of possible amplitudes only with a decay to two pions. A recent paper by BaBar [121] has shown that there is a significant contribution from $\rho(1450)^0 \rightarrow K^+ K^-$. In order to test the effect of this contribution on $D^0 \rightarrow K^+ K^- \pi^+ \pi^-$, the model building method has been rerun with 11 additional allowed amplitudes containing $\rho(1450)^0 \rightarrow K^+ K^-$. The same amplitudes have been selected in the exact same order, with the addition of one amplitude, $D^0 \rightarrow \rho(1450)^0 \rho(770)^0$ in D-wave. The resulting model is shown in Table 5.3. Since this amplitude represents a very small contribution and the remaining model is unchanged, this is treated as a systematic uncertainty.

Table 5.2 – Modulus and phase of the fit parameters along with the fit fractions of the amplitudes included in the alternative model using five additional amplitudes.

Amplitude	$|c_k|$	$\arg(c_k)$ [rad]	Fit fraction [%]
$D^0 \to [\phi(1020)(\rho-\omega)^0]_{L=0}$	1 (fixed)	0 (fixed)	24.12 ± 0.40
$D^0 \to K_1(1400)^+ K^-$	0.65 ± 0.01	0.99 ± 0.02	19.34 ± 0.47
$D^0 \to K_1(1270)^+ K^-$	0.45 ± 0.01	2.07 ± 0.02	19.28 ± 0.39
$D^0 \to [K^-\pi^+]_{L=0}[K^+\pi^-]_{L=0}$	0.29 ± 0.00	−0.57 ± 0.02	19.20 ± 0.36
$D^0 \to [K^*(892)^0\bar{K}^*(892)^0]_{L=0}$	0.28 ± 0.00	−0.29 ± 0.02	9.36 ± 0.21
$D^0 \to K^*(1680)^0[K^-\pi^+]_{L=0}$	2.18 ± 0.03	0.45 ± 0.02	6.22 ± 0.15
$D^0 \to [K^*(892)^0\bar{K}^*(892)^0]_{L=1}$	0.26 ± 0.00	1.21 ± 0.02	4.81 ± 0.16
$D^0 \to K_1(1270)^- K^+$	0.22 ± 0.01	2.14 ± 0.03	4.45 ± 0.18
$D^0 \to [K^+K^-]_{L=0}[\pi^+\pi^-]_{L=0}$	0.14 ± 0.00	−2.39 ± 0.03	4.18 ± 0.21
$D^0 \to K_1(1400)^- K^+$	0.25 ± 0.01	0.02 ± 0.04	2.94 ± 0.19
$D^0 \to [K^*(1680)^0\bar{K}^*(892)^0]_{L=0}$	0.82 ± 0.02	3.00 ± 0.03	2.79 ± 0.15
$D^0 \to [\bar{K}^*(1680)^0 K^*(892)^0]_{L=1}$	0.99 ± 0.02	−2.77 ± 0.02	2.64 ± 0.11
$D^0 \to \bar{K}^*(1680)^0[K^+\pi^-]_{L=0}$	1.32 ± 0.03	1.12 ± 0.02	2.44 ± 0.09
$D^0 \to [\phi(1020)(\rho-\omega)^0]_{L=2}$	1.29 ± 0.03	0.56 ± 0.02	2.25 ± 0.08
$D^0 \to [K^*(892)^0\bar{K}^*(892)^0]_{L=2}$	0.67 ± 0.02	2.83 ± 0.03	1.73 ± 0.09
$D^0 \to \phi(1020)[\pi^+\pi^-]_{L=0}$	0.05 ± 0.00	−1.70 ± 0.04	1.43 ± 0.09
$D^0 \to [K^*(1680)^0\bar{K}^*(892)^0]_{L=1}$	0.69 ± 0.02	0.15 ± 0.03	1.30 ± 0.08
$D^0 \to [\phi(1020)\rho(1450)^0]_{L=1}$	0.76 ± 0.03	1.21 ± 0.04	0.98 ± 0.09
$D^0 \to a_0(980)^0 f_2(1270)^0$	1.52 ± 0.06	0.33 ± 0.04	0.70 ± 0.05
$D^0 \to a_1(1260)^+\pi^-$	0.20 ± 0.01	−2.86 ± 0.07	0.50 ± 0.06
$D^0 \to a_1(1260)^-\pi^+$	0.19 ± 0.01	0.22 ± 0.06	0.45 ± 0.06
$D^0 \to [K^*(1680)^0\bar{K}^*(892)^0]_{L=2}$	1.41 ± 0.09	−2.45 ± 0.07	0.45 ± 0.06
$D^0 \to [\phi(1020)(\rho-\omega)^0]_{L=1}$	0.16 ± 0.01	0.25 ± 0.07	0.44 ± 0.05
$D^0 \to [K^+K^-]_{L=0}(\rho-\omega)^0$	0.21 ± 0.02	3.02 ± 0.08	0.30 ± 0.04
$D^0 \to [\phi(1020)f_2(1270)^0]_{L=1}$	1.41 ± 0.09	1.70 ± 0.06	0.19 ± 0.03
$D^0 \to [K^*(892)^0\bar{K}_2^*(1430)^0]_{L=1}$	1.44 ± 0.09	2.10 ± 0.07	0.15 ± 0.02
$D^0 \to [K_2^*(1430)^0\bar{K}_2^*(1430)^0]_{L=0}$	6.27 ± 0.57	1.66 ± 0.10	0.11 ± 0.02
$D^0 \to [f_2(1270)^0 f_2(1270)^0]_{L=0}$	0.78 ± 0.08	−1.55 ± 0.11	0.08 ± 0.02
$D^0 \to [\bar{K}^*(892)^0 K_2^*(1430)^0]_{L=2}$	0.91 ± 0.11	−0.44 ± 0.10	0.05 ± 0.01
$D^0 \to [\phi(1020)f_2(1270)^0]_{L=2}$	0.68 ± 0.08	−1.14 ± 0.10	0.04 ± 0.01
		Sum of fit fractions	132.92 ± 0.98
		χ^2/ndf	9092/8113 = 1.12

$a_1(1260)^+ \to [\phi(1020)\pi^+]_{L=0}$	1 (fixed)	0 (fixed)	100

$K_1(1270)^+ \to [K^*(892)^0\pi^+]_{L=0}$	0.65 ± 0.02	0.56 ± 0.03	53.37 ± 0.89
$K_1(1270)^+ \to [(\rho-\omega)^0 K^+]_{L=0}$	1 (fixed)	0 (fixed)	45.45 ± 1.88
$K_1(1270)^+ \to [K^+\pi^-]_{L=0}\pi^+$	0.71 ± 0.03	−1.83 ± 0.04	7.60 ± 0.56
$K_1(1270)^+ \to [K^*(892)^0\pi^+]_{L=2}$	0.97 ± 0.05	−2.65 ± 0.04	2.15 ± 0.17
$K_1(1270)^+ \to [\rho(1450)^0 K^+]_{L=0}$	0.47 ± 0.07	−1.79 ± 0.13	1.31 ± 0.42
		Sum of fit fractions	109.88 ± 2.19

$K_1(1400)^+ \to [K^*(892)^0\pi^+]_{L=0}$	1 (fixed)	0 (fixed)	102.92 ± 0.27
$K_1(1400)^+ \to [\rho(1450)^0 K^+]_{L=2}$	1.82 ± 0.16	2.76 ± 0.09	0.84 ± 0.15
		Sum of fit fractions	103.77 ± 0.40

Table 5.3 – Modulus and phase of the fit parameters along with the fit fractions of the amplitudes of the alternative model that includes the amplitude $D^0 \to \rho(1450)^0 \rho(770)^0$ in D-wave.

Amplitude	$|c_k|$	$\arg(c_k)$ [rad]	Fit fraction [%]
$D^0 \to [\phi(1020)(\rho - \omega)^0]_{L=0}$	1 (fixed)	0 (fixed)	23.83 $\pm$ 0.16
$D^0 \to K_1(1270)^+ K^-$	0.46 $\pm$ 0.01	2.02 $\pm$ 0.02	19.26 $\pm$ 0.30
$D^0 \to K_1(1400)^+ K^-$	0.64 $\pm$ 0.00	1.02 $\pm$ 0.01	19.23 $\pm$ 0.31
$D^0 \to [K^-\pi^+]_{L=0}[K^+\pi^-]_{L=0}$	0.28 $\pm$ 0.00	-0.58 $\pm$ 0.01	17.68 $\pm$ 0.26
$D^0 \to [K^*(892)^0 \bar{K}^*(892)^0]_{L=0}$	0.28 $\pm$ 0.00	-0.27 $\pm$ 0.01	9.32 $\pm$ 0.13
$D^0 \to K^*(1680)^0 [K^-\pi^+]_{L=0}$	2.28 $\pm$ 0.02	0.44 $\pm$ 0.01	6.73 $\pm$ 0.13
$D^0 \to [K^*(892)^0 \bar{K}^*(892)^0]_{L=1}$	0.27 $\pm$ 0.00	1.22 $\pm$ 0.01	4.89 $\pm$ 0.08
$D^0 \to K_1(1270)^- K^+$	0.22 $\pm$ 0.00	2.13 $\pm$ 0.02	4.34 $\pm$ 0.15
$D^0 \to [K^*(1680)^0 \bar{K}^*(892)^0]_{L=0}$	0.86 $\pm$ 0.01	2.99 $\pm$ 0.02	3.05 $\pm$ 0.09
$D^0 \to [K^+ K^-]_{L=0}[\pi^+\pi^-]_{L=0}$	0.12 $\pm$ 0.00	-2.42 $\pm$ 0.03	3.01 $\pm$ 0.11
$D^0 \to K_1(1400)^- K^+$	0.24 $\pm$ 0.01	0.10 $\pm$ 0.02	2.76 $\pm$ 0.16
$D^0 \to [\bar{K}^*(1680)^0 K^*(892)^0]_{L=1}$	1.00 $\pm$ 0.02	-2.75 $\pm$ 0.01	2.65 $\pm$ 0.08
$D^0 \to \bar{K}^*(1680)^0 [K^+\pi^-]_{L=0}$	1.34 $\pm$ 0.02	1.05 $\pm$ 0.02	2.50 $\pm$ 0.08
$D^0 \to [\phi(1020)(\rho - \omega)^0]_{L=2}$	1.25 $\pm$ 0.02	0.49 $\pm$ 0.02	2.08 $\pm$ 0.06
$D^0 \to [K^*(892)^0 \bar{K}^*(892)^0]_{L=2}$	0.67 $\pm$ 0.01	2.79 $\pm$ 0.02	1.70 $\pm$ 0.06
$D^0 \to \phi(1020)[\pi^+\pi^-]_{L=0}$	0.05 $\pm$ 0.00	-1.72 $\pm$ 0.03	1.52 $\pm$ 0.05
$D^0 \to [K^*(1680)^0 \bar{K}^*(892)^0]_{L=1}$	0.73 $\pm$ 0.02	0.15 $\pm$ 0.02	1.43 $\pm$ 0.06
$D^0 \to [\phi(1020)\rho(1450)^0]_{L=1}$	0.77 $\pm$ 0.01	1.18 $\pm$ 0.02	1.01 $\pm$ 0.04
$D^0 \to a_0(980)^0 f_2(1270)^0$	1.49 $\pm$ 0.05	0.30 $\pm$ 0.03	0.67 $\pm$ 0.04
$D^0 \to [K^*(1680)^0 \bar{K}^*(892)^0]_{L=2}$	1.49 $\pm$ 0.07	-2.40 $\pm$ 0.05	0.49 $\pm$ 0.04
$D^0 \to a_1(1260)^+ \pi^-$	0.19 $\pm$ 0.01	-2.79 $\pm$ 0.03	0.45 $\pm$ 0.03
$D^0 \to a_1(1260)^- \pi^+$	0.18 $\pm$ 0.01	0.17 $\pm$ 0.03	0.43 $\pm$ 0.03
$D^0 \to [\phi(1020)(\rho - \omega)^0]_{L=1}$	0.16 $\pm$ 0.00	0.28 $\pm$ 0.03	0.42 $\pm$ 0.02
$D^0 \to [K^+ K^-]_{L=0}(\rho - \omega)^0$	0.19 $\pm$ 0.01	3.03 $\pm$ 0.06	0.26 $\pm$ 0.03
$D^0 \to [\rho(1450)^0 (\rho - \omega)^0]_{L=2}$	-0.66 $\pm$ 0.07	0.33 $\pm$ 0.12	0.22 $\pm$ 0.03
$D^0 \to [\phi(1020) f_2(1270)^0]_{L=1}$	1.40 $\pm$ 0.07	1.71 $\pm$ 0.04	0.19 $\pm$ 0.02
$D^0 \to [K^*(892)^0 \bar{K}_2^*(1430)^0]_{L=1}$	1.50 $\pm$ 0.08	2.02 $\pm$ 0.06	0.16 $\pm$ 0.02
		Sum of fit fractions	130.25 $\pm$ 0.65
		χ^2/ndf	9099/8119 = 1.12
$a_1(1260)^+ \to [\phi(1020)\pi^+]_{L=0}$	1 (fixed)	0 (fixed)	100
$K_1(1270)^+ \to [K^*(892)^0 \pi^+]_{L=0}$	0.63 $\pm$ 0.01	0.61 $\pm$ 0.02	50.99 $\pm$ 0.66
$K_1(1270)^+ \to [(\rho - \omega)^0 K^+]_{L=0}$	1 (fixed)	0 (fixed)	45.77 $\pm$ 1.42
$K_1(1270)^+ \to [K^+\pi^-]_{L=0}\pi^+$	0.58 $\pm$ 0.02	-1.70 $\pm$ 0.04	5.08 $\pm$ 0.30
$K_1(1270)^+ \to [K^*(892)^0 \pi^+]_{L=2}$	0.96 $\pm$ 0.04	-2.55 $\pm$ 0.03	2.12 $\pm$ 0.14
$K_1(1270)^+ \to [\rho(1450)^0 K^+]_{L=0}$	0.23 $\pm$ 0.06	-2.54 $\pm$ 0.18	0.31 $\pm$ 0.18
		Sum of fit fractions	104.27 $\pm$ 1.54
$K_1(1400)^+ \to [K^*(892)^0 \pi^+]_{L=0}$	1 (fixed)	0 (fixed)	100

Table 5.4 – Statistical and systematic uncertainties (in %) on the fit fractions. Values smaller than 0.0005% are displayed as "0.000". The sources of systematic uncertainty are described in the text in the same order as shown in this table.

Amplitude	Stat.	Total Syst.	Sel. Eff.	Alt. Bkg 1	Alt. Bkg 2	RBW $\rho(770)^0$	Alt. S-wave	Mass & width	Res. radius	Sig bias	Bkg bias	Mistag bias	Det. As. bias	Alt. Models
$D^0 \to [\phi(1020)(\rho-\omega)^0]_{L=0}$	0.382	0.495	0.183	0.054	0.046	0.226	0.095	0.110	0.075	0.271	0.122	0.020	0.018	0.200
$D^0 \to K_1(1400)^+ K^-$	0.600	1.463	0.137	0.053	0.316	0.033	0.161	1.236	0.286	0.048	0.102	0.062	0.031	0.603
$D^0 \to [K^-\pi^+]_{L=0}[K^+\pi^-]_{L=0}$	0.347	0.935	0.034	0.065	0.459	0.040	0.246	0.193	0.051	0.051	0.235	0.061	0.018	0.703
$D^0 \to K_1(1270)^+ K^-$	0.521	0.982	0.031	0.045	0.085	0.016	0.139	0.734	0.116	0.113	0.151	0.083	0.030	0.582
$D^0 \to [K^*(892)^0 \bar{K}^*(892)^0]_{L=0}$	0.207	0.277	0.023	0.027	0.037	0.001	0.127	0.087	0.047	0.064	0.046	0.011	0.013	0.205
$D^0 \to K^*(1680)^0[K^-\pi^+]_{L=0}$	0.148	0.368	0.010	0.031	0.023	0.014	0.217	0.069	0.050	0.021	0.072	0.007	0.007	0.271
$D^0 \to [K^*(892)^0 \bar{K}^*(892)^0]_{L=1}$	0.155	0.181	0.009	0.015	0.063	0.001	0.043	0.064	0.058	0.028	0.076	0.009	0.008	0.112
$D^0 \to K_1(1270)^- K^+$	0.180	0.405	0.001	0.021	0.089	0.016	0.112	0.147	0.023	0.018	0.061	0.065	0.011	0.335
$D^0 \to [K^+ K^-]_{L=0}[\pi^+\pi^-]_{L=0}$	0.168	0.723	0.002	0.036	0.034	0.031	0.293	0.074	0.038	0.007	0.047	0.021	0.008	0.651
$D^0 \to K_1(1400)^- K^+$	0.192	0.394	0.074	0.029	0.029	0.003	0.025	0.158	0.018	0.011	0.031	0.056	0.009	0.343
$D^0 \to [K^*(1680)^0 \bar{K}^*(892)^0]_{L=0}$	0.147	0.189	0.096	0.037	0.020	0.004	0.109	0.059	0.025	0.011	0.014	0.008	0.008	0.092
$D^0 \to [\bar{K}^*(1680)^0 K^*(892)^0]_{L=1}$	0.105	0.093	0.016	0.012	0.026	0.001	0.032	0.035	0.046	0.013	0.021	0.006	0.009	0.050
$D^0 \to \bar{K}^*(1680)^0[K^+\pi^-]_{L=0}$	0.091	0.275	0.004	0.018	0.072	0.000	0.174	0.042	0.014	0.005	0.056	0.015	0.007	0.185
$D^0 \to [\phi(1020)(\rho-\omega)^0]_{L=2}$	0.076	0.077	0.023	0.008	0.013	0.062	0.005	0.013	0.019	0.006	0.014	0.005	0.007	0.020
$D^0 \to [K^*(892)^0 \bar{K}^*(892)^0]_{L=2}$	0.095	0.099	0.030	0.010	0.017	0.014	0.069	0.053	0.016	0.015	0.013	0.005	0.005	0.013
$D^0 \to \phi(1020)[\pi^+\pi^-]_{L=0}$	0.090	0.325	0.005	0.009	0.002	0.010	0.313	0.022	0.014	0.012	0.022	0.005	0.005	0.081
$D^0 \to [K^*(1680)^0 \bar{K}^*(892)^0]_{L=1}$	0.080	0.096	0.000	0.008	0.043	0.003	0.022	0.013	0.021	0.009	0.029	0.014	0.004	0.071
$D^0 \to [\phi(1020)\rho(1450)]_{L=1}$	0.089	0.045	0.007	0.007	0.007	0.020	0.023	0.013	0.017	0.005	0.017	0.006	0.006	0.012
$D^0 \to a_0(980)^0 f_2(1270)^0$	0.052	0.083	0.005	0.008	0.026	0.002	0.048	0.027	0.010	0.002	0.015	0.013	0.004	0.050
$D^0 \to a_1(1260)^+\pi^-$	0.055	0.220	0.002	0.005	0.003	0.066	0.206	0.016	0.019	0.004	0.007	0.005	0.004	0.028
$D^0 \to a_1(1260)^-\pi^+$	0.063	0.156	0.002	0.008	0.000	0.051	0.139	0.018	0.013	0.003	0.021	0.007	0.003	0.039
$D^0 \to [\phi(1020)(\rho-\omega)^0]_{L=1}$	0.049	0.028	0.001	0.003	0.004	0.014	0.011	0.009	0.014	0.002	0.006	0.009	0.003	0.007
$D^0 \to [K^*(1680)^0 \bar{K}^*(892)^0]_{L=2}$	0.048	0.059	0.010	0.006	0.030	0.003	0.009	0.018	0.008	0.002	0.004	0.003	0.003	0.044
$D^0 \to [K^+ K^-]_{L=0}(\rho-\omega)^0$	0.036	0.054	0.003	0.007	0.022	0.000	0.039	0.015	0.004	0.004	0.010	0.003	0.002	0.023
$D^0 \to [\phi(1020) f_2(1270)^0]_{L=1}$	0.024	0.075	0.002	0.003	0.008	0.002	0.074	0.003	0.005	0.002	0.001	0.002	0.002	0.006
$D^0 \to [K^*(892)^0 \bar{K}_2^*(1430)^0]_{L=1}$	0.020	0.024	0.003	0.002	0.005	0.001	0.002	0.017	0.009	0.001	0.005	0.001	0.001	0.012
$K_1(1270)^+ \to [K^*(892)^0\pi^+]_{L=0}$	1.058	3.213	0.050	0.100	0.000	0.022	0.443	1.917	0.559	0.129	0.299	0.054	0.060	2.453
$K_1(1270)^+ \to [(\rho-\omega)^0 K^+]_{L=0}$	1.993	4.352	0.300	0.253	1.152	1.780	2.301	2.110	0.961	0.145	0.758	0.095	0.099	1.733
$K_1(1270)^+ \to [K^+\pi^-]_{L=0}\pi^+$	0.484	1.660	0.015	0.073	0.041	0.045	0.188	0.303	0.148	0.078	0.024	0.029	0.070	1.608
$K_1(1270)^+ \to [K^*(892)^0\pi^+]_{L=2}$	0.169	0.195	0.035	0.015	0.037	0.000	0.041	0.139	0.026	0.006	0.024	0.009	0.008	0.113
$K_1(1270)^+ \to [\rho(1450)^0 K^+]_{L=0}$	0.472	1.041	0.138	0.072	0.365	0.244	0.446	0.335	0.199	0.042	0.169	0.026	0.025	0.696
$D^0 \to [\phi(1020)\rho(770)^0]_{L=0}$	0.463	0.275	0.024	0.019	0.086	0.160	0.023	0.159	0.059	0.036	0.043	0.024	0.026	0.090
$D^0 \to [\phi(1020)\omega(782)]_{L=0}$	0.106	0.041	0.002	0.005	0.008	0.021	0.001	0.015	0.014	0.020	0.006	0.007	0.006	0.013
$D^0 \to [\phi(1020)\rho(770)^0]_{L=1}$	4.107	1.696	0.333	0.123	0.436	0.728	0.746	0.367	0.728	0.306	0.450	0.326	0.456	0.444
$D^0 \to [\phi(1020)\omega(782)]_{L=1}$	1.577	0.515	0.053	0.049	0.104	0.138	0.166	0.116	0.184	0.112	0.179	0.131	0.240	0.190
$D^0 \to [\phi(1020)\rho(770)^0]_{L=2}$	1.690	0.778	0.038	0.068	0.076	0.424	0.310	0.255	0.162	0.060	0.093	0.124	0.121	0.428
$D^0 \to [\phi(1020)\omega(782)]_{L=2}$	0.270	0.116	0.005	0.010	0.015	0.038	0.019	0.024	0.020	0.042	0.018	0.018	0.025	0.086
$D^0 \to [K^+ K^-]_{L=0}\rho(770)^0$	5.895	3.492	0.054	0.530	0.665	0.238	1.471	1.561	0.681	0.368	0.892	0.310	0.317	2.285
$D^0 \to [K^+ K^-]_{L=0}\omega(782)$	3.259	3.642	0.799	0.272	0.713	0.056	1.000	0.736	0.201	0.261	0.416	0.202	0.174	3.184
$K_1(1270)^+ \to [\rho(770)^0 K^+]_{L=0}$	1.981	3.806	0.189	0.229	0.729	0.630	0.216	1.007	0.586	0.065	0.152	0.574	0.106	3.420
$K_1(1270)^+ \to [\omega(782) K^+]_{L=0}$	0.220	0.191	0.015	0.015	0.040	0.082	0.149	0.035	0.035	0.011	0.047	0.011	0.011	0.023

Table 5.5 – Statistical and systematic uncertainties on the fit parameters shown for all floating components. Values smaller than 0.0005 are displayed as "0.000". The sources of systematic uncertainty are described in the text in the same order as shown in this table. For each amplitude, the first value quoted is the modulus and the second is the phase of the complex fit parameter.

Amplitude	Stat.	Total Syst.	Sel. Eff.	Alt. Bkg 1	Alt. Bkg 2	RBW $\rho(770)^0$	Alt. S-wave	Mass & width	Res. radius	Sig bias	Bkg bias	Mistag bias	Det. As. bias	Alt. Models
$D^0 \to K_1(1400)^+K^-$	0.011	0.031	0.005	0.001	0.006	0.002	0.002	0.018	0.022	0.001	0.002	0.001	0.001	0.007
	0.022	0.053	0.007	0.002	0.001	0.014	0.011	0.047	0.007	0.001	0.004	0.001	0.001	0.014
$D^0 \to [K^-\pi^+]_{L=0}[K^+\pi^-]_{L=0}$	0.004	0.008	0.001	0.001	0.003	0.001	0.001	0.002	0.005	0.000	0.002	0.000	0.000	0.004
	0.015	0.104	0.003	0.002	0.007	0.014	0.102	0.008	0.006	0.001	0.001	0.002	0.001	0.007
$D^0 \to K_1(1270)^+K^-$	0.011	0.017	0.000	0.001	0.006	0.005	0.012	0.006	0.004	0.000	0.002	0.001	0.000	0.006
	0.027	0.050	0.006	0.003	0.006	0.004	0.011	0.022	0.007	0.001	0.005	0.004	0.001	0.041
$D^0 \to [K^*(892)^0\bar{K}^*(892)^0]_{L=0}$	0.004	0.018	0.001	0.001	0.001	0.001	0.002	0.002	0.017	0.000	0.001	0.000	0.000	0.004
	0.016	0.025	0.000	0.002	0.003	0.014	0.012	0.014	0.008	0.001	0.003	0.001	0.001	0.003
$D^0 \to K^*(1680)^0[K^-\pi^+]_{L=0}$	0.036	0.624	0.011	0.006	0.007	0.003	0.042	0.618	0.067	0.001	0.015	0.002	0.002	0.033
	0.016	0.030	0.000	0.002	0.006	0.013	0.018	0.016	0.007	0.001	0.001	0.003	0.001	0.004
$D^0 \to [K^*(892)^0\bar{K}^*(892)^0]_{L=1}$	0.005	0.017	0.001	0.001	0.001	0.001	0.001	0.002	0.016	0.000	0.002	0.000	0.000	0.002
	0.021	0.027	0.000	0.002	0.001	0.014	0.006	0.014	0.012	0.001	0.004	0.002	0.001	0.011
$D^0 \to K_1(1270)^-K^+$	0.006	0.011	0.000	0.001	0.000	0.002	0.004	0.004	0.002	0.000	0.000	0.002	0.000	0.009
	0.029	0.075	0.008	0.003	0.010	0.004	0.003	0.016	0.007	0.002	0.006	0.002	0.001	0.071
$D^0 \to [K^+K^-]_{L=0}[\pi^+\pi^-]_{L=0}$	0.003	0.018	0.001	0.001	0.000	0.001	0.013	0.001	0.002	0.000	0.001	0.000	0.000	0.012
	0.030	0.163	0.005	0.005	0.013	0.014	0.158	0.014	0.008	0.002	0.011	0.003	0.001	0.028
$D^0 \to K_1(1400)^-K^+$	0.008	0.018	0.002	0.001	0.002	0.000	0.001	0.005	0.008	0.000	0.001	0.002	0.000	0.015
	0.042	0.088	0.019	0.008	0.000	0.016	0.012	0.041	0.013	0.002	0.018	0.005	0.002	0.068
$D^0 \to [K^*(1680)^0\bar{K}^*(892)^0]_{L=0}$	0.023	0.218	0.017	0.006	0.002	0.001	0.018	0.214	0.034	0.001	0.002	0.001	0.001	0.009
	0.029	0.047	0.004	0.005	0.000	0.013	0.031	0.020	0.006	0.001	0.005	0.004	0.002	0.024
$D^0 \to [\bar{K}^*(1680)^0K^*(892)^0]_{L=1}$	0.022	0.276	0.007	0.002	0.006	0.003	0.004	0.272	0.043	0.001	0.005	0.001	0.002	0.014
	0.022	0.029	0.001	0.002	0.011	0.014	0.009	0.013	0.006	0.001	0.006	0.002	0.001	0.013
$D^0 \to \bar{K}^*(1680)^0[K^+\pi^-]_{L=0}$	0.029	0.373	0.004	0.005	0.018	0.003	0.051	0.361	0.041	0.001	0.018	0.004	0.002	0.057
	0.024	0.031	0.006	0.004	0.008	0.016	0.009	0.015	0.008	0.001	0.002	0.001	0.001	0.014
$D^0 \to [\phi(1020)(\rho-\omega)^0]_{L=2}$	0.031	0.018	0.002	0.003	0.005	0.010	0.002	0.005	0.008	0.001	0.002	0.002	0.002	0.009
	0.023	0.019	0.001	0.003	0.002	0.011	0.011	0.005	0.003	0.001	0.005	0.001	0.001	0.006
$D^0 \to [K^*(892)^0\bar{K}^*(892)^0]_{L=2}$	0.018	0.043	0.003	0.002	0.002	0.001	0.012	0.010	0.039	0.001	0.003	0.001	0.001	0.003
	0.027	0.040	0.002	0.003	0.010	0.013	0.010	0.018	0.011	0.001	0.003	0.001	0.001	0.028
$D^0 \to \phi(1020)[\pi^+\pi^-]_{L=0}$	0.001	0.004	0.000	0.000	0.000	0.000	0.004	0.000	0.001	0.000	0.000	0.000	0.000	0.001
	0.040	0.368	0.002	0.005	0.008	0.006	0.368	0.011	0.006	0.002	0.005	0.002	0.004	0.019
$D^0 \to [K^*(1680)^0\bar{K}^*(892)^0]_{L=1}$	0.021	0.203	0.003	0.002	0.012	0.001	0.004	0.201	0.027	0.001	0.007	0.004	0.001	0.015
	0.031	0.040	0.002	0.003	0.007	0.014	0.001	0.022	0.015	0.001	0.009	0.001	0.002	0.023
$D^0 \to [\phi(1020)\rho(1450)^0]_{L=1}$	0.035	0.068	0.000	0.003	0.004	0.006	0.008	0.062	0.025	0.002	0.005	0.002	0.002	0.007
	0.038	0.038	0.004	0.002	0.003	0.027	0.015	0.014	0.013	0.001	0.005	0.002	0.002	0.006
$D^0 \to a_0(980)^0 f_2(1270)^0$	0.058	0.189	0.001	0.009	0.026	0.005	0.049	0.169	0.035	0.003	0.014	0.014	0.005	0.047
	0.038	0.190	0.008	0.006	0.021	0.015	0.063	0.176	0.015	0.004	0.007	0.003	0.003	0.019
$D^0 \to a_1(1260)^+\pi^-$	0.011	0.042	0.000	0.001	0.000	0.014	0.038	0.005	0.008	0.000	0.002	0.001	0.001	0.006
	0.067	0.380	0.009	0.008	0.007	0.011	0.375	0.033	0.011	0.003	0.005	0.003	0.003	0.047
$D^0 \to a_1(1260)^-\pi^+$	0.014	0.031	0.000	0.002	0.000	0.011	0.026	0.006	0.005	0.000	0.004	0.001	0.001	0.008
	0.060	0.431	0.018	0.008	0.013	0.045	0.426	0.031	0.015	0.003	0.015	0.006	0.004	0.023
$D^0 \to [\phi(1020)(\rho-\omega)^0]_{L=1}$	0.011	0.005	0.000	0.001	0.001	0.002	0.003	0.002	0.002	0.001	0.001	0.002	0.001	0.001
	0.071	0.027	0.011	0.003	0.007	0.002	0.006	0.012	0.016	0.004	0.004	0.007	0.007	0.004
$D^0 \to [K^*(1680)^0\bar{K}^*(892)^0]_{L=2}$	0.089	0.354	0.024	0.012	0.059	0.009	0.020	0.335	0.039	0.004	0.008	0.005	0.005	0.080
	0.084	0.150	0.022	0.020	0.013	0.013	0.046	0.028	0.007	0.007	0.005	0.006	0.005	0.135
$D^0 \to [K^+K^-]_{L=0}(\rho-\omega)^0$	0.015	0.035	0.002	0.003	0.008	0.003	0.033	0.006	0.002	0.001	0.002	0.001	0.001	0.007
	0.084	0.292	0.029	0.015	0.052	0.010	0.165	0.036	0.016	0.007	0.045	0.014	0.004	0.225
$D^0 \to [\phi(1020)f_2(1270)^0]_{L=1}$	0.095	0.257	0.003	0.010	0.026	0.005	0.251	0.017	0.032	0.003	0.005	0.006	0.006	0.029
	0.061	0.373	0.007	0.007	0.011	0.012	0.371	0.012	0.014	0.002	0.017	0.004	0.004	0.004
$D^0 \to [K^*(892)^0\bar{K}_2^*(1430)^0]_{L=1}$	0.086	0.131	0.019	0.011	0.020	0.001	0.005	0.089	0.074	0.006	0.023	0.007	0.004	0.046
	0.067	0.087	0.023	0.008	0.012	0.013	0.043	0.054	0.013	0.003	0.010	0.007	0.005	0.039
$K_1(1270)^+ \to [K^*(892)^0\pi^+]_{L=0}$	0.016	0.040	0.002	0.002	0.008	0.005	0.014	0.024	0.023	0.001	0.007	0.001	0.001	0.011
	0.031	0.052	0.001	0.003	0.009	0.020	0.003	0.043	0.013	0.001	0.005	0.004	0.002	0.015
$K_1(1270)^+ \to [K^+\pi^-]_{L=0}\pi^+$	0.027	0.094	0.003	0.004	0.009	0.003	0.027	0.014	0.014	0.003	0.006	0.001	0.003	0.087
	0.042	0.083	0.015	0.008	0.042	0.019	0.013	0.023	0.011	0.001	0.014	0.003	0.002	0.058
$K_1(1270)^+ \to [K^*(892)^0\pi^+]_{L=2}$	0.044	0.060	0.011	0.004	0.019	0.007	0.016	0.030	0.037	0.002	0.003	0.002	0.002	0.022
	0.041	0.045	0.000	0.004	0.005	0.012	0.017	0.017	0.009	0.002	0.004	0.002	0.003	0.034
$K_1(1270)^+ \to [\rho(1450)^0K^+]_{L=0}$	0.068	0.187	0.023	0.012	0.056	0.038	0.080	0.076	0.023	0.005	0.026	0.005	0.004	0.128
	0.100	0.445	0.051	0.019	0.007	0.104	0.175	0.154	0.051	0.010	0.027	0.006	0.005	0.356
$D^0 \to [\phi(1020)\omega(782)]_{L=0}$	0.004	0.003	0.000	0.000	0.000	0.002	0.000	0.001	0.002	0.000	0.000	0.000	0.000	0.001
	0.042	0.036	0.002	0.002	0.007	0.025	0.003	0.020	0.011	0.003	0.003	0.002	0.002	0.007
$D^0 \to [\phi(1020)\omega(782)]_{L=1}$	0.052	0.018	0.002	0.002	0.004	0.003	0.006	0.004	0.009	0.006	0.005	0.004	0.007	0.006
	0.194	0.069	0.017	0.005	0.016	0.030	0.029	0.030	0.026	0.011	0.011	0.011	0.013	0.019
$D^0 \to [\phi(1020)\omega(782)]_{L=2}$	0.032	0.014	0.001	0.001	0.002	0.008	0.002	0.003	0.004	0.005	0.002	0.002	0.002	0.007
	0.167	0.059	0.002	0.007	0.001	0.037	0.029	0.021	0.010	0.006	0.009	0.014	0.010	0.019
$D^0 \to [K^+K^-]_{L=0}\omega(782)$	0.098	0.098	0.020	0.008	0.016	0.008	0.013	0.021	0.013	0.003	0.005	0.006	0.005	0.089
	0.186	0.149	0.033	0.017	0.050	0.011	0.017	0.056	0.021	0.017	0.042	0.013	0.009	0.110
$K_1(1270)^+ \to [\omega(782)K^+]_{L=0}$	0.012	0.011	0.001	0.001	0.002	0.003	0.008	0.003	0.005	0.001	0.002	0.001	0.001	0.002
	0.074	0.057	0.015	0.004	0.001	0.037	0.022	0.023	0.019	0.003	0.004	0.005	0.004	0.013

5.7 Systematic on *CP* violation measurement

It is not obvious to know if any systematic effect cancels out for the *CP* violation fit. Therefore, all the systematic uncertainties mentioned previously are also studied for this measurement. The exact same procedures are used as for the evaluation of the systematic uncertainties for the nominal fit. The size of the systematic uncertainties on the parameters $\overline{|c_k|}$ and $\overline{\arg(c_k)}$ are similar to the fit parameters of the nominal fit $|c_k|$ and $\arg(c_k)$ and are therefore not shown here. Table 5.6 shows the systematic uncertainties of the *CP* asymmetry $A_{\mathscr{F}_k}$, whereas Table 5.7 shows the systematic uncertainties on the modulus asymmetry $A_{|c_k|}$ and phase difference $\Delta\arg(c_k)$.

Table 5.6 – Statistical and systematic uncertainties (in %) on $A_{\mathscr{F}_k}$. Values smaller than 0.0005% are displayed as "0.000". The sources of systematic uncertainty are described in the text in the same order as shown in this table.

Amplitude	Stat.	Total Syst.	Sel. Eff.	Alt. Bkg 1	Alt. Bkg 2	RBW $\rho(770)^0$	Alt. S-wave	Mass & width	Res. radius	Sig bias	Bkg bias	Mistag bias	Det. As. bias	Alt. Models
$D^0 \to [\phi(1020)(\rho-\omega)^0]_{L=0}$	1.496	0.193	0.008	0.027	0.032	0.034	0.102	0.028	0.029	0.046	0.048	0.071	0.045	0.103
$D^0 \to K_1(1400)^+ K^-$	2.087	0.280	0.001	0.032	0.111	0.027	0.129	0.140	0.037	0.085	0.056	0.073	0.077	0.071
$D^0 \to [K^-\pi^+]_{L=0}[K^+\pi^-]_{L=0}$	1.816	0.659	0.015	0.043	0.113	0.020	0.628	0.058	0.029	0.065	0.053	0.055	0.083	0.058
$D^0 \to K_1(1270)^+ K^-$	1.716	0.207	0.036	0.026	0.082	0.015	0.050	0.061	0.021	0.128	0.050	0.061	0.046	0.052
$D^0 \to [K^*(892)^0\overline{K}^*(892)^0]_{L=0}$	2.172	0.480	0.010	0.040	0.374	0.022	0.233	0.034	0.025	0.067	0.077	0.070	0.097	0.084
$D^0 \to K^*(1680)^0[K^-\pi^+]_{L=0}$	2.167	0.412	0.052	0.046	0.346	0.020	0.056	0.058	0.032	0.076	0.114	0.063	0.064	0.102
$D^0 \to [K^*(892)^0\overline{K}^*(892)^0]_{L=1}$	3.152	0.292	0.016	0.031	0.009	0.015	0.084	0.038	0.031	0.110	0.098	0.146	0.116	0.134
$D^0 \to K_1(1270)^- K^+$	3.520	0.540	0.037	0.051	0.255	0.000	0.040	0.113	0.076	0.281	0.100	0.228	0.130	0.212
$D^0 \to [K^+K^-]_{L=0}[\pi^+\pi^-]_{L=0}$	5.058	3.119	0.245	0.140	0.101	0.100	3.066	0.182	0.081	0.162	0.181	0.151	0.184	0.268
$D^0 \to K_1(1400)^- K^+$	6.050	0.963	0.055	0.171	0.071	0.014	0.209	0.627	0.131	0.442	0.275	0.224	0.172	0.292
$D^0 \to [K^*(1680)^0\overline{K}^*(892)^0]_{L=0}$	5.247	1.515	0.086	0.170	0.337	0.065	1.304	0.289	0.160	0.244	0.230	0.161	0.267	0.350
$D^0 \to [\overline{K}^*(1680)^0 K^*(892)^0]_{L=1}$	3.896	0.444	0.014	0.044	0.165	0.008	0.007	0.033	0.041	0.134	0.214	0.137	0.131	0.255
$D^0 \to \overline{K}^*(1680)^0[K^+\pi^-]_{L=0}$	3.748	1.070	0.027	0.078	0.908	0.026	0.234	0.129	0.046	0.266	0.219	0.192	0.156	0.246
$D^0 \to [\phi(1020)(\rho-\omega)^0]_{L=2}$	3.277	0.462	0.051	0.061	0.220	0.066	0.158	0.048	0.051	0.219	0.163	0.102	0.128	0.152
$D^0 \to [K^*(892)^0\overline{K}^*(892)^0]_{L=2}$	4.963	0.687	0.220	0.095	0.042	0.034	0.375	0.132	0.049	0.162	0.179	0.188	0.247	0.311
$D^0 \to \phi(1020)[\pi^+\pi^-]_{L=0}$	6.078	0.802	0.291	0.180	0.230	0.163	0.302	0.109	0.121	0.339	0.183	0.190	0.257	0.281
$D^0 \to [K^*(1680)^0\overline{K}^*(892)^0]_{L=1}$	5.342	0.553	0.008	0.065	0.017	0.019	0.297	0.084	0.095	0.212	0.156	0.155	0.166	0.276
$D^0 \to [\phi(1020)\rho(1450)^0]_{L=1}$	8.527	1.102	0.133	0.129	0.178	0.144	0.178	0.240	0.360	0.344	0.432	0.518	0.347	0.463
$D^0 \to a_0(980)^0 f_2(1270)^0$	7.190	1.305	0.212	0.196	0.359	0.012	0.689	0.733	0.190	0.265	0.217	0.311	0.302	0.370
$D^0 \to a_1(1260)^+\pi^-$	11.700	7.042	0.437	0.256	0.257	1.031	6.833	0.419	0.367	0.524	0.642	0.344	0.498	0.379
$D^0 \to a_1(1260)^-\pi^+$	13.672	2.860	0.742	0.349	0.189	0.879	2.052	0.429	0.432	0.982	0.519	0.405	0.646	0.551
$D^0 \to [\phi(1020)(\rho-\omega)^0]_{L=1}$	10.999	1.357	0.330	0.149	0.359	0.006	0.125	0.565	0.494	0.344	0.339	0.578	0.554	0.358
$D^0 \to [K^*(1680)^0\overline{K}^*(892)^0]_{L=2}$	14.304	3.535	0.549	0.646	2.042	0.115	2.266	0.347	0.243	0.642	0.469	0.479	0.430	1.110
$D^0 \to [K^+K^-]_{L=0}(\rho-\omega)^0$	12.534	2.791	0.018	0.316	2.014	0.032	1.182	0.578	0.128	0.943	0.630	0.514	0.380	0.437
$D^0 \to [\phi(1020)f_2(1270)^0]_{L=1}$	13.301	2.985	0.124	0.355	0.584	0.284	2.660	0.210	0.298	0.460	0.436	0.392	0.395	0.654
$D^0 \to [K^*(892)^0\overline{K}_2^*(1430)^0]_{L=1}$	10.805	1.810	0.477	0.171	0.830	0.065	1.066	0.588	0.237	0.332	0.380	0.327	0.325	0.566

Table 5.7 – Statistical and systematic uncertainties (in %) on the *CP*-violation parameters shown for all floating components. Values smaller than 0.0005% are displayed as "0.000". The sources of systematic uncertainty are described in the text in the same order as shown in this table. For each amplitude, the first value quoted is the modulus asymmetry and the second is the phase difference.

Amplitude	Stat.	Total Syst.	Sel. Eff.	Alt. Bkg 1	Alt. Bkg 2	RBW $\rho(770)^0$	Alt. S-wave	Mass & width	Res. radius	Sig bias	Bkg bias	Mistag bias	Det. As. bias	Alt. Models
$D^0 \to K_1(1400)^+ K^-$	1.084	0.200	0.004	0.021	0.072	0.030	0.095	0.074	0.026	0.039	0.071	0.050	0.057	0.076
	1.469	0.251	0.008	0.032	0.026	0.022	0.155	0.067	0.022	0.049	0.099	0.069	0.069	0.101
$D^0 \to [K^-\pi^+]_{L=0}[K^+\pi^-]_{L=0}$	1.134	0.304	0.004	0.024	0.040	0.007	0.263	0.025	0.019	0.035	0.065	0.062	0.053	0.089
	1.349	0.292	0.004	0.031	0.081	0.004	0.134	0.039	0.020	0.084	0.123	0.107	0.115	0.106
$D^0 \to K_1(1270)^+ K^-$	0.999	0.190	0.014	0.019	0.025	0.025	0.076	0.035	0.014	0.063	0.045	0.110	0.045	0.085
	1.444	0.232	0.033	0.027	0.056	0.004	0.114	0.037	0.021	0.045	0.076	0.067	0.065	0.132
$D^0 \to [K^*(892)^0\overline{K}^*(892)^0]_{L=0}$	1.299	0.265	0.001	0.024	0.171	0.028	0.066	0.022	0.022	0.041	0.114	0.082	0.076	0.084
	1.471	0.205	0.000	0.033	0.066	0.001	0.063	0.030	0.019	0.051	0.101	0.070	0.083	0.081
$D^0 \to K^*(1680)^0[K^-\pi^+]_{L=0}$	1.309	0.262	0.030	0.027	0.189	0.027	0.074	0.030	0.025	0.042	0.063	0.058	0.064	0.101
	1.491	0.214	0.052	0.032	0.079	0.012	0.032	0.056	0.018	0.048	0.068	0.067	0.066	0.123
$D^0 \to [K^*(892)^0\overline{K}^*(892)^0]_{L=1}$	1.713	0.220	0.004	0.019	0.021	0.010	0.093	0.024	0.023	0.065	0.082	0.083	0.108	0.091
	2.002	0.239	0.037	0.026	0.027	0.005	0.068	0.033	0.015	0.087	0.104	0.093	0.095	0.111
$D^0 \to K_1(1270)^- K^+$	1.707	0.436	0.023	0.030	0.144	0.017	0.031	0.056	0.046	0.134	0.135	0.213	0.179	0.217
	2.074	0.311	0.023	0.044	0.064	0.019	0.144	0.063	0.019	0.065	0.092	0.101	0.117	0.167
$D^0 \to [K^+K^-]_{L=0}[\pi^+\pi^-]_{L=0}$	2.482	1.521	0.119	0.069	0.066	0.033	1.483	0.087	0.042	0.078	0.110	0.114	0.167	0.148
	2.647	1.557	0.002	0.072	0.665	0.026	1.341	0.106	0.084	0.136	0.241	0.133	0.135	0.218
$D^0 \to K_1(1400)^- K^+$	2.879	0.687	0.024	0.089	0.052	0.024	0.155	0.317	0.067	0.211	0.207	0.292	0.274	0.288
	3.547	1.049	0.161	0.155	0.823	0.032	0.248	0.122	0.113	0.137	0.230	0.172	0.252	0.344
$D^0 \to [K^*(1680)^0\overline{K}^*(892)^0]_{L=0}$	2.673	0.775	0.047	0.084	0.153	0.015	0.603	0.141	0.085	0.114	0.270	0.128	0.160	0.223
	2.763	0.821	0.140	0.064	0.650	0.023	0.179	0.119	0.068	0.153	0.203	0.149	0.199	0.225
$D^0 \to [\overline{K}^*(1680)^0 K^*(892)^0]_{L=1}$	2.063	0.256	0.003	0.025	0.099	0.013	0.049	0.020	0.029	0.069	0.095	0.106	0.109	0.120
	2.087	0.278	0.024	0.030	0.118	0.016	0.060	0.035	0.020	0.067	0.095	0.102	0.149	0.102
$D^0 \to \overline{K}^*(1680)^0[K^+\pi^-]_{L=0}$	1.959	0.628	0.010	0.041	0.438	0.004	0.168	0.061	0.027	0.138	0.094	0.202	0.127	0.290
	2.249	0.328	0.023	0.045	0.058	0.041	0.125	0.045	0.031	0.073	0.196	0.106	0.102	0.128
$D^0 \to [\phi(1020)(\rho-\omega)^0]_{L=2}$	1.883	0.314	0.022	0.034	0.094	0.050	0.130	0.027	0.021	0.121	0.096	0.149	0.093	0.113
	1.991	0.469	0.077	0.055	0.206	0.086	0.146	0.037	0.015	0.159	0.147	0.184	0.122	0.206
$D^0 \to [K^*(892)^0\overline{K}^*(892)^0]_{L=2}$	2.510	0.419	0.114	0.051	0.005	0.034	0.239	0.067	0.029	0.083	0.127	0.118	0.114	0.215
	2.617	0.449	0.055	0.084	0.015	0.001	0.071	0.046	0.062	0.105	0.159	0.291	0.121	0.210
$D^0 \to \phi(1020)[\pi^+\pi^-]_{L=0}$	3.078	0.650	0.142	0.088	0.099	0.064	0.100	0.059	0.060	0.181	0.343	0.205	0.332	0.247
	3.900	0.677	0.107	0.128	0.235	0.183	0.255	0.082	0.083	0.134	0.282	0.182	0.200	0.304
$D^0 \to [K^*(1680)^0\overline{K}^*(892)^0]_{L=1}$	2.752	0.465	0.000	0.034	0.008	0.027	0.199	0.048	0.049	0.121	0.204	0.238	0.136	0.197
	2.988	0.425	0.034	0.039	0.008	0.007	0.024	0.051	0.030	0.120	0.176	0.168	0.236	0.211
$D^0 \to [\phi(1020)\rho(1450)^0]_{L=1}$	4.120	0.561	0.063	0.064	0.073	0.055	0.059	0.127	0.174	0.161	0.258	0.195	0.183	0.291
	3.342	0.593	0.005	0.037	0.194	0.062	0.085	0.088	0.145	0.180	0.245	0.201	0.193	0.320
$D^0 \to a_0(980)^0 f_2(1270)^0$	3.564	0.694	0.110	0.099	0.196	0.011	0.295	0.361	0.095	0.130	0.208	0.186	0.202	0.241
	3.341	0.834	0.105	0.105	0.226	0.023	0.614	0.233	0.073	0.116	0.189	0.183	0.223	0.231
$D^0 \to a_1(1260)^+\pi^-$	5.640	3.660	0.223	0.130	0.145	0.536	3.476	0.214	0.194	0.255	0.591	0.312	0.427	0.405
	6.148	1.268	0.031	0.125	0.486	0.176	0.595	0.140	0.131	0.205	0.665	0.288	0.293	0.530
$D^0 \to a_1(1260)^-\pi^+$	7.025	1.921	0.378	0.183	0.079	0.460	1.088	0.222	0.229	0.460	0.723	0.618	0.542	0.776
	5.554	4.327	0.102	0.150	0.369	0.205	4.197	0.175	0.082	0.193	0.332	0.280	0.704	0.368
$D^0 \to [\phi(1020)(\rho-\omega)^0]_{L=1}$	5.173	0.759	0.169	0.075	0.196	0.020	0.072	0.279	0.243	0.200	0.279	0.312	0.270	0.271
	5.468	0.611	0.060	0.072	0.243	0.001	0.117	0.100	0.032	0.170	0.240	0.263	0.252	0.247
$D^0 \to [K^*(1680)^0\overline{K}^*(892)^0]_{L=2}$	7.064	1.872	0.284	0.331	1.063	0.076	1.212	0.175	0.122	0.321	0.362	0.392	0.361	0.380
	8.124	1.312	0.110	0.479	0.098	0.145	0.418	0.325	0.180	0.261	0.435	0.709	0.391	0.474
$D^0 \to [K^+K^-]_{L=0}(\rho-\omega)^0$	6.000	1.866	0.005	0.158	1.024	0.033	0.540	0.293	0.066	0.480	0.501	0.826	0.465	0.805
	6.250	1.125	0.185	0.168	0.181	0.025	0.730	0.410	0.253	0.201	0.273	0.281	0.317	0.333
$D^0 \to [\phi(1020) f_2(1270)^0]_{L=1}$	6.710	1.686	0.066	0.178	0.276	0.159	1.381	0.109	0.163	0.232	0.405	0.326	0.490	0.443
	6.038	1.688	0.161	0.119	0.253	0.034	1.355	0.128	0.081	0.240	0.535	0.294	0.368	0.565
$D^0 \to [K^*(892)^0\overline{K}_2^*(1430)^0]_{L=1}$	5.194	1.038	0.236	0.086	0.401	0.016	0.586	0.298	0.115	0.171	0.381	0.314	0.229	0.287
	6.351	1.364	0.036	0.130	0.307	0.049	0.565	0.473	0.164	0.335	0.434	0.356	0.723	0.475

5.8 Cross-checks

Some cross-checks are performed to test additional effects. They are linked to choices made during the selection, to the resolution of the detector and to the selection efficiencies. All the effects described in this section are small compared to the systematic uncertainties considered in the analysis and are therefore neglected. In addition, a partial-wave analysis is performed to see if no resonance has been forgotten.

5.8.1 Δm cut

The Δm cut has been applied to increase the purity of the sample by removing an obvious background. Since the background description could also take this effect into account, a fit is performed by removing this cut. The result of this test can be found in Appendix F. This result is compared to the nominal fit and the average size of the difference between the two is 0.17σ, where σ is the total systematic uncertainty of the nominal fit. We choose to apply this cut because the fit without it shows a slightly worse $\chi^2/$ndf.

5.8.2 K_S^0 veto

It is observed that the K_S^0 veto shapes the phase space with strongly varying efficiencies. A fit is performed on a sample without this K_S^0 veto and where the $D^0 \to K_S^0 K^+ K^-$ mode is added incoherently to the $D^0 \to K^+ K^- \pi^+ \pi^-$ mode. The shape of the K_S^0 meson has been parametrised as a single Gaussian, whose components have been fixed from a fit to the data. The result of this fit is shown in Fig. 5.3, along with the parameters of the Gaussian function.

One issue is that a complete amplitude analysis of the mode $D^0 \to K_S^0 K^+ K^-$ should be done in order to come up with a decent model for that component only. This model, which would contain a coherent sum of amplitudes, would then need to be added incoherently to the rest of the model for $D^0 \to K^+ K^- \pi^+ \pi^-$. For the current test only two amplitudes are added
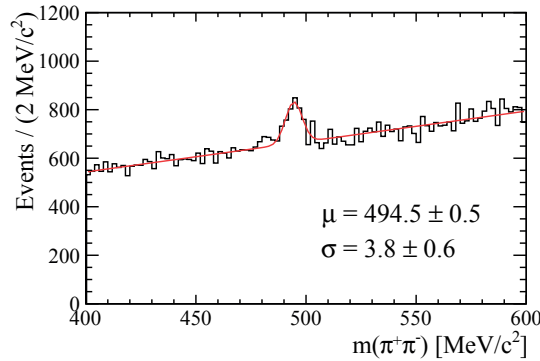
Figure 5.3 – Fit of the dipion mass in the K_S^0 region with a linear background and a single Gaussian for the resonance.
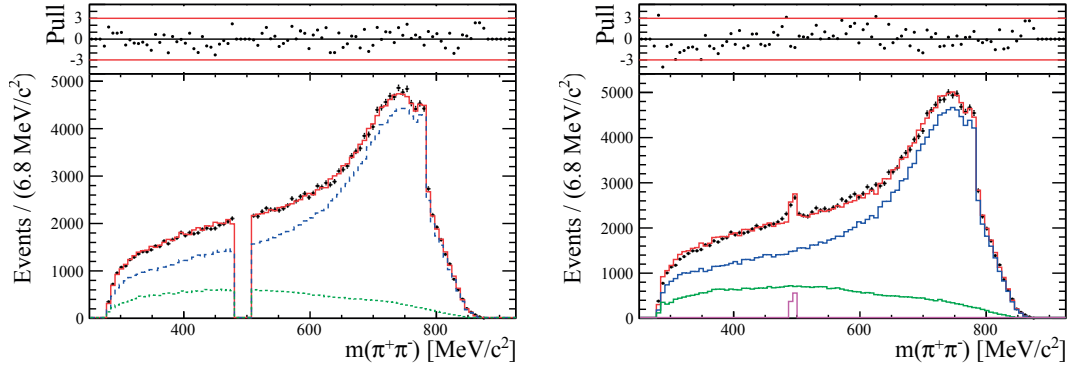
Figure 5.4 – Nominal dipion mass on the left and dipion mass without K_S^0 veto along with the alternative D^0 model on the right. The full model is shown in red, the signal component in blue, the background component in green and the K_S^0 component in magenta.

incoherently, $D^0 \to \phi K_S^0$ and $D^0 \to K_S^0 [K^+ K^-]_{L=0}$. The various fractions are fixed from a fit to the full $\pi^+ \pi^-$ invariant mass ($f_s = 82.1\%$, $f_b = 17.5\%$ and $f_{K_S^0} = 0.4\%$). The only visible difference in the various projections arises in the dipion invariant mass, shown in Fig. 5.4. The resulting model can be found in Appendix F. The average deviation with respect to the nominal fit is 0.18σ, where σ is the total systematic uncertainty of the nominal fit.

5.8.3 Multiple candidates

There are 1.7% of the events that contain multiple candidates in data. As mentioned in Sec. 3.5.2, one of the multiple candidates has been chosen randomly. This choice has been recommended in Ref. [122]. Nevertheless we want to verify that it is indeed better than to keep all multiple candidates. A fit is therefore performed by keeping them all and is compared to the nominal fit. The result of this test can be found in Appendix F. The average deviation with respect to the nominal fit is 0.07σ, where σ is the total systematic uncertainty of the nominal fit. The quality of the fit is slightly worse when keeping all multiple candidates, we therefore choose to keep the selection unchanged.

5.8.4 Resolution

In the amplitude fit, the resolution is neglected. This choice is justified by the fact that the D^0 mass constraint renders the detector resolution negligible. If any resolution issue should subsist, it would be most visible in the region of the narrow $\phi(1020)^0$ resonance. One of the test performed is to redo the amplitude fit to the data while enlarging the nominal width of the $\phi(1020)^0$ meson by the estimated resolution from MC studies. The MC sample reproduces well the resolution in data due to the fact that it has been reconstructed as the data by the LHCb framework and it has been reweighted for the momenta. The result of this test can be found in Appendix F. The average deviation with respect to the nominal fit is 0.03σ, where σ is the total systematic uncertainty of the nominal fit. The effect can therefore be safely neglected.

5.8.5 Selection efficiencies

Since the efficiencies depend on the kinematics of the system, one method to evaluate the quality of their description in the MC is to perform the amplitude fit in bins of the D^0 p_T. Only two bins will be considered (either $D^0 p_T < 5.25$ GeV/c or $D^0 p_T > 5.25$ GeV/c), as splitting the data in more bins introduces large statistical fluctuations that are hard to disentangle from the systematic uncertainties. The sidebands have also been separated in two bins of D^0 p_T and the correction due to the shift of the resonances has been applied separately in both bins. The MC has also been split in two bins.

The goal is to assess if the results of the fits on the two subsamples are compatible. In order to do this, a χ^2 is computed from the fit results and the covariance matrices. First two vectors (c_a and c_b) are created, containing all moduli and phases of each fit. Then the difference of the two vectors is taken as

$$\boldsymbol{\Delta} = \boldsymbol{c}_a - \boldsymbol{c}_b. \tag{5.15}$$

The two covariance matrices ($\mathcal{M}_a$ and $\mathcal{M}_b$) are summed:

$$\mathcal{M} = \mathcal{M}_a + \mathcal{M}_b. \tag{5.16}$$

And finally the χ^2 is computed as

$$\chi^2 = \boldsymbol{\Delta}^T \mathcal{M}^{-1} \boldsymbol{\Delta}. \tag{5.17}$$

In order to decide whether this χ^2 is significant or not, it is compared to a set of fits where the data sample has been split in two, randomly. A χ^2 is computed in the same way 1000 times for different random splitting and a distribution of the χ^2 is built. This distribution represents the null hypothesis where the two fits are compatible. The value of the χ^2 for the split in bins of p_T is compared to the null distribution in Fig. 5.5. The value falls well within the null distribution
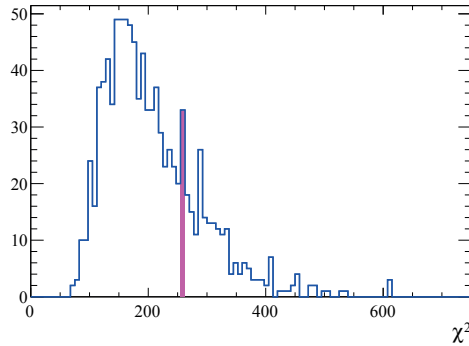
Figure 5.5 – Value of the χ^2 for the split in bins of p_T (in magenta) compared to the distribution of the null hypothesis for 1000 random splitting (in blue).

and it is therefore considered that the two fits are compatible and no systematic uncertainty is assigned for this effect.

5.8.6 Partial-wave analysis

In order to verify that no obvious resonance has been forgotten, the data and the resulting model are projected on the normalised spherical associated Legendre polynomials (*i.e.* on the spherical harmonics without azimuthal dependence). This allows to decouple the data and the fit into the *S*, *P* and *D* waves. These polynomials are defined as

$$Y_l^m(\theta, \phi = 0) = \sqrt{\frac{(2l+1)}{4\pi} \frac{(l-m)!}{(l+m)!}} P_l^m(\cos\theta), \tag{5.18}$$

where

$$P_l^m(x) = \frac{(-1)^m}{2^l \, l!} (1 - x^2)^{\frac{m}{2}} \frac{d^{l+m}}{dx^{l+m}} (x^2 - 1)^l \tag{5.19}$$

are the associated Legendre polynomials.

All two-body invariant masses distributions are inspected. They are weighted with these polynomials where l is taken from 1 to 6, m is kept at 0 and θ is taken as the helicity angle of one of the two particles of the two-body system. No obvious discrepancy is observed, we are therefore confident that no major component is missing. All the plots are shown in Appendix G. Some small discrepancies are observed in the $K^+\pi^+$ and $K^-\pi^-$ projections around 800 MeV/c^2. They are however hard to interpret, since no resonance is expected to arise in these mass combinations.

6 Results and discussions

6.1 *CP*-averaged model of $D^0 \to K^+ K^- \pi^+ \pi^-$ decays

A visualisation of the nominal fit results is provided in several projections by showing the histogram of the data sample superimposed with the histogram of the MC sample, where each MC event at phase-space point $\boldsymbol{x}_i$ is given the weight

$$w_s(\boldsymbol{x}_i) = N_{\text{data}} \, f_s \, \frac{S(\boldsymbol{x}_i; \boldsymbol{c})}{\frac{1}{N_{\text{MC}}} \sum_{k=1}^{N_{\text{MC}}} \frac{S(\boldsymbol{x}_k; \boldsymbol{c})}{S^{\text{gen}}(\boldsymbol{x}_k)}} \qquad \text{for the signal model (in blue),} \qquad (6.1)$$

$$w_b(\boldsymbol{x}_i) = N_{\text{data}} \, (1 - f_s) \, B(\boldsymbol{x}_i) \qquad \text{fo the background model (in green),} \qquad (6.2)$$

$$w(\boldsymbol{x}_i) = w_s(\boldsymbol{x}_i) + w_b(\boldsymbol{x}_i) \qquad \text{for the total model (in red),} \qquad (6.3)$$

where $\boldsymbol{c}$ are the fit parameters that maximize the likelihood. The projections on the five CM variables are shown in Fig. 6.1. The projections on 26 other variables in this 5D space are shown in Appendix H. All projections show a good agreement between the fitted model and the data. The remaining small discrepancies are accounted for by the systematic uncertainties. The resulting fit parameters are shown in Table 6.1 for all the D^0 amplitudes, in Table 6.2 for the decays of the 3-body amplitudes and in Table 6.3 for the $\rho - \omega$ interference parameters.
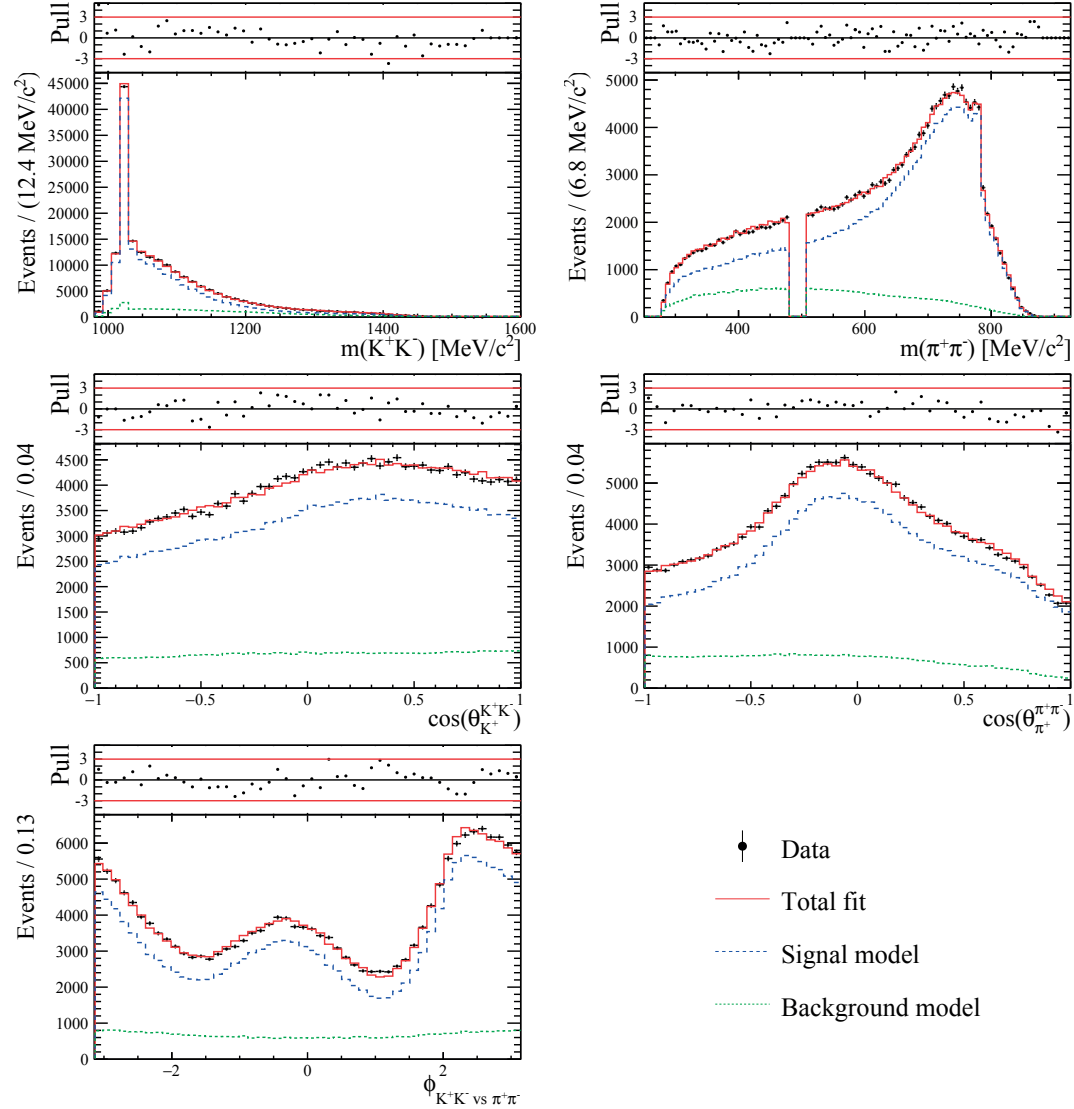
Figure 6.1 – Distributions of the five CM variables for the selected $D^0 \to K^+ K^- \pi^+ \pi^-$ candidates (black points with error bars). The results of the five-dimensional amplitude fit is superimposed with the signal model (dashed blue), the background model (dotted green) and the total fit function (plain red). The plot on top of each distribution shows the normalised residuals (differences between the data points and the fit results, divided by the quadratic sum of the statistical uncertainties of the data and MC samples).

Table 6.1 – Modulus and phase of the fit parameters along with fit fractions and significances σ of the amplitudes included in the model. The substructures of the three-body resonances are listed in Table 6.2. The first uncertainty is statistical and the second is systematic.

Amplitude	$|c_k|$	$\arg(c_k)$ [rad]	Fit fraction [%]	σ
$D^0 \to [\phi(1020)(\rho-\omega)^0]_{L=0}$	1 (fixed)	0 (fixed)	$23.82 \pm 0.38 \pm 0.50$	> 40
$D^0 \to K_1(1400)^+K^-$	$0.614 \pm 0.011 \pm 0.031$	$1.05 \pm 0.02 \pm 0.05$	$19.08 \pm 0.60 \pm 1.46$	> 40
$D^0 \to [K^-\pi^+]_{L=0}[K^+\pi^-]_{L=0}$	$0.282 \pm 0.004 \pm 0.008$	$-0.60 \pm 0.02 \pm 0.10$	$18.46 \pm 0.35 \pm 0.94$	> 40
$D^0 \to K_1(1270)^+K^-$	$0.452 \pm 0.011 \pm 0.017$	$2.02 \pm 0.03 \pm 0.05$	$18.05 \pm 0.52 \pm 0.98$	> 40
$D^0 \to [K^*(892)^0\bar{K}^*(892)^0]_{L=0}$	$0.259 \pm 0.004 \pm 0.018$	$-0.27 \pm 0.02 \pm 0.03$	$9.18 \pm 0.21 \pm 0.28$	> 40
$D^0 \to K^*(1680)^0[K^-\pi^+]_{L=0}$	$2.359 \pm 0.036 \pm 0.624$	$0.44 \pm 0.02 \pm 0.03$	$6.61 \pm 0.15 \pm 0.37$	> 40
$D^0 \to [K^*(892)^0\bar{K}^*(892)^0]_{L=1}$	$0.249 \pm 0.005 \pm 0.017$	$1.22 \pm 0.02 \pm 0.03$	$4.90 \pm 0.16 \pm 0.18$	> 40
$D^0 \to K_1(1270)^-K^+$	$0.220 \pm 0.006 \pm 0.011$	$2.09 \pm 0.03 \pm 0.07$	$4.29 \pm 0.18 \pm 0.41$	> 40
$D^0 \to [K^+K^-]_{L=0}[\pi^+\pi^-]_{L=0}$	$0.120 \pm 0.003 \pm 0.018$	$-2.49 \pm 0.03 \pm 0.16$	$3.14 \pm 0.17 \pm 0.72$	> 37
$D^0 \to K_1(1400)^-K^+$	$0.236 \pm 0.008 \pm 0.018$	$0.04 \pm 0.04 \pm 0.09$	$2.82 \pm 0.19 \pm 0.39$	> 33
$D^0 \to [K^*(1680)^0\bar{K}^*(892)^0]_{L=0}$	$0.823 \pm 0.023 \pm 0.218$	$2.99 \pm 0.03 \pm 0.05$	$2.75 \pm 0.15 \pm 0.19$	> 37
$D^0 \to [\bar{K}^*(1680)^0K^*(892)^0]_{L=1}$	$1.009 \pm 0.022 \pm 0.276$	$-2.76 \pm 0.02 \pm 0.03$	$2.70 \pm 0.11 \pm 0.09$	> 40
$D^0 \to \bar{K}^*(1680)^0[K^+\pi^-]_{L=0}$	$1.379 \pm 0.029 \pm 0.373$	$1.06 \pm 0.02 \pm 0.03$	$2.41 \pm 0.09 \pm 0.27$	> 40
$D^0 \to [\phi(1020)(\rho-\omega)^0]_{L=2}$	$1.311 \pm 0.031 \pm 0.018$	$0.54 \pm 0.02 \pm 0.02$	$2.29 \pm 0.08 \pm 0.08$	> 40
$D^0 \to [K^*(892)^0\bar{K}^*(892)^0]_{L=2}$	$0.652 \pm 0.018 \pm 0.043$	$2.85 \pm 0.03 \pm 0.04$	$1.85 \pm 0.09 \pm 0.10$	> 40
$D^0 \to \phi(1020)[\pi^+\pi^-]_{L=0}$	$0.049 \pm 0.001 \pm 0.004$	$-1.71 \pm 0.04 \pm 0.37$	$1.49 \pm 0.09 \pm 0.33$	> 30
$D^0 \to [K^*(1680)^0\bar{K}^*(892)^0]_{L=1}$	$0.747 \pm 0.021 \pm 0.203$	$0.14 \pm 0.03 \pm 0.04$	$1.48 \pm 0.08 \pm 0.10$	> 40
$D^0 \to [\phi(1020)\rho(1450)^0]_{L=1}$	$0.762 \pm 0.035 \pm 0.068$	$1.17 \pm 0.04 \pm 0.04$	$0.98 \pm 0.09 \pm 0.05$	> 24
$D^0 \to a_0(980)^0f_2(1270)^0$	$1.524 \pm 0.058 \pm 0.189$	$0.21 \pm 0.04 \pm 0.19$	$0.70 \pm 0.05 \pm 0.08$	> 27
$D^0 \to a_1(1260)^+\pi^-$	$0.189 \pm 0.011 \pm 0.042$	$-2.84 \pm 0.07 \pm 0.38$	$0.46 \pm 0.05 \pm 0.22$	> 17
$D^0 \to a_1(1260)^-\pi^+$	$0.188 \pm 0.014 \pm 0.031$	$0.18 \pm 0.06 \pm 0.43$	$0.45 \pm 0.06 \pm 0.16$	> 14
$D^0 \to [\phi(1020)(\rho-\omega)^0]_{L=1}$	$0.160 \pm 0.011 \pm 0.005$	$0.28 \pm 0.07 \pm 0.03$	$0.43 \pm 0.05 \pm 0.03$	> 18
$D^0 \to [K^*(1680)^0\bar{K}^*(892)^0]_{L=2}$	$1.218 \pm 0.089 \pm 0.354$	$-2.44 \pm 0.08 \pm 0.15$	$0.33 \pm 0.05 \pm 0.06$	> 14
$D^0 \to [K^+K^-]_{L=0}(\rho-\omega)^0$	$0.195 \pm 0.015 \pm 0.035$	$2.95 \pm 0.08 \pm 0.29$	$0.27 \pm 0.04 \pm 0.05$	> 15
$D^0 \to [\phi(1020)f_2(1270)^0]_{L=1}$	$1.388 \pm 0.095 \pm 0.257$	$1.71 \pm 0.06 \pm 0.37$	$0.18 \pm 0.02 \pm 0.07$	> 14
$D^0 \to [K^*(892)^0\bar{K}_2^*(1430)^0]_{L=1}$	$1.530 \pm 0.086 \pm 0.131$	$2.01 \pm 0.07 \pm 0.09$	$0.18 \pm 0.02 \pm 0.02$	> 20
		Sum of fit fractions	$129.32 \pm 1.09 \pm 2.38$	
		χ^2/ndf	$9242/8121 = 1.14$	

Table 6.2 – Parameters of the amplitudes contributing to the three-body decays of the $a_1(1260)^+$, $K_1(1270)^+$ and $K_1(1400)^+$. The first uncertainty is statistical and the second is systematic.

Amplitude	$|c_k|$	$\arg(c_k)$ [rad]	Fit fraction [%]	σ
$a_1(1260)^+ \to [\phi(1020)\pi^+]_{L=0}$	1 (fixed)	0 (fixed)	100	> 19
$K_1(1270)^+ \to [K^*(892)^0\pi^+]_{L=0}$	$0.584 \pm 0.016 \pm 0.040$	$0.63 \pm 0.03 \pm 0.05$	$51.22 \pm 1.06 \pm 3.21$	> 40
$K_1(1270)^+ \to [(\rho-\omega)^0K^+]_{L=0}$	1 (fixed)	0 (fixed)	$49.58 \pm 1.99 \pm 4.35$	> 40
$K_1(1270)^+ \to [K^+\pi^-]_{L=0}\pi^+$	$0.612 \pm 0.027 \pm 0.094$	$-1.94 \pm 0.04 \pm 0.08$	$6.27 \pm 0.48 \pm 1.66$	> 26
$K_1(1270)^+ \to [K^*(892)^0\pi^+]_{L=2}$	$0.859 \pm 0.044 \pm 0.060$	$-2.53 \pm 0.04 \pm 0.05$	$2.03 \pm 0.17 \pm 0.20$	> 24
$K_1(1270)^+ \to [\rho(1450)^0K^+]_{L=0}$	$0.482 \pm 0.068 \pm 0.187$	$-2.37 \pm 0.10 \pm 0.45$	$1.50 \pm 0.47 \pm 1.04$	> 5
		Sum of fit fractions	$110.60 \pm 2.20 \pm 5.76$	
$K_1(1400)^+ \to [K^*(892)^0\pi^+]_{L=0}$	1 (fixed)	0 (fixed)	100	> 40

Table 6.3 – Parameters of the $\rho - \omega$ interference for all relevant amplitudes. The first uncertainty is statistical and the second is systematic.

Amplitude	$|\tilde{c}_k|$	$\arg(\tilde{c}_k)$ [rad]	Fit fraction [%]
$D^0 \rightarrow [\phi(1020)\rho(770)^0]_{L=0}$	1 (fixed)	0 (fixed)	$92.55 \pm 0.46 \pm 0.28$
$D^0 \rightarrow [\phi(1020)\omega(782)]_{L=0}$	$0.114 \pm 0.004 \pm 0.003$	$1.30 \pm 0.04 \pm 0.04$	$1.42 \pm 0.11 \pm 0.04$
		Sum of fit fractions	$93.96 \pm 0.40 \pm 0.28$
$D^0 \rightarrow [\phi(1020)\rho(770)^0]_{L=1}$	1 (fixed)	0 (fixed)	$83.11 \pm 4.11 \pm 1.70$
$D^0 \rightarrow [\phi(1020)\omega(782)]_{L=1}$	$0.254 \pm 0.052 \pm 0.018$	$1.32 \pm 0.19 \pm 0.07$	$4.33 \pm 1.58 \pm 0.52$
		Sum of fit fractions	$87.45 \pm 2.99 \pm 1.78$
$D^0 \rightarrow [\phi(1020)\rho(770)^0]_{L=2}$	1 (fixed)	0 (fixed)	$94.64 \pm 1.69 \pm 0.78$
$D^0 \rightarrow [\phi(1020)\omega(782)]_{L=2}$	$0.162 \pm 0.032 \pm 0.014$	$1.50 \pm 0.17 \pm 0.06$	$0.71 \pm 0.27 \pm 0.12$
		Sum of fit fractions	$95.35 \pm 1.54 \pm 0.79$
$D^0 \rightarrow [K^+K^-]_{L=0}\rho(770)^0$	1 (fixed)	0 (fixed)	$85.41 \pm 5.89 \pm 3.49$
$D^0 \rightarrow [K^+K^-]_{L=0}\omega(782)$	$0.494 \pm 0.098 \pm 0.098$	$-0.95 \pm 0.19 \pm 0.15$	$9.24 \pm 3.26 \pm 3.64$
		Sum of fit fractions	$94.65 \pm 5.03 \pm 5.04$
$K_1(1270)^+ \rightarrow [\rho(770)^0 K^+]_{L=0}$	1 (fixed)	0 (fixed)	$139.03 \pm 1.98 \pm 3.81$
$K_1(1270)^+ \rightarrow [\omega(782)K^+]_{L=0}$	$0.159 \pm 0.012 \pm 0.011$	$1.36 \pm 0.07 \pm 0.06$	$1.52 \pm 0.22 \pm 0.19$
		Sum of fit fractions	$140.55 \pm 1.90 \pm 3.81$

6.2   *CP* violation results

The data set is split according to the charge of the muon in order to separate the D^0 decays from the $\overline{D}^0$ decays. The D^0 sample contains $98\,413$ events out of which $81\,513 \pm 373$ are signal candidates with a purity of 0.828 ± 0.004. The $\overline{D}^0$ sample contains $98\,235$ events out of which $81\,397 \pm 374$ are signal candidates with a purity of 0.829 ± 0.004. The *CP* violation fit described in Sec. 4.9 is applied on these two samples. Table 6.4 shows the resulting *CP* violation parameters, the average moduli and phases are not shown for a purpose of clarity in the table. They are virtually identical to the moduli and phases from the *CP* averaged fit in Table 6.1. All the asymmetry parameters are compatible with zero. The most significant deviation, observed for the phase difference for the $D^0 \rightarrow [\phi(1020)^0\rho(1450)^0]_{L=1}$ amplitude, corresponds to a 2.8σ statistical fluctuation.

Table 6.4 – *CP* violation parameters fitted simultaneously to the D^0 and (*CP*-transformed) $\overline{D}^0$ samples. The first uncertainty is statistical and the second is systematic.

Amplitude	$A_{|c_k|}$ [%]	$\Delta \arg(c_k)$ [%]	$A_{\mathcal{F}_k}$ [%]
$D^0 \to [\phi(1020)(\rho-\omega)^0]_{L=0}$	0 (fixed)	0 (fixed)	$-1.8 \pm\ 1.5 \pm 0.2$
$D^0 \to K_1(1400)^+ K^-$	$-1.4 \pm 1.1 \pm 0.2$	$1.3 \pm 1.5 \pm 0.3$	$-4.5 \pm\ 2.1 \pm 0.3$
$D^0 \to [K^-\pi^+]_{L=0}[K^+\pi^-]_{L=0}$	$1.9 \pm 1.1 \pm 0.3$	$-1.2 \pm 1.3 \pm 0.3$	$2.0 \pm\ 1.8 \pm 0.7$
$D^0 \to K_1(1270)^+ K^-$	$-0.4 \pm 1.0 \pm 0.2$	$-1.1 \pm 1.4 \pm 0.2$	$-2.6 \pm\ 1.7 \pm 0.2$
$D^0 \to [K^*(892)^0 \overline{K}^*(892)^0]_{L=0}$	$-1.3 \pm 1.3 \pm 0.3$	$-1.7 \pm 1.5 \pm 0.2$	$-4.3 \pm\ 2.2 \pm 0.5$
$D^0 \to K^*(1680)^0[K^-\pi^+]_{L=0}$	$2.2 \pm 1.3 \pm 0.3$	$1.4 \pm 1.5 \pm 0.2$	$2.6 \pm\ 2.2 \pm 0.4$
$D^0 \to [K^*(892)^0 \overline{K}^*(892)^0]_{L=1}$	$-0.4 \pm 1.7 \pm 0.2$	$3.7 \pm 2.0 \pm 0.2$	$-2.6 \pm\ 3.2 \pm 0.3$
$D^0 \to K_1(1270)^- K^+$	$2.6 \pm 1.7 \pm 0.4$	$-0.1 \pm 2.1 \pm 0.3$	$3.3 \pm\ 3.5 \pm 0.5$
$D^0 \to [K^+K^-]_{L=0}[\pi^+\pi^-]_{L=0}$	$3.5 \pm 2.5 \pm 1.5$	$-5.5 \pm 2.6 \pm 1.6$	$5.1 \pm\ 5.1 \pm 3.1$
$D^0 \to K_1(1400)^- K^+$	$0.2 \pm 2.9 \pm 0.7$	$2.5 \pm 3.5 \pm 1.0$	$-1.3 \pm\ 6.0 \pm 1.0$
$D^0 \to [K^*(1680)^0 \overline{K}^*(892)^0]_{L=0}$	$4.0 \pm 2.7 \pm 0.8$	$-5.4 \pm 2.8 \pm 0.8$	$6.2 \pm\ 5.2 \pm 1.5$
$D^0 \to [\overline{K}^*(1680)^0 K^*(892)^0]_{L=1}$	$-0.4 \pm 2.1 \pm 0.3$	$0.4 \pm 2.1 \pm 0.3$	$-2.5 \pm\ 3.9 \pm 0.4$
$D^0 \to \overline{K}^*(1680)^0[K^+\pi^-]_{L=0}$	$2.1 \pm 2.0 \pm 0.6$	$-1.8 \pm 2.2 \pm 0.3$	$2.4 \pm\ 3.7 \pm 1.1$
$D^0 \to [\phi(1020)(\rho-\omega)^0]_{L=2}$	$0.8 \pm 1.9 \pm 0.3$	$-1.2 \pm 2.0 \pm 0.5$	$-0.1 \pm\ 3.3 \pm 0.5$
$D^0 \to [K^*(892)^0 \overline{K}^*(892)^0]_{L=2}$	$-0.6 \pm 2.5 \pm 0.4$	$0.6 \pm 2.6 \pm 0.4$	$-3.0 \pm\ 5.0 \pm 0.7$
$D^0 \to \phi(1020)[\pi^+\pi^-]_{L=0}$	$3.8 \pm 3.1 \pm 0.7$	$-0.5 \pm 3.9 \pm 0.7$	$5.8 \pm\ 6.1 \pm 0.8$
$D^0 \to [K^*(1680)^0 \overline{K}^*(892)^0]_{L=1}$	$1.6 \pm 2.8 \pm 0.5$	$0.7 \pm 3.0 \pm 0.4$	$1.3 \pm\ 5.3 \pm 0.6$
$D^0 \to [\phi(1020)\rho(1450)^0]_{L=1}$	$4.6 \pm 4.1 \pm 0.6$	$9.3 \pm 3.3 \pm 0.6$	$7.5 \pm\ 8.5 \pm 1.1$
$D^0 \to a_0(980)^0 f_2(1270)^0$	$1.6 \pm 3.6 \pm 0.7$	$-7.3 \pm 3.3 \pm 0.8$	$1.5 \pm\ 7.2 \pm 1.3$
$D^0 \to a_1(1260)^+ \pi^-$	$-4.4 \pm 5.6 \pm 3.7$	$9.3 \pm 6.1 \pm 1.3$	$-10.6 \pm 11.7 \pm 7.0$
$D^0 \to a_1(1260)^- \pi^+$	$-3.4 \pm 7.0 \pm 1.9$	$-5.8 \pm 5.6 \pm 4.3$	$-8.7 \pm 13.7 \pm 2.9$
$D^0 \to [\phi(1020)(\rho-\omega)^0]_{L=1}$	$2.1 \pm 5.2 \pm 0.8$	$-12.2 \pm 5.5 \pm 0.6$	$2.4 \pm 11.0 \pm 1.4$
$D^0 \to [K^*(1680)^0 \overline{K}^*(892)^0]_{L=2}$	$5.2 \pm 7.1 \pm 1.9$	$-5.6 \pm 8.1 \pm 1.3$	$8.5 \pm 14.3 \pm 3.5$
$D^0 \to [K^+K^-]_{L=0}(\rho-\omega)^0$	$11.7 \pm 6.0 \pm 1.9$	$4.8 \pm 6.2 \pm 1.1$	$21.3 \pm 12.5 \pm 2.8$
$D^0 \to [\phi(1020) f_2(1270)^0]_{L=1}$	$2.7 \pm 6.7 \pm 1.7$	$0.9 \pm 6.0 \pm 1.7$	$3.6 \pm 13.3 \pm 3.0$
$D^0 \to [K^*(892)^0 \overline{K}_2^*(1430)^0]_{L=1}$	$3.9 \pm 5.2 \pm 1.0$	$6.8 \pm 6.4 \pm 1.4$	$6.1 \pm 10.8 \pm 1.8$

In order to verify that the *CP* violation is working as expected, the dataset is randomly split in two instead of splitting it according to the flavour of the D^0. No *CP* violation is expected to arise when performing the *CP* violation fit on these two samples. The resulting asymmetry parameters are indeed compatible with no *CP* violation with similar uncertainties as the nominal result. Then, in order to check the significance of the deviation observed in data in the absence of *CP* violation, two tests are performed by splitting the dataset randomly many times. First, we perform the *CP* violation fit on these randomly-split samples. The largest deviation among all the asymmetry parameters exceeds 2.8σ in 35% of the fits, confirming that the deviation observed in data is not significant. The second test is to perform the nominal amplitude fit separately on these randomly-split samples and compute the χ^2 between the two fit results as explained in Sec. 5.8.5 in order to build a null distribution. This null distribution
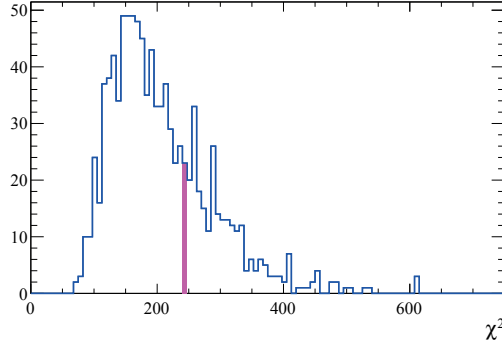
Figure 6.2 – Value of the χ^2 computed between the D^0 and $\overline{D}^0$ samples (in magenta) compared to the distribution of the null hypothesis for 1000 random splitting (in blue).

represents the "no-CP violation" hypothesis. The amplitude fit is also performed on the D^0 and $\overline{D}^0$ samples separately and the obtained χ^2 value is compared to the null distribution in Fig. 6.2. It is observed that the χ^2 computed between the D^0 and the $\overline{D}^0$ samples falls well within the null distribution and confirms that no CP violation is observed.

6.3   Comparison with previous results

The resulting D^0 model of Table. 6.1 is compared to the CLEO-legacy-data model [47] summarised in Table 1.1. The main components are present in both models. The $D^0 \rightarrow \phi(1020)^0 \rho(770)^0$ components are compatible between the two models. However, the $D^0 \rightarrow K^*(892)^0 \overline{K}^*(892)^0$ components do not have the same hierarchy between the three angular momentum configurations in the two models. The component $D^0 \rightarrow K_1(1270)^+ K^-$ is found to be slightly smaller in this analysis, whereas the component $D^0 \rightarrow K_1(1400)^+ K^-$ is found to be bigger. There is an important difference between the two models however, the strong decays are not enforced to have the same pattern in the CLEO-legacy-data model. Therefore it contains some strong CP violation, while it has been forbidden in this analysis. The component $D^0 \rightarrow K^*(1680)^+ K^-$ is the only one from the CLEO model that has not been selected in this analysis, even though it was available in the list of possible amplitudes.

A dataset more than 50 times larger than the one analysed by CLEO has been used for this analysis, which brings a significant improvement on the statistical uncertainties of the various amplitudes. The statistical uncertainties of the fit fractions in the CLEO analysis ranged from $\sim 0.3\%$ to $\sim 2.6\%$ whereas the current statistical uncertainties range from $\sim 0.02\%$ to $\sim 0.6\%$. Regarding the CP violation measurements, a significant improvement is also provided with this new analysis. The sensitivity on all the asymmetry parameters ranges from $\sim 1\%$ to $\sim 15\%$, while it ranged from $\sim 10\%$ to $\sim 50\%$ in the CLEO analysis.

6.4   Discussion, outlook and conclusion

A few features in the model are worth noting. First the components $D^0 \rightarrow \phi(1020)^0 \rho(1450)^0$ and $D^0 \rightarrow \overline{K}^*(1680)^0 K^*(892)^0$ appear only in P-wave without their S and D counterparts, which are also allowed. The $K_1(1270)^+$ is going to $\rho(1450)^0 K^+$ with a significance of only 5σ, which is relatively small compared to the other components. The $a_1(1260)^+$ is decaying only to $\phi(1020)^0 \pi^+$, while a contribution of $\overline{K}^*(892)^0 K^+$ is reported by the PDG [24]. Finally, the $\rho - \omega$ interference seems to be relatively different between the decay modes.

The determination of this model is dominated by systematic uncertainties, most notably those due to the values used for the nominal mass and width of less well-known resonances such as the $K^*(1680)^0$, the parametrisation of the S-wave components and the alternative models.

This analysis provides the best model for the $D^0 \rightarrow K^+ K^- \pi^+ \pi^-$ decay to date. This model is used for a search for CP violation. At this level of sensitivity, no CP violation is observed. This is compatible with the Standard Model predictions and rules out any large contribution from New Physics. This result is expected to be important for other analyses as well, such as the measurement of the CKM angle γ in $B^\pm \rightarrow DK^\pm$ decays, which requires a precise model describing the signal [49]. With the model developed in this analysis, such a measurement is now possible at LHCb using the $D^0 \rightarrow K^+ K^- \pi^+ \pi^-$ subdecay.

The CP violation measurements are statistically dominated. In order to reach the level of $10^{-3} - 10^{-4}$ predicted by the Standard Model, more statistics is therefore needed. The addition of the full Run 2 data collected at a centre-of-mass energy of $13\,\mathrm{TeV}$, which will be available at the end of this year (2018), represents a large increase in statistics when compared to the $3\,\mathrm{fb}^{-1}$ collected at centre-of-mass energies of 7 and $8\,\mathrm{TeV}$ used in this analysis. The Run 2 sample is expected to correspond to an integrated luminosity of $\sim 6\,\mathrm{fb}^{-1}$. The increase in energy as well as various improvements in the tracking and the trigger allow the naive extrapolation that $1\,\mathrm{fb}^{-1}$ in Run 2 is worth at least $2\,\mathrm{fb}^{-1}$ in Run 1. This means that an increase of the statistics by a factor 5 in the semileptonic mode alone is possible. Since the trigger issue of the prompt sample ($D^{*+} \rightarrow D^0 \pi^+$) in Run 1 has been fixed, one could use the Run 2 sample to increase the signal yield even more. This might however complicate the treatment of the phase-space efficiencies and a special treatment will have to be applied to combine the two samples. The prompt sample is expected to be 4–5 times larger than the sample from semi-leptonic b decays [63], mostly due to the fact that the $c\bar{c}$ production cross-section is much larger than the $b\bar{b}$ one. If the Run 2 prompt sample is added, an increase by a factor 20 might therefore be reachable. In order to achieve the permil level on the statistical uncertainties of all the CP asymmetries, one might however need to wait for the $50\,\mathrm{fb}^{-1}$ of Runs 3 and 4.

This analysis pushed the boundaries of current knowledge of CP violation in charm decays by further cornering the allowed level of CP violation in the amplitudes of the $D^0 \rightarrow K^+ K^- \pi^+ \pi^-$ decay mode. It pioneered the search for CP violation using high statistics four-body amplitude analyses at LHCb, with promising prospects for the future.

A Mass dependencies

In Sec. 2.3.5.2, particles are reconstructed with the 2011 and 2014 maps and their average measured mass tested for dependencies. All the related plots are shown in Figs. A.1–A.5. The variables on the horizontal axis of these plots are defined in the bullet list of Sec. 2.3.5.2.
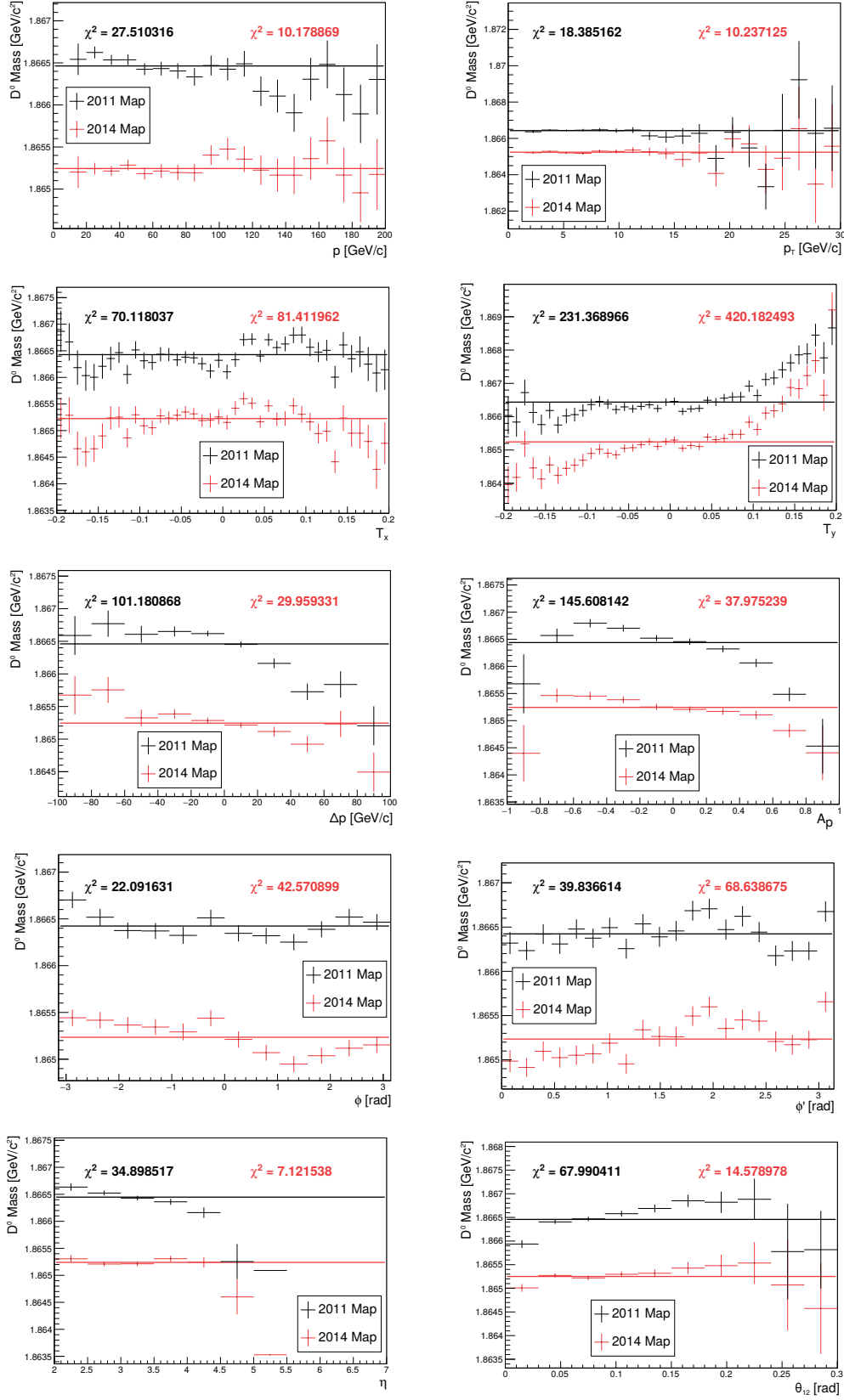
Figure A.1 – Dependencies of the D^0 reconstructed mass.
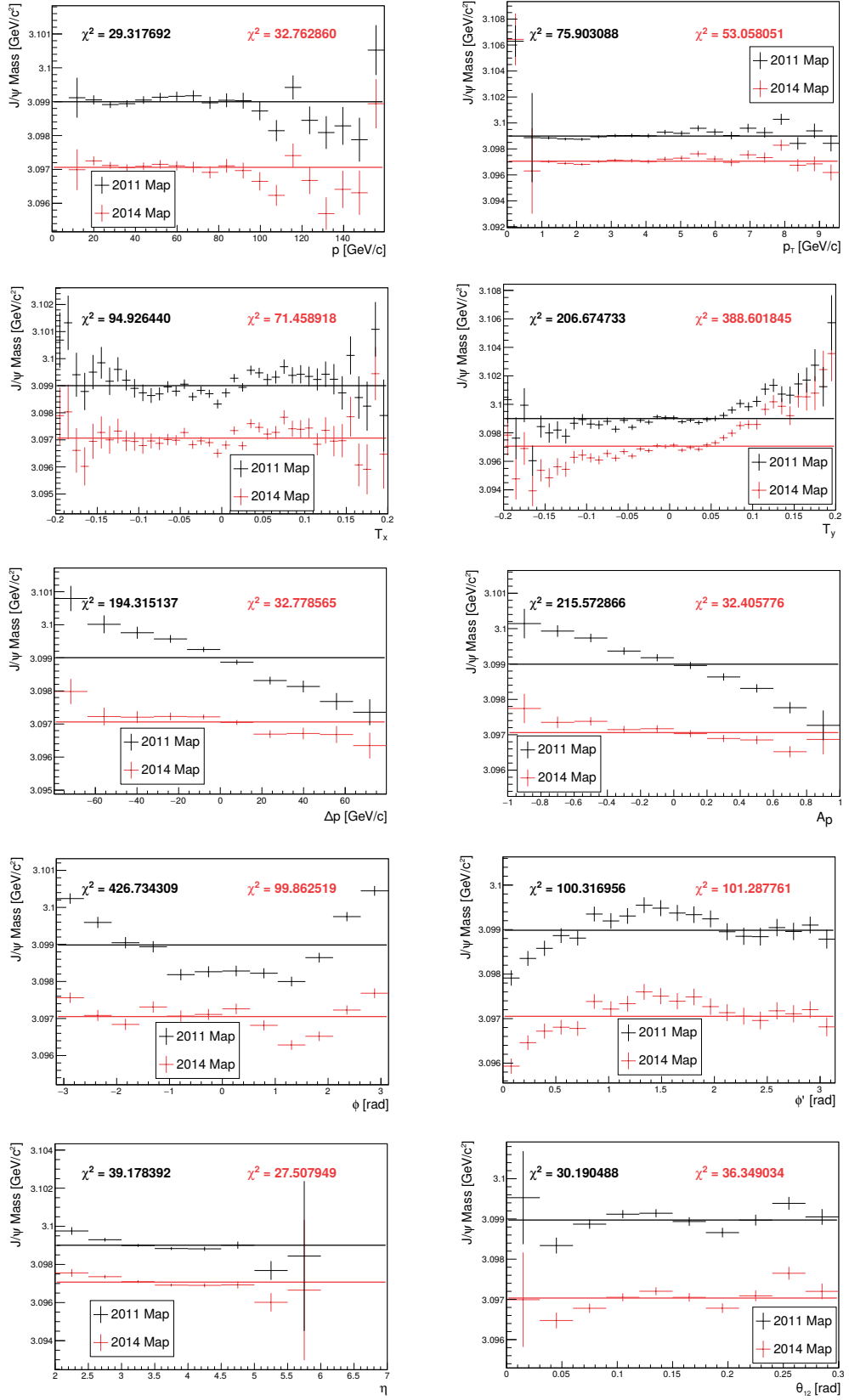
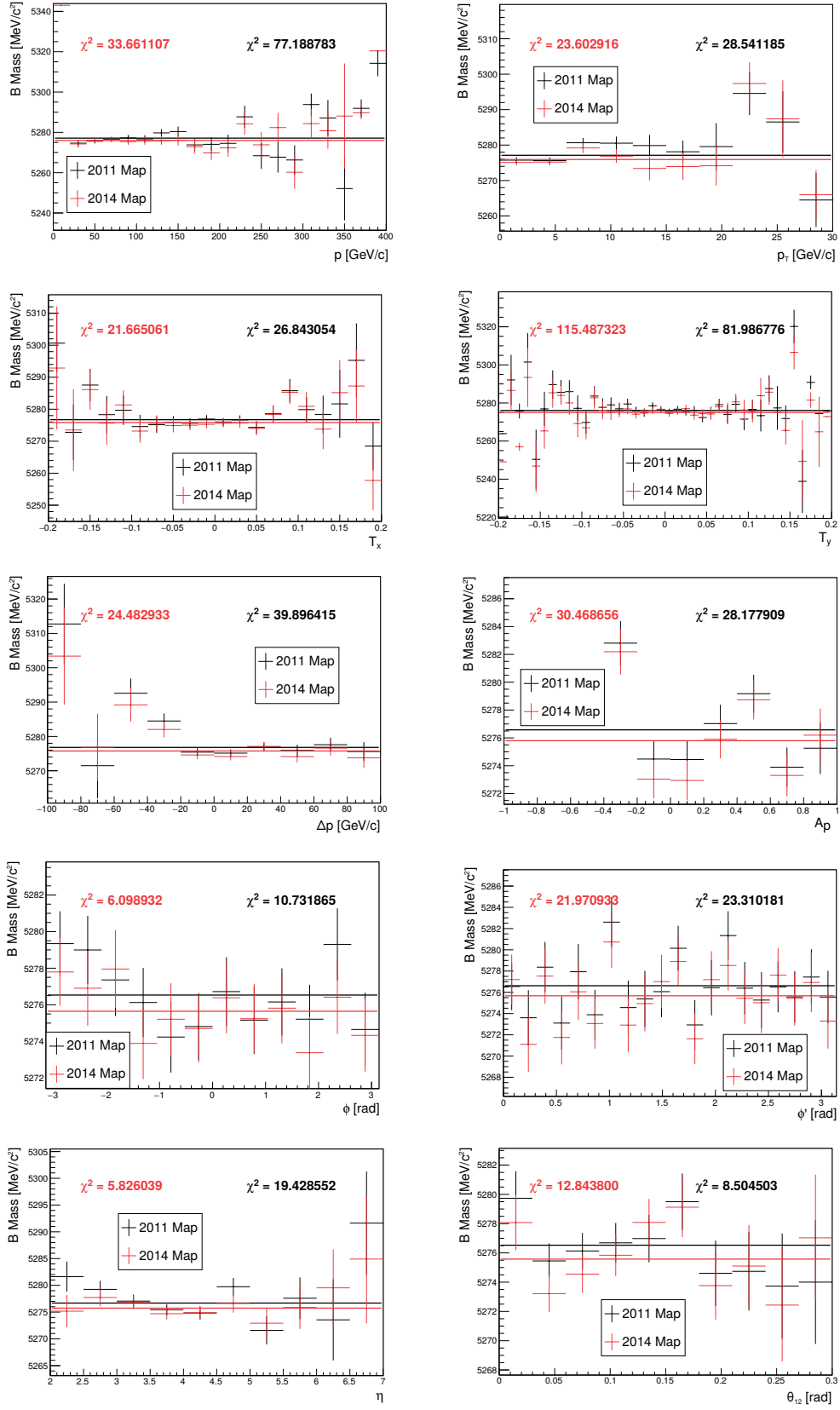Figure A.2 – Dependencies of the J/ψ reconstructed mass.
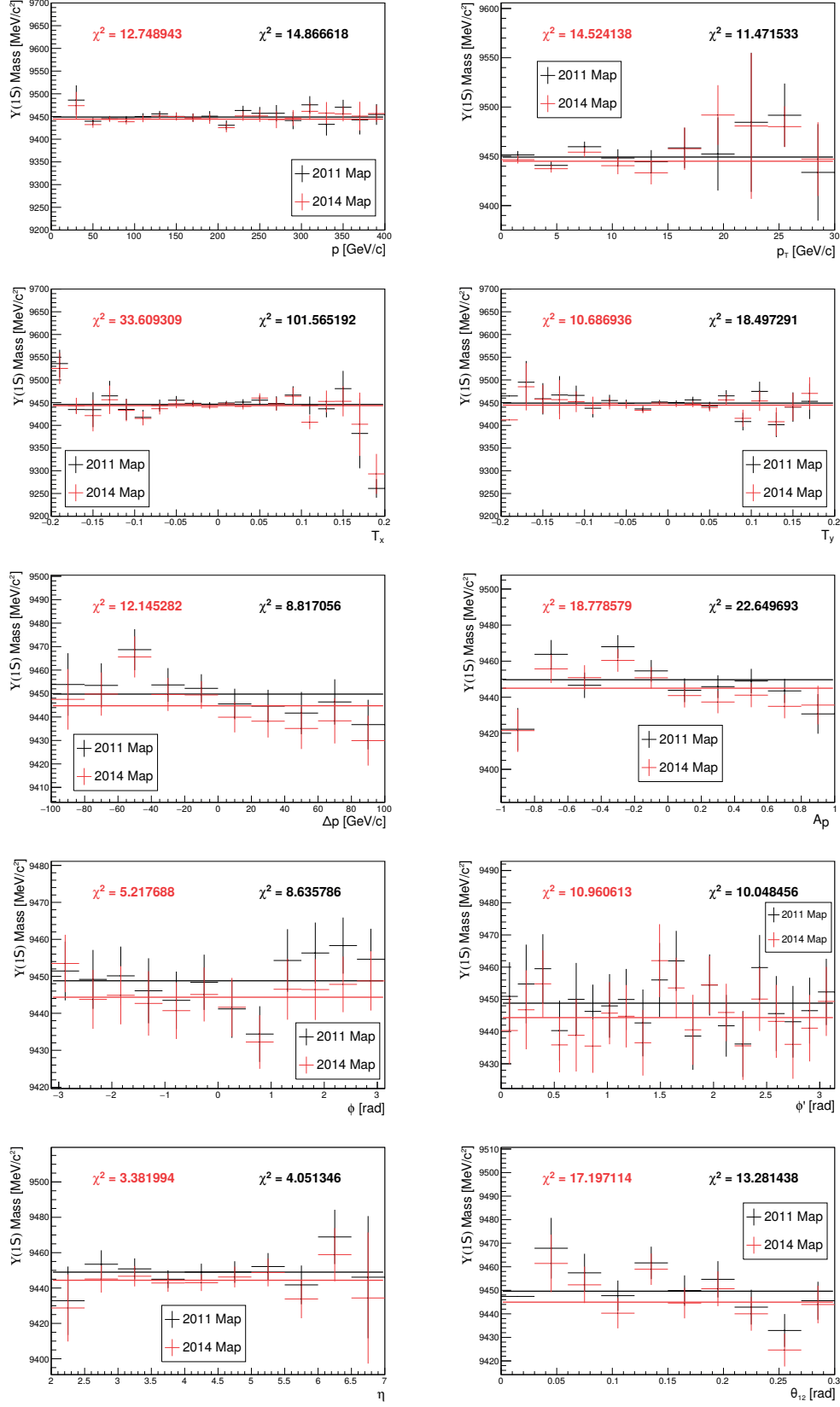
Figure A.3 – Dependencies of the $\Upsilon(1S)$ reconstructed mass.
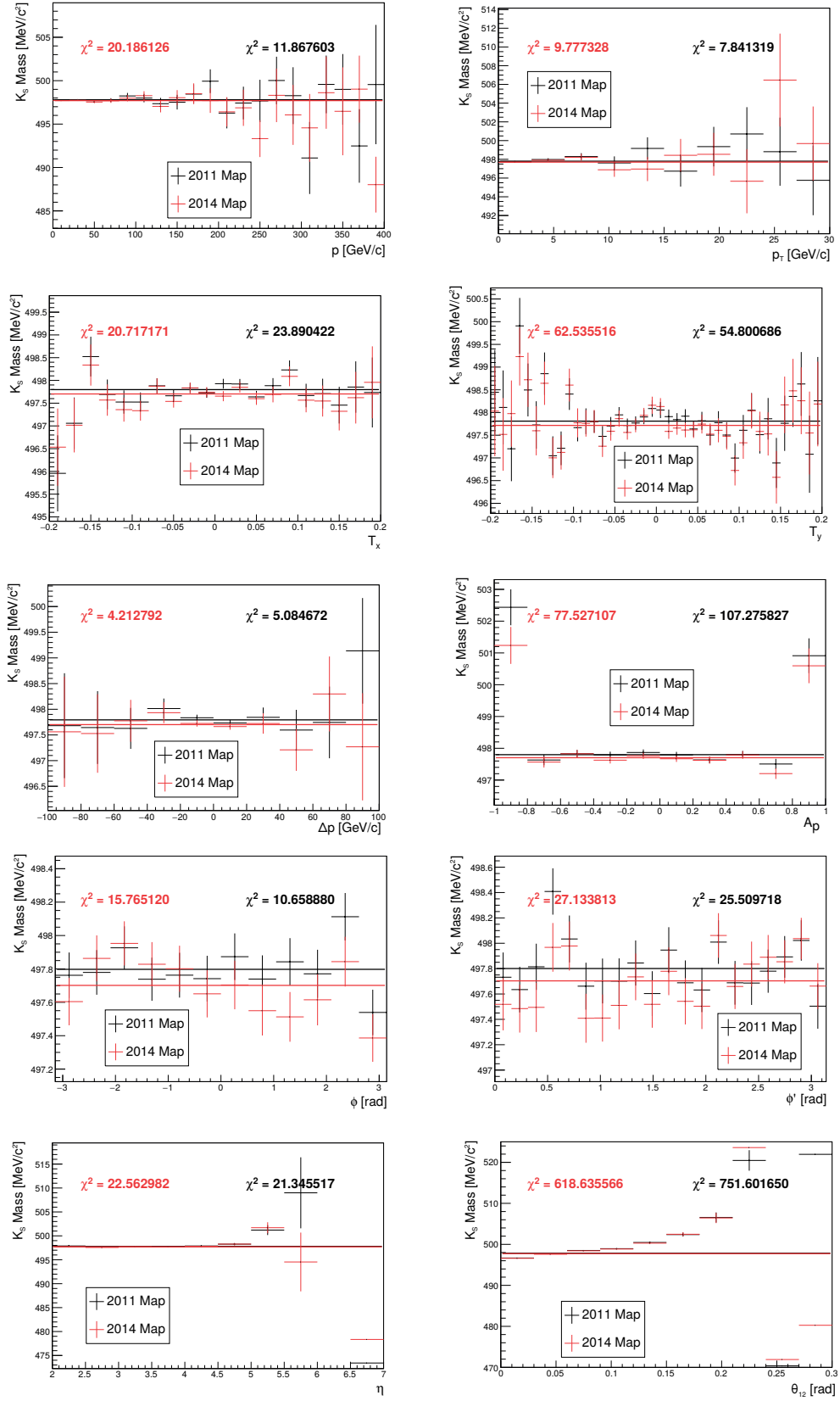
Figure A.4 – Dependencies of the K^0_S reconstructed mass.

Figure A.5 – Dependencies of the B^+ reconstructed mass.

B List of amplitudes

Tables B.1–B.4 list all the amplitudes that have been considered in this analysis. Since there are some ambiguous cases, the final daughter particles are always specified in parentheses next to their mother particle. An angular momentum between two systems A and B is indicated with the notation $[AB]_L$.

Table B.1 – List of all the amplitudes that match $D^0 \to (K^+K^-)(\pi^+\pi^-)$.

$D^0 \to [[K^+K^-]_{L=0}[\pi^+\pi^-]_{L=0}]_{L=0}$
$D^0 \to [[K^+K^-]_{L=0}\omega(782)^0(\pi^+\pi^-)]_{L=1}$
$D^0 \to [[K^+K^-]_{L=0}\rho(1450)^0(\pi^+\pi^-)]_{L=1}$
$D^0 \to [[K^+K^-]_{L=0}\rho(770)^0(\pi^+\pi^-)]_{L=1}$
$D^0 \to [a_0(980)^0(K^+K^-)[\pi^+\pi^-]_{L=0}]_{L=0}$
$D^0 \to [a_0(980)^0(K^+K^-)\omega(782)^0(\pi^+\pi^-)]_{L=1}$
$D^0 \to [a_0(980)^0(K^+K^-)\rho(1450)^0(\pi^+\pi^-)]_{L=1}$
$D^0 \to [a_0(980)^0(K^+K^-)\rho(770)^0(\pi^+\pi^-)]_{L=1}$
$D^0 \to [a_0(980)^0(K^+K^-)f_2(1270)^0(\pi^+\pi^-)]_{L=2}$
$D^0 \to [\phi(1020)^0(K^+K^-)[\pi^+\pi^-]_{L=0}]_{L=1}$
$D^0 \to [\phi(1020)^0(K^+K^-)\omega(782)^0(\pi^+\pi^-)]_{L=0}$
$D^0 \to [\phi(1020)^0(K^+K^-)\omega(782)^0(\pi^+\pi^-)]_{L=1}$
$D^0 \to [\phi(1020)^0(K^+K^-)\omega(782)^0(\pi^+\pi^-)]_{L=2}$
$D^0 \to [\phi(1020)^0(K^+K^-)\rho(1450)^0(\pi^+\pi^-)]_{L=0}$
$D^0 \to [\phi(1020)^0(K^+K^-)\rho(1450)^0(\pi^+\pi^-)]_{L=1}$
$D^0 \to [\phi(1020)^0(K^+K^-)\rho(1450)^0(\pi^+\pi^-)]_{L=2}$
$D^0 \to [\phi(1020)^0(K^+K^-)\rho(770)^0(\pi^+\pi^-)]_{L=0}$
$D^0 \to [\phi(1020)^0(K^+K^-)\rho(770)^0(\pi^+\pi^-)]_{L=1}$
$D^0 \to [\phi(1020)^0(K^+K^-)\rho(770)^0(\pi^+\pi^-)]_{L=2}$
$D^0 \to [\phi(1020)^0(K^+K^-)f_2(1270)^0(\pi^+\pi^-)]_{L=1}$
$D^0 \to [\phi(1020)^0(K^+K^-)f_2(1270)^0(\pi^+\pi^-)]_{L=2}$
$D^0 \to [f_2(1270)^0(K^+K^-)[\pi^+\pi^-]_{L=0}]_{L=2}$
$D^0 \to [f_2(1270)^0(K^+K^-)\omega(782)^0(\pi^+\pi^-)]_{L=1}$
$D^0 \to [f_2(1270)^0(K^+K^-)\omega(782)^0(\pi^+\pi^-)]_{L=2}$
$D^0 \to [f_2(1270)^0(K^+K^-)\rho(1450)^0(\pi^+\pi^-)]_{L=1}$
$D^0 \to [f_2(1270)^0(K^+K^-)\rho(1450)^0(\pi^+\pi^-)]_{L=2}$
$D^0 \to [f_2(1270)^0(K^+K^-)\rho(770)^0(\pi^+\pi^-)]_{L=1}$
$D^0 \to [f_2(1270)^0(K^+K^-)\rho(770)^0(\pi^+\pi^-)]_{L=2}$
$D^0 \to [f_2(1270)^0(K^+K^-)f_2(1270)^0(\pi^+\pi^-)]_{L=0}$
$D^0 \to [a_2(1320)^0(K^+K^-)[\pi^+\pi^-]_{L=0}]_{L=2}$
$D^0 \to [a_2(1320)^0(K^+K^-)\omega(782)^0(\pi^+\pi^-)]_{L=1}$
$D^0 \to [a_2(1320)^0(K^+K^-)\omega(782)^0(\pi^+\pi^-)]_{L=2}$
$D^0 \to [a_2(1320)^0(K^+K^-)\rho(1450)^0(\pi^+\pi^-)]_{L=1}$
$D^0 \to [a_2(1320)^0(K^+K^-)\rho(1450)^0(\pi^+\pi^-)]_{L=2}$
$D^0 \to [a_2(1320)^0(K^+K^-)\rho(770)^0(\pi^+\pi^-)]_{L=1}$
$D^0 \to [a_2(1320)^0(K^+K^-)\rho(770)^0(\pi^+\pi^-)]_{L=2}$
$D^0 \to [a_2(1320)^0(K^+K^-)f_2(1270)^0(\pi^+\pi^-)]_{L=0}$

Table B.2 – List of all the amplitudes that match $D^0 \to (K^+\pi^-)(K^-\pi^+)$.

$D^0 \to [K^+\pi^-]_{L=0}[K^-\pi^+]_{L=0}$

$D^0 \to [K^*(892)^0(K^+\pi^-)[K^-\pi^+]_{L=0}]_{L=1}$
$D^0 \to [\bar{K}^*(892)^0(K^-\pi^+)[K^+\pi^-]_{L=0}]_{L=1}$

$D^0 \to [K^*(892)^0(K^+\pi^-)\bar{K}^*(892)^0(K^-\pi^+)]_{L=0}$
$D^0 \to [K^*(892)^0(K^+\pi^-)\bar{K}^*(892)^0(K^-\pi^+)]_{L=1}$
$D^0 \to [K^*(892)^0(K^+\pi^-)\bar{K}^*(892)^0(K^-\pi^+)]_{L=2}$

$D^0 \to [K^*(892)^0(K^+\pi^-)\bar{K}_2^*(1430)^0(K^-\pi^+)]_{L=1}$
$D^0 \to [\bar{K}^*(892)^0(K^-\pi^+)K_2^*(1430)^0(K^+\pi^-)]_{L=1}$
$D^0 \to [K^*(892)^0(K^+\pi^-)\bar{K}_2^*(1430)^0(K^-\pi^+)]_{L=2}$
$D^0 \to [\bar{K}^*(892)^0(K^-\pi^+)K_2^*(1430)^0(K^+\pi^-)]_{L=2}$

$D^0 \to [K_2^*(1430)^0(K^+\pi^-)[K^-\pi^+]_{L=0}]_{L=2}$
$D^0 \to [\bar{K}_2^*(1430)^0(K^-\pi^+)[K^+\pi^-]_{L=0}]_{L=2}$
$D^0 \to [K_2^*(1430)^0(K^+\pi^-)\bar{K}_2^*(1430)^0(K^-\pi^+)]_{L=0}$

$D^0 \to [K^*(1680)^0(K^+\pi^-)[K^-\pi^+]_{L=0}]_{L=1}$
$D^0 \to [\bar{K}^*(1680)^0(K^-\pi^+)[K^+\pi^-]_{L=0}]_{L=1}$

Table B.3 – List of all the amplitudes that match $D^0 \to (K^+K^-\pi^+)(\pi^-)$. A similar set of amplitudes matching $D^0 \to (K^+K^-\pi^-)(\pi^+)$ is considered, but not listed here.

$D^0 \to [a_1(1260)^+[\bar{K}^*(892)^0(K^-\pi^+)K^+]_{L=0}\pi^-]_{L=1}$
$D^0 \to [a_1(1260)^+[\bar{K}^*(892)^0(K^-\pi^+)K^+]_{L=2}\pi^-]_{L=1}$
$D^0 \to [a_1(1260)^+[\phi(1020)^0(K^+K^-)\pi^+]_{L=0}\pi^-]_{L=1}$
$D^0 \to [a_1(1260)^+[\phi(1020)^0(K^+K^-)\pi^+]_{L=2}\pi^-]_{L=1}$
$D^0 \to [a_1(1260)^+[f_2(1270)^0(K^+K^-)\pi^+]_{L=1}\pi^-]_{L=1}$

Table B.4 – List of all the amplitudes that match $D^0 \to (K^+\pi^+\pi^-)(K^-)$. A similar set of amplitudes matching $D^0 \to (K^-\pi^+\pi^-)(K^+)$ is considered, but not listed here.

$D^0 \to [K_1(1270)^+[[K^+\pi^-]_{L=0}\pi^+]_{L=1}K^-]_{L=1}$
$D^0 \to [K_1(1270)^+[[\pi^+\pi^-]_{L=0}K^+]_{L=1}K^-]_{L=1}$
$D^0 \to [K_1(1270)^+[\rho(770)^0(\pi^+\pi^-)K^+]_{L=0}K^-]_{L=1}$
$D^0 \to [K_1(1270)^+[\rho(770)^0(\pi^+\pi^-)K^+]_{L=2}K^-]_{L=1}$
$D^0 \to [K_1(1270)^+[\omega(782)^0(\pi^+\pi^-)K^+]_{L=0}K^-]_{L=1}$
$D^0 \to [K_1(1270)^+[\omega(782)^0(\pi^+\pi^-)K^+]_{L=2}K^-]_{L=1}$
$D^0 \to [K_1(1270)^+[K^*(892)^0(K^+\pi^-)\pi^+]_{L=0}K^-]_{L=1}$
$D^0 \to [K_1(1270)^+[K^*(892)^0(K^+\pi^-)\pi^+]_{L=2}K^-]_{L=1}$
$D^0 \to [K_1(1270)^+[\rho(1450)^0(\pi^+\pi^-)K^+]_{L=0}K^-]_{L=1}$
$D^0 \to [K_1(1270)^+[\rho(1450)^0(\pi^+\pi^-)K^+]_{L=2}K^-]_{L=1}$

$D^0 \to [K_1(1400)^+[[K^+\pi^-]_{L=0}\pi^+]_{L=1}K^-]_{L=1}$
$D^0 \to [K_1(1400)^+[[\pi^+\pi^-]_{L=0}K^+]_{L=1}K^-]_{L=1}$
$D^0 \to [K_1(1400)^+[\rho(770)^0(\pi^+\pi^-)K^+]_{L=0}K^-]_{L=1}$
$D^0 \to [K_1(1400)^+[\rho(770)^0(\pi^+\pi^-)K^+]_{L=2}K^-]_{L=1}$
$D^0 \to [K_1(1400)^+[\omega(782)^0(\pi^+\pi^-)K^+]_{L=0}K^-]_{L=1}$
$D^0 \to [K_1(1400)^+[\omega(782)^0(\pi^+\pi^-)K^+]_{L=2}K^-]_{L=1}$
$D^0 \to [K_1(1400)^+[K^*(892)^0(K^+\pi^-)\pi^+]_{L=0}K^-]_{L=1}$
$D^0 \to [K_1(1400)^+[K^*(892)^0(K^+\pi^-)\pi^+]_{L=2}K^-]_{L=1}$
$D^0 \to [K_1(1400)^+[\rho(1450)^0(\pi^+\pi^-)K^+]_{L=0}K^-]_{L=1}$
$D^0 \to [K_1(1400)^+[\rho(1450)^0(\pi^+\pi^-)K^+]_{L=2}K^-]_{L=1}$

$D^0 \to [K_2^*(1430)^+[\rho(770)^0(\pi^+\pi^-)K^+]_{L=2}K^-]_{L=2}$
$D^0 \to [K_2^*(1430)^+[\omega(782)^0(\pi^+\pi^-)K^+]_{L=2}K^-]_{L=2}$
$D^0 \to [K_2^*(1430)^+[K^*(892)^0(K^+\pi^-)\pi^+]_{L=2}K^-]_{L=2}$
$D^0 \to [K_2^*(1430)^+[\rho(1450)^0(\pi^+\pi^-)K^+]_{L=2}K^-]_{L=2}$

$D^0 \to [K(1460)^+[[K^+\pi^-]_{L=0}\pi^+]_{L=0}K^-]_{L=0}$
$D^0 \to [K(1460)^+[[\pi^+\pi^-]_{L=0}K^+]_{L=0}K^-]_{L=0}$
$D^0 \to [K(1460)^+[\rho(770)^0(\pi^+\pi^-)K^+]_{L=1}K^-]_{L=0}$
$D^0 \to [K(1460)^+[\omega(782)^0(\pi^+\pi^-)K^+]_{L=1}K^-]_{L=0}$
$D^0 \to [K(1460)^+[K^*(892)^0(K^+\pi^-)\pi^+]_{L=1}K^-]_{L=0}$
$D^0 \to [K(1460)^+[\rho(1450)^0(\pi^+\pi^-)K^+]_{L=1}K^-]_{L=0}$

$D^0 \to [K^*(1680)^+[\rho(770)^0(\pi^+\pi^-)K^+]_{L=1}K^-]_{L=1}$
$D^0 \to [K^*(1680)^+[\omega(782)^0(\pi^+\pi^-)K^+]_{L=1}K^-]_{L=1}$
$D^0 \to [K^*(1680)^+[K^*(892)^0(K^+\pi^-)\pi^+]_{L=1}K^-]_{L=1}$
$D^0 \to [K^*(1680)^+[\rho(1450)^0(\pi^+\pi^-)K^+]_{L=1}K^-]_{L=1}$

C Background PDF

The background reweighting procedure described in Sec. 4.5.2 takes into account the 31 variables of Table 3.1. The resulting distributions are shown in Fig. 4.6 for the five CM variables and here in Figs. C.1–C.6 for the remaining 26 variables.
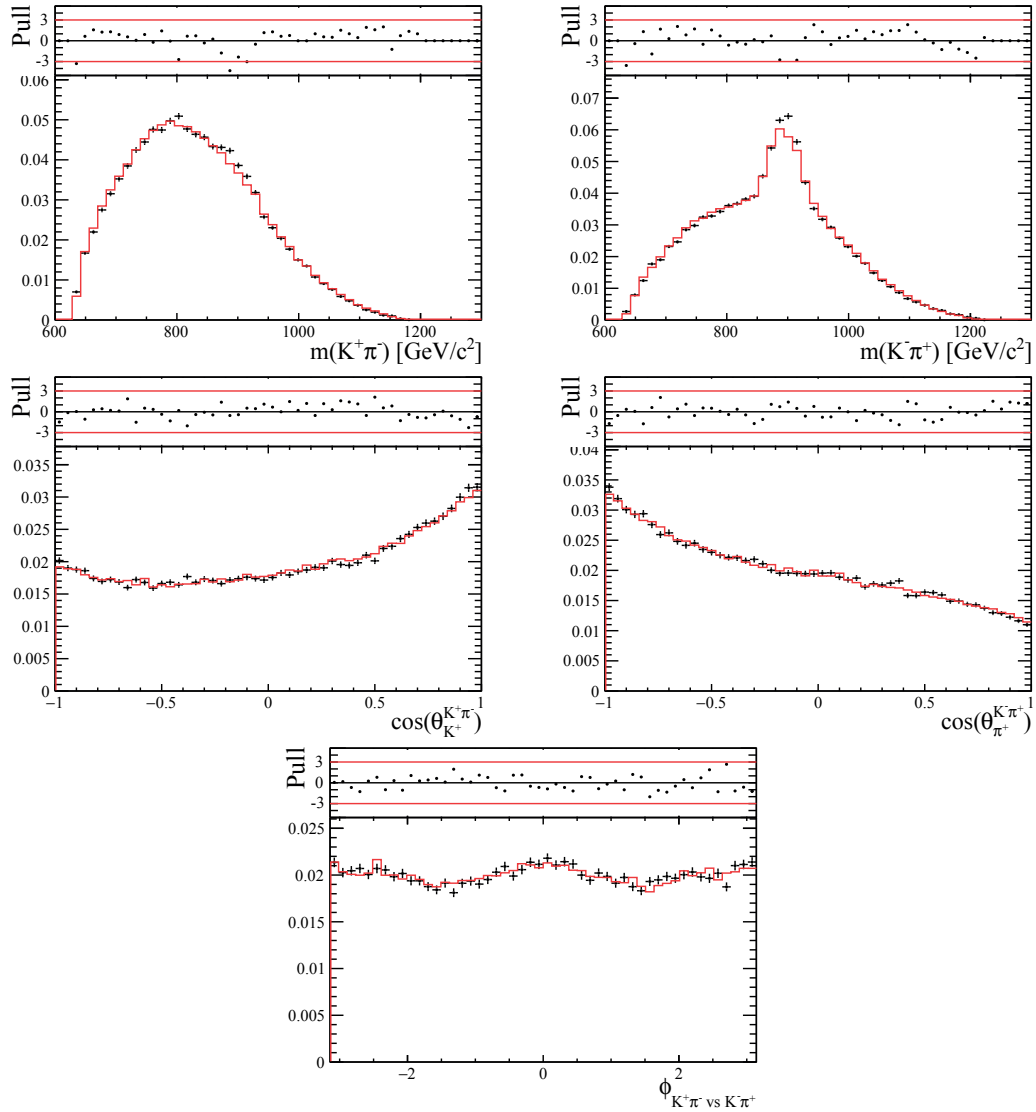
Figure C.1 – Background distributions of the five variables of the opposite-sign $K\pi$ system. The black points represent the data sideband events, and the red points the MC events after the reweighting procedure.
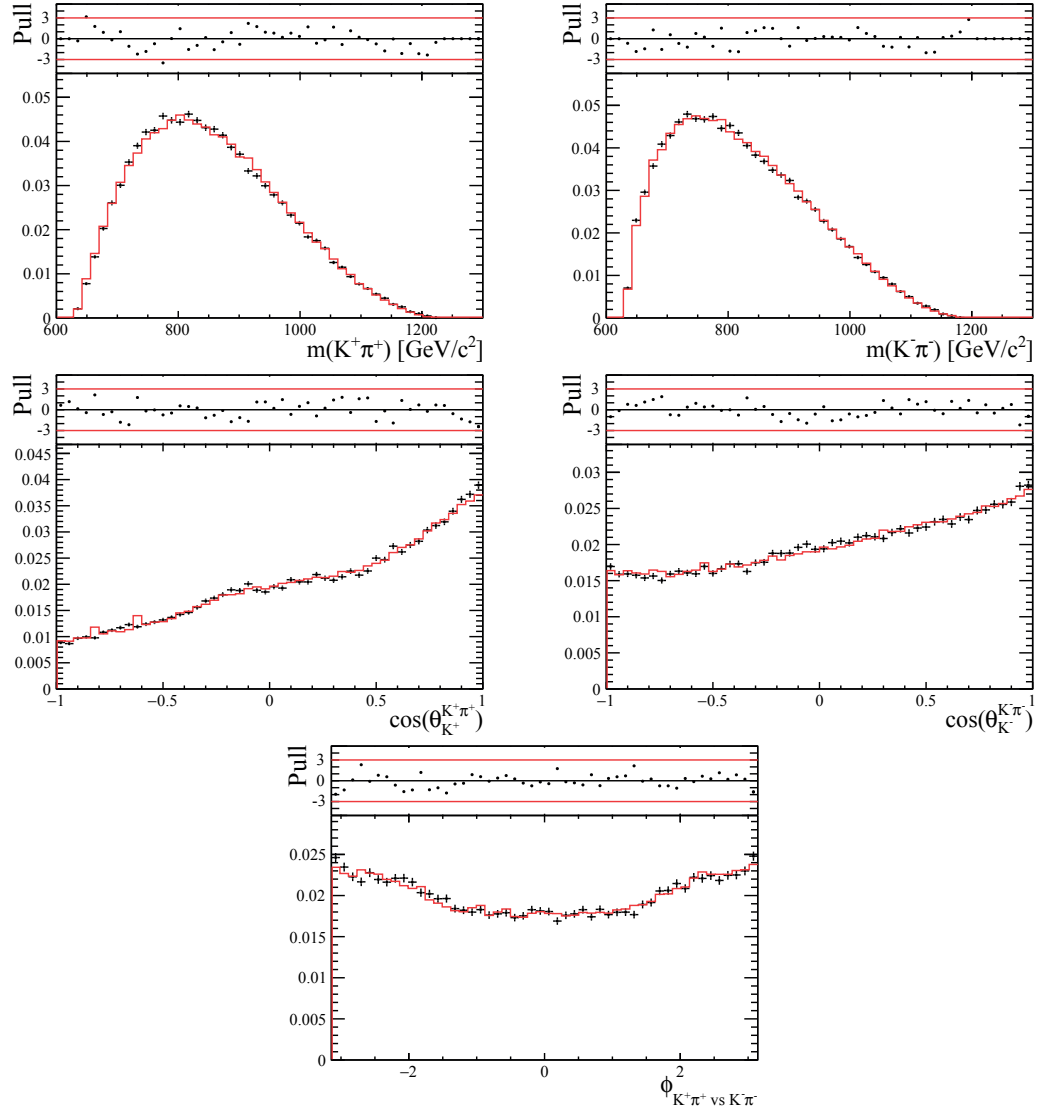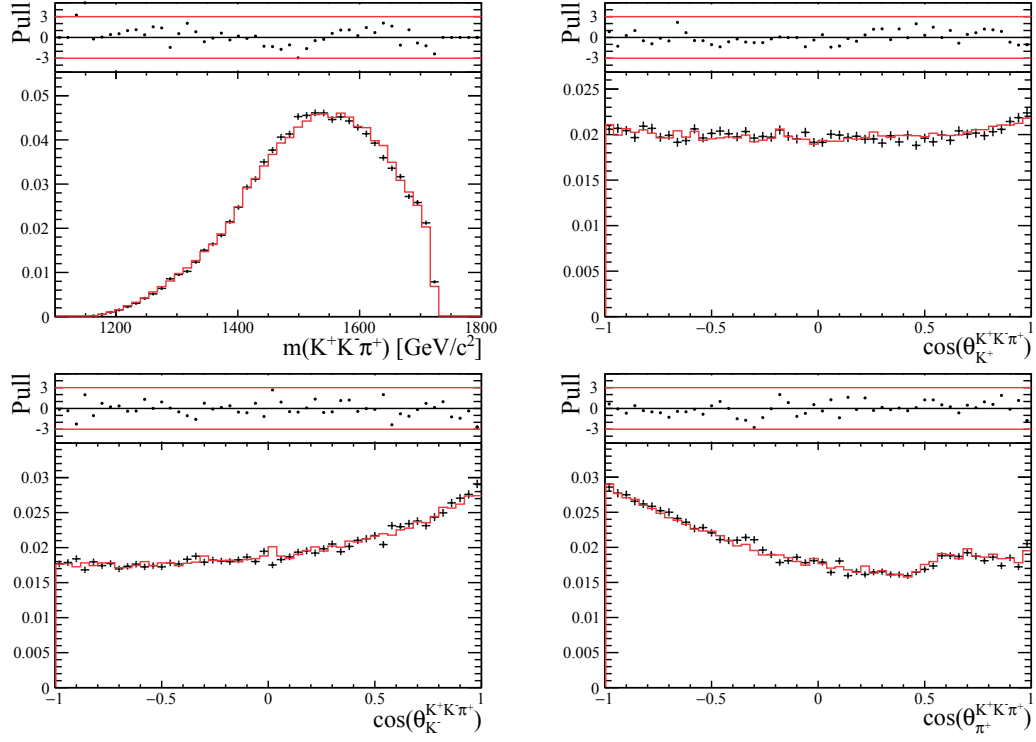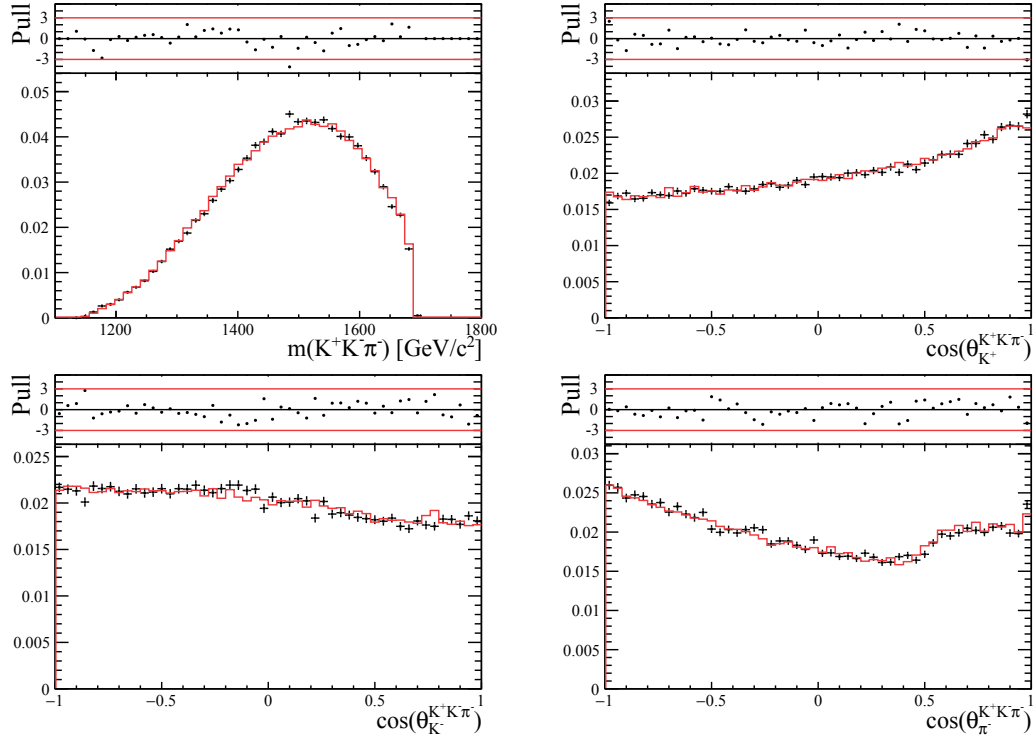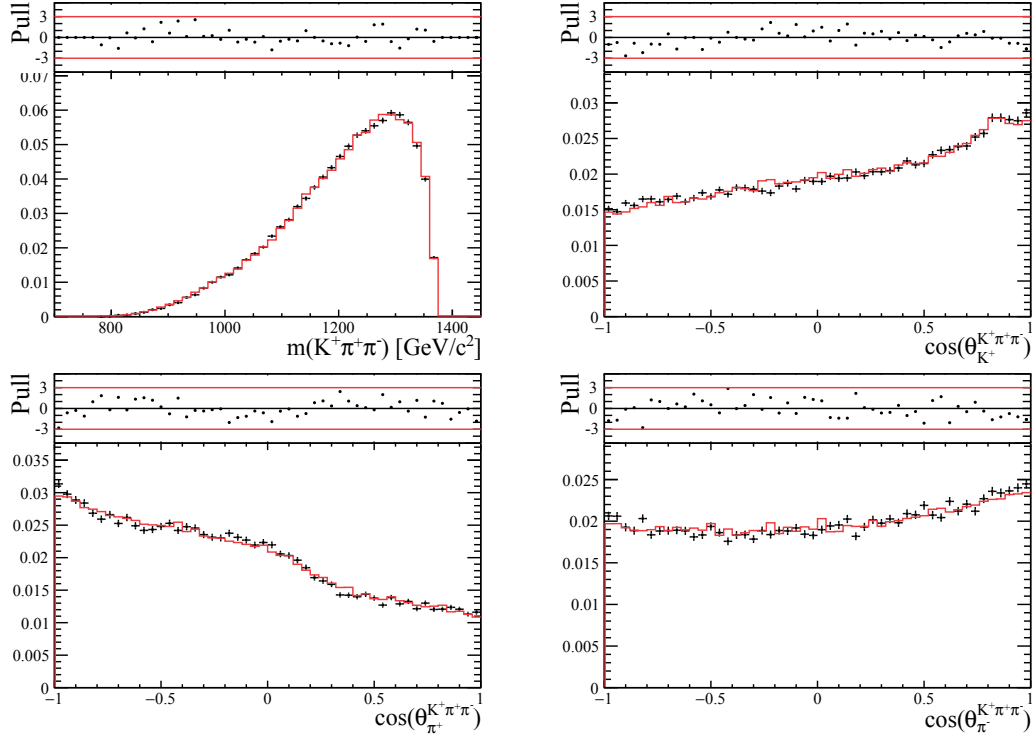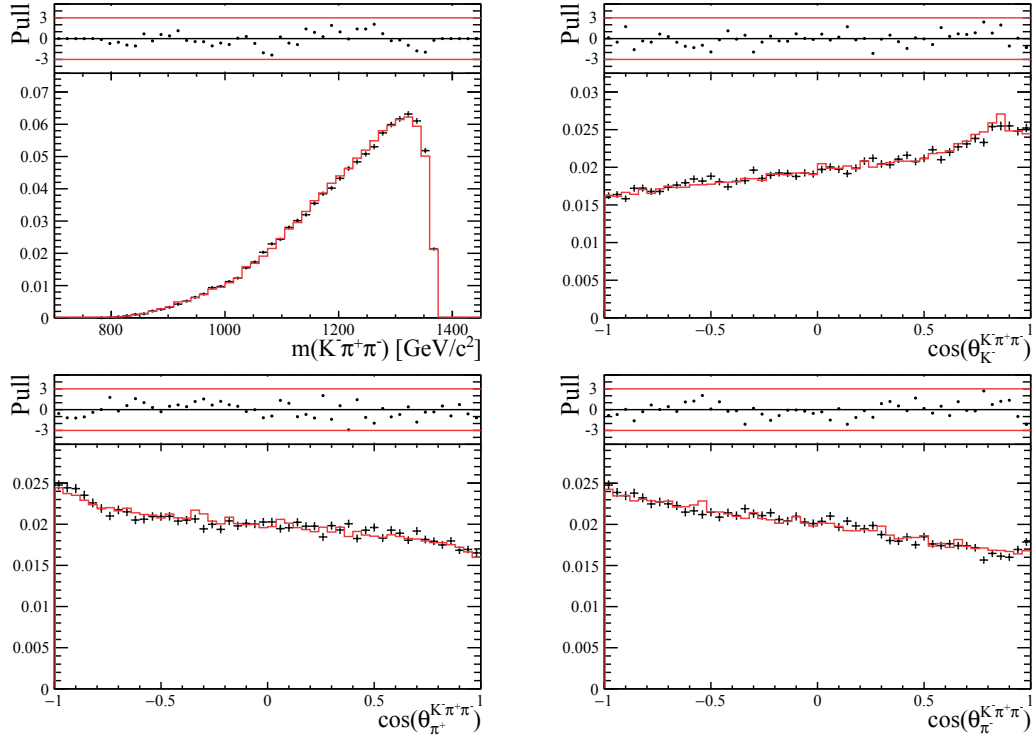
Figure C.2 – Background distributions of the five variables of the same-sign $K\pi$ system. The black points represent the data sideband events, and the red points the MC events after the reweighting procedure.

Figure C.3 – Background distributions of the four variables of the $K^+K^-\pi^+$ system. The black points represent the data sideband events, and the red points the MC events after the reweighting procedure.

Figure C.4 – Background distributions of the four variables of the $K^+K^-\pi^-$ system. The black points represent the data sideband events, and the red points the MC events after the reweighting procedure.

129

Figure C.5 – Background distributions of the four variables of the $K^+\pi^+\pi^-$ system. The black points represent the data sideband events, and the red points the MC events after the reweighting procedure.

Figure C.6 – Background distributions of the four variables of the $K^-\pi^+\pi^-$ system. The black points represent the data sideband events, and the red points the MC events after the reweighting procedure.

D Alternative background PDF

The method chosen to create a 5D background distribution is to reweight the MC integration sample to make it match the 5D distribution observed in the data sidebands. We developed an alternative to `hep_ml` to perform this reweighting. The resulting background PDF is used in order to assign a systematic uncertainty for the background description.

The reweighting procedure uses histograms. The 5D phase space is projected onto four histograms, one 2D histogram for the two masses variables (which are strongly correlated) and three 1D histograms for the angles. Then, one takes each event of the MC sample, checks in which bin it falls in the four histograms, calculates the ratio between the bin contents for the data sidebands and the MC sample, and finally multiplies these four ratios to obtain an overall weight per event. It has been observed that this method does not work properly if only projections on the five default CM variables are used. After the reweighting, the distributions of these five variables are correctly reproduced but the other projections are not. This can be explained considering that the mechanism to reweight the distributions does not take all the correlations into account.

The solution found to overcome this correlation problem, is to keep the four separate histograms, but to iteratively reweight the MC sample for the 31 different variables listed in Table 3.1. The variables are grouped in 7 different sets as shown in Table 3.1. The first three sets correspond to two-body systems, with one 2D projection (two two-body masses) and three 1D projections (cosines of helicity angles and angle between decay planes), and the last four sets correspond to three-body systems, with four 1D projections (mass and cosines of helicity angles).

Once the weights for each MC event have been determined such as to reproduce the data-sideband histograms of one set of variables, they are updated by repeating the process for the next set of variables. The procedure is iterated on the seven sets in the following order: 2, 3, 4, 5, 6, 7, 1. The CM variables are reweighted last such that they show the best agreement. These weights contain the information of all the variables from Table 3.1.

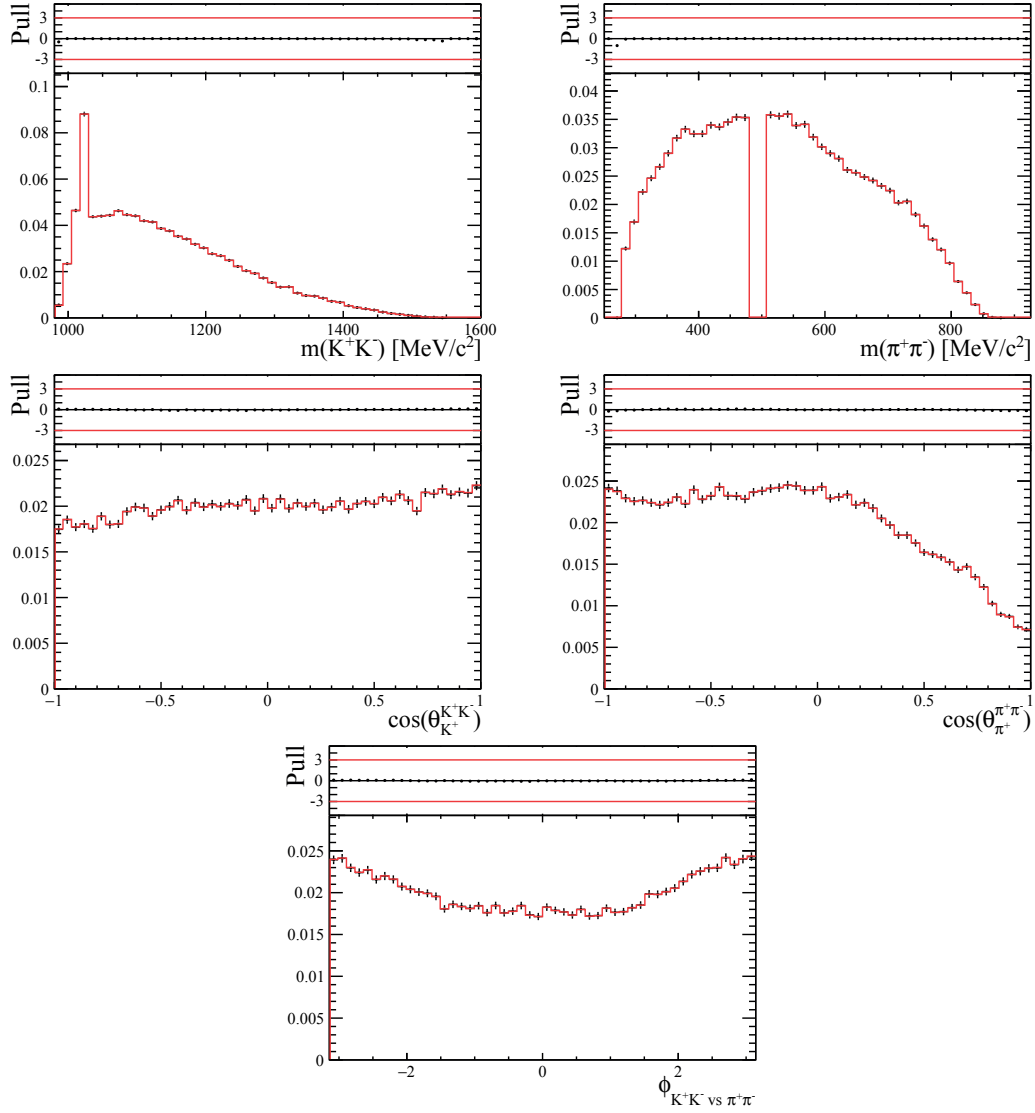Fig. D.1 to D.7 show the projections of the data sidebands along with the reweighted MC.

Figure D.1 – Background distributions of the five variables of Set 1. The black points represent the data sidebands events, and the red points the MC events after the reweighting procedure.
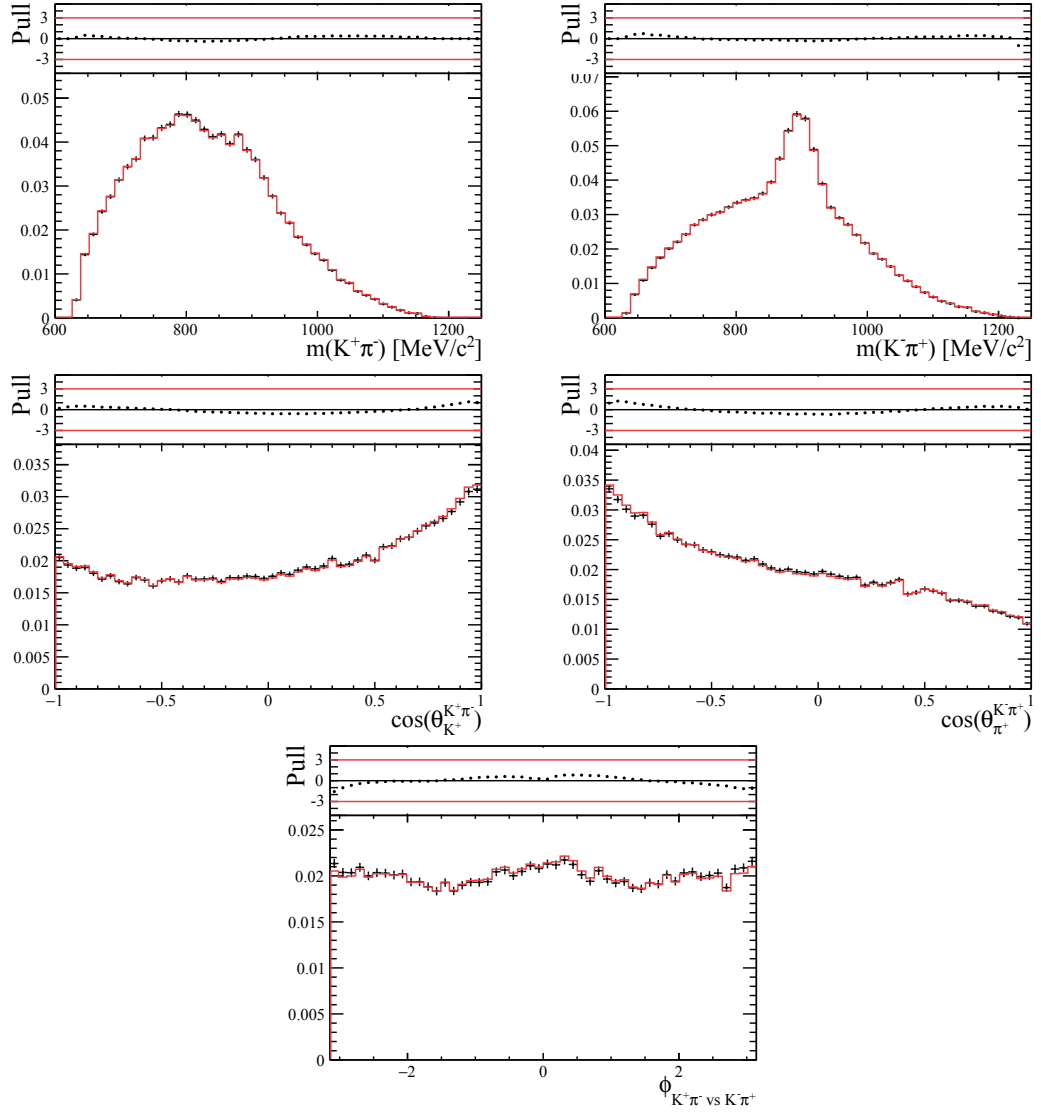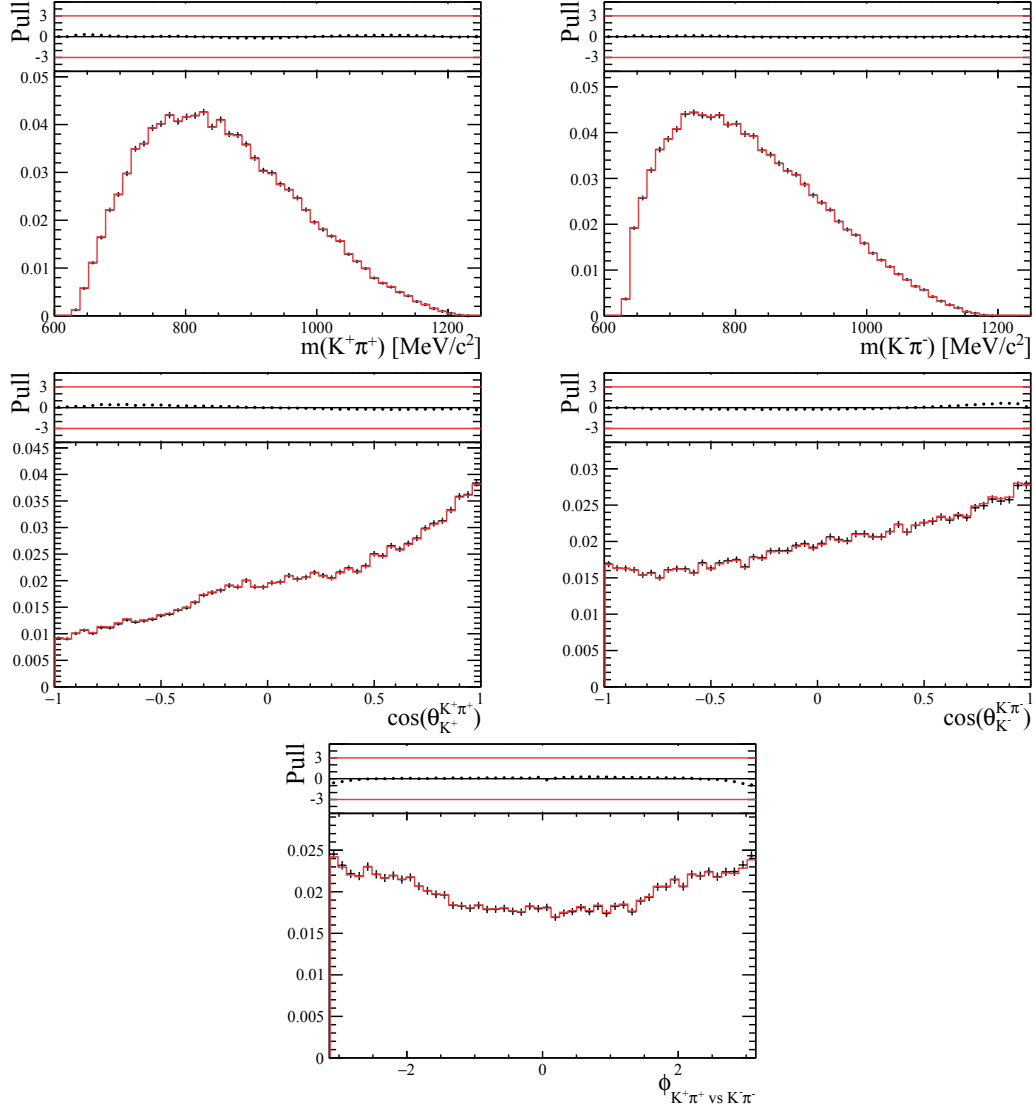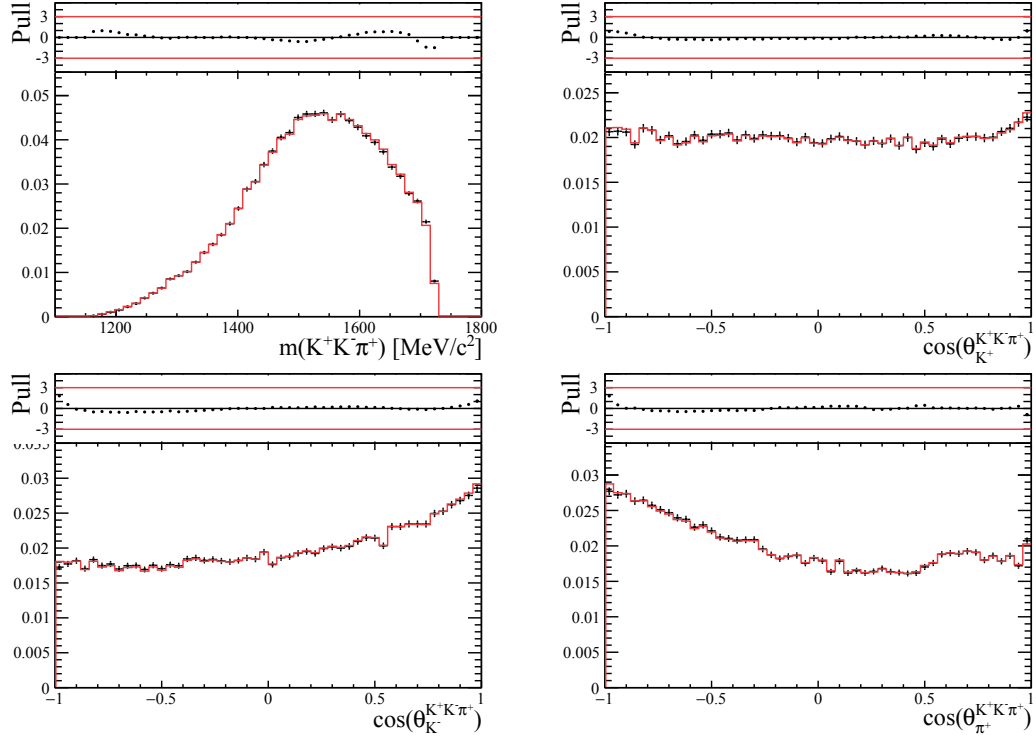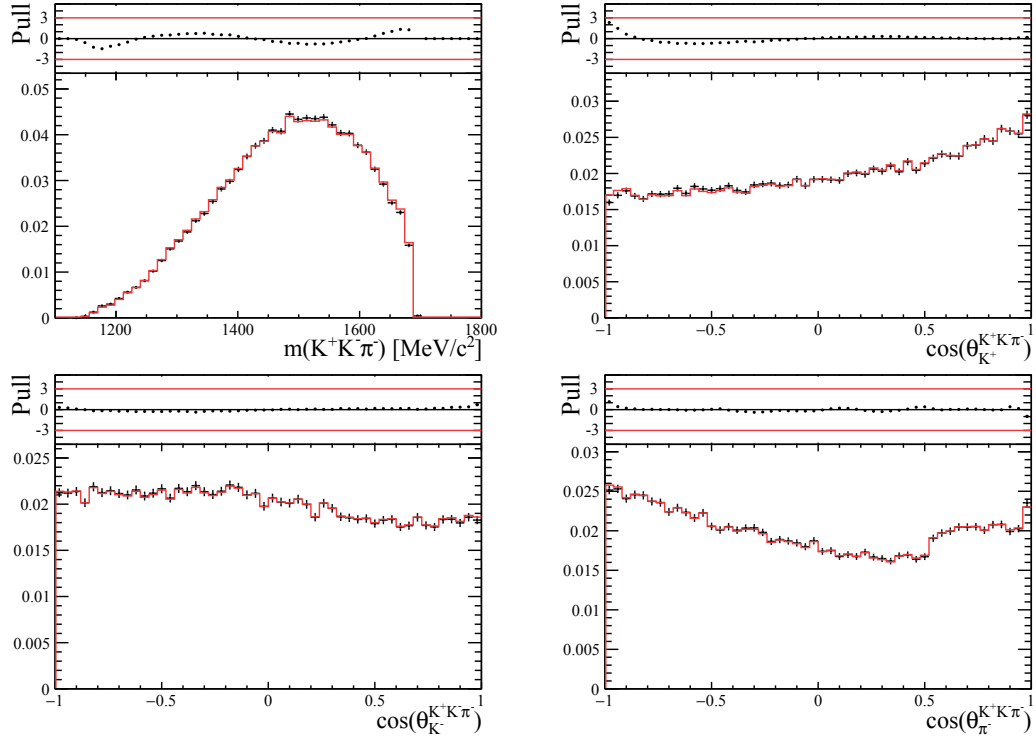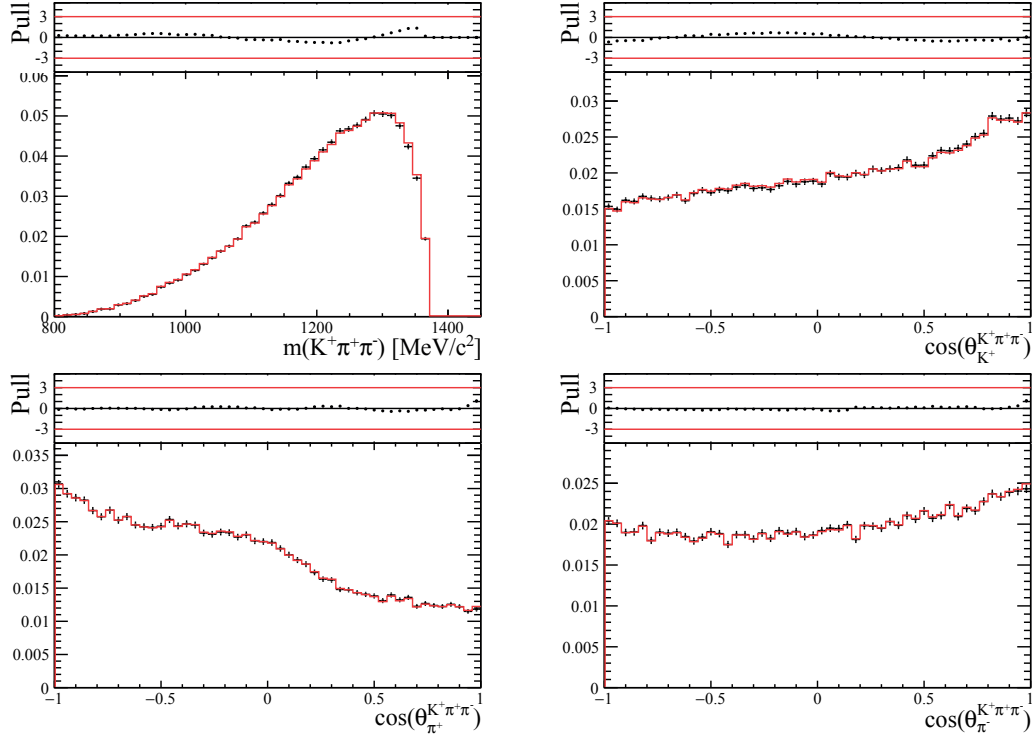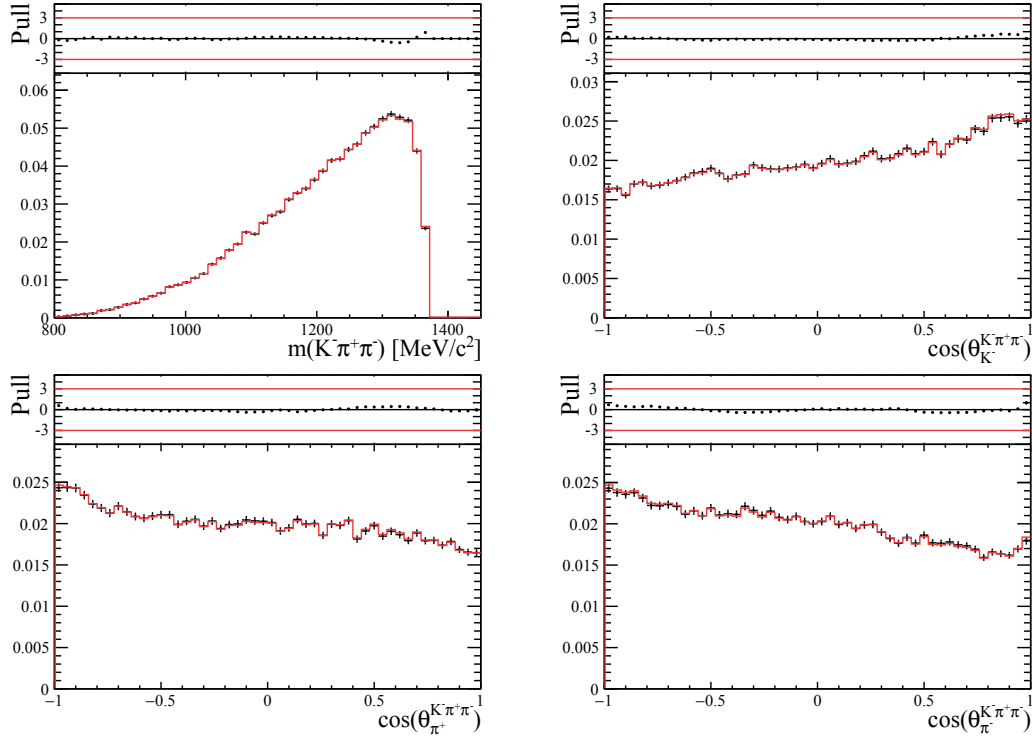
Figure D.2 – Background distributions of the five variables of Set 2. The black points represent the data sidebands events, and the red points the MC events after the reweighting procedure.

Figure D.3 – Background distributions of the five variables of Set 3. The black points represent the data sidebands events, and the red points the MC events after the reweighting procedure.

Figure D.4 – Background distributions of the four variables of Set 4. The black points represent the data sidebands events, and the red points the MC events after the reweighting procedure.

Figure D.5 – Background distributions of the four variables of Set 5. The black points represent the data sidebands events, and the red points the MC events after the reweighting procedure.

Figure D.6 – Background distributions of the four variables of Set 6. The black points represent the data sidebands events, and the red points the MC events after the reweighting procedure.

Figure D.7 – Background distributions of the four variables of Set 7. The black points represent the data sidebands events, and the red points the MC events after the reweighting procedure.

E | Fit bias

The means and the widths of the modulus, phase and fit fraction are shown for all the pseudo-experiments performed for the systematic uncertainties studies in Figs. E.1 to E.8.
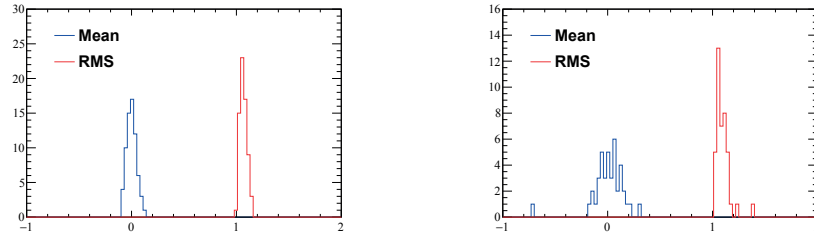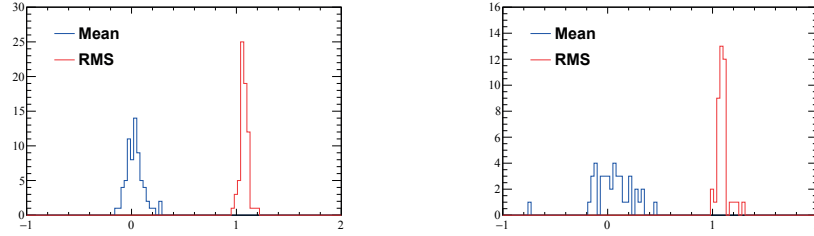

Figure E.1 – Distributions of the means and widths of the moduli and phases on the left and of the fit fractions on the right for the pseudoexperiments for signal only.
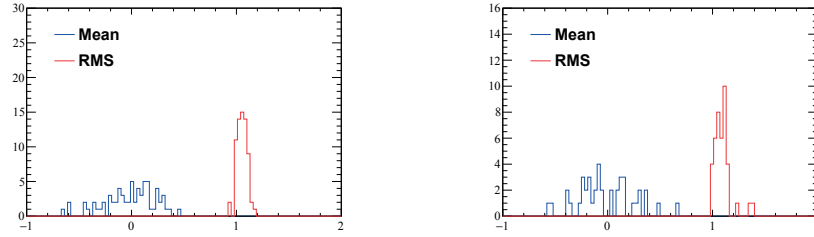
Figure E.2 – Distributions of the means and widths of the moduli and phases on the left and of the fit fractions on the right for the pseudoexperiments for signal and background.

Figure E.3 – Distributions of the means and widths of the moduli and phases on the left and of the fit fractions on the right for the pseudoexperiments for signal and mistag.
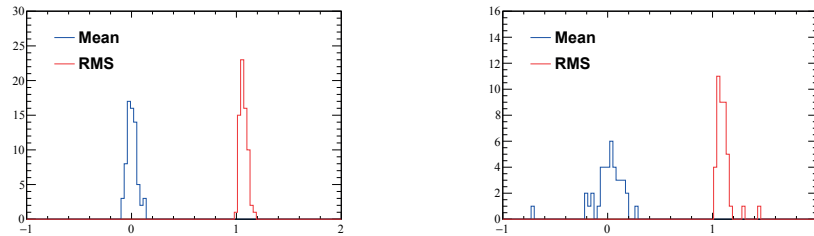

Figure E.4 – Distributions of the means and widths of the moduli and phases on the left and of the fit fractions on the right for the pseudoexperiments for signal and detection asymmetry.
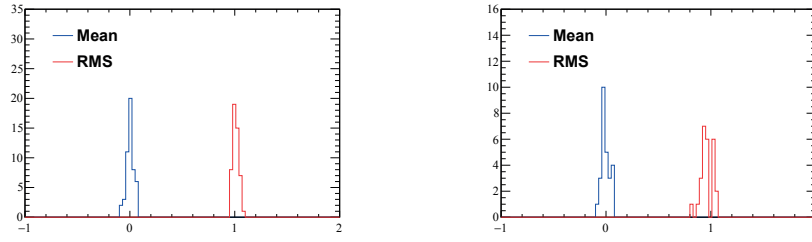
Figure E.5 – Distributions of the means and widths of the modulus asymmetries and phase differences on the left and of the fit fraction asymmetries on the right for the pseudoexperiments for signal only.
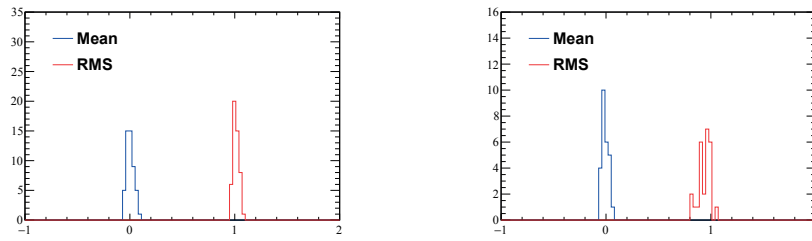

Figure E.6 – Distributions of the means and widths of the modulus asymmetries and phase differences on the left and of the fit fraction asymmetries on the right for the pseudoexperiments for signal and background.
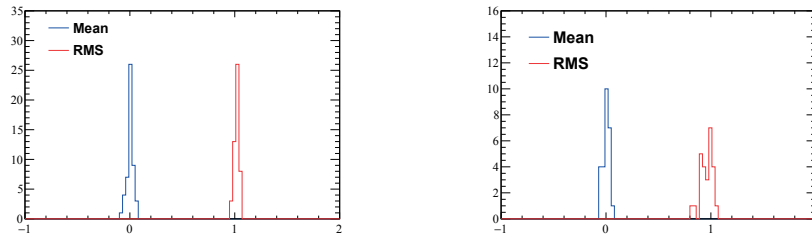

Figure E.7 – Distributions of the means and widths of the modulus asymmetries and phase differences on the left and of the fit fraction asymmetries on the right for the pseudoexperiments for signal and mistag.
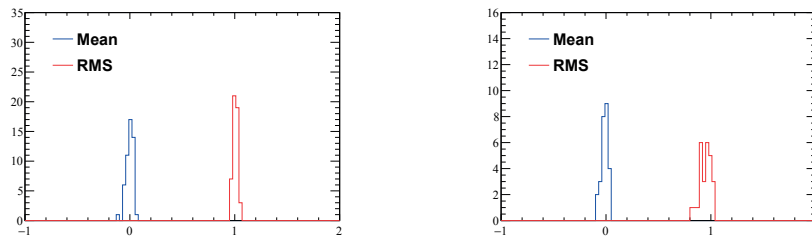

Figure E.8 – Distributions of the means and widths of the modulus asymmetries and phase differences on the left and of the fit fraction asymmetries on the right for the pseudoexperiments for signal and detection asymmetry.

F Result of the cross-checks

In section 5.8, we test different hypotheses. This section lists all the resulting models.

Table F.1 – Result of the fit performed without Δm cut.

Amplitude	$|c_k|$	$\arg(c_k)$ [rad]	Fit fraction [%]
$D^0 \to [\phi(1020)^0(\rho-\omega)^0]_{L=0}$	1 (fixed)	0 (fixed)	23.43 ± 0.37
$D^0 \to [K^-\pi^+]_{L=0}[K^+\pi^-]_{L=0}$	0.29 ± 0.00	−0.59 ± 0.01	18.82 ± 0.34
$D^0 \to K_1(1270)^+K^-$	0.46 ± 0.01	2.01 ± 0.02	18.37 ± 0.37
$D^0 \to K_1(1400)^+K^-$	0.63 ± 0.01	1.04 ± 0.02	18.20 ± 0.44
$D^0 \to [K^*(892)^0\bar{K}^*(892)^0]_{L=0}$	0.28 ± 0.00	−0.27 ± 0.02	9.10 ± 0.21
$D^0 \to K^*(1680)^0[K^-\pi^+]_{L=0}$	2.28 ± 0.03	0.47 ± 0.02	6.59 ± 0.15
$D^0 \to [K^*(892)^0\bar{K}^*(892)^0]_{L=1}$	0.27 ± 0.00	1.23 ± 0.02	4.97 ± 0.16
$D^0 \to K_1(1270)^-K^+$	0.23 ± 0.01	2.10 ± 0.03	4.40 ± 0.17
$D^0 \to [K^+K^-]_{L=0}[\pi^+\pi^-]_{L=0}$	0.12 ± 0.00	−2.45 ± 0.03	3.25 ± 0.16
$D^0 \to K_1(1400)^-K^+$	0.25 ± 0.01	0.04 ± 0.04	2.89 ± 0.19
$D^0 \to [K^*(1680)^0\bar{K}^*(892)^0]_{L=0}$	0.83 ± 0.02	2.99 ± 0.03	2.80 ± 0.15
$D^0 \to [\bar{K}^*(1680)^0K^*(892)^0]_{L=1}$	1.01 ± 0.02	−2.75 ± 0.02	2.66 ± 0.10
$D^0 \to \bar{K}^*(1680)^0[K^+\pi^-]_{L=0}$	1.31 ± 0.03	1.07 ± 0.02	2.35 ± 0.09
$D^0 \to [\phi(1020)^0(\rho-\omega)^0]_{L=2}$	1.33 ± 0.03	0.55 ± 0.02	2.30 ± 0.08
$D^0 \to [K^*(892)^0\bar{K}^*(892)^0]_{L=2}$	0.70 ± 0.02	2.88 ± 0.03	1.84 ± 0.10
$D^0 \to [K^*(1680)^0\bar{K}^*(892)^0]_{L=1}$	0.76 ± 0.02	0.14 ± 0.03	1.50 ± 0.08
$D^0 \to \phi(1020)^0[\pi^+\pi^-]_{L=0}$	0.05 ± 0.00	−1.70 ± 0.04	1.45 ± 0.09
$D^0 \to [\phi(1020)^0\rho(1450)^0]_{L=1}$	0.76 ± 0.04	1.19 ± 0.04	0.97 ± 0.09
$D^0 \to a_0(980)^0f_2(1270)^0$	1.47 ± 0.06	0.24 ± 0.04	0.64 ± 0.05
$D^0 \to a_1(1260)^-\pi^+$	0.19 ± 0.01	0.17 ± 0.06	0.48 ± 0.06
$D^0 \to a_1(1260)^+\pi^-$	0.18 ± 0.01	−2.79 ± 0.07	0.43 ± 0.05
$D^0 \to [\phi(1020)^0(\rho-\omega)^0]_{L=1}$	0.16 ± 0.01	0.27 ± 0.07	0.42 ± 0.05
$D^0 \to [K^*(1680)^0\bar{K}^*(892)^0]_{L=2}$	1.21 ± 0.09	−2.47 ± 0.09	0.32 ± 0.05
$D^0 \to [K^+K^-]_{L=0}(\rho-\omega)^0$	0.20 ± 0.01	3.10 ± 0.08	0.28 ± 0.03
$D^0 \to \phi(1020)^0f_{\underline{2}}(1270)^0$	1.43 ± 0.09	1.74 ± 0.06	0.19 ± 0.02
$D^0 \to K^*(892)^0\bar{K}^*_2(1430)^0$	1.49 ± 0.09	2.00 ± 0.07	0.16 ± 0.02

Sum of fit fractions   128.80 ± 0.93
χ^2/ndf   9400/8123 = 1.16

$a_1(1260)^+ \to [\phi(1020)^0\pi^+]_{L=0}$	1 (fixed)	0 (fixed)	100

$K_1(1270)^+ \to [K^*(892)^0\pi^+]_{L=0}$	0.62 ± 0.02	0.59 ± 0.03	51.21 ± 0.88
$K_1(1270)^+ \to [(\rho-\omega)^0K^+]_{L=0}$	1 (fixed)	0 (fixed)	47.32 ± 1.77
$K_1(1270)^+ \to [K^+\pi^-]_{L=0}\pi^+$	0.63 ± 0.03	−1.88 ± 0.04	6.20 ± 0.46
$K_1(1270)^+ \to [K^*(892)^0\pi^+]_{L=2}$	0.91 ± 0.05	−2.55 ± 0.04	1.97 ± 0.16
$K_1(1270)^+ \to [\rho(1450)^0K^+]_{L=0}$	0.39 ± 0.07	−2.22 ± 0.12	0.93 ± 0.34

Sum of fit fractions   107.63 ± 2.03

$K_1(1400)^+ \to [K^*(892)^0\pi^+]_{L=0}$	1 (fixed)	0 (fixed)	100

Table F.2 – Result of the fit performed without K_S^0 veto.

Amplitude	$|c_k|$	arg(c_k) [rad]	Fit fraction [%]
$D^0 \to [\phi(1020)^0(\rho-\omega)^0]_{L=0}$	1 (fixed)	0 (fixed)	23.08 ± 0.29
$D^0 \to K_1(1400)^+ K^-$	0.63 ± 0.01	1.05 ± 0.01	18.44 ± 0.30
$D^0 \to K_1(1270)^+ K^-$	0.46 ± 0.00	2.02 ± 0.01	18.38 ± 0.23
$D^0 \to [K^-\pi^+]_{L=0}[K^+\pi^-]_{L=0}$	0.28 ± 0.00	−0.59 ± 0.01	18.26 ± 0.28
$D^0 \to [K^*(892)^0\bar{K}^*(892)^0]_{L=0}$	0.28 ± 0.00	−0.26 ± 0.01	9.31 ± 0.14
$D^0 \to K^*(1680)^0[K^-\pi^+]_{L=0}$	2.27 ± 0.03	0.46 ± 0.01	6.57 ± 0.12
$D^0 \to [K^*(892)^0\bar{K}^*(892)^0]_{L=1}$	0.27 ± 0.00	1.22 ± 0.01	4.99 ± 0.08
$D^0 \to K_1(1270)^- K^+$	0.23 ± 0.00	2.09 ± 0.02	4.41 ± 0.12
$D^0 \to [K^+ K^-]_{L=0}[\pi^+\pi^-]_{L=0}$	0.12 ± 0.00	−2.49 ± 0.02	3.02 ± 0.14
$D^0 \to K_1(1400)^- K^+$	0.25 ± 0.01	0.03 ± 0.03	2.88 ± 0.12
$D^0 \to [K^*(1680)^0\bar{K}^*(892)^0]_{L=0}$	0.82 ± 0.02	3.01 ± 0.02	2.78 ± 0.11
$D^0 \to [\bar{K}^*(1680)^0 K^*(892)^0]_{L=1}$	1.02 ± 0.02	−2.75 ± 0.02	2.74 ± 0.08
$D^0 \to \bar{K}^*(1680)^0[K^+\pi^-]_{L=0}$	1.34 ± 0.02	1.05 ± 0.02	2.46 ± 0.08
$D^0 \to [\phi(1020)^0(\rho-\omega)^0]_{L=2}$	1.33 ± 0.02	0.55 ± 0.02	2.29 ± 0.06
$D^0 \to [K^*(892)^0\bar{K}^*(892)^0]_{L=2}$	0.70 ± 0.01	2.87 ± 0.02	1.86 ± 0.06
$D^0 \to [K^*(1680)^0\bar{K}^*(892)^0]_{L=1}$	0.75 ± 0.02	0.14 ± 0.02	1.50 ± 0.06
$D^0 \to \phi(1020)^0[\pi^+\pi^-]_{L=0}$	0.05 ± 0.00	−1.70 ± 0.03	1.44 ± 0.05
$D^0 \to [\phi(1020)^0\rho(1450)^0]_{L=1}$	0.76 ± 0.02	1.20 ± 0.03	0.97 ± 0.04
$D^0 \to a_0(980)^0 f_2(1270)^0$	1.50 ± 0.05	0.23 ± 0.03	0.67 ± 0.04
$D^0 \to a_1(1260)^-\pi^+$	0.20 ± 0.01	0.17 ± 0.04	0.50 ± 0.05
$D^0 \to a_1(1260)^+\pi^-$	0.19 ± 0.01	−2.78 ± 0.05	0.47 ± 0.03
$D^0 \to [\phi(1020)^0(\rho-\omega)^0]_{L=1}$	0.16 ± 0.00	0.26 ± 0.05	0.43 ± 0.02
$D^0 \to [K^*(1680)^0\bar{K}^*(892)^0]_{L=2}$	1.21 ± 0.05	−2.44 ± 0.06	0.32 ± 0.03
$D^0 \to [K^+ K^-]_{L=0}(\rho-\omega)^0$	0.20 ± 0.01	3.00 ± 0.05	0.28 ± 0.02
$D^0 \to \phi(1020)^0 f_2(1270)^0$	1.45 ± 0.08	1.72 ± 0.05	0.20 ± 0.02
$D^0 \to K^*(892)^0\bar{K}_2^*(1430)^0$	1.52 ± 0.08	2.02 ± 0.06	0.16 ± 0.02

| | | Sum of fit fractions | 128.43 ± 0.67 |
| | | χ^2/ndf | 9347/8121 = 1.15 |

| $D^0 \to K_S^0[K^+ K^-]_{L=0}$ | 1 (fixed) | 0 (fixed) | 51.10 ± 3.57 |
| $D^0 \to [\phi(1020)^0 K_S^0]_{L=0}$ | 4.97 ± 0.36 | 3.13 ± 1.41 | 48.90 ± 3.57 |

| | | Sum of fit fractions | 100 |

| $a_1(1260)^+ \to [\phi(1020)^0\pi^+]_{L=0}$ | 1 (fixed) | 0 (fixed) | 100 |

$K_1(1270)^+ \to [K^*(892)^0\pi^+]_{L=0}$	0.61 ± 0.01	0.60 ± 0.01	50.87 ± 0.60
$K_1(1270)^+ \to [(\rho-\omega)^0 K^+]_{L=0}$	1 (fixed)	0 (fixed)	48.34 ± 0.71
$K_1(1270)^+ \to [K^+\pi^-]_{L=0}\pi^+$	0.59 ± 0.02	−1.93 ± 0.02	5.66 ± 0.34
$K_1(1270)^+ \to [K^*(892)^0\pi^+]_{L=2}$	0.92 ± 0.03	−2.55 ± 0.03	2.08 ± 0.13
$K_1(1270)^+ \to [\rho(1450)^0 K^+]_{L=0}$	0.45 ± 0.02	−2.42 ± 0.08	1.26 ± 0.10

| | | Sum of fit fractions | 108.22 ± 0.81 |

| $K_1(1400)^+ \to [K^*(892)^0\pi^+]_{L=0}$ | 1 (fixed) | 0 (fixed) | 100 |

Table F.3 – Result of the fit performed while keeping all the multiple candidates.

Amplitude	$|c_k|$			$\arg(c_k)$ [rad]			Fit fraction [%]		
$D^0 \to [\phi(1020)^0(\rho-\omega)^0]_{L=0}$	1 (fixed)			0 (fixed)			23.69	$\pm$	0.38
$D^0 \to [K^-\pi^+]_{L=0}[K^+\pi^-]_{L=0}$	0.28	$\pm$	0.00	-0.60	$\pm$	0.01	18.57	$\pm$	0.35
$D^0 \to K_1(1400)^+K^-$	0.63	$\pm$	0.01	1.04	$\pm$	0.02	18.47	$\pm$	0.45
$D^0 \to K_1(1270)^+K^-$	0.46	$\pm$	0.01	2.01	$\pm$	0.02	18.35	$\pm$	0.37
$D^0 \to [K^*(892)^0\bar{K}^*(892)^0]_{L=0}$	0.28	$\pm$	0.00	-0.27	$\pm$	0.02	9.19	$\pm$	0.21
$D^0 \to K^*(1680)^0[K^-\pi^+]_{L=0}$	2.26	$\pm$	0.03	0.46	$\pm$	0.02	6.57	$\pm$	0.15
$D^0 \to [K^*(892)^0\bar{K}^*(892)^0]_{L=1}$	0.27	$\pm$	0.00	1.21	$\pm$	0.02	4.98	$\pm$	0.16
$D^0 \to K_1(1270)^-K^+$	0.22	$\pm$	0.01	2.10	$\pm$	0.03	4.34	$\pm$	0.17
$D^0 \to [K^+K^-]_{L=0}[\pi^+\pi^-]_{L=0}$	0.12	$\pm$	0.00	-2.49	$\pm$	0.03	3.11	$\pm$	0.17
$D^0 \to K_1(1400)^-K^+$	0.25	$\pm$	0.01	0.05	$\pm$	0.04	2.83	$\pm$	0.19
$D^0 \to [K^*(1680)^0\bar{K}^*(892)^0]_{L=0}$	0.82	$\pm$	0.02	2.99	$\pm$	0.03	2.79	$\pm$	0.15
$D^0 \to [\bar{K}^*(1680)^0K^*(892)^0]_{L=1}$	1.01	$\pm$	0.02	-2.75	$\pm$	0.02	2.70	$\pm$	0.11
$D^0 \to \bar{K}^*(1680)^0[K^+\pi^-]_{L=0}$	1.31	$\pm$	0.03	1.06	$\pm$	0.02	2.37	$\pm$	0.09
$D^0 \to [\phi(1020)^0(\rho-\omega)^0]_{L=2}$	1.31	$\pm$	0.03	0.54	$\pm$	0.02	2.29	$\pm$	0.08
$D^0 \to [K^*(892)^0\bar{K}^*(892)^0]_{L=2}$	0.70	$\pm$	0.02	2.86	$\pm$	0.03	1.86	$\pm$	0.10
$D^0 \to [K^*(1680)^0\bar{K}^*(892)^0]_{L=1}$	0.75	$\pm$	0.02	0.13	$\pm$	0.03	1.48	$\pm$	0.08
$D^0 \to \phi(1020)^0[\pi^+\pi^-]_{L=0}$	0.05	$\pm$	0.00	-1.71	$\pm$	0.04	1.47	$\pm$	0.09
$D^0 \to [\phi(1020)^0\rho(1450)^0]_{L=1}$	0.76	$\pm$	0.04	1.18	$\pm$	0.04	0.98	$\pm$	0.09
$D^0 \to a_0(980)^0f_2(1270)^0$	1.54	$\pm$	0.06	0.23	$\pm$	0.04	0.71	$\pm$	0.05
$D^0 \to a_1(1260)^+\pi^-$	0.19	$\pm$	0.01	-2.82	$\pm$	0.07	0.47	$\pm$	0.05
$D^0 \to a_1(1260)^-\pi^+$	0.19	$\pm$	0.01	0.17	$\pm$	0.06	0.47	$\pm$	0.06
$D^0 \to [\phi(1020)^0(\rho-\omega)^0]_{L=1}$	0.16	$\pm$	0.01	0.26	$\pm$	0.07	0.43	$\pm$	0.05
$D^0 \to [K^*(1680)^0\bar{K}^*(892)^0]_{L=2}$	1.21	$\pm$	0.09	-2.45	$\pm$	0.08	0.32	$\pm$	0.05
$D^0 \to [K^+K^-]_{L=0}(\rho-\omega)^0$	0.20	$\pm$	0.02	3.02	$\pm$	0.08	0.28	$\pm$	0.04
$D^0 \to \phi(1020)^0f_2(1270)^0$	1.40	$\pm$	0.09	1.71	$\pm$	0.06	0.19	$\pm$	0.02
$D^0 \to K^*(892)^0\bar{K}^*_2(1430)^0$	1.54	$\pm$	0.09	2.01	$\pm$	0.07	0.17	$\pm$	0.02
				Sum of fit fractions			129.06	$\pm$	0.94
				χ^2/ndf			9285/8123 = 1.14		

$a_1(1260)^+ \to [\phi(1020)^0\pi^+]_{L=0}$	1 (fixed)			0 (fixed)			100		

$K_1(1270)^+ \to [K^*(892)^0\pi^+]_{L=0}$	0.61	$\pm$	0.02	0.60	$\pm$	0.03	51.19	$\pm$	0.88
$K_1(1270)^+ \to [(\rho-\omega)^0K^+]_{L=0}$	1 (fixed)			0 (fixed)			48.13	$\pm$	1.78
$K_1(1270)^+ \to [K^+\pi^-]_{L=0}\pi^+$	0.60	$\pm$	0.03	-1.92	$\pm$	0.04	5.80	$\pm$	0.46
$K_1(1270)^+ \to [K^*(892)^0\pi^+]_{L=2}$	0.91	$\pm$	0.04	-2.55	$\pm$	0.04	2.00	$\pm$	0.16
$K_1(1270)^+ \to [\rho(1450)^0K^+]_{L=0}$	0.44	$\pm$	0.06	-2.35	$\pm$	0.11	1.18	$\pm$	0.38
				Sum of fit fractions			108.31	$\pm$	2.04

$K_1(1400)^+ \to [K^*(892)^0\pi^+]_{L=0}$	1 (fixed)			0 (fixed)			100		

Table F.4 – Result of the fit performed with an enlarged $\phi(1020)^0$ meson.

Amplitude	$|c|$	arg(c) [rad]	Fit fraction [%]
$D^0 \to [\phi(1020)^0(\rho-\omega)^0]_{L=0}$	1 (fixed)	0 (fixed)	23.86 $\pm$ 0.38
$D^0 \to [K^-\pi^+]_{L=0}[K^+\pi^-]_{L=0}$	0.28 $\pm$ 0.00	-0.60 $\pm$ 0.01	18.55 $\pm$ 0.35
$D^0 \to K_1(1400)^+K^-$	0.63 $\pm$ 0.01	1.03 $\pm$ 0.02	18.48 $\pm$ 0.46
$D^0 \to K_1(1270)^+K^-$	0.46 $\pm$ 0.01	2.02 $\pm$ 0.02	18.37 $\pm$ 0.37
$D^0 \to [K^*(892)^0\bar{K}^*(892)^0]_{L=0}$	0.28 $\pm$ 0.00	-0.28 $\pm$ 0.02	9.24 $\pm$ 0.21
$D^0 \to K^*(1680)^0[K^-\pi^+]_{L=0}$	2.24 $\pm$ 0.03	0.45 $\pm$ 0.02	6.50 $\pm$ 0.15
$D^0 \to [K^*(892)^0\bar{K}^*(892)^0]_{L=1}$	0.27 $\pm$ 0.00	1.21 $\pm$ 0.02	4.96 $\pm$ 0.16
$D^0 \to K_1(1270)^-K^+$	0.22 $\pm$ 0.01	2.10 $\pm$ 0.03	4.30 $\pm$ 0.17
$D^0 \to [K^+K^-]_{L=0}[\pi^+\pi^-]_{L=0}$	0.12 $\pm$ 0.00	-2.51 $\pm$ 0.03	3.16 $\pm$ 0.17
$D^0 \to K_1(1400)^-K^+$	0.24 $\pm$ 0.01	0.04 $\pm$ 0.04	2.82 $\pm$ 0.19
$D^0 \to [K^*(1680)^0\bar{K}^*(892)^0]_{L=0}$	0.82 $\pm$ 0.02	2.99 $\pm$ 0.03	2.80 $\pm$ 0.15
$D^0 \to [\bar{K}^*(1680)^0K^*(892)^0]_{L=1}$	1.00 $\pm$ 0.02	-2.76 $\pm$ 0.02	2.69 $\pm$ 0.11
$D^0 \to \bar{K}^*(1680)^0[K^+\pi^-]_{L=0}$	1.31 $\pm$ 0.03	1.07 $\pm$ 0.02	2.37 $\pm$ 0.09
$D^0 \to [\phi(1020)^0(\rho-\omega)^0]_{L=2}$	1.31 $\pm$ 0.03	0.54 $\pm$ 0.02	2.30 $\pm$ 0.08
$D^0 \to [K^*(892)^0\bar{K}^*(892)^0]_{L=2}$	0.69 $\pm$ 0.02	2.86 $\pm$ 0.03	1.84 $\pm$ 0.10
$D^0 \to \phi(1020)^0[\pi^+\pi^-]_{L=0}$	0.05 $\pm$ 0.00	-1.71 $\pm$ 0.04	1.49 $\pm$ 0.09
$D^0 \to [K^*(1680)^0\bar{K}^*(892)^0]_{L=1}$	0.74 $\pm$ 0.02	0.13 $\pm$ 0.03	1.46 $\pm$ 0.08
$D^0 \to [\phi(1020)^0\rho(1450)^0]_{L=1}$	0.76 $\pm$ 0.04	1.17 $\pm$ 0.04	0.99 $\pm$ 0.09
$D^0 \to a_0(980)^0f_2(1270)^0$	1.52 $\pm$ 0.06	0.24 $\pm$ 0.04	0.70 $\pm$ 0.05
$D^0 \to a_1(1260)^-\pi^+$	0.19 $\pm$ 0.01	0.18 $\pm$ 0.06	0.46 $\pm$ 0.06
$D^0 \to a_1(1260)^+\pi^-$	0.19 $\pm$ 0.01	-2.82 $\pm$ 0.07	0.46 $\pm$ 0.05
$D^0 \to [\phi(1020)^0(\rho-\omega)^0]_{L=1}$	0.16 $\pm$ 0.01	0.28 $\pm$ 0.07	0.43 $\pm$ 0.05
$D^0 \to [K^*(1680)^0\bar{K}^*(892)^0]_{L=2}$	1.20 $\pm$ 0.09	-2.44 $\pm$ 0.08	0.32 $\pm$ 0.05
$D^0 \to [K^+K^-]_{L=0}(\rho-\omega)^0$	0.20 $\pm$ 0.01	3.00 $\pm$ 0.08	0.27 $\pm$ 0.04
$D^0 \to \phi(1020)^0f_2(1270)^0$	1.40 $\pm$ 0.09	1.72 $\pm$ 0.06	0.19 $\pm$ 0.02
$D^0 \to K^*(892)^0\bar{K}_2^*(1430)^0$	1.52 $\pm$ 0.09	2.01 $\pm$ 0.07	0.17 $\pm$ 0.02
		Sum of fit fractions	129.17 $\pm$ 0.94
		χ^2/ndf	9217/8123 = 1.13
$a_1(1260)^+ \to [\phi(1020)^0\pi^+]_{L=0}$	1 (fixed)	0 (fixed)	100
$K_1(1270)^+ \to [K^*(892)^0\pi^+]_{L=0}$	0.61 $\pm$ 0.02	0.59 $\pm$ 0.03	51.31 $\pm$ 0.88
$K_1(1270)^+ \to [(\rho-\omega)^0K^+]_{L=0}$	1 (fixed)	0 (fixed)	48.24 $\pm$ 1.79
$K_1(1270)^+ \to [K^+\pi^-]_{L=0}\pi^+$	0.60 $\pm$ 0.03	-1.93 $\pm$ 0.04	5.80 $\pm$ 0.46
$K_1(1270)^+ \to [K^*(892)^0\pi^+]_{L=2}$	0.91 $\pm$ 0.04	-2.56 $\pm$ 0.04	2.01 $\pm$ 0.16
$K_1(1270)^+ \to [\rho(1450)^0K^+]_{L=0}$	0.45 $\pm$ 0.06	-2.33 $\pm$ 0.10	1.25 $\pm$ 0.39
		Sum of fit fractions	108.61 $\pm$ 2.07
$K_1(1400)^+ \to [K^*(892)^0\pi^+]_{L=0}$	1 (fixed)	0 (fixed)	100

G Partial-wave analysis

Figures G.1 to G.6 show the two-body invariant masses projected on the spherical normalised associated Legendre polynomials.
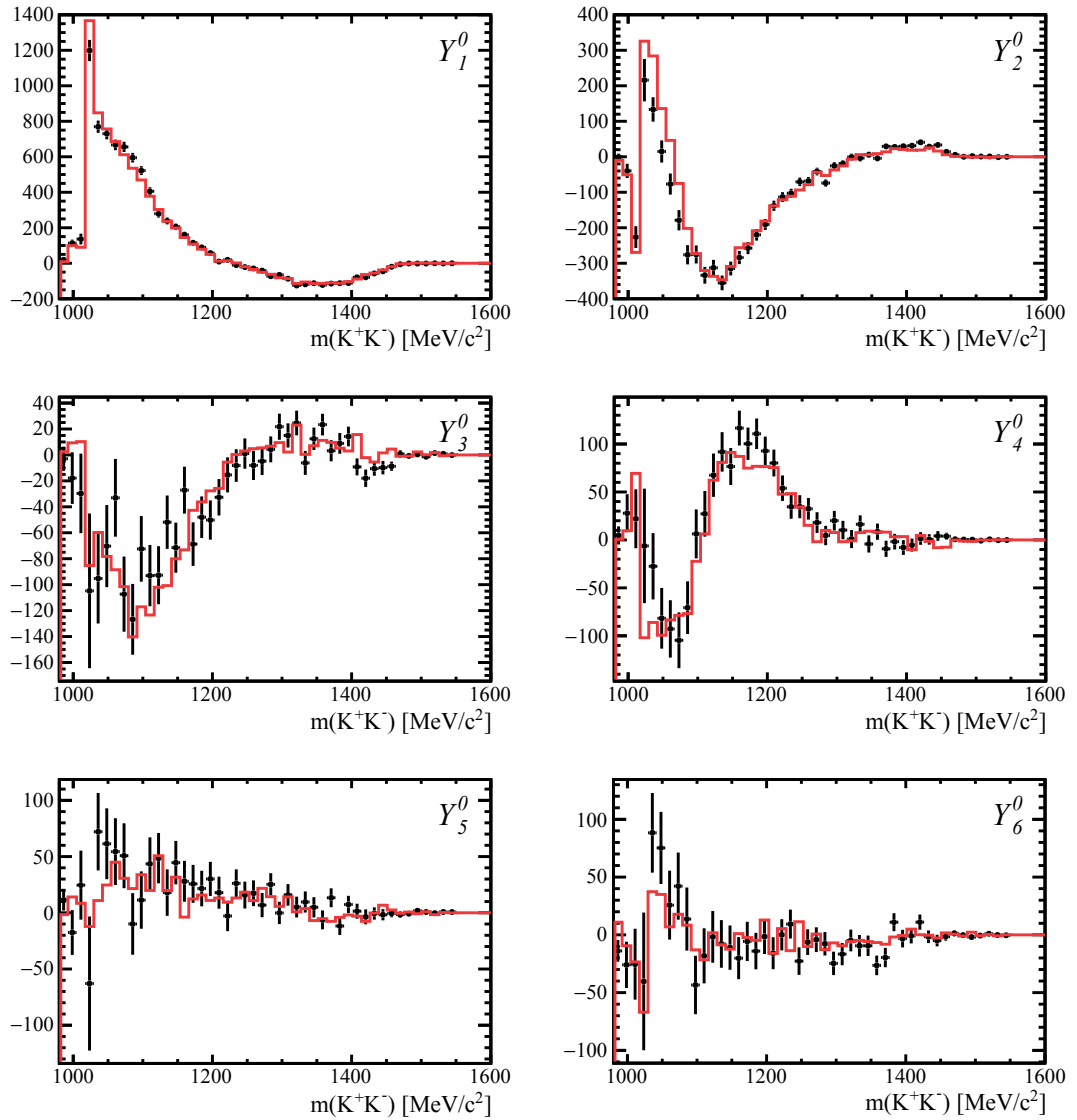

Figure G.1 – Distributions of the K^+K^- invariant mass, for the data (black points) and the model (red line), projected on the first six spherical normalised associated Legendre polynomials.
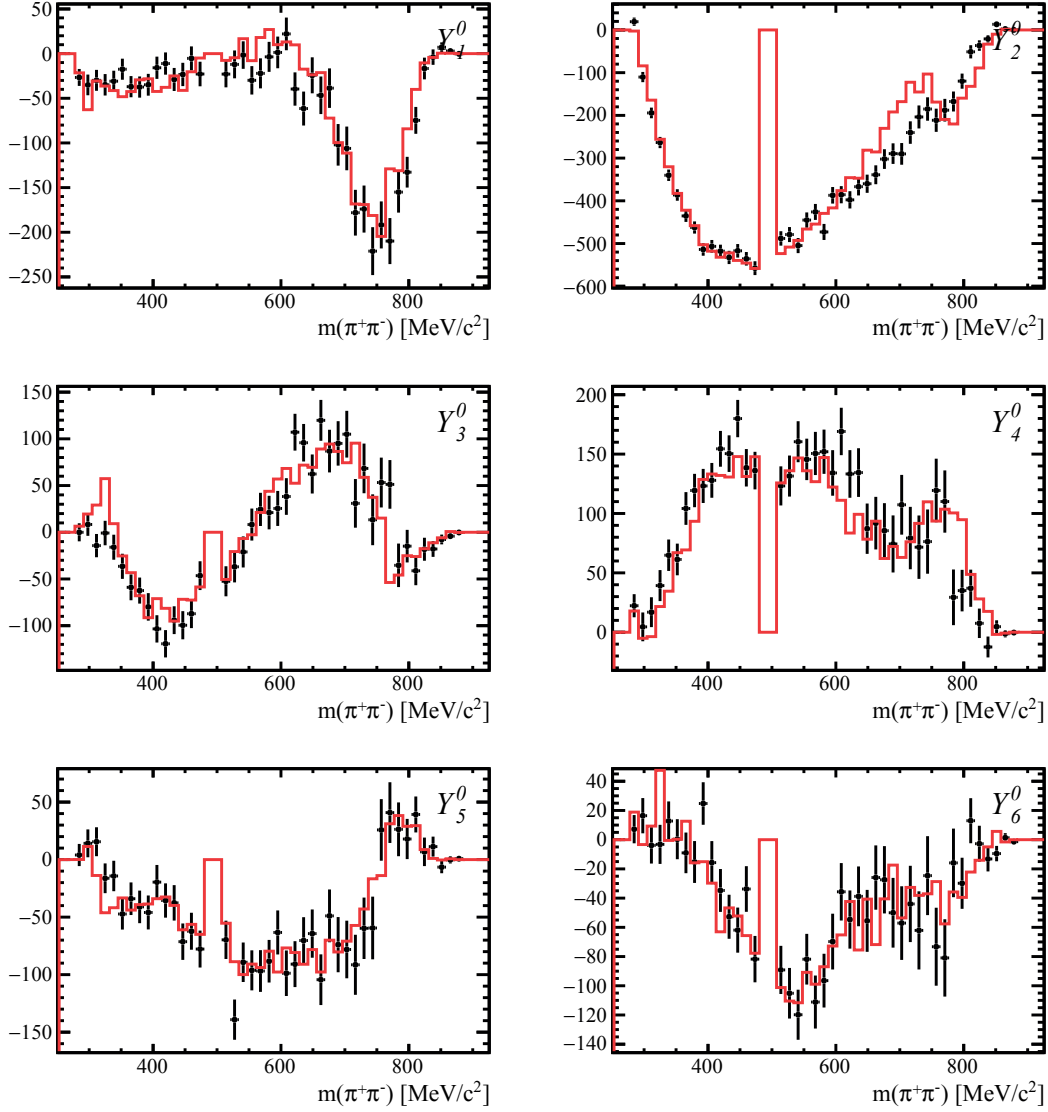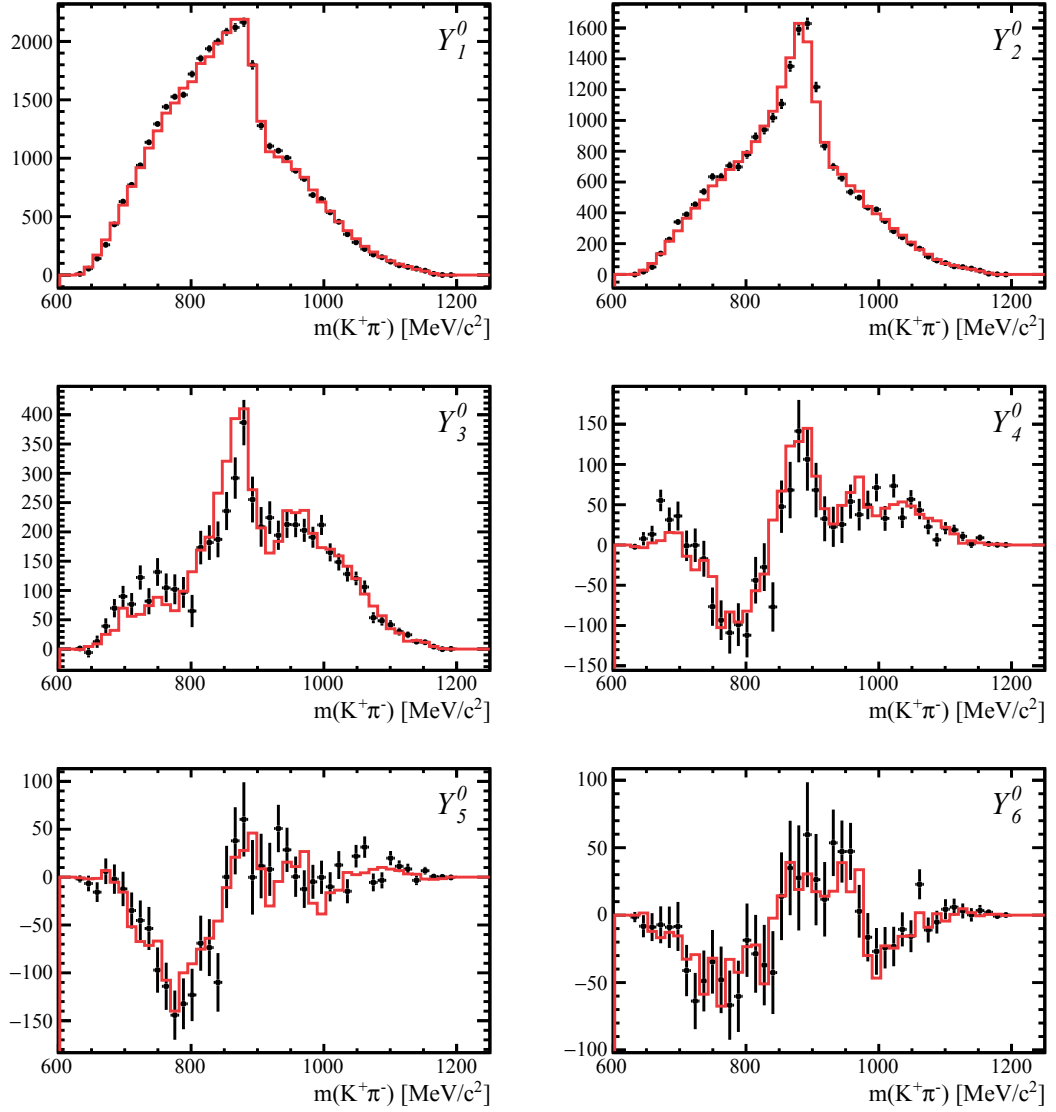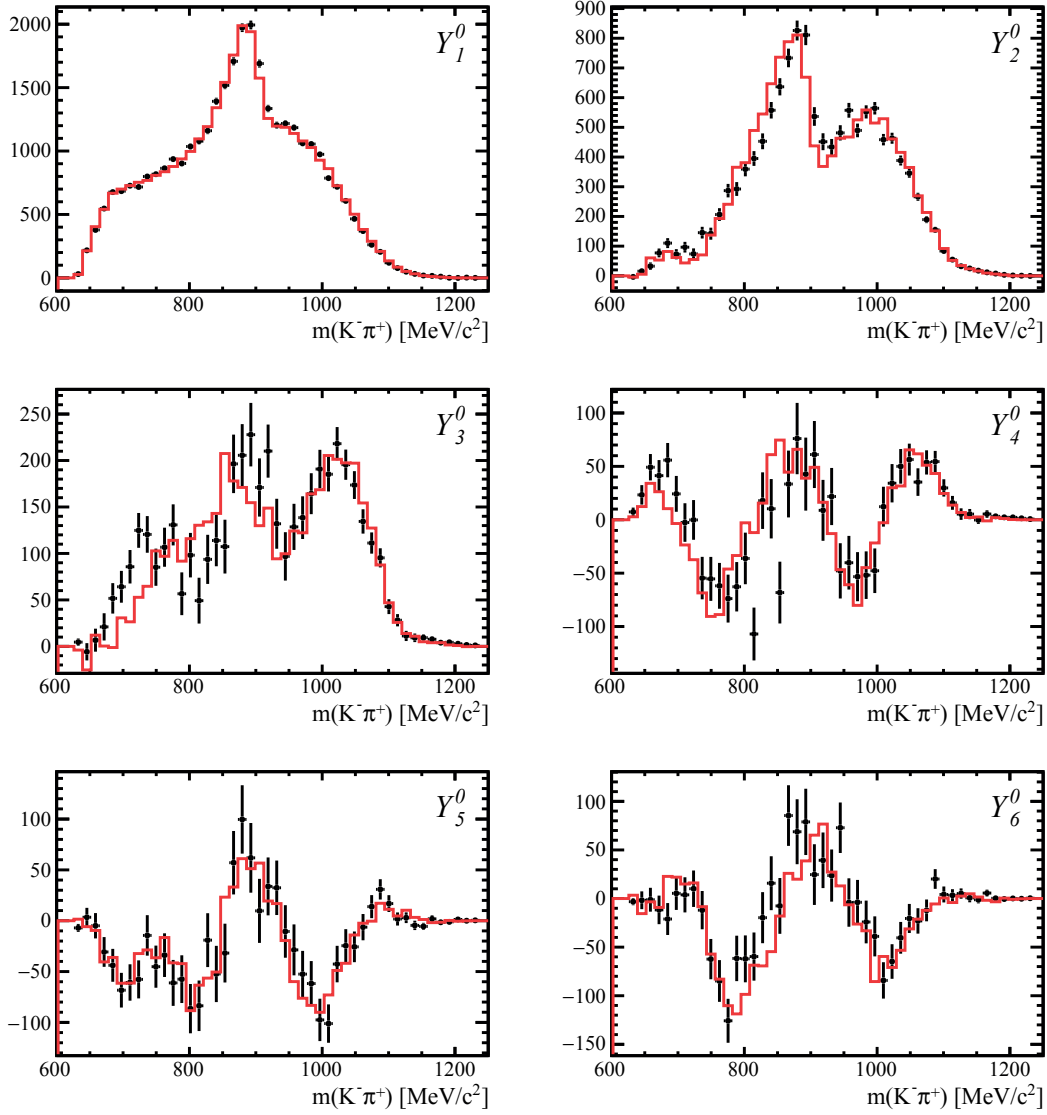
Figure G.2 – Distributions of the $\pi^+\pi^-$ invariant mass, for the data (black points) and the model (red line), projected on the first six spherical normalised associated Legendre polynomials.
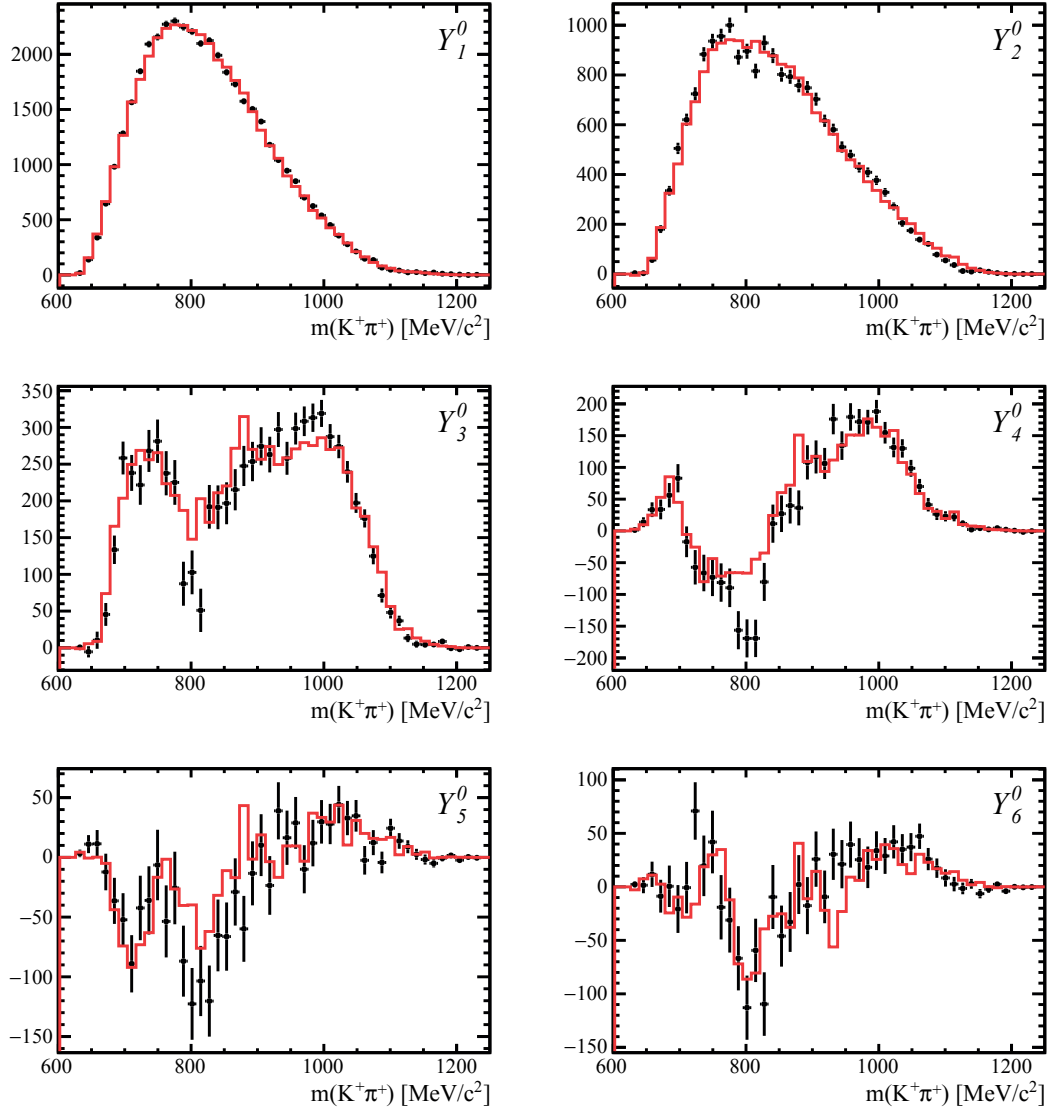
Figure G.3 – Distributions of the $K^+\pi^-$ invariant mass, for the data (black points) and the model (red line), projected on the first six spherical normalised associated Legendre polynomials.

Figure G.4 – Distributions of the $K^-\pi^+$ invariant mass, for the data (black points) and the model (red line), projected on the first six spherical normalised associated Legendre polynomials.
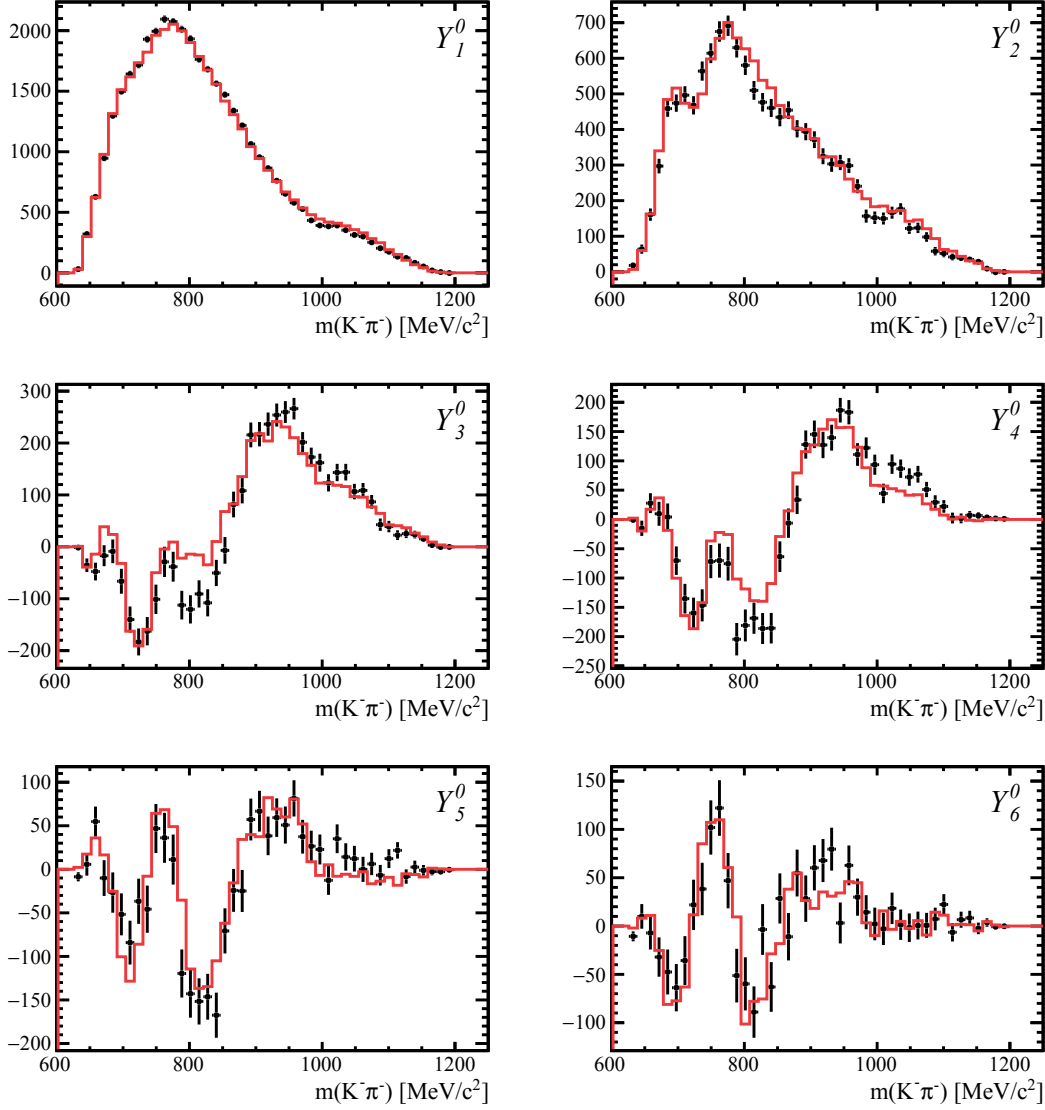
Figure G.5 – Distributions of the $K^+\pi^+$ invariant mass, for the data (black points) and the model (red line), projected on the first six spherical normalised associated Legendre polynomials.

Figure G.6 – Distributions of the $K^-\pi^-$ invariant mass, for the data (black points) and the model (red line), projected on the first six spherical normalised associated Legendre polynomials.

H Fit results

31 variables are used in order to visualise the complicated five-dimensional phase space. The result of the fit has been shown on the five nominal CM variables in Fig. 6.1 and the 26 remaining variables are shown here in Figs. H.1–H.6.
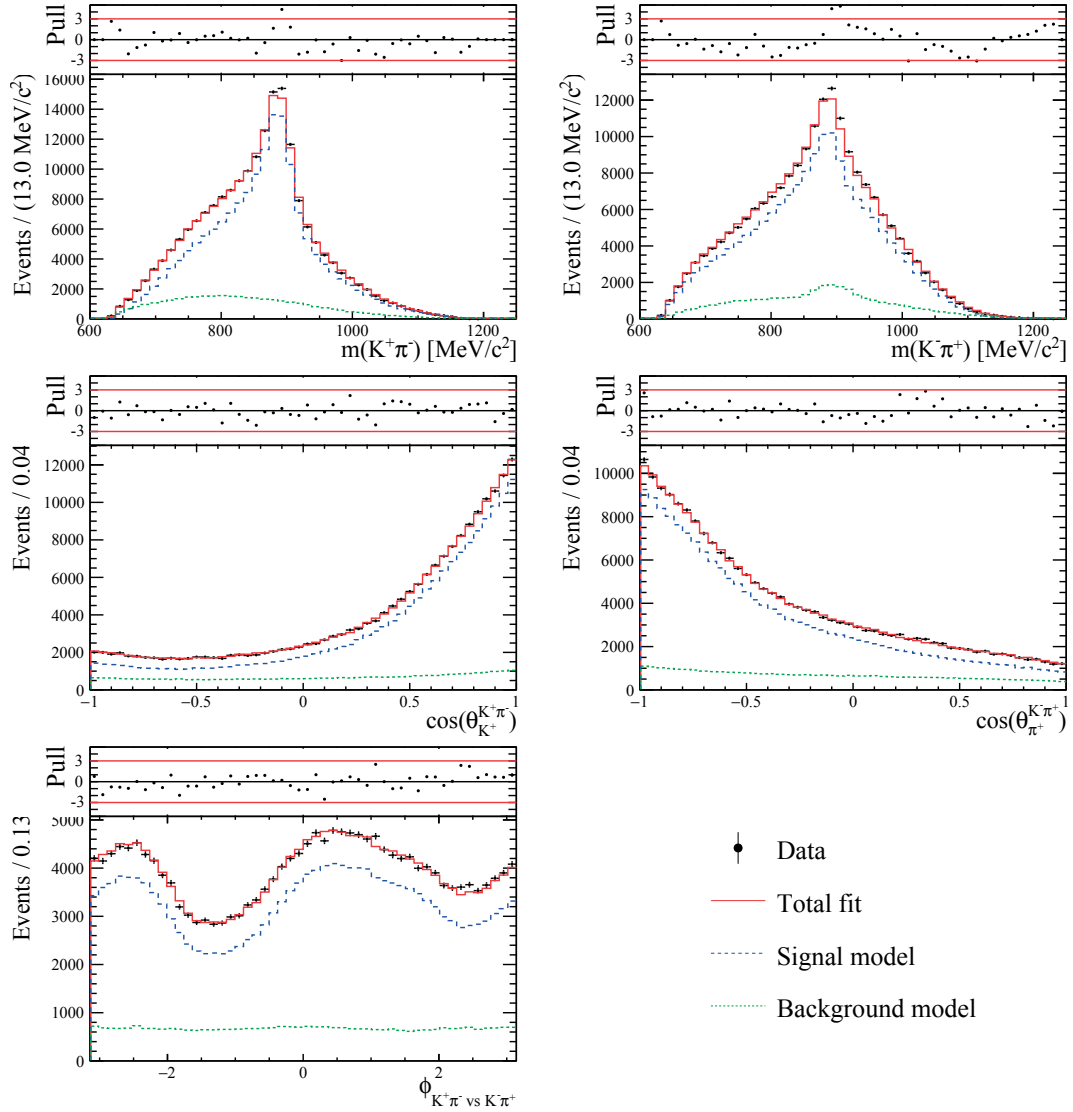

Figure H.1 – Distributions of five variables defined using the opposite-sign $K\pi$ system for the selected $D^0 \rightarrow K^+K^-\pi^+\pi^-$ candidates (black points with error bars). The results of the five-dimensional amplitude fit is superimposed with the signal model (dashed blue), the background model (dotted green) and the total fit function (plain red). The plot on top of each distribution shows the normalised residuals (differences between the data points and the fit results, divided by the quadratic sum of the statistical uncertainties of the data and MC samples).
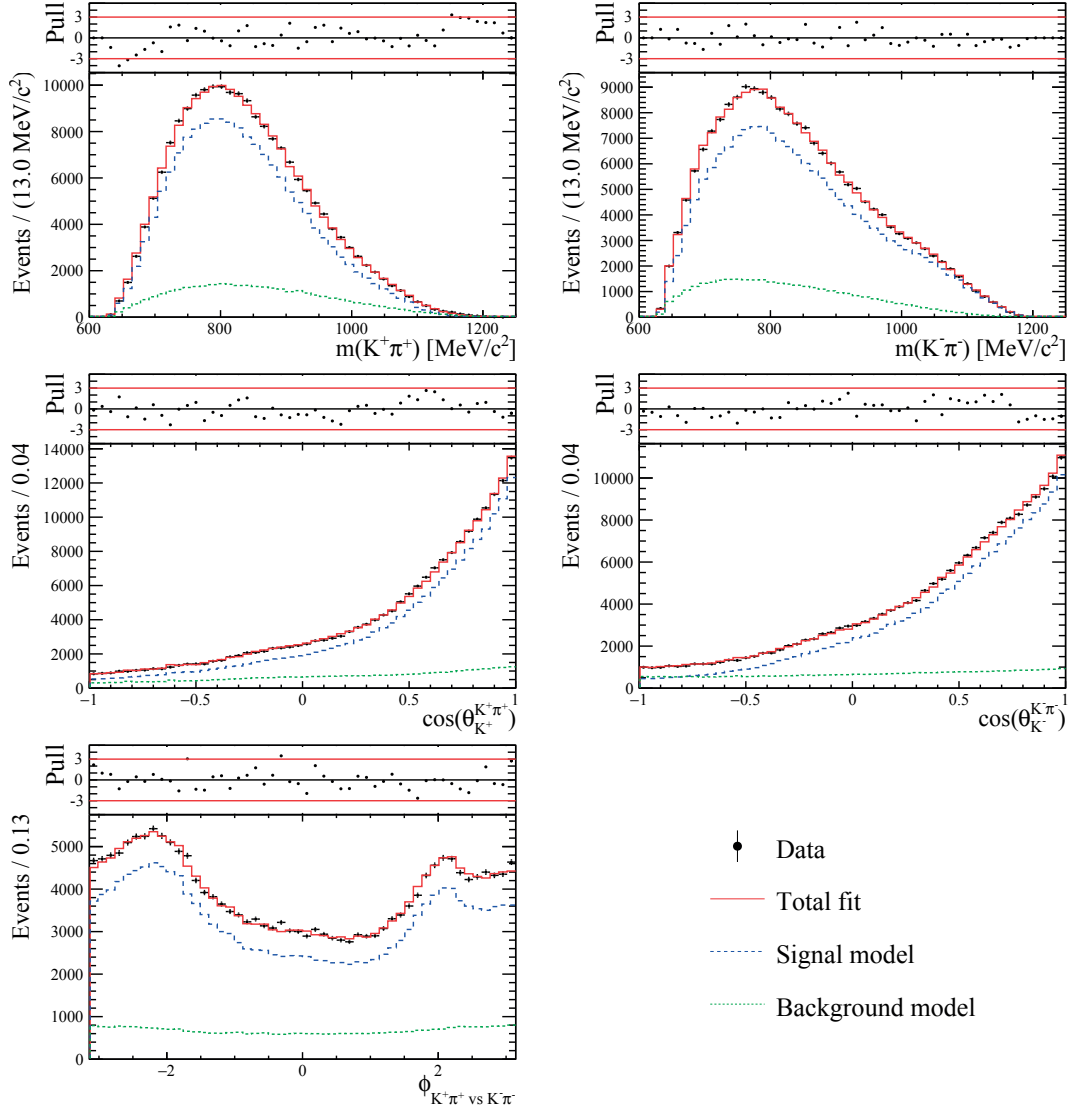
Figure H.2 – Distributions of five variables defined using the same-sign $K\pi$ system for the selected $D^0 \rightarrow K^+K^-\pi^+\pi^-$ candidates (black points with error bars). The results of the five-dimensional amplitude fit is superimposed with the signal model (dashed blue), the background model (dotted green) and the total fit function (plain red). The plot on top of each distribution shows the normalised residuals (differences between the data points and the fit results, divided by the quadratic sum of the statistical uncertainties of the data and MC samples).
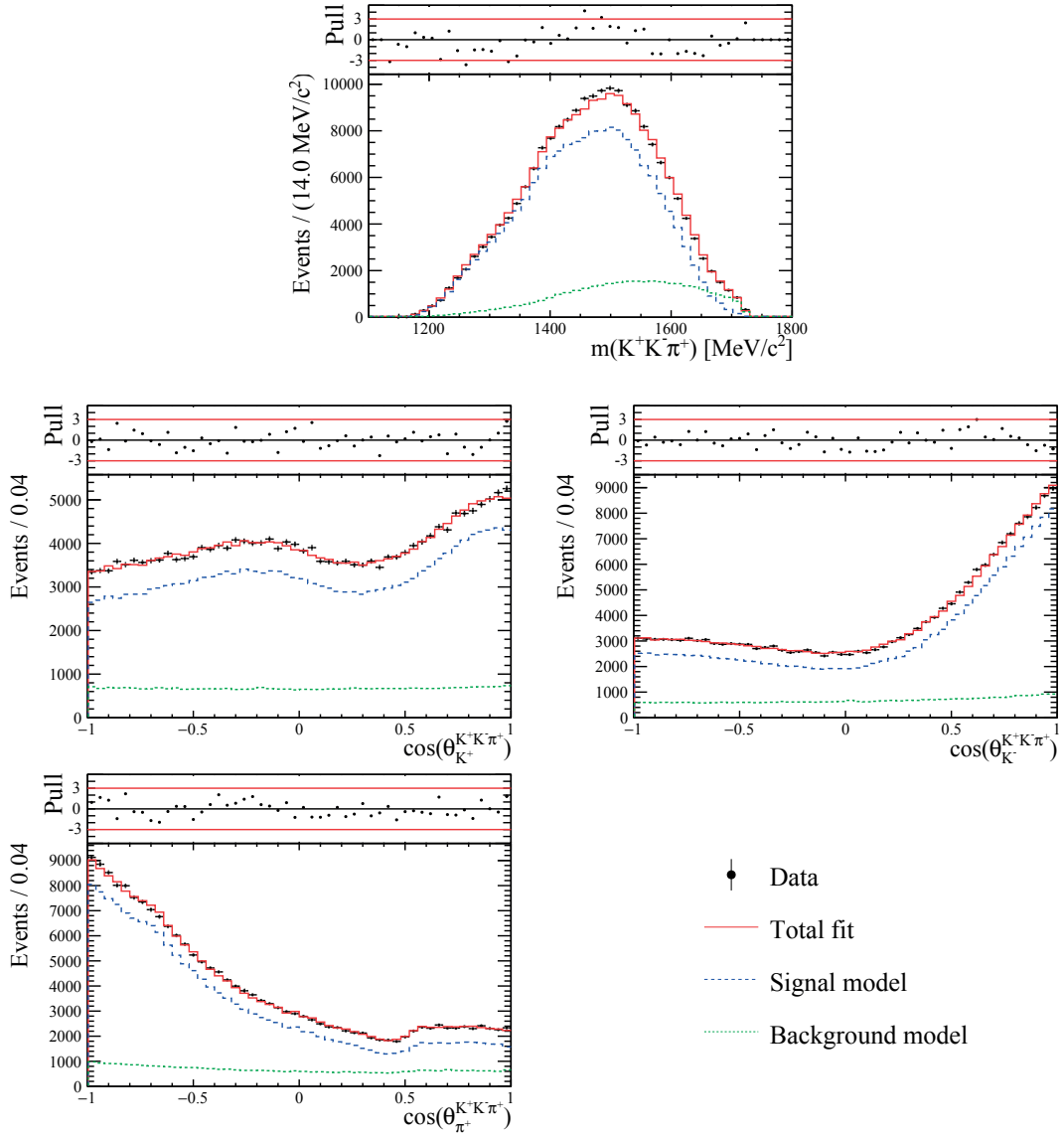
Figure H.3 – Distributions of four variables defined using the $K^+K^-\pi^+$ system for the selected $D^0 \to K^+K^-\pi^+\pi^-$ candidates (black points with error bars). The results of the five-dimensional amplitude fit is superimposed with the signal model (dashed blue), the background model (dotted green) and the total fit function (plain red). The plot on top of each distribution shows the normalised residuals (differences between the data points and the fit results, divided by the quadratic sum of the statistical uncertainties of the data and MC samples).
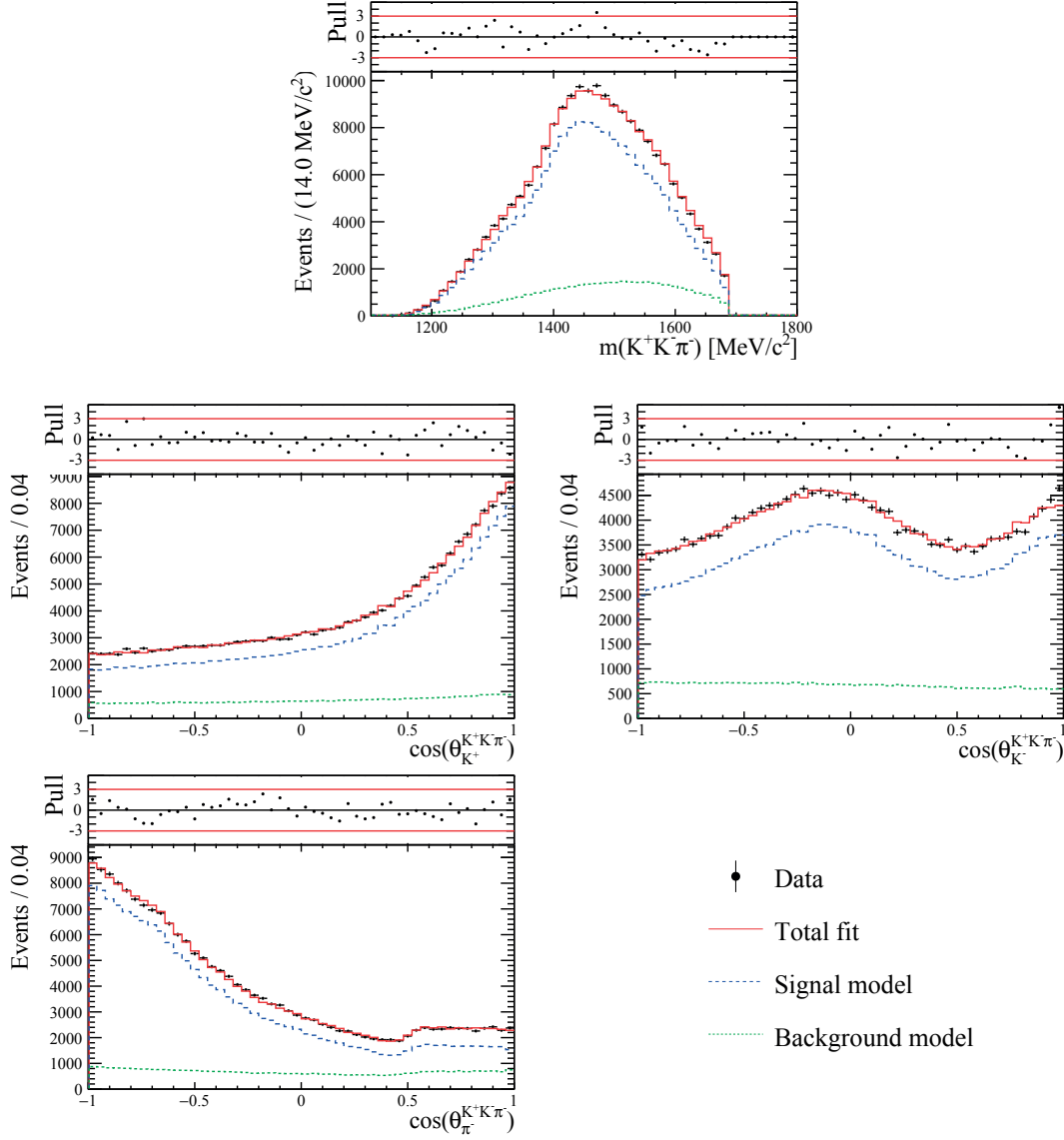
Figure H.4 – Distributions of four variables defined using the $K^+K^-\pi^-$ system for the selected $D^0 \rightarrow K^+K^-\pi^+\pi^-$ candidates (black points with error bars). The results of the five-dimensional amplitude fit is superimposed with the signal model (dashed blue), the background model (dotted green) and the total fit function (plain red). The plot on top of each distribution shows the normalised residuals (differences between the data points and the fit results, divided by the quadratic sum of the statistical uncertainties of the data and MC samples).

Figure H.5 – Distributions of four variables defined using the $K^+\pi^+\pi^-$ system for the selected $D^0 \rightarrow K^+K^-\pi^+\pi^-$ candidates (black points with error bars). The results of the five-dimensional amplitude fit is superimposed with the signal model (dashed blue), the background model (dotted green) and the total fit function (plain red). The plot on top of each distribution shows the normalised residuals (differences between the data points and the fit results, divided by the quadratic sum of the statistical uncertainties of the data and MC samples).
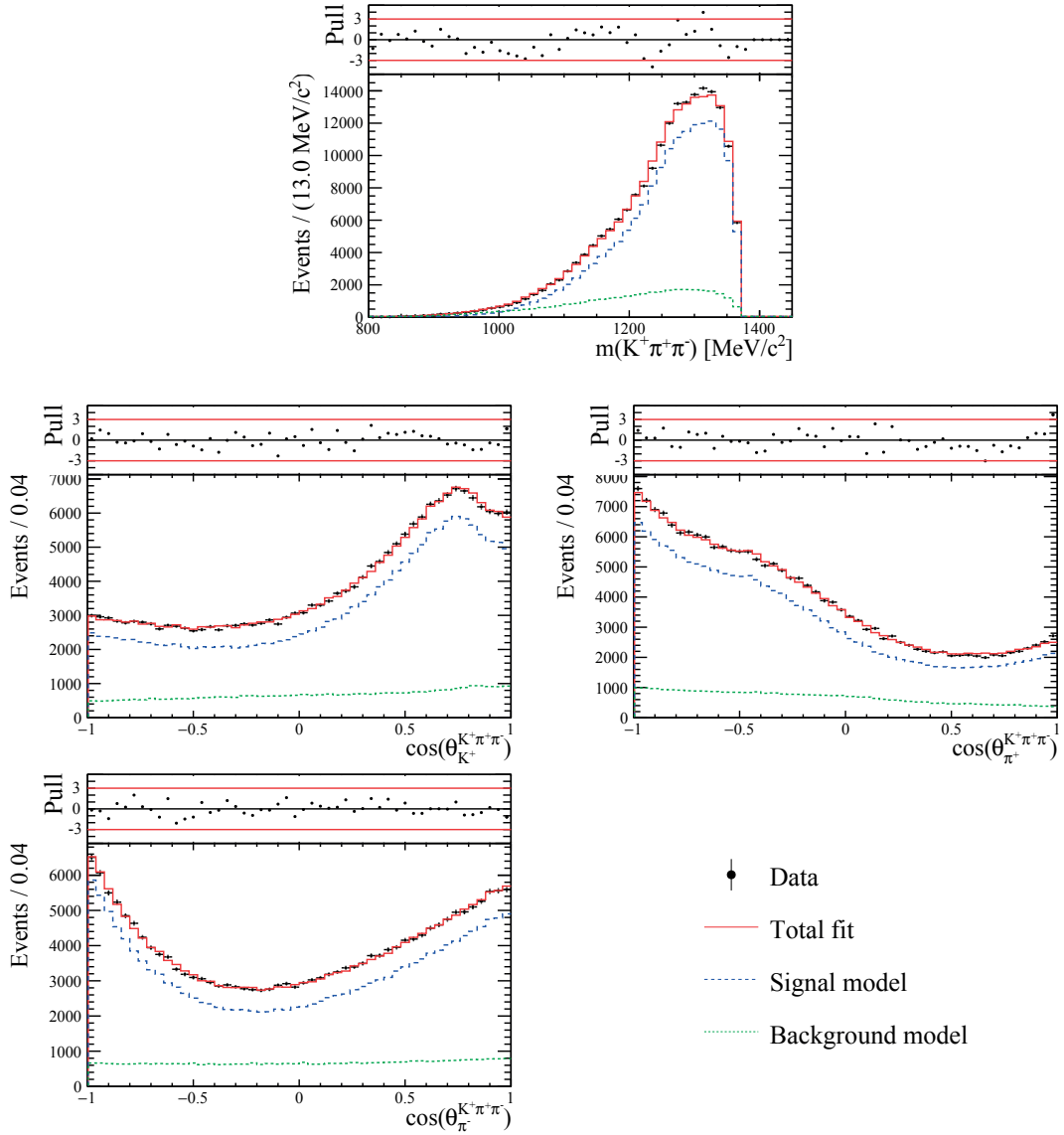
Figure H.6 – Distributions of four variables defined using the $K^-\pi^+\pi^-$ system for the selected $D^0 \rightarrow K^+K^-\pi^+\pi^-$ candidates (black points with error bars). The results of the five-dimensional amplitude fit is superimposed with the signal model (dashed blue), the background model (dotted green) and the total fit function (plain red). The plot on top of each distribution shows the normalised residuals (differences between the data points and the fit results, divided by the quadratic sum of the statistical uncertainties of the data and MC samples).
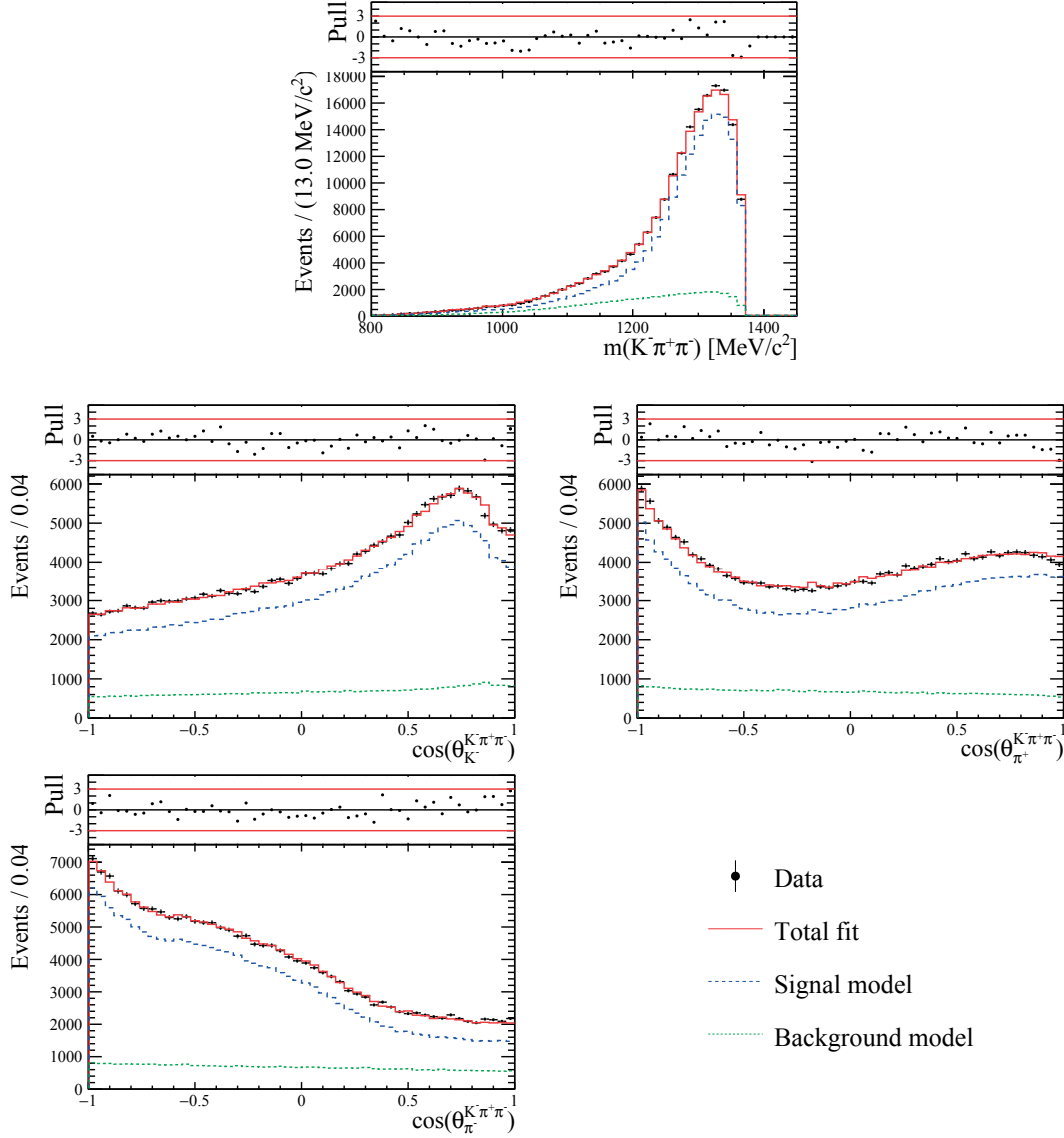
Bibliography

[1] ATLAS collaboration, G. Aad *et al.*, *Observation of a new particle in the search for the Standard Model Higgs boson with the ATLAS detector at the LHC*, Phys. Lett. **B716** (2012) 1, `arXiv:1207.7214`.

[2] CMS collaboration, S. Chatrchyan *et al.*, *Observation of a new boson at a mass of 125 GeV with the CMS experiment at the LHC*, Phys. Lett. **B716** (2012) 30, `arXiv:1207.7235`.

[3] LHCb collaboration, R. Aaij *et al.*, *Test of lepton universality with $B^0 \to K^{*0} \ell^+ \ell^-$ decays*, JHEP **08** (2017) 055, `arXiv:1705.05802`.

[4] LHCb collaboration, R. Aaij *et al.*, *Measurement of the ratio of the $\mathscr{B}(B^0 \to D^{*-} \tau^+ \nu_\tau)$ and $\mathscr{B}(B^0 \to D^{*-} \mu^+ \nu_\mu)$ branching fractions using three-prong τ-lepton decays*, Phys. Rev. Lett. **120** (2018) 171802, `arXiv:1708.08856`.

[5] Super-Kamiokande collaboration, Y. Fukuda *et al.*, *Evidence for oscillation of atmospheric neutrinos*, Phys. Rev. Lett. **81** (1998) 1562, `arXiv:hep-ex/9807003`.

[6] Planck collaboration, N. Aghanim *et al.*, *Planck 2018 results. VI. Cosmological parameters*, `arXiv:1807.06209`.

[7] *Wikimedia, MissMJ, PBS NOVA, Fermilab, Office of Science, United States Department of Energy, Particle Data Group*, https://commons.wikimedia.org/wiki/File:Standard_Model_of_Elementary_Particles.svg.

[8] A. Einstein, *Die Grundlage der allgemeinen Relativitätstheorie*, Ann. Phys. **354** (1916) 769.

[9] A. D. Sakharov, *Violation of CP invariance, C asymmetry, and baryon asymmetry of the universe*, Pisma Zh. Eksp. Teor. Fiz. **5** (1967) 32, Usp. Fiz. Nauk. **161** (1991) 61.

[10] P. Huet and E. Sather, *Electroweak baryogenesis and standard model CP violation*, Phys. Rev. **D51** (1995) 379, `arXiv:hep-ph/9404302`.

[11] DES collaboration, T. M. C. Abbott *et al.*, *Dark Energy Survey year 1 results: Cosmological constraints from galaxy clustering and weak lensing*, Phys. Rev. **D98** (2018) 043526, `arXiv:1708.01530`.

[12] M. Milgrom, *A modification of the Newtonian dynamics as a possible alternative to the hidden mass hypothesis*, Astrophys. J. **270** (1983) 365.

Bibliography

[13] SNO, Q. R. Ahmad *et al.*, *Measurement of the rate of* $\nu_e + d \rightarrow p + p + e^-$ *interactions produced by* ^8B *solar neutrinos at the Sudbury Neutrino Observatory*, Phys. Rev. Lett. **87** (2001) 071301, `arXiv:nucl-ex/0106015`.

[14] SNO collaboration, Q. R. Ahmad *et al.*, *Direct evidence for neutrino flavor transformation from neutral current interactions in the Sudbury Neutrino Observatory*, Phys. Rev. Lett. **89** (2002) 011301, `arXiv:nucl-ex/0204008`.

[15] LHCb collaboration, R. Aaij *et al.*, *Test of lepton universality using* $B^+ \rightarrow K^+ \ell^+ \ell^-$ *decays*, Phys. Rev. Lett. **113** (2014) 151601, `arXiv:1406.6482`.

[16] Belle collaboration, M. Huschle *et al.*, *Measurement of the branching ratio of* $\bar{B} \rightarrow D^{(*)} \tau^- \bar{\nu}_\tau$ *relative to* $\bar{B} \rightarrow D^{(*)} \ell^- \bar{\nu}_\ell$ *decays with hadronic tagging at Belle*, Phys. Rev. **D92** (2015) 072014, `arXiv:1507.03233`.

[17] LHCb collaboration, R. Aaij *et al.*, *Angular analysis of the* $B^0 \rightarrow K^* e^+ e^-$ *decay in the low-q^2 region*, JHEP **04** (2015) 064, `arXiv:1501.03038`.

[18] LHCb collaboration, R. Aaij *et al.*, *Angular analysis of the* $B^0 \rightarrow K^{*0} \mu^+ \mu^-$ *decay using* $3\,fb^{-1}$ *of integrated luminosity*, JHEP **02** (2016) 104, `arXiv:1512.04442`.

[19] N. Cabibbo, *Unitary symmetry and leptonic decays*, Phys. Rev. Lett. **10** (1963) 531, erratum ibid. 168 (1968) 1926.

[20] M. Kobayashi and T. Maskawa, *CP-violation in the renormalizable theory of weak interaction*, Progress of Theoretical Physics **49** (1973) 652.

[21] L. Wolfenstein, *Parametrization of the Kobayashi-Maskawa matrix*, Phys. Rev. Lett. **51** (1983) 1945.

[22] Y. H. Ahn, H.-Y. Cheng, and S. Oh, *Wolfenstein parametrization at higher order: seeming discrepancies and their resolution*, Phys. Lett. **B703** (2011) 571, `arXiv:1106.0935`.

[23] C. Jarlskog, *Commutator of the quark mass matrices in the Standard electroweak Model and a measure of maximal CP nonconservation*, Phys. Rev. Lett. **55** (1985) 1039.

[24] Particle Data Group, M. Tanabashi *et al.*, *Review of particle physics*, Phys. Rev. **D98** (2018) 030001.

[25] CKMfitter group, J. Charles *et al.*, *Current status of the Standard Model CKM fit and constraints on* $\Delta F = 2$ *new physics*, Phys. Rev. **D91** (2015) 073007, `arXiv:1501.05013`, updated results and plots available at `http://ckmfitter.in2p3.fr/`.

[26] J. H. Christenson, J. W. Cronin, V. L. Fitch, and R. Turlay, *Evidence for the* 2π *decay of the* K_2^0 *meson*, Phys. Rev. Lett. **13** (1964) 138.

[27] NA31 collaboration, H. Burkhardt *et al.*, *First evidence for direct CP violation*, Phys. Lett. **B206** (1988) 169.

[28] NA48 collaboration, V. Fanti *et al.*, *A new measurement of direct CP violation in two pion decays of the neutral kaon*, Phys. Lett. **B465** (1999) 335, `arXiv:hep-ex/9909022`.

[29] KTeV collaboration, A. Alavi-Harati *et al.*, *Observation of direct CP violation in $K_{S,L} \to \pi\pi$ decays*, Phys. Rev. Lett. **83** (1999) 22, `arXiv:hep-ex/9905060`.

[30] Belle collaboration, K. Abe *et al.*, *Observation of large CP violation in the neutral B meson system*, Phys. Rev. Lett. **87** (2001) 091802, `arXiv:hep-ex/0107061`.

[31] BaBar collaboration, B. Aubert *et al.*, *Observation of CP violation in the B^0 meson system*, Phys. Rev. Lett. **87** (2001) 091801, `arXiv:hep-ex/0107013`.

[32] BaBar collaboration, B. Aubert *et al.*, *Direct CP violating asymmetry in $B^0 \to K^+\pi^-$ decays*, Phys. Rev. Lett. **93** (2004) 131801, `arXiv:hep-ex/0407057`.

[33] Belle collaboration, Y. Chao *et al.*, *Evidence for direct CP violation in $B^0 \to K^+\pi^-$ decays*, Phys. Rev. Lett. **93** (2004) 191802, `arXiv:hep-ex/0408100`.

[34] Belle collaboration, A. Poluektov *et al.*, *Evidence for direct CP violation in the decay $B \to D^{(*)}K$, $D \to K_S^0 \pi^+\pi^-$ and measurement of the CKM phase ϕ_3*, Phys. Rev. **D81** (2010) 112002, `arXiv:1003.3360`.

[35] BaBar collaboration, P. del Amo Sanchez *et al.*, *Measurement of CP observables in $B^\pm \to D_{CP}K^\pm$ decays and constraints on the CKM angle γ*, Phys. Rev. D **82** (2010) 072004, `arXiv:1007.0504`.

[36] LHCb collaboration, R. Aaij *et al.*, *Observation of CP violation in $B^\pm \to DK^\pm$ decays*, Phys. Lett. **B712** (2012) 203, erratum ibid. **B713** (2012) 351, `arXiv:1203.3662`.

[37] LHCb collaboration, R. Aaij *et al.*, *First observation of CP violation in the decays of B_s^0 mesons*, Phys. Rev. Lett. **110** (2013) 221601, `arXiv:1304.6173`.

[38] F. Buccella *et al.*, *Nonleptonic weak decays of charmed mesons*, Phys. Rev. **D51** (1995) 3478, `arXiv:hep-ph/9411286`.

[39] Y. Grossman, A. L. Kagan, and Y. Nir, *New physics and CP violation in singly Cabibbo suppressed D decays*, Phys. Rev. **D75** (2007) 036008, `arXiv:hep-ph/0609178`.

[40] A. Khodjamirian and A. A. Petrov, *Direct CP asymmetry in $D \to \pi^+\pi^-$ and $D \to K^+K^-$ in QCD-based approach*, Phys. Lett. **B774** (2017) 235 , `arXiv:1706.07780`.

[41] A. N. Rozanov and M. I. Vysotsky, $(\Delta A_{CP})_{LHCb}$ *and the fourth generation*, `arXiv:1111.6949`.

[42] Y. Hochberg and Y. Nir, *Relating direct CP violation in D decays and the forward-backward asymmetry in $t\bar{t}$ production*, Phys. Rev. Lett. **108** (2012) 261601, `arXiv:1112.5268`.

[43] A. A. Petrov, *CP violation in charm*, eConf **C070805** (2007) 11, `arXiv:0711.1564`.

[44] LHCb collaboration, R. Aaij *et al.*, *Measurement of the difference of time-integrated CP asymmetries in $D^0 \to K^- K^+$ and $D^0 \to \pi^- \pi^+$ decays*, Phys. Rev. Lett. **116** (2016) 191601, `arXiv:1602.03160`.

[45] E. Franco, S. Mishima, and L. Silvestrini, *The Standard Model confronts CP violation in $D^0 \to \pi^+ \pi^-$ and $D^0 \to K^+ K^-$*, JHEP **05** (2012) 140, `arXiv:1203.3131`.

[46] CLEO collaboration, M. Artuso *et al.*, *Amplitude analysis of $D^0 \to K^+ K^- \pi^+ \pi^-$*, Phys. Rev. **D85** (2012) 122002, `arXiv:1201.5716`.

[47] P. d'Argent *et al.*, *Amplitude analyses of $D^0 \to \pi^+ \pi^- \pi^+ \pi^-$ and $D^0 \to K^+ K^- \pi^+ \pi^-$ decays*, JHEP **05** (2017) 143, `arXiv:1703.08505`.

[48] A. Giri, Y. Grossman, A. Soffer, and J. Zupan, *Determining γ using $B^\pm \to D K^\pm$ with multibody D decays*, Phys. Rev. **D68** (2003) 054018, `arXiv:hep-ph/0303187`.

[49] J. Rademacker and G. Wilkinson, *Determining the unitarity triangle γ with a four-body amplitude analysis of $B^\pm \to (K^+ K^- \pi^+ \pi^-)_D K^\pm$ decays*, Phys. Lett. **B647** (2007) 400, `arXiv:hep-ph/0611272`.

[50] LHCb collaboration, *Update of the LHCb combination of the CKM angle γ using $B \to D K$ decays*, LHCb-CONF-2018-002.

[51] FOCUS collaboration, J. M. Link *et al.*, *Study of the $D^0 \to K^+ K^- \pi^+ \pi^-$*, Phys. Lett. **B610** (2005) 225, `arXiv:hep-ex/0411031`.

[52] LHCb collaboration, R. Aaij *et al.*, *Search for CP violation using T-odd correlations in $D^0 \to K^+ K^- \pi^+ \pi^-$ decays*, JHEP **10** (2014) 005, `arXiv:1408.1299`.

[53] A. Puig, *The LHCb trigger in 2011 and 2012*, CERN-LHCb-PUB-2014-046, Nov. 2014.

[54] M. Schubiger *et al.*, *Magnetic field map with 2014 measurements for the LHCb dipole magnet*, CERN-LHCb-INT-2015-034, Oct. 2015.

[55] M. Schubiger, M. Martinelli, and O. Schneider, *Search for CP violation in the $D^0 \to K^+ K^- \pi^+ \pi^-$ decay through a full amplitude analysis*, CERN-LHCb-ANA-2017-064, Nov. 2017.

[56] E. Mobs, *The CERN accelerator complex*, https://cds.cern.ch/record/2197559.

[57] LHCb collaboration, A. A. Alves Jr. *et al.*, *The LHCb detector at the LHC*, JINST **3** (2008) S08005.

[58] LHCb collaboration, R. Aaij *et al.*, *LHCb detector performance*, Int. J. Mod. Phys. **A30** (2015) 1530022, `arXiv:1412.6352`.

[59] C. Elsasser, *$b\bar{b}$ production angle plots*, https://lhcb.web.cern.ch/lhcb/speakersbureau/html/bb_ProductionAngles.html.

[60] TOTEM collaboration, G. Antchev *et al.*, *Luminosity-independent measurements of total, elastic and inelastic cross-sections at $\sqrt{s}$ = 7 TeV*, Europhys. Lett. **101** (2013) 21004.

[61] ATLAS collaboration, M. Aaboud *et al.*, *Measurement of the total cross section from elastic scattering in pp collisions at $\sqrt{s}$ = 8 TeV with the ATLAS detector*, Phys. Lett. **B761** (2016) 158, `arXiv:1607.06605`.

[62] LHCb collaboration, R. Aaij *et al.*, *Expression of interest for a phase-II LHCb upgrade: Opportunities in flavour physics, and beyond, in the HL-LHC era*, CERN-LHCC-2017-003, Feb. 2017.

[63] LHCb collaboration, R. Aaij *et al.*, *Physics case for an LHCb Upgrade II — Opportunities in flavour physics, and beyond, in the HL-LHC era*, CERN-LHCC-2018-026 LHCb-PUB-2018-009, May 2018.

[64] R. Aaij *et al.*, *The LHCb trigger and its performance in 2011*, JINST **8** (2013) P04022, `arXiv:1211.3055`.

[65] C. Elsasser, *LHCb trigger schemes*, https://lhcb.web.cern.ch/lhcb/speakersbureau/html/TriggerScheme.html.

[66] R. Aaij *et al.*, *Performance of the LHCb Vertex Locator*, JINST **9** (2014) P09007, `arXiv:1405.7808`.

[67] R. Arink *et al.*, *Performance of the LHCb Outer Tracker*, JINST **9** (2014) P01002, `arXiv:1311.3893`.

[68] LHCb collaboration, R. Aaij *et al.*, *LHCb inner tracker: Technical Design Report*, CERN-LHCC-2002-029, LHCb-TDR-008, Nov. 2002.

[69] M. Adinolfi *et al.*, *Performance of the LHCb RICH detector at the LHC*, Eur. Phys. J. **C73** (2013) 2431, `arXiv:1211.6759`.

[70] I. Machikhiliyan and the LHCb calorimeter group, *Current status and performance of the LHCb electromagnetic and hadron calorimeters*, J. Phys. Conf. Ser. **293** (2011) 012052.

[71] E. P. Olloqui and the LHCb collaboration, *LHCb preshower (PS) and scintillating pad detector (SPD): commissioning, calibration, and monitoring*, J. Phys. Conf. Ser. **160** (2009) 012046.

[72] A. A. Alves Jr. *et al.*, *Performance of the LHCb muon system*, JINST **8** (2013) P02022, `arXiv:1211.1346`.

[73] A. Keune, A. Hicheur, and G. Conti, *Magnetic field parametrisations*, CERN-LHCb-INT-2010-002, Apr. 2010.

[74] LHCb collaboration, R. Aaij *et al.*, *LHCb magnet: Technical Design Report*, CERN-LHCC-2000-007, LHCb-TDR-001, Jan. 2000.

Bibliography

[75] J. Prisciandaro, F. Blanc, and T. Nakada, *Improved magnetic field map with 2011 measurements for the LHCb dipole magnet*, CERN-LHCb-INT-2012-012, Mar. 2012.

[76] F. James and M. Winkler, *MINUIT user's guide*, INSPIRE-1258345, Jun. 2004.

[77] N. Cabibbo and A. Maksymowicz, *Angular correlations in K_{e4} decays and determination of low-energy $\pi - \pi$ phase shifts*, Phys. Rev. **137** (1965) B438, erratum ibid. **168** (1968) 1926.

[78] Y. Amhis, J. He, and M. Needham, *Momentum scale calibration for early 2011 data*, CERN-LHCb-INT-2011-053, Dec. 2011.

[79] M. Needham, *Momentum scale calibration using resonances*, CERN-LHCb-2008-037, Jul. 2008.

[80] G. Conti and M. Needham, *Momentum scale calibration using 2009 and 2010 data*, CERN-LHCb-INT-2010-048, Oct. 2010.

[81] M. Needham, *Precision measurement of D meson mass diffferences*, CERN-LHCb-ANA-2012-110, Nov. 2012.

[82] W. D. Hulsbergen, *Decay chain fitting with a Kalman filter*, Nucl. Instrum. Meth. **A552** (2005) 566 .

[83] *LHCb Doxygen page for cone isolation variables*, http://lhcb-doxygen.web.cern.ch/lhcb-doxygen/davinci/v41r4/d1/da3/class_rel_info_cone_variables.html.

[84] *LHCb Doxygen page for vertex isolation variables*, http://lhcb-doxygen.web.cern.ch/lhcb-doxygen/davinci/v41r4/dd/d36/class_rel_info_vertex_isolation.html.

[85] A. Hoecker *et al.*, *TMVA: toolkit for multivariate data analysis*, PoS **ACAT** (2007) 040, arXiv:physics/0703039.

[86] R. Brun and F. Rademakers, *ROOT: An object oriented data analysis framework*, Nucl. Instrum. Meth. **A389** (1997) 81.

[87] Y. Freund and R. E. Schapire, *A decision-theoretic generalization of on-line learning and an application to boosting*, J. Comp. Syst. Sci. **55** (1997) 119 .

[88] *LHCb twiki page on PID correction with Meerkat*, https://twiki.cern.ch/twiki/bin/view/LHCb/MeerkatPIDResampling.

[89] *LHCb twiki page of package PIDCalib*, https://twiki.cern.ch/twiki/bin/view/LHCb/PIDCalibPackage.

[90] M. Needham, *Momentum smearing tools*, LHCb Tracking and Alignment meeting, Apr. 2013.

[91] *LHCb gitlab page of TrackSmearState*, https://gitlab.cern.ch/lhcb/Analysis/blob/master/Phys/DaVinciTrackScaling/src/TrackSmearState.cpp.

[92] A. Rogozhnikov, *Reweighting with Boosted Decision Trees*, J. Phys. Conf. Ser. **762** (2016) 012036, arXiv:1608.05806.

[93] M. Pivk and F. R. Le Diberder, *Plots: A statistical tool to unfold data distributions*, Nucl. Instrum. Meth. **A555** (2005) 356, arXiv:physics/0402083.

[94] D. Herndon, P. Söding and R. J. Cashmore, *Generalized isobar model formalism*, Phys. Rev. **D11** (1975) 3165.

[95] R. M. Sternheimer and S. J. Lindenbaum, *Extension of the isobaric nucleon model for pion production in pion-nucleon, nucleon-nucleon, and antinucleon-nucleon interactions*, Phys. Rev. **123** (1961) 333.

[96] J. M. Blatt and V. F. Weisskopf, *Theoretical nuclear physics*, Chapter VIII. 5, Springer (1952) .

[97] B. S. Zou and D. V. Bugg, *Covariant tensor formalism for partial wave analyses of ψ decay to mesons*, Eur. Phys. J. **A16** (2003) 537, arXiv:hep-ph/0211457.

[98] *LHCb gitlab page of AmpGen*, https://gitlab.cern.ch/lhcb/Gauss/tree/master/Gen/AmpGen.

[99] LHCb collaboration, R. Aaij *et al.*, *Studies of the resonance structure in $D^0 \to K^{\mp}\pi^{\pm}\pi^{+}\pi^{-}$ decays*, Eur. Phys. J. **C78** (2018) 443, arXiv:1712.08609.

[100] G. Breit and E. Wigner, *Capture of slow neutrons*, Phys. Rev. **49** (1936) 519.

[101] CLEO collaboration, D. M. Asner *et al.*, *Hadronic structure in the decay $\tau^{-} \to \nu_{\tau}\pi^{-}\pi^{0}\pi^{0}$ and the sign of the tau neutrino helicity*, Phys. Rev. **D61** (1999) 012002, arXiv:hep-ex/9902022.

[102] P. Lichard and M. Vojik, *An alternative parametrization of the pion form-factor and the mass and width of $\rho(770)$*, arXiv:hep-ph/0611163.

[103] S. M. Flatté, *Coupled-channel analysis of the $\pi\eta$ and $K\bar{K}$ systems near $K\bar{K}$ threshold*, Phys. Lett. **B63** (1976) 224 .

[104] V. V. Anisovich and A. V. Sarantsev, *The analysis of reactions $\pi N \to 2$ mesons $+ N$ within reggeon exchanges. 1. Fit and results*, arXiv:0806.1601.

[105] G. J. Gounaris and J. J. Sakurai, *Finite-width corrections to the vector-meson-dominance prediction for $\rho \to e^{+}e^{-}$*, Phys. Rev. Lett. **21** (1968) 244.

[106] S. U. Chung *et al.*, *Partial wave analysis in K-matrix formalism*, Annalen der Physik **507** (1995) 404.

Bibliography

[107] V. V. Anisovich and A. V. Sarantsev, *K-matrix analysis of the ($IJ^{PC} = 00^{++}$)-wave in the mass region below 1900 MeV*, Eur. Phys. J. **A16** (2003) 229, arXiv:hep-ph/0204328.

[108] BaBar collaboration, B. Aubert *et al.*, *Improved measurement of the CKM angle γ in $B^{\mp} \to D^{(*)}K^{(*\mp)}$ decays with a Dalitz plot analysis of D decays to $K_S^0\pi^+\pi^-$ and $K_S^0K^+K^-$*, Phys. Rev. **D78** (2008) 034023, arXiv:0804.2089.

[109] S. L. Adler, *Sum rules for the axial-vector coupling-constant renormalization in β decay*, Phys. Rev. **140** (1965) B736, errata ibid. **149** (1966) 1294 and ibid. **175** (1968) 2224.

[110] J. Back *et al.*, *LAURA^{++}: A dalitz plot fitter*, Comput. Phys. Commun. **231** (2018) 198, arXiv:1711.09854.

[111] J. M. Link *et al.*, *Dalitz plot analysis of the $D^+ \to K^-\pi^+\pi^+$ decay in the FOCUS experiment*, Phys. Lett. **B653** (2007) 1 , arXiv:0705.2248.

[112] R. N. Cahn and P. V. Landshoff, *Mystery of the Delta (980)*, Nucl. Phys. **B266** (1986) 451.

[113] W. Rarita and J. Schwinger, *On a theory of particles with half-integral spin*, Phys. Rev. **60** (1941) 61.

[114] S. Harnew, *Binning and visualising multi-dimensional data*, https://github.com/samharnew/HyperPlot.

[115] S. S. Wilks, *The large-sample distribution of the likelihood ratio for testing composite hypotheses*, Ann. Math. Statist. **9** (1938) 60.

[116] LHCb collaboration, R. Aaij *et al.*, *Studies of the resonance structure in $D^0 \to K_S^0 K^{\pm}\pi^{\mp}$ decays*, Phys. Rev. **D93** (2016) 052018, arXiv:1509.06628.

[117] B. Efron, *Bootstrap methods: Another look at the jackknife*, Ann. Statist. **7** (1979) 1.

[118] J. Fu, M. Martinelli, and N. Neri, *Search for CP violation using T-odd correlations in $D^0 \to K^+K^-\pi^+\pi^-$ decays*, CERN-LHCb-ANA-2014-033, Mar. 2014.

[119] A. Davis *et al.*, *Measurement of the $K^-\pi^+$ two-track detection asymmetry in Run 2 using the Turbo stream*, CERN-LHCb-INT-2017-023, Sep. 2017.

[120] D. Aston *et al.*, *A study of $K^-\pi^+$ scattering in the reaction $K^-p \to K^-\pi^+n$ at 11 GeV/c*, Nucl. Phys. **B296** (1988) 493.

[121] BaBar collaboration, J. P. Lees *et al.*, *Dalitz plot analyses of $J/\psi \to \pi^+\pi^-\pi^0$, $J/\psi \to K^+K^-\pi^0$, and $J/\psi \to K_S^0 K^{\pm}\pi^{\mp}$ produced via e^+e^- annihilation with initial-state radiation*, Phys. Rev. **D95** (2017) 072007, arXiv:1702.01551.

[122] P. Koppenburg, *Dealing with multiple candidates – an update*, CERN-LHCb-INT-2016-045, Nov. 2016.

162

Maxime SCHUBIGER

Rue du Nord 3
1700 Fribourg
maxime.schubiger@cern.ch   18 April 1989
+41 (0)79 682 05 30   Swiss citizen
OrcID : 0000-0001-9330-1440   ResearcherID : D-1585-2018

Education

EPFL, École polytechnique fédérale de Lausanne, Lausanne

- PhD in particle physics   09.2014-12.2018
  - Search for *CP* violation through an amplitude analysis of $D^0 \to K^+ K^- \pi^+ \pi^-$ decays at LHCb
  - PhD advisor: Prof. Olivier Schneider
- Master in physics   09.2012-02.2014
- Bachelor in physics   09.2009-08.2012

Employment

CHUV, Centre hospitalier universitaire vaudois, Lausanne

- Civil service on image reconstruction from brain MRI scans   03.2014-06.2014
  - Advisor: Dr. Antoine Lutti

Responsibilities

LHCb collaboration

- Alignment piquet   08.2016-current
- Stripping liaison   01.2016-12.2017

Summer schools

SLAC, Stanford University, California, USA

- SLAC Summer Institute : Cosmic opportunities   08.2017
  - Dark matter candidates
  - Large scale structures in the universe
  - Cosmic microwave background

Zuoz, Graubünden, Switzerland

- CHIPP Summer School : Exothiggs   08.2016
  - The standard model and extensions
  - Higgs mechanism
  - Exotic searches

Student supervision

Semester project supervision

- Systematic search for *CP* violation in prompt $D^0 \to K^+K^-\pi^+\pi^-$ decays using triple-product asymmetries

Teaching activities

- Introduction to nuclear and particle physics I & II
  - 3rd year bachelor students
  - Spring semester 2017 and fall semester 2017
- Nuclear physics practical work
  - 3rd year bachelor students
  - Spring semester 2015
- General physics I (mechanics)
  - 1st year bachelor students
  - Fall semester 2014, 2015 and 2016

Active membership in scientific societies

Member of CHIPP (Swiss Institute of Particle Physics)

Personal skills

Languages

- Bilingual :   French-Swiss German
- English :   Level C1, Cambridge Certificate of Advanced English
- German :   Level C1

Digital competences

- Programming languages :   C++, python, Matlab
- Office softwares :   Latex, Microsoft Office
- High energy physics :   Root, LHCb softwares

Hobbies and personal interest

- 1st trumpet in the wind orchestra "La Gérinia" (category excellence)
- Cinema
- Strategic board games
- Skiing